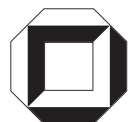


Dissertationsreihe am Institut für Hydromechanik
der Universität Karlsruhe (TH)
Heft 2008/1

Hydrodynamic Processes
at the Water-Sediment Interface
of Streambeds

Martin Detert



Martin Detert

**Hydrodynamic Processes
at the Water-Sediment Interface of Streambeds**

Dissertationsreihe am Institut für Hydromechanik
der Universität Karlsruhe (TH)

Heft 2008/1

Hydrodynamic Processes at the Water-Sediment Interface of Streambeds

by
Martin Detert



universitätsverlag karlsruhe

Dissertation, genehmigt von der
Fakultät für Bauingenieur-, Geo- und Umweltwissenschaften
der Universität Fridericiana zu Karlsruhe (TH), 2008

Referenten: Prof. Gerhard H. Jirka
Prof. Vladimir Nikora
Prof. Dr.-Ing. habil. Andreas Dittrich

Impressum

Universitätsverlag Karlsruhe
c/o Universitätsbibliothek
Straße am Forum 2
D-76131 Karlsruhe
www.uvka.de



Dieses Werk ist unter folgender Creative Commons-Lizenz
lizenziert: <http://creativecommons.org/licenses/by-nc-nd/2.0/de/>

Universitätsverlag Karlsruhe 2008
Print on Demand

ISSN: 1439-4111
ISBN: 978-3-86644-244-3

Hydrodynamic Processes at the Water-Sediment Interface of Streambeds

for Obtaining the Academical Degree of a
DOCTORAL-ENGINEER
at the Department of Civil Engineering, Geo- and Environmental Science
of the University Fridericiana, Karlsruhe (Germany)
approved
DISSERTATION

submitted by
Dipl.-Ing. Martin Detert
from Gehlenbeck (East-Westphalia)

Date of the Oral Exam: 25th April 2008

Supervisor: Prof. Gerhard H. Jirka, Ph.D.
Co-Advisors: Prof. Vladimir Nikora, Ph.D.
Prof. Dr.-Ing. habil. Andreas Dittrich

Karlsruhe, May 2008

Abstract

This thesis focuses on hydrodynamic processes above and within granular beds such as in gravel bed streams, rivers and man-made canals. As a core of the work, laboratory flume experiments were performed. The interaction between turbulent flow and three different kinds of porous beds was investigated. A 2D Particle Image Velocimetry system measuring in streamwise vertical or horizontal planes above the bed was used, synchronized with a sensor array of 16 miniaturized piezometric pressure sensors within and slightly above the bed. This setup enabled the 2D-visualization and quantification of instantaneous simultaneous velocity and pressure fields in the near-bed region. Results under stable bed conditions showed alternating large-scale wedge-like structures of uniform momentum, inclined downstream at an angle of $10 - 20^\circ$ to the bed. Accompanying this, a significant pressure drop was observed in regions where fluid with high velocity interacted with slower moving fluid in the sense of a sweep event. Conditional sampling techniques showed that this flow-pressure interaction is a characteristic pattern. The decay in pressure can lead to the initial lift needed for the entrainment of single grains. Furthermore, it can be seen as the fundamental promoter for the exchange of mass and momentum from the free stream to the hyporrheic interstice – a vitally important factor for the ecological equilibrium of the whole aquatic system. Finally, the experimental findings were used to develop a 'sediment cleaner' formula. This relation predicts the depth within a porous bed from which fine sediment of a given size can be removed by turbulence. Thus, a tool is given to estimate the morphological and in turn ecological efficiency of flash floods downstream of water power plants.

Kurzfassung

Thema dieser Arbeit ist die Erforschung hydrodynamischer Prozesse oberhalb und innerhalb eines überströmten Kiesbettes. Laborexperimente bilden dabei den Schwerpunkt zur Untersuchung der Interaktion zwischen der turbulenten Gerinneströmung und drei Varianten einer porösen Sohle. Ein 2D Particle Image Velocimetry System wurde eingesetzt zur Messung in einer vertikal in Strömungsrichtung aufgespannten Ebene sowie in mehreren horizontalen Ebenen über dem Kiesbett. Jeweils synchron dazu kam eine aus 16 miniaturisierten piezometrischen Drucksensoren bestehende Anordnung innerhalb und leicht oberhalb der porösen Sohle zum Einsatz. Dieser messtechnische Aufbau ermöglichte die zweidimensionale Visualisierung und Quantifizierung von instantanen, simultanen Geschwindigkeits- und Druckfeldern. Ergebnisse bei unbewegter Sohle zeigen kohärente, alternierende, großskalige und keilförmige Strömungsstrukturen. Sie weisen einen typischen, in Strömungsrichtung zur Horizontalen geneigten Winkel von $10 - 20^\circ$ auf. Begleitend hierzu tritt ein signifikanter Druckabfall in Regionen auf, in denen Fluidballen geringer Geschwindigkeit im Sinne eines sweep Ereignisses von Zonen hoher Geschwindigkeit 'überrollt' werden. Mit Hilfe einer conditional sampling Methode konnte gezeigt werden, dass diese Geschwindigkeits-Druck Interaktion einem wiederkehrenden, charakteristischen Muster folgt. Die wirkenden Kräfte sind ausreichend für die initiale Bewegung eines Einzelkornes. Sie können als fundamentaler Motor für den Transport von Masse und Impuls von der Aussenströmung hin zum hyporheischen Interstitial gesehen werden – letztendlich ein lebenswichtiger und entscheidender Faktor für das Gleichgewicht des gesamten aquatischen Ökosystems. Mit den experimentellen Ergebnissen wurde eine 'Sediment-Reinigungs'-Formulierung entwickelt. Diese Beziehung schätzt in einem granularen Bett die Tiefe, bis zu der feines Sediment in Folge von Turbulenzeinwirkung ausgetragen wird. Damit kann z.B. bei Spülfluten durch Wasserkraftwerke vorab eine Beurteilung der morphologischen – und damit auch der ökologischen – Wirksamkeit erfolgen.

Contents

1	Introduction	1
1.1	Background	1
1.2	Research Objectives and Overview	3
2	Governing Processes	5
2.1	Fundamental Equations	5
2.2	Shear Stresses in Open-Channel Flow	7
2.3	Velocity Distributions	12
2.3.1	Free flow	13
2.3.2	Roughness Layer	14
2.3.3	Subsurface Layer	14
2.4	Turbulence Statistics	16
2.4.1	Energy Cascade	16
2.4.2	Turbulence Intensities	17
2.5	Coherent Structures	20
2.6	Fluid Pressure and Resulting Forces	24
2.6.1	Turbulence-Induced Wall Pressure	25
2.6.2	Fluid Forces on Single Particles	26
2.7	Initial Sediment Motion	28
2.7.1	Analytic Approach and Uncertainties in Design Load	28
2.7.2	Shields' Critical Shear Stress Concept	31
2.7.3	Refinements and Further Approaches	32
2.7.4	Role of coherent structures	35
2.8	Concluding Remarks	37
3	Experimental Studies	39
3.1	Laboratory Facilities	39
3.2	Particle Image Velocimetry (PIV)	40
3.3	Acoustic Doppler Current Profiler (ADCP)	43
3.4	Miniaturized Piezo-resistive Pressure Sensors	46
3.5	Bed Material	49
3.6	Experimental Program	52

4	Experimental Results	55
4.1	Bulk Parameters	55
4.2	Measured Velocities	59
4.2.1	Time averaged flow	59
4.2.2	Turbulence intensities	63
4.2.3	Stresses	68
4.2.4	Flow Structures	70
4.3	Measurements of Pressure Fluctuations	80
4.3.1	Time series	81
4.3.2	Histograms	82
4.3.3	Turbulence intensities	86
4.4	Simultaneous Consideration of Velocity and Pressure Fluctuations (Event analysis)	92
4.4.1	Time Series	92
4.4.2	Splicing method	93
4.4.3	Synoptic View	97
4.4.4	Conditional Sampling	105
4.5	Concluding Discussion	109
5	Application: Washout of Fine Sediments	113
5.1	Problem Description	113
5.2	Cleaning Fine Sediment from Gravel	113
5.3	Implementation and Discussion	117
6	Summary and Recommendations	119
6.1	Summary	119
6.2	Recommendations for further studies	120

1 Introduction

1.1 Background

Hydrodynamics plays an important role in most of the physical processes at riverbeds. It controls the mechanisms of erosion and sedimentation, as well as the exchange of mass and momentum between the main flow and the hyporrheic interstice, *i.e.* the void volume in a gravel bed. In this, hydrodynamic processes influence decisively the quality of the habitat for micro-organisms like insects, larvae and fish spawn. Moreover, the hydraulic exchange regulates the reactive processes of the microbial biomass in the form of algae, bacteriae and fungi, as well as the inclusion or mobilization of pollutants and persistent substances like heavy metals or dioxin. Fig. 1.1 gives a schematic illustration on how hydrodynamics influences the physical and biological processes at a streambed.

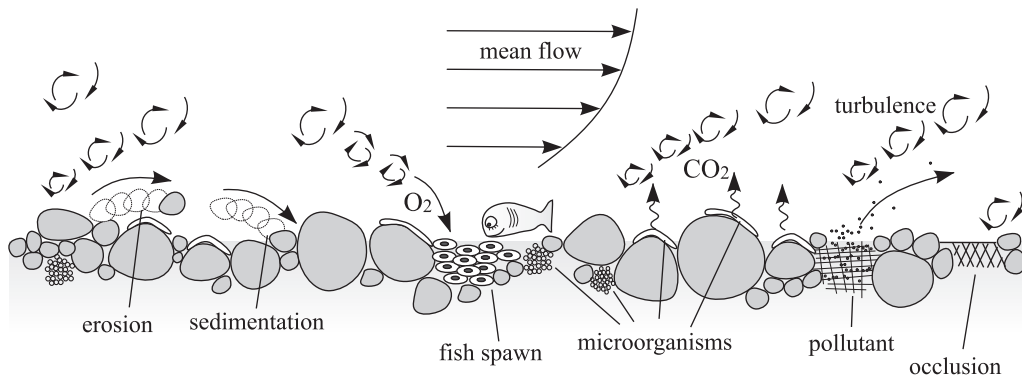


Figure 1.1: Schematic illustration of turbulence-related phenomena such as sediment transport, flow-biota interactions and pollutant spreading.

The adequate knowledge of sediment transport is one of the main challenges in hydraulic engineering. In the idealized case of undisturbed intact river dynamics, the bed load transport is balanced by both erosion and sedimentation processes. The bed texture is re-ordered from time to time, mainly due to flood events. Occlusion effects are seldom and a broad biological diversity is predominant. However, in most European rivers the effects of bed load feeding are actually strongly attenuated by barrages in the upper reaches as well as regulation works and urban developments in the confluences. The result is a deficit in bed load. For instance, the Elbe River deepens by 1-2 cm/year in a length of 110 km between Torgau and Wittenberg. Consequently, a decreased water level causes – beside the problems for navigation – negative effects on the ground water level and in turn on the whole ecosystem of the floodplain.

1 Introduction

Predicting the morphodynamic development of a river bed depends essentially on the adequate modeling of small-scale processes in the order of milliseconds and sub-millimeters to get aggregate information on the river evolution over much larger time and space scales. Over the last 100 years much research work has been done to obtain insight into the background of bed stability. Shields (1936) developed the concept of a critical shear stress to estimate the boundary between a stable and a moving bed, established by averaged parameters of flow and granular material. Until the present day, the majority of prediction techniques have been based on this classical work or empirical modifications thereof, and highly time dependent flow dynamics are not explicitly taken into consideration. The reason is trivial: the understanding of hydrodynamical processes and their interaction with a porous bed is not developed far enough. Consequently, a considerable scatter between predicted and actual morphodynamic development is inevitable. To minimize this scatter, a thorough understanding of the physical mechanisms is needed. For a derivation of a physically-founded description of the flow-induced, fluctuating forces acting on the bed, information on both the dynamical structure of the open-channel flow and the interstitial pore flow, as well as their interaction, is necessary.

Kline *et al.* (1967) showed that turbulent flow is not simply chaotic, but includes well-organized coherent structures. Inspired by these findings, various studies on turbulent coherent flow structures were carried out thereafter, for both smooth walls (*e.g.* Head & Bandyopadhyay, 1981; Zhou *et al.*, 1996; Adrian *et al.*, 2000*b*) and also for rough beds (*e.g.* Grass *et al.*, 1991; Shvidchenko & Pender, 2001; Stösser *et al.*, 2005). Macro-turbulent coherent structures in natural rivers, similar to those reported for laboratory experiments, were revealed to be elongated in shape and scale with the flow depth (Roy *et al.*, 2004). Sutherland (1967) and Jackson (1976) pioneered the relations between coherent structures and sediment erosion and transport. Experimental results show that these structures play an important role at the incipient point of grain motion (*e.g.* Drake *et al.*, 1988; Sechet & Le Guennec, 1999; Hofland & Booij, 2004). Thereby, progress in the way of studying coherent structures depends essentially on the development of computer power for data processing and numerical simulations as well as on refinements in measurement and data analyzing techniques, especially for flow visualization.

Most of the above mentioned studies focused on the velocity field in a vertical stream-wise plane, disregarding its lateral extension as well as the bed permeability. Pressure measurements were conducted with much less intensity in the past, mainly due to their reduced applicability in water flume experiments. However, since recent developments in measurement techniques overcame their shortcomings, high-resolution pressure measurements can be conducted also in rough bed flows (*e.g.* Hofland *et al.*, 2005).

A comprehensive measurement campaign has to be conducted to develop a synoptic understanding of the individual hydrodynamic processes and especially their interaction with a porous river bed. Not until then can a detailed knowledge about the hydrodynamic processes serve both engineers and biologists as a tool to understand, to predict, and to improve the ecological development of the whole aquatic habitat of a river.

1.2 Research Objectives and Overview

This thesis focuses on the hydrodynamical processes that occur in the main flow and within rough porous beds. Laboratory measurements and their detailed analysis are the core of this work. The hydrodynamics of open-channel flow, interstitial pore flow, and especially their interaction are investigated in a physical flume experiment.

The first aim of this thesis is a refined understanding of the hydrodynamics of flow and pressure above and within a porous river bed. To do so, simultaneous measurements of the physical loads due to both velocity fields and pressure fields – respectively on top and within the porous bed as well as in the turbulent open-channel flow – will be performed. To this end, miniaturized pressure sensors have to be developed, calibrated and tested. A particle image velocimetry (PIV) system has to be adapted to the flume conditions. Rough-bed flow measurements will then be based, for the first time, on the simultaneous use of an array of pressure sensors and an image velocimetry technique. A synoptic view of instantaneous pressure fields and velocity fields will be realized by analysis techniques applied to the data sets obtained. Key topics are the identification and the quantification of relationships between instantaneous flow fields (including the region below roughness tops) and resulting bed-pressure fields. The bed-pressure is closely connected to the velocity field and gives a direct insight into the turbulent flow regime as well as to drag and lift forces.

The second aim is to significantly improve the understanding of the physical processes involved in erosion and near-bed transport of sediments. The findings concerning typical pressure-fields and closely connected flow structures provides a useful basis for confirming and supplementing existing entrainment models. The principal findings will be involved in these models. The attainment of this objective will provide a basis for future development of an advanced conceptual framework for designing better relationships for predicting sediment entrainment.

The thesis contains the following elements:

- The governing processes are elucidated by a literature review (Chapter 2).
- A description is presented of the arrangement and instrumentation of the experimental flume. An image velocimetry system was installed and calibrated for measuring near-bed flow structures, highly resolved in time and space. Miniaturized pressure sensors were developed, tested and inserted (Chapter 3).
- The experimental results are analyzed and presented in comparison with the state of research elaborated in Chapter 2. Data analysis techniques are spatial filtering, spectral analysis and spectral separation techniques, FIR-filtering, cross- and autocorrelation, and vortex identification techniques. Taylor's hypothesis is used to transform time series of pressure to spatial pressure fields. Data analysis techniques like splicing methods of vector fields and conditional sampling techniques help to identify the essential physical processes. In this, the mechanisms of interaction between the outer flow and the hyporrheic interstitial flow are described. The results are discussed (Chapter 4).

1 Introduction

- As an example, a practical approach is developed to predict the wash-out effect of fine sediment in a stable porous bed, based on the principal findings of the experimental study (Chapter 5).
- A summary reflects the essential findings of this thesis. Recommendations concerning open questions and forthcoming research projects are given (Chapter 6).

2 Governing Processes

Abstract. *A literature review concerning the hydrodynamic processes above and within porous beds underlying open-channel flow is given. The governing equations are presented, including double averaging methodology. In turbulent open-channel flow, the momentum transfer within the fluid domain is directly linked to the drag at the bed-wall perimeter. Shear essentially dominates the velocity distribution. A flow layer concept is introduced for mean velocities, based on characteristic length and time scales. A distinction is made between the free flow, the flow in the roughness layer and the subsurface flow in a porous bed. Then, the properties of turbulence are handled. Turbulence is realized at the expense of mean-flow energy, where turbulent energy is transferred in a cascading process of eddies and finally is dissipated at the smallest scales. Turbulence intensity distributions are given for open-channel flow as well as for porous bed flow. However, turbulent flows are not simply chaotic and random: related and self-sustaining flow patterns can be observed repeatedly, so-called coherent structures. A fluid domain is characterized by both flow velocities and pressure. Fluid pressure, turbulent wall pressure fluctuations, and the resulting forces on single grains are treated subsequently. Several approaches to sediment entrainment are presented.*

2.1 Fundamental Equations

Fluid motions are described by the mass conservation equation,

$$\frac{\partial \rho}{\partial t} + \frac{\partial \rho u_i}{\partial x_i} = 0 , \quad (2.1)$$

and by the Navier¹-Stokes² momentum conservation equations, respectively,

$$\frac{\partial u_i}{\partial t} + u_j \frac{\partial u_i}{\partial x_j} = g_i - \frac{1}{\rho} \frac{\partial p}{\partial x_i} + \frac{\partial}{\partial x_j} \left(\nu \frac{\partial u_i}{\partial x_j} \right) , \quad (2.2)$$

where $i, j = [1, 2, 3]$ following the Einstein³-notation. The spatial coordinates are $x_{i,j}$ and t denotes time. $u_i = i^{\text{th}}$ component of the velocity vector, $p =$ pressure, $g_i = i^{\text{th}}$ component of gravitational acceleration, $\rho =$ fluid density and $\nu =$ kinematic viscosity. Unfortunately, exact analytical solutions are only available for a few exceptions, like laminar flow with simple geometrical boundaries. The remaining analytically unsolvable flow problems can be approximated by numerical methods, however.

¹Claude Louis Marie Henri Navier: * 1785 in Dijon (F); † 1836 in Paris (F)

²Sir George Gabriel Stokes: * 1819 in Skreen (IRL); † 1903 in Cambridge(UK)

³Albert Einstein: * 1879 in Ulm (D); † 1955 in Princeton (USA)

2 Governing Processes

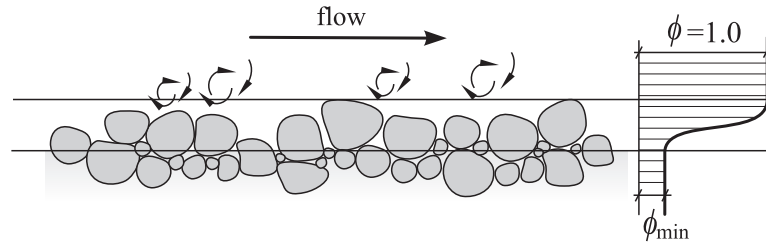


Figure 2.1: Flow influenced by the heterogeneity of a rough permeable bed and definition of the roughness geometry function ϕ .

To describe the turbulent flow above and within a rough and porous bed, some modifications of eqs 2.1 and 2.2 have to be carried out as additional drag forces have to be considered. Fig. 2.1 gives a sketch of the flow situation. Nikora *et al.* (2001) suggested to use a double averaging methodology (DAM) to describe the hydraulics in the near-bed region. In DAM, the porosity of the near-bed region is considered by the roughness geometry function. It is defined as

$$\phi = V_f/V_o \quad \text{with } 1 \geq \phi \geq 0, \quad (2.3)$$

where V_f is the volume of fluid within the total volume V_o . The spatial averaging is carried out over thin layers parallel to the mean bed. The instantaneous velocity is temporally and spatially decomposed as

$$u_i = \bar{u}_i + u_i' \quad (2.4a)$$

$$= (\langle \bar{u}_i \rangle + \tilde{u}_i) + u_i'. \quad (2.4b)$$

Here, the straight overbar and angle brackets denote the temporal and spatial average of flow variables, respectively. The prime denotes temporal fluctuations, the tilde denotes spatial fluctuations in the time-averaged flow variable. Eq. 2.4a is also called a Reynolds⁴-decomposition. If flow over a fixed bed, $\langle \phi(t) \rangle = 0$, is considered, the double-averaged (*i.e.* in time and space) versions of eqs 2.1 and 2.2 can now be written as (Nikora *et al.*, 2007a)

$$\rho \frac{\partial \phi}{\partial t} + \rho \frac{\partial \phi \langle \bar{u}_i \rangle}{\partial x_i} = 0 \quad (2.5)$$

and

⁴Osborne Reynolds: * 1842 in Belfast (UK); † 1912 in Watchet (UK)

$$\begin{aligned}
 \frac{\partial \langle \bar{u}_i \rangle}{\partial t} + \langle \bar{u}_j \rangle \frac{\partial \langle \bar{u}_i \rangle}{\partial x_j} = & g_i - \frac{1}{\phi \rho} \frac{\partial \phi \langle \bar{p} \rangle}{\partial x_i} - \underbrace{\frac{1}{\phi} \frac{\partial \phi \langle \bar{u}'_i \bar{u}'_j \rangle}{\partial x_j}}_{\text{turbulence term}} - \underbrace{\frac{1}{\phi} \frac{\partial \phi \langle \tilde{u}_i \tilde{u}_j \rangle}{\partial x_j}}_{\text{form-induced term}} + \underbrace{\frac{1}{\phi} \frac{\partial}{\partial x_j} \phi \left\langle \nu \frac{\partial \bar{u}_i}{\partial x_j} \right\rangle}_{\text{viscosity term}} \\
 & + \underbrace{\frac{1}{\rho} \frac{1}{V_f} \iint_{S_{\text{int}}} \bar{p} n_i dS}_{\text{pressure drag term}} - \underbrace{\frac{1}{V_f} \iint_{S_{\text{int}}} \left(\nu \frac{\partial \bar{u}_i}{\partial x_j} \right) n_j dS}_{\text{viscous drag term}}, \tag{2.6}
 \end{aligned}$$

where $\rho \langle \bar{u}'_i \bar{u}'_j \rangle$ and $\rho \langle \tilde{u}_i \tilde{u}_j \rangle$ are respectively called the spatially averaged Reynolds (or turbulent) stresses and the form-induced (or dispersive) stresses, while $\nu \partial \langle \bar{u}_i \rangle / \partial x_j$ denotes the viscous stresses. Note that the viscous term sometimes is neglected for special cases (*e.g.* Coleman *et al.*, 2007). This may not be valid between gravel particles, however. Further on, the two terms on the right hand side respect to the pressure drag and the viscous drag. S_{int} is the roughness-fluid surface interface within the averaging volume, n_i is the i^{th} component of the unit vector normal to the surface element dS and directed into the fluid. For the incompressible fluid phase $\rho = \text{const.}$, thus $\partial \rho / \partial t = 0$ holds, and for steady water flow $\partial(\cdot) / \partial t = 0$ is valid in general. Consequently, eqs 2.5 and 2.6 can be made less complex (not shown here).

2.2 Shear Stresses in Open-Channel Flow

In turbulent open-channel flow, the momentum transfer within the fluid domain is directly linked to the drag at the bed-wall perimeter and also dominates the velocity distribution. Thus, an in-depth understanding of the flow is based on the knowledge of the momentum flux. In the following, the distribution of the different stress terms in 2D and 3D flow as well as in uniform and non-uniform flow will be worked out. A right-handed coordinate system is implied as illustrated in fig. 2.2, where x is orientated positive in global, stream-wise flow direction, y in upwards vertical and z in transverse direction. $x = 0$ holds at a typical point of interest, *e.g.* the mid of a measurement area. $y = 0$ defines a notional wall level. Hereinafter, the mean bed level gives the zero-plane, as found by a log-fit of the

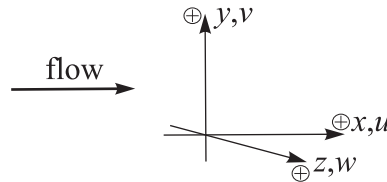


Figure 2.2: Definition of a right-handed coordinate system and the corresponding velocity components, as used hereinafter. The transverse axis is directed out of the plane.

2 Governing Processes

mean streamwise $\langle \bar{u} \rangle$ to zero. $z = 0$ is located in the centerline of the flow (river, channel, or flume). The velocity components u, v and w correspond to x, y and z , respectively.

2D Uniform Flow (Wide Channels). In case of a steady, uniform 2D flow, the fluid motion is independent of the lateral dimension z and only differences in vertical direction, y , are of interest, thus $\partial(\cdot)/\partial x = 0$. Consequently, eq. 2.6 can be simplified. After integration along the streamwise axis the result reads

$$\underbrace{\rho g S_b (h - y)}_{\text{gravity term}} = \underbrace{-\rho \langle \overline{u'v'} \rangle - \rho \langle \tilde{u}\tilde{v} \rangle + \nu \frac{\partial \langle \bar{u} \rangle}{\partial y}}_{\text{fluid stresses } \langle \bar{\tau} \rangle (y)}, \quad (2.7)$$

where h is the water depth, and S_b is the mean bed slope with $dx/dy = \tan \alpha = S_b \approx \sin \alpha$. Note that eq. 2.7 holds for the flow above the roughness tops. Below, two drag terms (viscous and pressure) will appear in this equation serving as momentum sinks. The right hand side of eq. 2.7 depicts the components of the double-averaged fluid stresses, $\langle \bar{\tau} \rangle (y)$, the left hand side is the gravity term. Fig. 2.3 gives an illustration of the distribution of the particular stresses. The vertical distribution is linear, from zero at the water surface to a maximum at the theoretical (notional) wall level, as balanced by the right hand side terms.

In a 2D approach where no side wall friction is possible, $\tau_o \equiv \langle \bar{\tau} \rangle (y=0)$ is given per definition. Consequently, the stress that acts on the boundary follows from eq. 2.7 to be

$$\tau_o = \rho g S_b h. \quad (2.8)$$

Eq. 2.8 represents a simple force balance between the gravity component of the fluid mass (right hand side) and the reaction of the bed (left hand side).

As the form induced stress and the viscous stress are of minor importance at a certain distance from the bed, the vertical distribution of the Reynolds stresses becomes linear in the far bed region. As direct measurements of shear stresses are difficult, this linearity is often used to extrapolate to the total fluid stress that acts on the perimeter P .

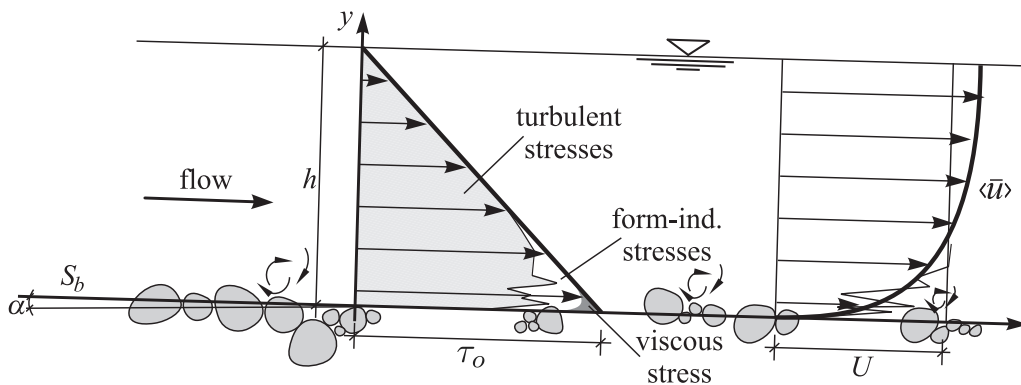


Figure 2.3: Uniform, turbulent 2D open-channel flow. Vertical distribution of stresses and velocities.

3D Uniform Flow (Narrow Channels with Wall Effects). The aforementioned elaborations considered the flow from a 2D view, independent of the lateral extension z . The influence of side walls was not taken into consideration. Let the side walls in a 3D flow be frictionless, then eq. 2.8 would be valid. However, in real flows this is never the case. To satisfy the force balance eq. 2.8 has to be modified: The water depth h in eq. 2.8 has to be replaced by the hydraulic radius, $R_h = A/P$, with A being the area of the cross section. Then the boundary shear, $\tau_o \equiv \langle \bar{\tau}_o \rangle_P$, as a spatial average over the wetted perimeter P reads

$$\tau_o = \rho g S_b R_h . \quad (2.9)$$

Fig. 2.4 shows the shear stress distribution at the perimeter of a rectangular flume with an aspect ratio of $B/h = 2$, where B is the flume breadth. Within a crude approach the averaged shear stresses at the bed, $\langle \bar{\tau}_o \rangle_b$, and at the sidewalls, $\langle \bar{\tau}_o \rangle_s$, are approximately of the same magnitude. However, this approach is misleading, as the observed shear distribution is indeed non-even. Associated with this, secondary currents become prominent: Superposed on the dominating streamwise main flow, near-wall fluid is transported upwards to the water surface and there, the flow goes in direction to the flume centerline. As a consequence, the location of the maximum velocity, δ_h , is shifted from the water surface towards the bed. Typically, the maximum flow velocity in the secondary currents is $< 5\%$ compared to the main flow velocity.

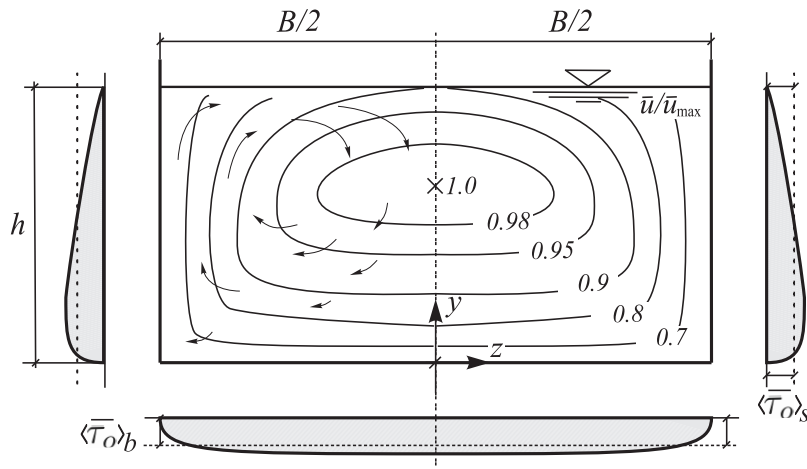


Figure 2.4: 3D open-channel flow. Idealized distribution of boundary shear and associated secondary currents in a rectangular, straight-lined flume ($B/h = 2$). Shear stress distribution estimated after Chow (1959), flow data taken from Nezu & Nakagawa (1993).

In open-channel flows, even if they are straight, the clarification of 3D motions in form of secondary currents is essential to understand the shear stress distribution. Nezu & Nakagawa (1993) gave a description to the primary Reynolds stresses, $-\rho \overline{u'v'}$, for a 3D view. In relation to time averaged properties (here: not the double-averaged characteristics),

2 Governing Processes

and by neglecting viscous stresses at a certain distance from the bed, they derived

$$-\overline{\rho u'v'}(y) = \rho g S_b (h - y) - \underbrace{\rho \int_{\hat{y}}^h \bar{v} \frac{\partial \bar{u}}{\partial y} dy - \rho \int_{\hat{y}}^h \bar{w} \frac{\partial \bar{u}}{\partial z} dy - \rho \int_{\hat{y}}^h \frac{\partial \overline{u'w'}}{\partial z} dy}_{\text{terms due to secondary currents}} . \quad (2.10)$$

As the additional terms on the right hand side cannot be neglected, an estimation of τ_o by a linear extrapolation of $-\overline{\rho u'v'}$ – as in 2D flows (eq. 2.8) – may lead to misinterpretation, since the Reynolds stress is different from the value due to the gravity component. However, experimental data indicate that the sum of the additional terms on the right hand side is almost constant over a wide region of both the water depth and channel width (Nezu & Nakagawa, 1993; Song, 1994; Yang *et al.*, 2004). Fig. 2.5 shows data of the vertical distribution of the primary Reynolds stresses for the case of $B/h = 2$. In fact, the value of $-\overline{\rho u'v'}$ approximately maintains its linear distribution in the mid region, but in the vicinity of the water-surface it becomes negative. This feature is connected to the velocity-dip phenomenon, where the maximum velocity, \bar{u}_{\max} at $\partial \bar{u} / \partial y = 0$ (factor in the second term on the right hand side of eq. 2.10), appears not at the free surface, but below at $y = \delta_h$. Its magnitude depends on the channel characteristics (*e.g.* cross section geometry, bed/wall roughness, channel aspect ratio) and the spatio-temporal flow variations. It is located in the region between $0.5h < \delta_h < h$, as between idealized 3D closed channel flow in a square duct and 2D-flow, respectively.

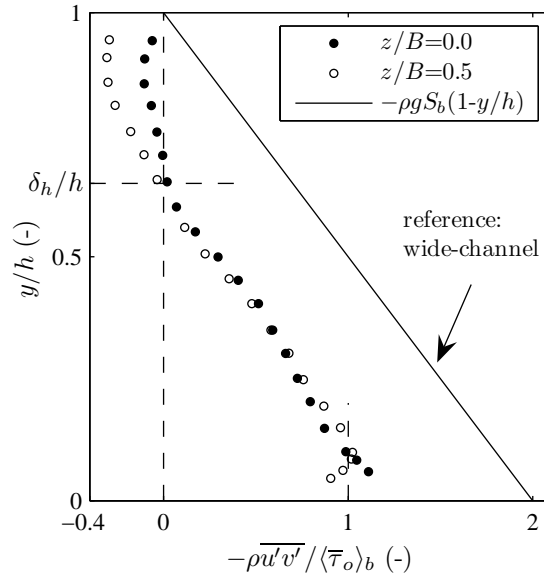


Figure 2.5: Measured vertical distributions of $-\overline{\rho u'v'}$ in a smooth rectangular channel ($B/h = 2$), where $\delta_h/h \simeq 0.65$ and $\tau_o \approx \langle \bar{\tau}_o \rangle_b$. Reference is given to a (hypothetical) 2D-case with frictionless sidewalls (eq. 2.8). Data from Nezu & Nakagawa (1993, p. 108).

Yang *et al.* (2004) gave an applicable formula to describe the velocity dip phenomenon in rectangular channels. They fitted experimental data from six papers and their own experiments. The following eq. 2.11 is deduced from their results. (Recall that in the present report $z = 0$ is located in the centerline of the flume.)

$$\delta_h/h = \left(1 + 1.3 \exp\left(\frac{|z| - B/2}{h}\right) \right)^{-1}. \quad (2.11)$$

For practical purposes in streams or man made channels it is of interest, to what portions the total fluid force, F_o , is carried out by respectively the bed and the side-walls. To approach the problem, a subdivision of friction forces is rearranged to

$$\tau_o \cdot dxP = \langle \bar{\tau}_o \rangle_b \cdot dxP_b + \langle \bar{\tau}_o \rangle_s \cdot dxP_s \quad (2.12a)$$

$$\Leftrightarrow F_o = F_b + F_s \quad (2.12b)$$

where the averaged bed friction is denoted as $\langle \bar{\tau}_o \rangle_b$ and the averaged side-wall friction is $\langle \bar{\tau}_o \rangle_s$, with the corresponding perimeter lengths of P_b and P_s , and the corresponding friction forces F_b and F_s , respectively. Knight *et al.* (1984) presented an empirical formula to predict the ratio F_s/F_o for rectangular open-channels as a function of B/h . Nezu & Nakagawa (1993, p.95) extended the relation to both B/h and the relative roughness $k_{s,b}/k_{s,s}$, with $k_{s,i}$ being the equivalent sand roughness for the bed and the side wall. Surprisingly, the relative roughness revealed to have only a marginal effect on the friction relation F_s/F_o . However, F_s has to be taken into consideration for rough bed open-channel flows, even if the side walls are smooth: for a rough bed and smooth walls, *e.g.* $k_{s,b}/k_{s,s} = 10^3$, and $B/h = 5$, a ratio of $F_s/F_o = 0.19$ holds. Consequently, a crude assumption of $k_{s,b}/k_{s,s} \rightarrow \infty$ would lead to an overestimation of the real bed shear $\langle \bar{\tau}_o \rangle_b$, here by 23%, whereas $k_{s,b}/k_{s,s} \rightarrow 1$ would underestimate $\langle \bar{\tau}_o \rangle_b$ by 18%. Several sidewall correction methods to compute the effective bed shear are reviewed in Cheng & Chua (2005). In addition to these correction methods, Guo & Julien (2005) presented a semi-analytical solution for smooth rectangular open-channel flows, which showed to be in good agreement with experimental data.

3D Non-Uniform Flow. Eq. 2.8 is strictly speaking only valid for $dh/dx = 0$. An extension to non-uniform flow can be made by following the momentum equation. In this, $\tau_o(x) \equiv \langle \bar{\tau}_o \rangle_P(x)$ is determined by

$$\tau_o(x) = \rho g S_b R_h - \rho \left(g R_h + \beta U^2 \frac{R_h}{h} \right) \frac{dh}{dx}. \quad (2.13)$$

In eq. 2.13,

$$\beta = (U^2 h)^{-1} \int (\bar{u}^2 + \overline{u'^2}) dh \quad (2.14)$$

is the momentum non-uniformity parameter (Fenton, 2005) and U is the bulk velocity. For a 2D, uniform flow with $dh/dx = 0$, eq. 2.13 again reduces to the simpler relation given in eq. 2.8. Reynolds-stresses at rough beds underlying non-uniform flow were intensively

studied by Song (1994). He showed that an accelerated flow causes a concave form, whereas an decelerated non-uniform flow gives a convex shape. Lately, Dey & Lambert (2005) theoretically developed equations for the Reynolds-stress distributions in 2D non-uniform flow and verified them by experimental data. Their results confirm the findings of Song (1994) concerning respectively a concave and convex shape of the turbulent stress distributions, correlated to the relative non-uniformity case.

2.3 Velocity Distributions

Depending on the significance of the fluid stress components, as well as on characteristic length, and velocity scales, several vertical layers can be distinguished in open-channel flows (*e.g.* Monin & Yaglom, 1971; Nezu & Nakagawa, 1993). Following the concept of Nikora *et al.* (2001), five different layers for rough permeable bed flow can be defined. These are from top to bottom: (1) the outer layer, (2) the logarithmic layer, (3) the form-induced sublayer (4) the interfacial sublayer, and (5) the subsurface layer. Fig. 2.6 likewise depicts these layers. They will be worked out in detail in the following. For the purpose of this report, a summary is chosen as free flow (1,2), roughness layer (3,4) and subsurface layer (5).

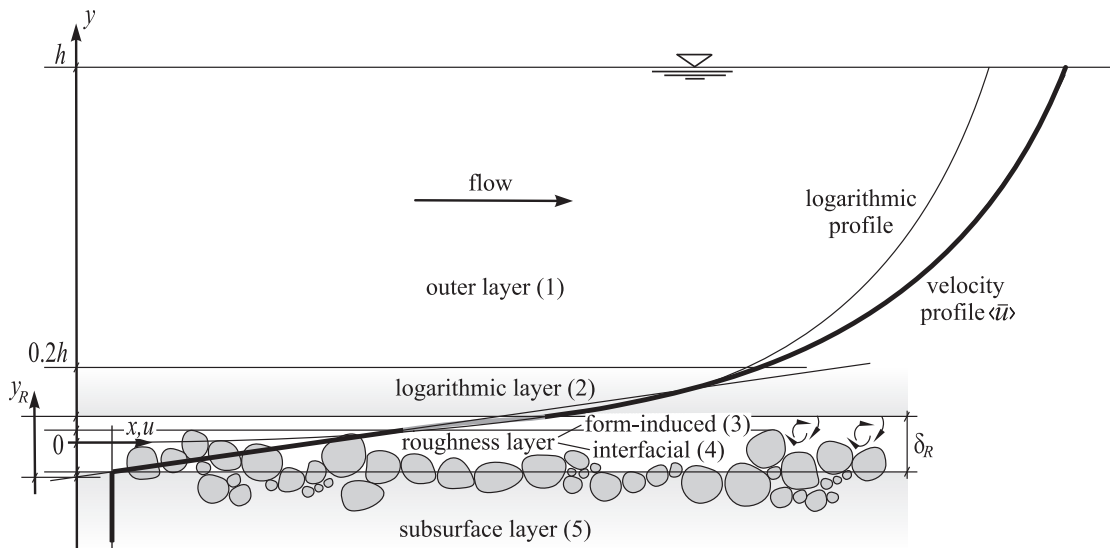


Figure 2.6: Flow layers for 2D open-channel flow with a rough permeable bed (after: Nikora *et al.*, 2001).

The following elaborations consider double-averaged 2D-flow conditions, although most of them also hold for 3D-flow underlying secondary currents. In case of the outer layer, some differences will be addressed.

2.3.1 Free flow

The **outer layer** and the **logarithmic layer** are regions where the viscous and form induced stresses are negligible. Typical length scales are h (or δ_h), the representative (medium) grain size as a measure of the geometrical roughness height d , and the shear stress τ_o , that has to be carried by the bed/side-wall boundaries. In its kinematic form the latter is called shear (stress) velocity or friction velocity, as it appears with units of [length/time]. It is defined as

$$u_* = \sqrt{\tau_o/\rho} . \quad (2.15)$$

The shear velocity u_* is a universal velocity scale for the whole flow regime. However, as τ_o varies around the perimeter and depends on the zero-plane definitions, the determination of u_* is often difficult. Pokrajac *et al.* (2006) worked out how different definitions of u_* significantly affect data interpretation. They denoted that there is no general consensus in literature on the appropriate choice of u_* for rough beds. Thus, comparisons between u_* from different experimental data have to be handled carefully. Typically, it reaches values of (0.05-0.10) U in natural flows.

Following Prandtl's⁵ mixing length approach, the vertical velocity profile in the logarithmic layer, the log-law, reads after integration for uniform, hydraulically rough flow

$$\frac{\langle \bar{u} \rangle (y)}{u_*} = \frac{1}{\kappa} \ln \frac{y}{k_s} + C . \quad (2.16)$$

The empirical universal von Kármán⁶ constant is $\kappa \simeq 0.41$ for high submergence flow, $k_s \ll h$. The integration constant for turbulent rough bed flow is typically $C \simeq 8.5 \pm 0.2$ (Song, 1994).

For a rough, porous bed several definitions of the reference horizon ($y = 0$) are available. Generally, it is set to a position below the top of the roughness elements. One approach is found by a best data fit to eq. 2.16 and then extrapolating to $u(y) = 0$. A simplified approach to the zero plane being below $0.25d$ of the roughness crest was made by van Rijn (1984). Referring to Nezu & Nakagawa (1993, pp. 26), for sand-grain roughnesses the range of (0.15-0.3) k_s is a gross standard for this vertical shift towards the bed. A detailed literature review to this is given in Dittrich (1998).

Experimental data has shown that Prandtl's mixing length approach is only valid in a near-bed region of less than $0.2h$, *i.e.* the logarithmic layer. Consequently, eq. 2.16 has to be modified for the outer layer. In analogy of boundary layer flow to shear flow in a wake, Coles (1956) introduced an empirical wake function ω . Nezu & Rodi (1986) showed that the wake function written as

$$\omega = \frac{2\Pi}{\kappa} \sin^2 \left(\frac{\pi y}{2h} \right) , \quad (2.17)$$

is suitable for open-channel flow. It has to be superposed on the right hand side of the log law in eq. 2.16 to give a more precise description of the outer layer flow. Coles'

⁵Ludwig Prandtl: * 1875 in Freising (D); † 1953 in Göttingen (D)

⁶Theodore von Kármán: * 1881 in Budapest (H) as Tódor Kármán; † 1963 in Aachen (D)

2 Governing Processes

wake strength parameter $\Pi = 0.15-0.30$ has a large variation for open-channel flows, as it depends on the flow conditions and the bulk Reynolds-number $Re_h = Uh/\nu$.

In case secondary currents are present, several authors propose to apply eq. 2.17 with the dip position δ_h instead of h (e.g. Song, 1994; Bezzola, 2002; Guo & Julien, 2008). Another approach was made by Yang *et al.* (2004). They found for the outer region that the velocity deviation from the log-law is proportional to $\ln(1 - y/h)$.

In case of smooth walls, the logarithmic layer is dominated by viscosity effects instead of roughness effects. The equivalent of the roughness length scale, k_s , is the viscous length scale ν/u_* , with ν being the kinematic viscosity. Yang (2005) proposed to use $\nu/u_{*b}(z)$ alternatively, as also k_s depends locally on the boundary parameter, whereas he stated that the left hand side in eq. 2.16 is still ruled by the global u_* . Concerning the outer layer, eq. 2.17 is applicable for rough and smooth wall flow.

2.3.2 Roughness Layer

The **form-induced sublayer** and the **interfacial sublayer** can be summarized as the roughness layers. The main characteristic scales of both are u_* and a set of scales that distinguishes the bed topography (k_s , d , ϕ , grain size distribution, grain shape). The form-induced sublayer occupies the region above the roughness crest, *i.e.* $\phi(y) = 1$ (see also fig. 2.1), and is influenced by flow separation from the roughness elements that cause form induced stresses. The interfacial sublayer occupies the region between the roughness crests and troughs, $\phi_{\min} < \phi(y) < 1$. For rough bed flow, like on sediment beds, Nikora *et al.* (2004) suggest a linear velocity distribution, where the form-induced sublayer with its transition function between logarithmic layer and the interfacial sublayer is neglected. Consequently, the interfacial sublayer becomes the thickness of the whole roughness layer, δ_R . Typical values are $\delta_R = (0.5 - 2) k_s$. For rough impermeable beds the velocity distribution can now be written as (Nikora *et al.*, 2001)

$$\frac{\langle \bar{u} \rangle(y)}{u_*} = C \frac{y_R}{\delta_R}, \quad (2.18)$$

where the vertical coordinate y_R is related to the theoretical log-law wall level as schematized in fig. 2.6. In the sense of Nikora *et al.* (2001), an approximation by $y_R \simeq y$ holds. Then $C \approx (5.3 - 5.6)$ applies for gravel beds and $C \approx 8.5$ for homogeneous sand roughness, both gained from only a small set of measurements.

For hydraulically smooth beds the viscous sublayer refers to the interfacial sublayer. The role of the form-induced sublayer is similar to that of the buffer sublayer, where the velocity profile is described by a hyperbolic tangent function between the viscous sublayer and the logarithmic layer.

2.3.3 Subsurface Layer

The upper boundary of the **subsurface layer** in permeable beds can be identified where $d\phi/dy \approx 0$, *i.e.* where a constant ϕ_{\min} is reached. The flow velocity is almost constant by $d\langle \bar{u} \rangle/dy = 0$. The flow is driven by the gravity force, by momentum flux and long

wave pressure differences induced from the above layers. Characteristic scales are u_* and the typical pore diameter d_f . Breugem (2005) suggested to use $d_f = \sqrt{K}$ to classify the effective pore diameter, with $K = \nu k_f/g$ being the porous medium (or intrinsic) permeability and k_f being the permeability coefficient.

A classical approach to turbulent flow in a saturated porous medium is made by the Forchheimer⁷-equation. In a macroscopic 1D view the pressure difference along a closed conduit with uniform flow reads

$$-\frac{1}{\rho g} \frac{d\langle \bar{p} \rangle}{dx} = \frac{1}{k_f} \langle \bar{u} \rangle + \frac{C_F}{g\sqrt{K}} \langle \bar{u} \rangle^2. \quad (2.19)$$

The dimensionless coefficient C_F has to be determined by experiments. For $C_F = 0$, eq. 2.19 represents the Darcy⁸-law for laminar groundwater flow. The filter velocity or effective velocity within the pores is determined by $\langle \bar{u}_f \rangle = \langle \bar{u} \rangle / \phi$. However, the approach made by eq. 2.19 pays no regard to the interaction with the above layers.

Several experimental and numerical studies were undertaken to investigate the exchange between porous medium flow and open-channel flow (Prinos, 2004). Unfortunately, most of the studies focussed on laminar outer flow and high porosities, as these conditions were easier to explore. Only a few reports are of explicit interest for gravel bed flows. Two of them are highlighted in the following:

Shimizu *et al.* (1990) examined the interaction between open-channel flow and seepage flow within a permeable medium of glass beads ($\phi = 0.35-0.38$, $h/d = 1-3$, $Re_h = Uh/\nu = 8 \cdot 10^3-4 \cdot 10^5$). Experiments were conducted to measure the velocity profile and the vertical mass transport in the porous medium beneath the free surface flow. Subsequently, Shimizu *et al.* derived a semi-empiric macroscopic model to describe a seepage-flow velocity profile based on an eddy-viscosity assumption. This profile decreases exponentially with increasing depth in porous medium. Far from the interfacial boundary, the seepage flow becomes uniform. In their work, a problem remained in determining the slip velocity $\langle \bar{u} \rangle(y=0)$ at the interface between the free surface flow and the porous medium, as it has to be identified by considering the degeneration of the free surface flow due to the alternation of transpiration through the permeable boundary. Shimizu *et al.* (1990) determined the slip velocity simply by curve fitting from measured velocities within the porous medium.

Detert *et al.* (2007) carried out measurements by a 3D particle tracking velocimetry system (3D-PTV) using miniaturized endoscopic stereo setups within artificial pores in a homogenous porous gravel bed underlying open-channel flow ($\phi \simeq 0.40$, $h/d = 20$, $Re_h = 6 \cdot 10^4-2 \cdot 10^5$). They gave $\langle \bar{u}_f \rangle / u_* < 0.25-1$ as a rule-of-thumb to characterize the subsurface layer flow in a gravel bed.

⁷Philipp Forchheimer: * 1852 in Vienna (A); † 1933 in Dürnstein (A)

⁸Henry Philibert Gaspard Darcy: * 1803 in Dijon (F); † 1858 in Paris (F)

2.4 Turbulence Statistics

2.4.1 Energy Cascade

The generation of turbulence is realized at the expense of mean-flow energy. In 2D uniform flows, the rate of turbulent energy generation (or production) is given by $G = -\overline{u'v'}\partial\langle\bar{u}\rangle/\partial y$. With ϵ being the total turbulent dissipation and D_{tv} representing both turbulent and viscous diffusion terms the turbulent energy equation is

$$G = \epsilon + D_{tv} . \quad (2.20)$$

The turbulence generation G produces fluctuations associated mainly with large-scale eddies closely related to the flow depth. The turbulent kinetic energy, k_E , of these large-scale eddies is then transferred to smaller-scaled eddies through a cascade process, controlled by the diffusion terms. Finally, the turbulent energy dissipates into heat by molecular viscosity at a rate of ϵ .

This cascade model accords to the Kolmogorov⁹ concept. As indicated in fig. 2.7, the auto-spectral distribution of turbulent velocities *e.g.* in streamwise direction, S_{uu} , consists of three ranges: (1) the production range, (2) the inertial subrange, where the spectra follow a $-5/3$ power-law and (3) a viscous range, where the spectra decay due to dissipation. The spectral variables are respectively the wave number $k = 2\pi/L$, with L being a characteristic length scale, and the frequency f . Cheng (1953) supplemented the Kolmogorov-model with one more region between (1) and (2), where the spectra $\sim k^{-1}$ ($\sim f^{-1}$). According to Nikora (1999), this scaling is the result of a strong interaction between the mean flow and its fluctuating part, whereas the $-5/3$ power-law is the result of a weak interaction.

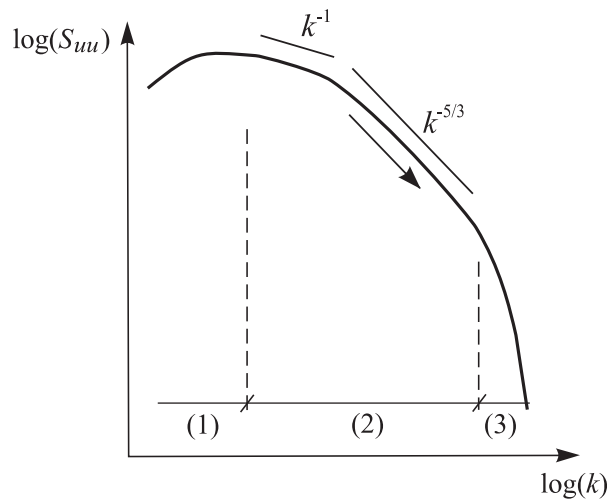


Figure 2.7: Idealized velocity auto-spectra $S_{uu}(k)$, in double-logarithmic scales. (1) Production range. (2) Inertial subrange. (3) Viscous range.

⁹Andrey Nikolaevic Kolmogorov: * 1903 in Tambov (Russia); † 1987 in Moscow (USSR)

Poggy *et al.* (2003) investigated experimentally auto-spectra of streamwise and wall-normal turbulent velocity components for rough walls. They found a strong anisotropy at smaller scales near the bed. The roughness strongly interacts with turbulence, destroying the scaling regions at small-scales through the imposition of its characteristic scales. Their spectra suggest a connection of the behaviors with the turbulent energy directly injected into the flow by the roughness elements.

2.4.2 Turbulence Intensities

A basic characteristic of turbulence properties is their intensities. By definition, the variance *e.g.* in streamwise direction, σ_u^2 , is related to its (one-sided) spectra by

$$\sigma_u^2 \equiv \int_0^\infty S_{uu} dk . \quad (2.21)$$

Universal functions to describe the turbulence are usually made by the standard deviation $\sqrt{\sigma^2(u)} = \sigma_u$ instead of the variance. The definition holds, *e.g.* in streamwise direction:

$$\sigma_u \equiv \sqrt{\sigma^2(u)} \equiv \sqrt{1/n \sum_{i=1}^n (u_i - \bar{u}_i)^2} , \quad (2.22)$$

where n = number discrete elements representing the time series.

Open-Channel Flow. Nezu & Rodi (1986) deduced semi-theoretical, exponential relations for $0.15 < y/h < 0.6$, where the turbulence generation is expected to be approximately equal to the dissipation rate, $G \simeq \epsilon$. For this equilibrium turbulent energy budget the turbulence intensities are described as

$$\frac{\sigma_{u_i}}{u_*} = D_i \exp\left(-C_i \frac{y}{h}\right) , \quad (2.23)$$

where D_i and C_i are empirical constants for the three velocity components, $u_i = [u, v, w]$. Nezu & Rodi (1986) suggested $D_i = [2.26, 1.23, -]$ and $C_i = [0.88, 0.67, -]$ for smooth beds. Nezu & Nakagawa (1993) found slightly different values. Again, the largest fluctuations occurred in streamwise direction; and remarkably, the fluctuations in a vertical direction are smaller than in a transversal direction: $D_i = [2.30, 1.27, 1.63]$ holds for a simplified $C_i = C = 1.0$.

In the 3D case, because of the influence of the walls, the maximum value of flow velocity appears at a distance from the bed δ_h smaller than the water depth h (see §2.2). Song (1994), and Carollo *et al.* (2005) found that the vertical distributions in this case scale by δ_h/h , with no substantial differences in comparison with the scaling by y/h for 2D flows without side wall effects. Consequently, y/h in eq. 2.23 should be replaced by y/δ_h in case secondary currents are present.

For rough bed flows, Kironoto & Graf (1994) fitted values as $D_i = [2.04, 1.14, -]$ and $C_i = [0.97, 0.76, -]$, indicating a reduction of turbulence intensities in the case of a rough

2 Governing Processes

bed. Song (1994) compared the findings of both Nezu & Nakagawa as well as Kironoto & Graf against his own measurements in rough bed flow. The vertical distribution of σ_u fell slightly below the curve given by Nezu & Nakagawa, but was in good agreement with the one given by Kironoto & Graf for an extended validity area, $0.05 < y/h < 0.9$. In contrast to this, the vertical turbulence intensity profile σ_v agreed with eq. 2.23 for both results only in the outer layer, as it was originally derived from Nezu & Nakagawa. Generally, the measured curve σ_v had a distinctive convex trend, whereas the predicted exponential trend would be rather concavely shaped. The maximum value revealed to be at $y(\sigma_{v,\max}) = 0.2-0.3 y/h$. Below that, σ_v showed a decreasing trend towards the bed. Physically this was explained as follows: the eddies created by the roughness of the bed are hindered in their vertical development near the bed just due to the boundary limitation. When y increases, the limitation successively decreases and the eddy becomes larger and larger (also stronger and stronger). At a certain y , it gets its maximum in size and intensity. Then, when continuing to go up, it is separated into smaller eddies. Near the surface, the size and intensity becomes minimum.

Bezzola (2002) compared several measurements of turbulence intensities over rough beds from literature, mainly for σ_u . Implicitly, his collection confirms with eq. 2.23 and the fitted values from Nezu & Nakagawa, but a qualitative analysis was omitted. Instead of this, the focus lied to the distribution in the roughness layer. Bezzola (2002) stated that σ_u is approximately constant or slightly decreasing in the roughness layer.

Carollo *et al.* (2005) gained turbulence intensities from a flow roughened with pebbles in varying density. Here, the relationship of Nezu & Rodi (1986) was tested positively. Furthermore the authors proposed an extended intensity distribution for σ_u , also applicable in the near-bed region. Their approach is similar to the one proposed by Nezu & Rodi (1986) with $\sigma_u/u_* = C y/(\nu/u_*)$ for smooth beds, combined with the empirical damping function given by van Driest (1956). Carollo *et al.* (2005) adopted a linear law to the near-bed intensities as follows:

$$\frac{\sigma_u}{\sigma_{u,\max}} = C \frac{y}{y(\sigma_{u,\max})}, \quad (2.24)$$

with $C = 1$ for an impermeable bed and combined eq. 2.24 with eq. 2.23. Finally, the distribution gets the form

$$\frac{\sigma_u}{u_*} = \frac{\sigma_{u,\max}}{u_*} \left(\exp(r) \exp(-rY)(1 - \exp(-Y)) + Y \exp(Y) \right), \quad (2.25)$$

where $Y = y/y(\sigma_{u,\max})$ and $r = 1/(e - 1) \approx 0.58$. Eq. 2.24 and eq. 2.25 contain two numerical parameters, $y(\sigma_{u,\max})$ and $\sigma_{u,\max}$ that have a clear physical-geometrical meaning. However, further tests on the applicability of eq. 2.25 are not on hand.

Porous Beds. Whereas turbulence intensities in open-channel flows are well investigated, the knowledge concerning the intensity distributions in porous beds is poor. Lately, some papers have been published that focussed on turbulent flow properties over and within porous beds.

Prinos *et al.* (2003) studied the characteristics of turbulent open-channel flow over a bundle of cylindrical rods aligned in a transverse direction, both experimentally and numerically by Reynolds-averaged Navier-Stokes (RANS) equations ($\phi = 0.44-0.83$, $h/d = 1-7$, $\text{Re}_U = 1 \cdot 10^1-2 \cdot 10^4$). Mean velocities inside the free flow region over a permeable bed decrease significantly, compared to those flows over a smooth impermeable bed. The authors attributed this to the penetration of turbulence and the associated momentum transfer in the upper part of the porous matrix. Penetration of turbulence to the upper part of the porous region results in significant levels of turbulent kinetic energy up to half a diameter of the roughness elements.

Breugem *et al.* (2006) computed the influence of wall permeability on turbulent flows by direct numeric simulations (DNS) of flow on top and through a porous medium of cubes ($\phi = 0.60-0.95$, $h/d = 100$, $\text{Re}_U = 5.5 \cdot 10^3$). They proposed the permeability Reynolds number, $\text{Re}_K = \sqrt{K}u_*/\nu$, with K being the porous medium permeability as a key parameter to classify a permeable wall. Re_K can be interpreted as the ratio of the effective pore diameter, \sqrt{K} to the typical length scale of near-wall eddies, ν/u_* . Breugem *et al.* showed that with increased Re_K , turbulence penetrates the permeable wall and wall-induced viscous effects become less important. Turbulence near a highly permeable wall is dominated by relatively large vortical structures, which are assumed to originate from Kelvin¹⁰-Helmholtz¹¹ instabilities, *i.e.* the growing of small disturbances in a shear flow. However, the simulated porosity was very high compared with natural gravel beds. A comparison of their results with experimental data is not available.

A model based on macroscopic RANS was implemented by Chan *et al.* (2007). They found that the thickness of turbulence penetration remains proportional to both the porosity, ϕ , and the Darcy number, $\text{Da} = K/(h + h_P)^2$, with h_P being the height of the porous region. Moreover, the increase in Da and ϕ significantly enhances the levels of turbulent shear stress within the upper part of the porous medium.

Additionally to averaged filter-velocity profiles, Detert *et al.* (2007) examined the distribution of the filter-velocity fluctuations. Fig. 2.8 illustrates that the damping of the turbulence intensities can be approximated by an exponential law. With their experimental conditions, the damping takes part essentially from the top of the roughness layer to $-y/d = 2-3$. Deeper in the porous bed, the fluctuations were observed to be almost constant, approximately at $\sigma_{u_f} \simeq 0.07u_*$. Thus, a distribution was given by

$$\sigma_{u_f}/u_* = D_u \exp\left(C_u \frac{y}{d}\right) + C \quad \text{for } y < -d, \quad (2.26)$$

with $[D_u, C_u, C] = [1.02, 1.08, 0.07]$ and $R^2 = 0.97$ or in a simplified manner with $[D_u, C_u, C] = [1.0, 1.0, 0.07]$ and $R^2 = 0.75$.

¹⁰William Thomson, since 1892 1st Baron Kelvin of Largs: * 1824 in Belfast (UK); † 1907 in Netherhall (UK)

¹¹Hermann Ludwig Ferdinand von Helmholtz: * 1821 in Potsdam (Prussia); † 08/09/1894 in Charlottenburg (D)

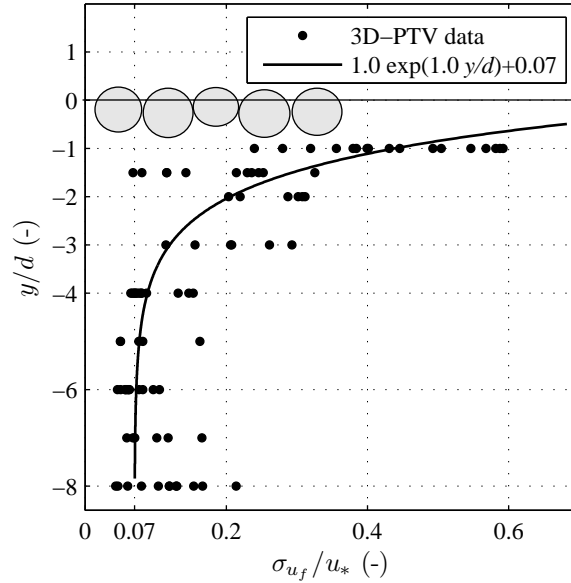


Figure 2.8: Velocity fluctuations σ_{u_f}/u_* within a porous gravel bed underlying open-channel flow. The turbulence intensity diminishes with gravel depth y/d . Data from Detert *et al.*, 2007, $Re_{*d} = u_*d/\nu = 260-640$, $y/h \simeq 20$, $\phi \simeq 0.4$.

2.5 Coherent Structures

Turbulent flows are not simply chaotic and random. Related and self-sustaining flow patterns can be observed repeatedly, on both smooth and rough beds. The structures consist of regions where at least one flow variable exhibits significant coherence over a spatio-temporal range significantly larger than the smallest local flow scales. These patterns are called coherent structures or coherent motions. Since it is apparent that these coherent motions are actually responsible for the production and dissipation of turbulence in a flow, the study of turbulent structure is of fundamental importance to the understanding of the dynamics in river flows. Robinson (1991) and lately Adrian (2007) provided useful reviews on the principal findings.

Often, the terms outward interaction, ejection, inward interaction and sweep are found in literature. They refer to the quadrants Q_i ($i=1..4$, counting counterclockwise) where the (u', v') -vector is present, in accordance to the 2D view quadrant-splitting theme given by Willmarth & Lu (1972). As u' and v' are typically correlated negatively, events of Q_2 (ejection) and Q_4 (sweep) are more likely. Consequently, events in this regions correspond to positive production, recalling that $G = -\overline{u'v'} / (\partial\langle\bar{u}\rangle/\partial y)$.

Smooth Walls. Smith & Metzler (1983) proposed a relatively complete conceptual model for the evolution of hairpin-shaped vortices in the near wall region of smooth walls, mainly based on their own visualization studies. This mechanism is the so-called bursting-phenomenon. It is described in the following, and fig. 2.9 gives a descriptive visualization

to this mechanism gained by DNS. In the near wall region at $y < 10\nu/u_*$, the streamwise velocity field is organized into alternating narrow, elongated streaks of high and low speed fluid. Their lateral spacing is about $100\nu/u_*$ and they are persistent and quiescent most of the time. Due to undulations, the streak is slightly lifted up. It starts to oscillate and then to unroll to an eddy. Subsequently, the eddy is deformed and its head moves away from the wall as it reaches the logarithmic layer, say $y < (50-100)\nu/u_*$. Because the two counter-rotating legs of the eddy are still in contact with the wall, the resulting structure acquires the form of an Ω , a horseshoe or a hairpin. The legs of this hairpin vortex are typically inclined at $\sim 45^\circ$ to the wall. They serve to pump fluid away from the bed (ejection) and accumulate low speed fluid packets between them. The heads of older and younger vortices originating from the bed are aligned in a streamwise array that forms an angle of $\sim (15-30)^\circ$ to the bed. Intermittently, it grows outward (bursts) and may agglomerate into large-scale rotational outer-region bulges; or it may breakdown into finer scales.

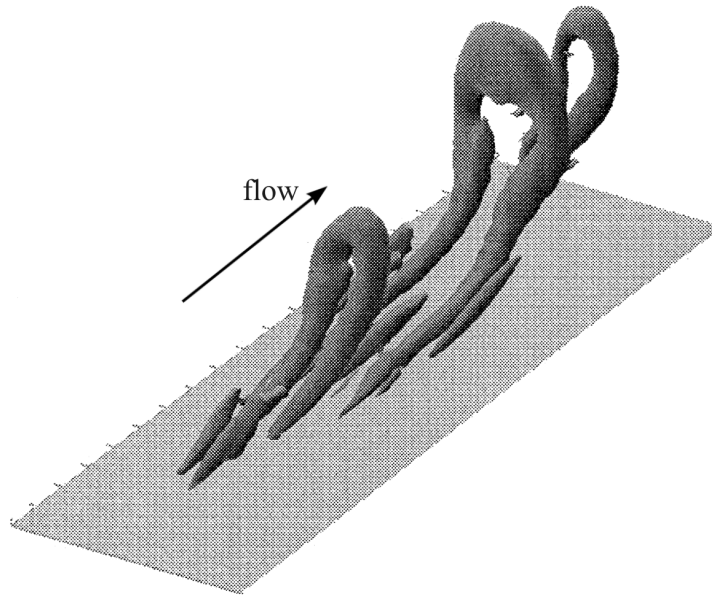


Figure 2.9: Visualization of a hairpin vortex packet, where in addition streaky structures can be seen. Taken from Zhou *et al.* (1999), DNS, $Re_{u_*} = \delta u_* / \nu = 180$. The streamwise length of the shown fluid domain is $1800\nu/u_*$.

Nezu & Nakagawa (1993, p. 228) brought two comments to the model of Smith & Metzler. First, the model includes no effect of the outer (flow layer) variables, although scaling laws are found for the bursting period that apply variables from the outer flow layer (*e.g.* Willmarth, 1975). Second, in Smith & Metzler's model sweep events are neglected, although measurements showed exactly the opposite (*e.g.* Raupach, 1972; Thomas & Bull, 1983). Therefore, Nezu & Nakagawa extended the near-wall model of Smith & Metzler to an approach applicable in open-channel flows. In their model the bursting motion is the

2 Governing Processes

active component, and bursting is triggered by sweep events. An agglomeration of many spanwise vortices (rollers) forms an interfacial shear layer between high speed and low speed zones, inclined from the wall at an angle of about 20° . As a result of a complicated, self organized feed-back mechanism of the recurrence of bursting motions and the related large-scale vortical motions, the shear layer forms coherent wedge-like structures that may extend over the entire flow depth up to the water surface.

A similar, but more refined model was presented by Adrian *et al.* (2000b), based on smooth-wall wind tunnel experiments using 2D PIV. Fig. 2.10 shows this structural model graphically. Hairpin vortices, and deformed versions thereof, are considered as a common basic flow structure with varying in size, age, aspect ratio, and symmetry. Originating from the bed, they align with their heads in almost straight lines, resulting in so-called hairpin vortex packages (HVP). The idealized packet forms a ramp inclined at approximately 12° in the streamwise direction. The rotation of the vortices causes the fluid under them to retard uniformly. Thus, individual fluid packets with uniform momentum flow are generated under packages of hairpin vortices. These structures grow upwards into the outer flow, become larger, faster and can also be interleaved with each other. Older, larger zones over-run younger, more recently generated packets; and in this, the older serve as the induced interior flow that promotes the HVP and the growth of the underlying younger packet by additional shear.

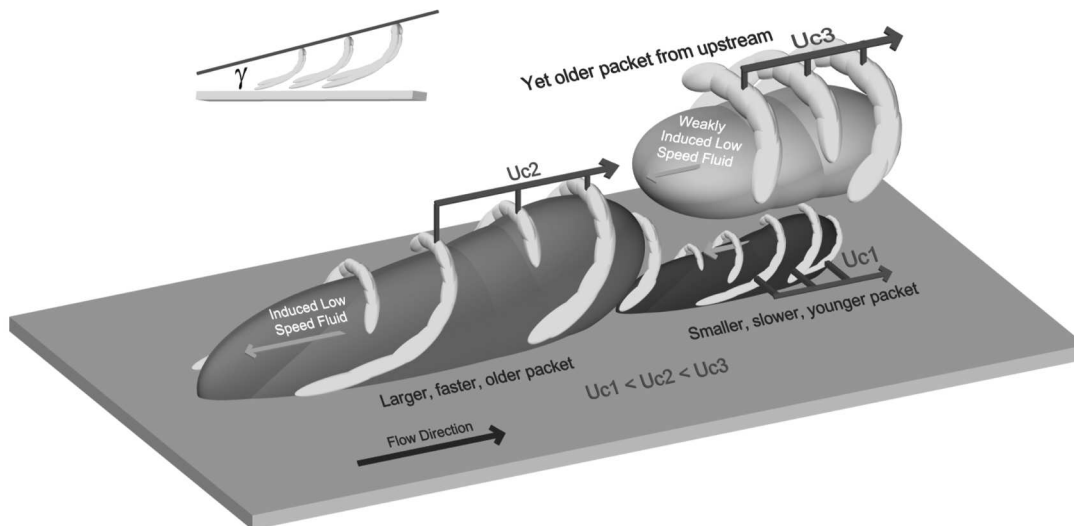


Figure 2.10: Conceptual model of coherent turbulent structures, consisting of zones of equal momentum travelling with velocity U_c and nested packets of hairpin vortices between them (Adrian, 2007). For open-channel flows, some packets are assumed to bulge up to the water surface causing weak boils (according to a model from Nezu & Nakagawa, 1993, p. 232).

Rough Walls. The aforementioned considerations incorporated (more or less) smooth wall boundaries, as the evolution of an initial hairpin vortex is due to an instability of the laminar sublayer and therefore scales with ν/u_* . However, the typical grain diameter d of a rough bed is naturally much larger. Therefore, the mechanism must be different. Arcalar & Smith (1987) showed that hairpin vortices can also be generated by vortex shedding from single roughness elements. Moreover, Zhou *et al.* (1996) showed that new vortices can be created by strong existing hairpin vortices as well. These mechanisms might explain that similar structural, coherent features were observed also for rough bed flows. In the following the principal findings for coherent motions in rough bed flow are described.

Grass *et al.* (1991) showed that streaky coherent motions are present near rough walls. The structures were visualized by a hydrogen bubble tracer technique. They found that the lateral streak-spacing λ_z scales with the diameter d of spherical elements. For geometrically similar roughness elements and packing densities $\lambda_z/d \simeq 3.2$ holds. Later, Grass & Mansour-Tehrani (1996) determined for a mono-layer of pebble roughness that $\lambda_z/k \simeq 3.1$, with $k_k = 0.83d$ being the roughness height. Defina (1996) conducted passive tracer experiments and found $\lambda_z/k_s \simeq 4$, for $y < 2 k_s$ with $k_s = 0.67 d$ for one layer of spheres, irrespective of water depth and channel slope. The author explained streak spacing by a well-defined first hierarchy of vortical structures just above the roughness elements. It was supposed to consist of two eddies that counter-rotate in vertical streamwise direction, similar to the elongated legs of a classical hairpin vortex. Stösser *et al.* (2005) confirmed the streak spacing results from Defina (1996). They found $\lambda_z/k_s = 3.9$ by using a Large-Eddy Simulation (LES) of flow over a channel bed roughened with a single layer of spheres. An estimation for the streamwise dimensions of rough bed streaks is given by Gyr & Müller (1996). They analysed the length of transport bodies at riverbeds and concluded that $\lambda_x/\lambda_z \simeq 5$. A visual comparison with the results from Stösser *et al.* (2005) roughly agrees with this order, whereas the visualizations of Defina indicate a more elongated shape.

For the outer flow layer on rough beds, coherent structures were observed, roughly consisting of ramp-like coherent areas accompanied by small-scale vortices (HVPs) in the bordering shear layer (Grass, 1971; Nezu & Nakagawa, 1993). Tomkins (2001) measured typical ramp-angles of about 10-20° in smooth-wall wind tunnel experiments, roughened with low-density hemispheres. In flume experiments, Shvidchenko & Pender (2001) observed large spanwise roller-like vortices that include secondary motions. They cover the entire water depth with longitudinal extensions of (4-5) h and lateral extensions of 2 h . Roy *et al.* (2004) measured large-scale wedge-like flow structures in natural, gravel-bed rivers by electromagnetic current meters and visualized their findings by video recording and correlation techniques. The structures are narrow and elongated, with either increased or decreased velocity over most of the water depth h . The average angle in the streamwise direction was estimated to be inclined at 25° to the bed. This angle is smaller than the angle of 36°, given earlier by Buffin-Bélanger *et al.* (2000) for natural river observations. However, it is more in the vicinity of the angles observed by Adrian *et al.* (2000b) and Tomkins (2001). The average longitudinal length scales were determined to be (3-5) h , the width was between (0.5-1) h . These values showed excellent

agreement with the characteristic scales they obtained from literature (9 quotations from 1972-2001). Jackson (1976) examined the duration and frequency of boils at the surface of river flows. He found a boiling frequency of 3-7 h/U , where U = bulk velocity. Gyr & Müller (1996) gave a burst frequency of 5-6 h/U as a rough relation for the mean time between two bursting events. Paiement-Paradis *et al.* (2003) analyzed from measurements at natural rivers that the frequency duration relations of large-scale turbulent flow structures follows a power function with exponents between -1.4 and -1.95 .

Lately, Flores & Jiménez (2006) and Hurther *et al.* (2007) did intensive investigations of flow over rough walls; the former by DNS over artificial roughness, the latter used an Acoustic Doppler velocity profiler (ADVP). Both studies supported close similarities of coherent structures over smooth and rough walls, with differences in scaling laws.

The state of research concerning the roles of coherent flow structures in relation to particle entrainment are worked out in §2.7.

2.6 Fluid Pressure and Resulting Forces

Understanding the genesis of the instantaneous local pressure needs a knowledge of the entire turbulent fluid domain. By taking the divergence of eq. 2.2, a Poisson¹²-equation for the fluctuating pressure p' within an incompressible flow reads (in Reynolds-decomposition, *e.g.* Chang *et al.*, 1999)

$$-\frac{1}{\rho}\nabla^2 p' = 2 \frac{\partial \bar{u}_i}{\partial x_j} \frac{\partial u'_j}{\partial x_i} + \frac{\partial^2}{\partial x_i \partial x_j} (u'_i u'_j - \overline{u'_i u'_j}) . \quad (2.27)$$

The first term on the right hand side is called the rapid (respectively linear or mean-shear) source term, because it responds immediately to a change in the mean velocity gradient. The second term is called the slow (or non linear or turbulence-turbulence) source term. It follows that both the velocity gradients and fluctuation gradients in the entire fluid domain influence p' at a certain moment, but the impact of single sources decreases with distance.

Reliable pressure measurements within turbulent flows are difficult, as an ideal probe had to be infinitesimally small not to disturb the flow. Point measurements lately conducted by Tsuji *et al.* (2007) are promising, but information about pressure fluctuations or entire pressure fields are only realizable by numerical simulations.

Kim (1989) analyzed the pressure fluctuations in a turbulent channel flow obtained from DNS. As shown in fig. 2.11, σ_p increases exponentially to the wall and reaches its maximum slightly above it. A detailed analysis revealed that the slow part is substantially larger than the rapid part, except very close to the wall, $y/\delta < 0.15$ (not shown in fig. 2.11), where δ = channel half width, here equal to the boundary layer thickness. Contours of constant pressure gradients revealed that those associated with $\partial p/\partial y$ and $\partial p/\partial z$ are somewhat elongated near the wall, but not those associated with $\partial p/\partial x$ (also not shown here).

¹²Siméon-Denis Poisson: * 1781 in Pithiviers (F); † 1840 in Paris (F)

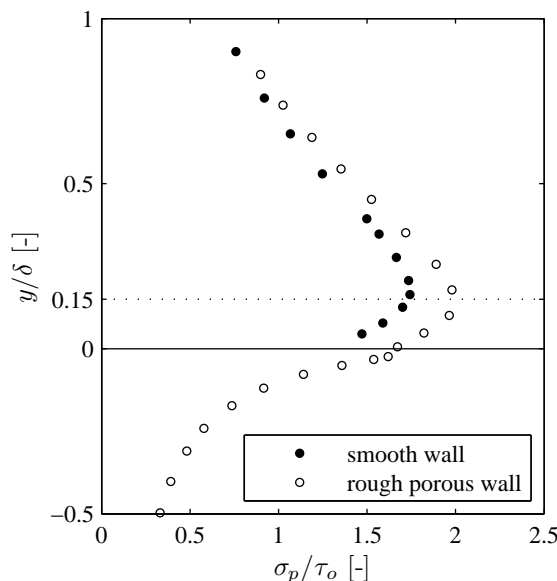


Figure 2.11: Intensities of pressure fluctuations. DNS results for σ_p/τ taken from Kim (1989) (smooth walls, $\text{Re}_{*\delta} = u_*\delta/\nu = 179$) and Breugem *et al.* (2006) (rough permeable wall, $\text{Re}_{*\delta} = u_*\delta/\nu = 176$, $\phi = 0.60$). Here, $y = 0$ refers to the smooth wall and the roughness tops, respectively.

Analysis of pressure fields of flow over and within a permeable bed was given by Breugem *et al.* (2006). They studied the influence of wall permeability on turbulent flows on top and through a porous medium of cubes by DNS. The vertical shape of σ_p in the free stream roughly confirms with those given by Kim (1989), supplemented by an exponential decrease inside the permeable wall (see fig. 2.11). The peak value just above the permeable wall is revealed to increase with the Re-number (compare eq. 2.28) and with ϕ , whereas the distinctiveness of streaks and $\sigma_{u,\max}$ is weakened. This is attributed to turbulent transport across the wall interface and the reduction in mean shear due to a weakening of respectively the wall-blocking and the wall-induced viscous effects. Similar observations were made in the observations of Krøgstad *et al.* (1992) and Krøgstad & Antonia (1999). However, a real validation of the results from Breugem *et al.* (2006) by experimental data is not available, especially for the turbulence intensity profiles.

2.6.1 Turbulence-Induced Wall Pressure

Whereas the measurement of pressure within a turbulent flow is extremely difficult, turbulence wall pressures (TWP) can be measured, as the measuring technique can be incorporated into the wall. TWP have mainly been studied in fields of acoustic, aeronautic or naval applications, with its experimental zenith in the 1970s and 1980s. A review is given by Eckelmann (1988).

Blake (1970) measured boundary-layer turbulent wall-pressure with pinhole microphones, on both smooth and rough boundaries. He showed that the shape of the pressure

2 Governing Processes

spectra are the same for both wall types, but they distinguish in their scaling. The former scales by viscous length ν/u_* and the latter by the average geometric roughness height k_k . For low frequencies, the wall pressures under a rough boundary layer flow showed the same scaling behavior as for the smooth wall. At the wall the magnitude of σ_p was found to be almost equal for smooth and rough walls.

Emmerling (1973) used an optical method to investigate the instantaneous structure of wall pressure fields. Zones of high-amplitude p' appeared in irregular time intervals and were theoretically associated with bursting phenomena. Maximal pressure peaks of up to $p_{\max} = 6 \sigma_p$ were observed. These values are of the same magnitude as the ones found by Schewe (1983), as he observed maximal pressure peaks of up to $p_{\max} = 7 \sigma_p$. These findings imply that the TWP can become very large, and must influence mass and momentum transfer in case of a permeable wall and possibly bed stability. Characteristic wall-pressure structures were found with high amplitudes whose sources are located in the buffer layer of the boundary layer. The mean characteristic wave length was identified to be $\lambda_x = 145 \nu/u_*$, indicating correlation with bursting phenomena. From the measured probability density he calculated that these structures play an important role in the wall region of the boundary layer.

Thomas & Bull (1983) simultaneously measured the TWP, fluctuations of velocity, and wall shear stress in boundary layer flow. Results are shown in fig. 2.12. A characteristic wall-pressure fluctuation was identified, where the corresponding flow structure is wedge-like. The structure resembles quite closely to the flow patterns that were already described in §2.5. The pressure-flow pattern was gained by conditional sampling on basis of the high-frequency activity of the TWP and the streamwise velocity fluctuations. The phase relationships indicated that fluid involved in the bursting process is subjected to a favorable streamwise pressure gradient by the characteristic wall pressure pattern at the time that the lift-up of low speed streaks in the wall region begins. In addition, estimations of the order of magnitude suggested that the pressure patterns cannot play an active role in the dynamics of the wall flow and are not the direct cause of the bursting process.

A scaling law for σ_p was given by Farabee & Casarella (1991). Based on data from literature (8 quotations, 1970-1990) and their own measurements, they developed a relation for σ_p depending on τ_o and $\text{Re}_{*\delta} = u_*\delta/\nu$. For $\text{Re}_{*\delta} > 333$, they proposed:

$$\frac{\sigma_p}{\tau_o} = \left(6.5 + 1.86 \ln \frac{\text{Re}_{*\delta}}{333} \right)^{1/2}. \quad (2.28)$$

2.6.2 Fluid Forces on Single Particles

Whereas the aforementioned descriptions referred to the pressure in a fluid or at a wall, the hydrodynamic forces acting on a single grain – also expressible as force per area, *i.e.* pressure – are not the same, as the flow is in direct interaction with the obstacle. In a 2D view, the terms drag and lift are used for respectively the streamwise and vertical component of the hydrodynamic force. Much research has been done on drag and lift. An excellent review is given by Hofland *et al.* (2005).

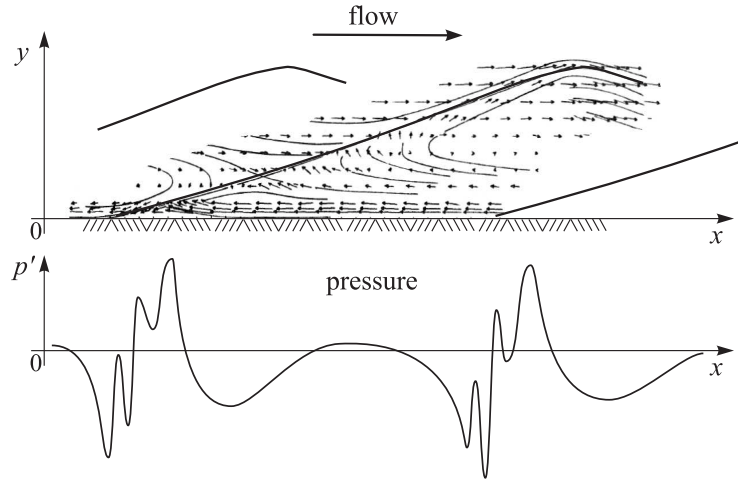


Figure 2.12: Conceptual model of large-scale flow structure, including the associated wall pressure fluctuations (modified after Thomas & Bull, 1983).

The time averaged force $\overrightarrow{\overline{F}}$ that acts on a particle is given by the classical approach

$$\overrightarrow{\overline{F}} = [\overline{F}_D, \overline{F}_L] = 1/2 \rho [C_D, C_L] A |\overline{u}_A| \overline{u}_A, \quad (2.29)$$

where the non-dimensional empirical coefficient is denoted by C_D for the drag \overline{F}_D and C_L for the lift \overline{F}_L . A is the projected area perpendicular to the reference velocity $\langle \overline{u} \rangle_A \equiv \overline{u}_A$. Mutual comparisons of C -values taken from literature are elusory, as many different definitions are used for the parameters used in eq. 2.29 (see Hofland *et al.*, 2005). Furthermore, if the particle is accelerated relatively to the fluid, an extra force has to be considered, as the fluid around the particle is also accelerated (Maxey & Riley, 1983).

A relation between the turbulent drag F'_D and the flow velocity can be derived by applying a Reynolds-decomposition on eq. 2.29. First, for instantaneous force

$$(F_D = \overline{F}_D + F'_D) \propto (u_A u_A = \overline{u}_A \overline{u}_A + 2 \overline{u}_A u'_A + u'_A u'_A). \quad (2.30)$$

Second, by averaging the above eq. 2.30 one obtains the mean force as

$$\overline{F}_D \propto \overline{u}_A \overline{u}_A + \overline{u'_A u'_A}. \quad (2.31)$$

Third, by subtracting \overline{F}_D from F'_D the results reads

$$F'_D \propto 2 \overline{u}_A u'_A + (u'_A u'_A - \overline{u'_A u'_A}). \quad (2.32)$$

Note that $\overline{u'_A u'_A} \equiv \sigma_u^2$ is the variance of u (eq. 2.22). Eq. 2.32 reveals a structure similar to eq. 2.27, with a mean shear (first term) and a turbulence-turbulence source (second term). If the ambient flow is rather uniform, the assumption $|u'_A| \ll \overline{u}_A$ is applicable and the second term can be disregarded. However, for stones with low protrusion, experimentally results are in the range $\sigma_{F_D} = (0.4-0.8) \overline{F}_D$ (Chepil, 1959; Cheng & Clyde, 1972; Xingkui

& Fontijn, 1993). This indicates that the assumption $|u'_A| = \mathcal{O}(\bar{u}_A)$ holds for extreme values close to the bed. Thus, the turbulence-turbulence term on the right hand side cannot be neglected near the bed – what is also in excellent accord with DNS results for the vertical σ_p distribution gained by Kim (1989).

For the fluctuating part of the lift, F'_L , the following ratio was proposed by van Radecke & Schulz-DuBois (1988)

$$F'_L \propto a \bar{u}_A u'_A + b \bar{u}_A v'_A, \quad (2.33)$$

with a and b being constants. The first term on the right hand side is caused by the Bernoulli¹³-effect. The second term is due to the fact that the instantaneous velocity vector is not aligned with the u component as it has a non-zero vertical component. It was shown by van Radecke & Schulz-DuBois that the first term in eq. 2.33 is responsible for most of the variance of the fluctuations. The second term is due to eddy shedding; it caused only a small part in the variance. Experimentally determined values for near-bed particles are $\sigma_{F_L} = (0.4-1.0) \bar{F}_L$ (Einstein & El-Samni, 1949; Chepil, 1959; Xingkui & Fontijn, 1993). Thus, for extreme values the assumption $|v'_A| \approx \mathcal{O}(\bar{u}_A)$ also holds. Consequently, the second term in eq. 2.33 is not negligible in the vicinity of the bed.

Many experimental investigations were undertaken to reveal the characteristics and to predict the drag and lift forces. The contribution of Hofland (2005) and co-workers hereto comprises up-to-date knowledge and advanced measuring techniques. Hofland *et al.* (2005) made measurements of pressures and simultaneous near-bed velocities in a flume roughened with crushed stones. Three pressure transducers were placed in a 30 mm cube made of stainless steel that was part of the granular bed. The magnitude of the fluctuating pressure was revealed to increase with the exposure relative to the stones upstream of the cube. Drag, caused by longitudinal velocity fluctuations, was seen as the source of the largest force fluctuations for the most exposed stones. However, this clear force origin weakened with subsiding exposure effects. Concluded from a quadrant analysis as developed by Nelson *et al.* (1995), they observed that both force components, F_D and F_L , were a function of the two velocity components u and v . At the moment of occurrence of the extreme values of u , the drag forces received an additional increase, and the lift forces an additional decrease due to the vertical velocity component. Furthermore, lift force fluctuations were attributed to eddy-shedding effects from upstream. Consequently, additional terms in form of $f(u, v)$ should be added to both eq. 2.32 and eq. 2.33.

2.7 Initial Sediment Motion

2.7.1 Analytic Approach and Uncertainties in Design Load

The incipient point of motion for bed particles can, in principle, be predicted from a force and momentum balance. The forces that have to be considered are the buoyancy corrected weight, G' , the contact forces with surrounding particles, F_{ci} , and the load due to the flow attack, $|F| = \sqrt{F_D^2 + F_L^2}$. Fig. 2.13 gives a sketch of these forces. If the displacing loads on the particle exceed the stabilizing loads, it will start to move.

¹³Daniel Bernoulli: * 1700 in Groningen (NL); † 1782 in Basel (CH)

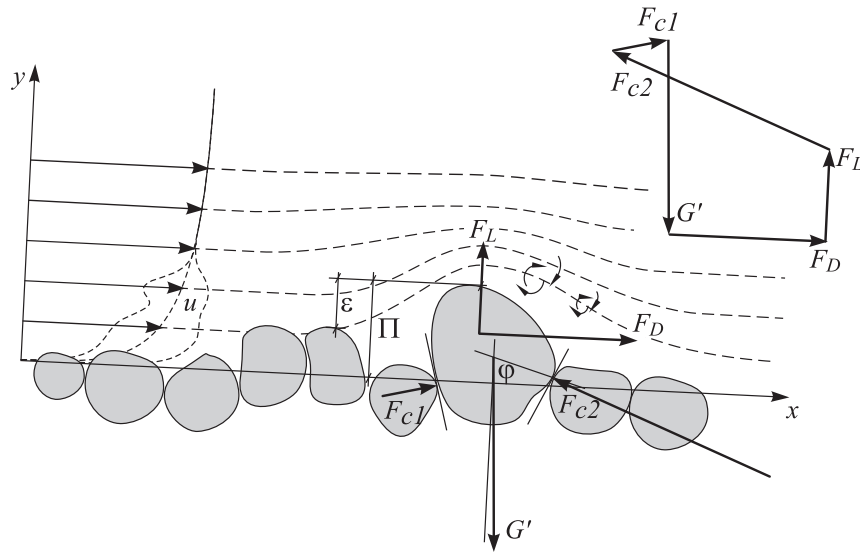


Figure 2.13: Force balance for a single grain (after Hofland, 2005).

A number of studies have attempted to predict threshold conditions based on force or momentum balance models (*e.g.* Bagnold, 1941; Chepil, 1959; Wiberg & Smith, 1987; Andrews & Smith, 1992; Ling, 1995; Wu & Chou, 2003; Vollmer & Kleinhans, 2007). However, all these studies suffer from uncertainties and shortcomings in assessing the load assumptions.

On the one hand, the hydrodynamic forces in these models are usually those according to the time averaged forces given by eq. 2.29, mostly ignoring flow properties such as spatio-temporal variabilities, flow submergence and turbulence. When turbulence is included in the models it is usually done by introducing a fluctuating velocity in eq. 2.29, equivalent to use a fluctuating u_* . On the other hand, the magnitude, ratio and influence of drag and lift depends on a wide range of features that characterizes the stones and their bedding. In a brief summation these are the shape, the size, the orientation, and the position, as well as the influence of interlocking. A detailed consideration is given in the following.

Shape. Typically, the shape of a stone is described by ratios of the length of the three principle body axes a , b , c , according to the shortest, intermediate and longest. A shape factor, defined as $SF = a/\sqrt{bc}$, can be regarded as an indication of the flatness of stones. Carling & Glaister (1992) found for various shapes of comparable diameter that the resisting force varied with a maximum of about 20%. Wang (1999) showed that the particle shape had no significant influence on the beginning of motion under clear water flow conditions. In opposite to this, Dittrich & Koll (2001) identified that flat particles own an increased stability of 65% compared with spherical particles.

Size. The diameter of a stone is the characteristic grain feature that is used most often. The size can be defined by the nominal diameter,

$$d_n = \sqrt[3]{m/\rho_s}, \quad (2.34)$$

2 Governing Processes

with m = mass of stone and ρ_s density of stone. It represents the edge of a cube with equal volume. Another possibility is to define the size by the smallest sieve opening through which the stone can pass. A sieve analysis then gives the particle size distribution of a granular material, where the grain size quantiles can be read out. The diameter, where 50% passed the sieves, the d_{50} , is often seen as the characteristic mean diameter. Meyer-Peter & Müller (1949) suggested a different method, where the decisive diameter d is computed by a weighted mean. It reads

$$d = \sum_{i=1}^n d_i \Delta p_i , \quad (2.35)$$

where d_i is mean grain size of the quantile i , and Δp_i is percentile of this grain size fraction.

Position. The position of a stone can be qualified by the parameters protrusion Π , exposure ε , and the grain pivoting angle φ (see fig. 2.13). For simplicity, in the literature protrusion and exposure are sometimes considered to be the same, as both give the top of the particle with respect to the bed level (*e.g.* Vollmer & Kleinhans, 2007). Indeed, the protrusion accords with the mean bed level, whereas the exposure refers to the local mean upstream bed level (Kirchner *et al.*, 1990). Thus, the exposure is more directly related to the hydrodynamic load. On average Π will increase with ε , only with more scatter. Which flow force component, F_D or F_L , becomes more prominent depends on the ratio Π/d (ε/d). If $\Pi/d \approx 0$, the particle is almost completely hidden. Then only a large F_L can lift the particle or rotate it by the pivot point. Fenton & Abbot (1977) made systematic experiments for a wide range of possible positions of bed elements. Protrusions for typical gravel beds, say $0.7 > \Pi/d > 0$, varied the resisting force by a factor of 10.

Orientation. Particle orientation is quantified according to the respective angles of the longest body axis to the main flow direction and the bed. In stable beds, stones may have two typical orientations, depending on the deposition regime, with the longest axis either across the flow (Nikora *et al.*, 1998) or along the flow (Aberle & Nikora, 2006). Once the stones are moving, the particles tend to roll with their longest axis perpendicular to the flow (Carling & Glaister, 1992), as the area A projected to the flow attack is maximal.

Hoffland (2005) approximated the influence of stone characteristics on crushed stone stability from a literature review. In reference to his elaborations for crushed rock, for a natural gravel bed it can be assumed that the protrusion and the orientation have the largest influence (both factor 10), whereas size (factor 2) and shape (factor 0.5) are seen to be of minor importance.

Interlocking. The influence of interlocking is characterized by the friction angle, $\langle\varphi\rangle$, also referred to as angle of repose. Unlike the pivoting angle, φ , the friction angle is a quantity that refers to an integral bulk parameter of the bed material. For a granular bed, $\langle\varphi\rangle$, depends on the package density, the surface roughness of single particles and the grain size distribution curve. With closer packing, higher roughness and flatter grading,

the interlocking effect and hence the resistance of the bed increases. According to Dittrich (1998), where a literature review considered the distinctiveness of armor layers (say $d_{85}/d_{15} < 3$), differences in interlocking may vary bed stability by a factor of 2. If cohesive properties become predominant due to the presence of silt or clay, data analysis given by van Rijn (2007) indicate that the bed resistance to motion can increase approximately by a factor of 10.

2.7.2 Shields' Critical Shear Stress Concept

The critical shear stress concept developed by Shields (1936) is seen to be the classical research on initiation of motion, although older approaches based on a bed stability criteria are available (*e.g.* Isbash, 1932; Hjulström, 1935). In his thesis, Shields reduced the problem description to two variables by means of dimensional analysis. The first variable is the dimensionless shear stress,

$$\Theta = \frac{\tau_o}{(\rho_s - \rho) g d} , \quad (2.36)$$

with ρ_s = particle density. This variable can also roughly be interpreted as the ratio of the load on the particle ($\tau_o \cdot d^2$) to the gravitational force on the particle that resists movement ($\propto (\rho_s - \rho) g d \cdot d^2$). By applying eq. 2.15, Θ can also be rewritten as the densimetric Froude¹⁴-number,

$$\text{Fr}_{*\Delta} = \frac{u_*^2}{\Delta g d} \equiv \Theta , \quad (2.37)$$

with

$$\Delta = \rho_s / \rho - 1 . \quad (2.38)$$

The second variable in Shields' approach is a threshold value,

$$\Theta_c = f(\text{Re}_{*d}) , \quad (2.39)$$

with $\text{Re}_{*d} = u_* d / \nu$ being the particle Reynolds-number. Initiation of motion occurs, when

$$\Theta > \Theta_c . \quad (2.40)$$

Eq. 2.40 gives a relation of $\text{Fr}_{*\Delta} > f(\text{Re}_{*d})$, as is illustrated in fig. 2.14. In literature, Θ_c is often denoted as the critical Shields'-parameter, whereas Θ is called Shields'-parameter.

Shields conducted laboratory flume experiments with noncohesive, nearly uniform grains of different densities over a wide range of Re_{*d} and uniform flow conditions. For fully developed rough flow ($\text{Re}_{*d} > 70$), as it is of interest for natural beds, Shields unfortunately carried out only four experiments. He found $\Theta_c = 0.029 - 0.039$ for $\text{Re}_{*d} = 70 - 220$. He supplemented the results with two data points from Gilbert (1914), where $\Theta_c = 0.033$ and 0.06 for $\text{Re}_{*d} = 230$ and 480 . Shields probably defined incipient-motion thresholds for his experiments by extrapolating stress-transport relations to a zero transport rate, as is popularly believed. In contrast, he defined incipient motion values for supplemental

¹⁴William Froude: * 1810 in Dartington (UK); † 1879 in Simonstown (SA)

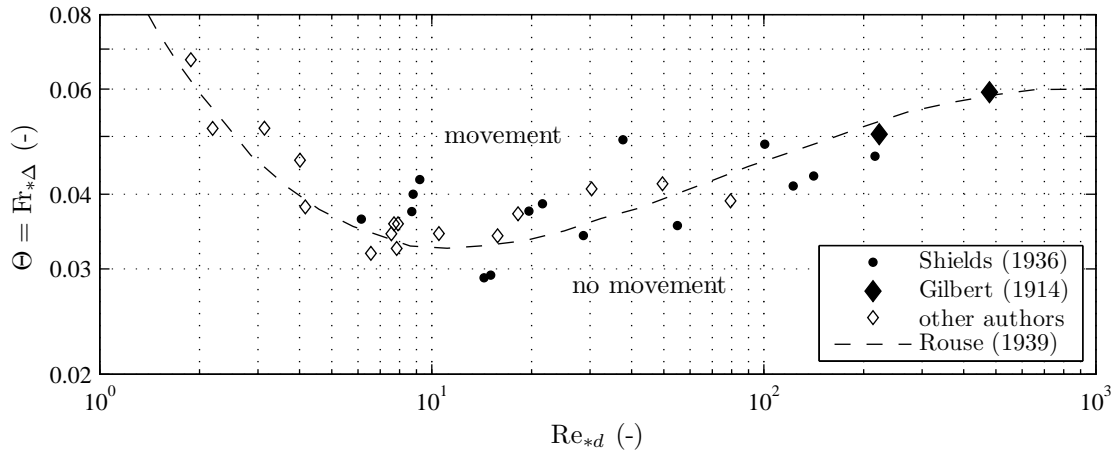


Figure 2.14: Redraft of Shields' diagram.

data sources using two differing thresholds of visually based movement. Unfortunately, citations of Shields' work often quote $\Theta_c = 0.06$, although he pointed out explicitly that this value was connected to strong uncertainties. Despite the wide success and familiarity of Shields' work, almost every redraft of his incipient-motion data contains errors. Further inconsistencies and misconceptions regarding Shields' work are identified and examined in Buffington (1999).

Reanalyzing Shields' data and correcting for sidewall effects and form drag, Gessler (1971) reported $\Theta_c \simeq 0.046$ for a 50% probability of movement in rough turbulent flow. Without consideration of the probability for movement, Miller *et al.* (1977) arrived at a similar value of $\Theta_c \simeq 0.045$ for rough turbulent flow using compiled flume data. Buffington & Montgomery (1997) reanalyzed data from 135 studies of incipient motion. They confirm with $\Theta_c \simeq 0.045$ as a typical value of visually determined mobility thresholds of laboratory mixtures. However, they found that Θ_c has a range of 0.030-0.086. Obviously, an unambiguous definition for the initial movement by means of Shields' approach is difficult. The main shortcomings are due to the assumptions of uniform flow without explicit consideration of turbulence, adopting d_{50} to characterize the bed and the disregard of a unsteady drag-lift ratio. But due to this simplicity, the critical shear stress concept has become, in turn, the most common method for estimation bed stability in field conditions.

2.7.3 Refinements and Further Approaches

Beside the analytic approaches by force-momentum balancing and the classical approach of Shields', countless attempts were undertaken to enhance the prediction of incipient sediment motion. As each of these models have their own new feature more or less combined with models hitherto existing, a distinct classification is difficult. For instance, grouping can be made by analytical approaches, models using stochastic methods, approaches with detailed consideration of the bed, engineering approaches and numerical approaches. The main features of these models are described in the following. However, other classifications are possible, *e.g.* most of the approaches are based on or related to Shields' concept and numerical models are typically mixed up with all approaches available.

Analytical approaches. Analytical approaches solve the force, the momentum balance or both, as introduced in §2.7.1. As the physics of the flow attack and the geometry of the bed are hard to describe, simplified assumptions have to be made. Usually, the grains are considered to be spherical, of the same size and cohesionless. In this, the models cope with the wide range of natural grain features and their bedding. Some approaches adopt the drag as being fully responsible for dislodging particles (Kalinske, 1947). Conversely, other models consider only the lift force (Einstein & El-Samni, 1949). However, most of the models include implicitly or explicitly both force components, modeled by eq. 2.29 or similar functions (*e.g.* Bagnold, 1941; Wiberg & Smith, 1987; Andrews & Smith, 1992). When 'turbulence' is considered in the models, it is usually done by introducing a fluctuating velocity in eq. 2.29, which is equivalent to using a fluctuating u_* (Ling, 1995). Latest models include influences of the turbulent fluctuations of flow and bed-pressure and grain protrusion (Vollmer & Kleinhaus, 2007). Most of them end up with comparisons to Shields' concept.

Stochastic approaches. These respect the fact that the load on a particle is a stochastic parameter that changes in time, and that the resisting force of the particles is also distributed stochastically, as it varies with particle. Grass (1970) introduced a stochastic concept of sediment entrainment. Transport is considered to occur for the overlapping tails of probability distributions representing the turbulent flow attack (*e.g.* τ_b) and the resistance of a random bed geometry (*e.g.* τ_c). In an averaged sense the strongest flow fluctuations move the smallest or most exposed sediment particles. Fig. 2.15 illustrates this approach. The probability P that $\tau_b > \tau_c$ holds, is defined by the following convolution (*e.g.* Hofland, 2005)

$$P(\tau_b > \tau_c) = \int_{\tau_c=0}^{\infty} P(\tau_c) \left(\int_{\tau_b=\tau_c}^{\infty} P(\tau_b) d\tau_b \right) d\tau_c . \quad (2.41)$$

Zanke (2003) shows that his probabilistic approach coincides with the Shields-curve ($Re_{*d} \approx 10-200$) for an entrainment risk of 10%. Wu & Chou (2003) studied the rolling and lifting probabilities for sediment entrainment by incorporating the probabilistic features of the turbulent fluctuation and bed grain geometry. For $\Theta_c < 0.05$ (or $\Theta_c > 0.6$),

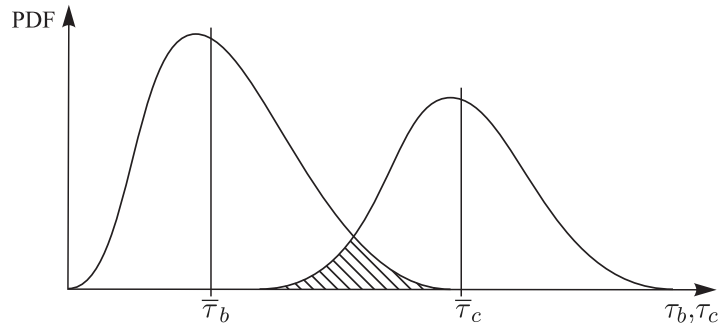


Figure 2.15: PDF-Sketches of $P(\tau_b)$, characterizing the flow attack and $P(\tau_c)$ characterizing the bed resistance against entrainment.

the rolling (or lifting) probability makes up more than 90% of the total entrainment probability and thus can be used as an approximation of the total probability of entrainment. The stochastic approach made by McEwan *et al.* (2004) showed for uniformly sized beds that $\Theta_c = 0.06$ corresponds to a point where 1-2% by weight of the surface is mobile.

Approaches considering non-uniform bed material. These approaches typically focus on adequate modeling of an armoring layer. An armoring layer is the result of a selective process of erosion where single, smaller grain size fractions are washed out. Approaches that refer to this problem are usually related to Shields' concept to a greater or lesser extent. They concentrate on finding a single characteristic grain size, *e.g.* d_{90} (Meyer-Peter & Müller, 1949), or ratios of different fractions, *e.g.* d_i/d_j (Schöberl, 1979; Parker & Klingeman, 1982) to simplify multimodal grain size distributions. The critical Shields-parameter Θ_c or according threshold values are typically fitted to data gained experimentally.

Engineering approaches. Generally, these approaches are based on stability criteria as proposed by Shields, Isbash (1932) and Hjulström (1935). The main difference between their approaches is that Isbash used the near-bed velocity (which is not specified explicitly), Hjulström (1935) preferred the depth averaged mean velocity, and Shields took the shear velocity to assess the flow attack. Due to its simplicity, the approach of Hjulström is frequently used to pre-estimate the initial sediment movement. Hjulström presented a design diagram, where he reduced the flow-sediment interaction to $\langle \bar{u} \rangle_h$ and d . If the mean flow velocity falls below the critical velocity, the bed is stable. A simplistic relation to describe the stability of an armoring layer was given by Chin (1985), where $\Theta_c = f(d_{50}/d_{\max})$.

Parker *et al.* (2003) offer the following adjusted version of the Shields criterion for the onset of gravel motion. $Re_{d\Delta}$ denotes a particle Reynolds number for gravel size d , defined as

$$Re_{d\Delta} = \frac{\sqrt{\Delta g d} d}{\nu}, \quad (2.42)$$

with $\Delta = \rho_s/\rho - 1$. Then, Θ_c can be estimated via

$$\Theta_c = 0.5 \left(0.22 Re_{d\Delta}^{-0.6} + 0.06 \cdot 10^{(-7.7 Re_{d\Delta}^{-0.6})} \right). \quad (2.43)$$

An essential advantage of this approach is that Θ_c is estimated independently of u_* , which makes it easier to handle in implementations.

Hofland (2005) presented several engineering approaches for the assessment of stone stability under non-uniform flows (Franken *et al.*, 1995; Pilarczyk, 2001; Hoffmans & Akkerman, 1998). They all used the Shields shear stress concept and model the flow attack with parameters including turbulence aspects. Various correction coefficients are rather arbitrary. Thus, the relations could be used respectively with large safety factors or as a rule-of-thumb.

Numerical approaches. These approaches seem promising in that flow submergence, particle protrusion, Reynolds number, and 3D flow effects can be explicitly accounted for if the local flow field is known. However, they still require assumptions about the

coupling between turbulent flow field and particulate forces. McEwan & Heald (2001) and Schmeeckle & Nelson (2003) used a numeric approach by solving equations of particle motion in response to an assumed flow field while accounting for the effects of particle collision and particle sheltering. Both of these discrete particle models were implemented assuming that lift forces can be neglected and that drag forces were proportional to local streamwise velocity. Based on approaches of Uittenbogaard *et al.* (1998) and Jongeling *et al.* (2003), Hofland (2005) formulated a method for evaluating the stability of bed protections under non-uniform flow. The output of a 3D RANS model gave the mean velocity and turbulent kinetic energy in the water column above the bed. This information was used to compute a local stability parameter, adapted to account for turbulence of varying relative intensity. Uhlmann & Fröhlich (2007) simulated turbulent flow in a horizontal plane channel over a bed of mobile spherical particles. All scales of fluid motion were resolved without modeling and the phase interface was accurately represented. Direct contact between particles was taken into account by an artificial short-range repulsion force. The results indicated possible scenarios for the onset of erosion through collective motion induced by buffer-layer streaks and subsequent saltation of individual particles.

2.7.4 Role of coherent structures

Sutherland (1967) gave a pioneering study for sediment transport considering the role of turbulence. He observed that turbulent flows entrained sediment particles from plane beds. He formulated an entrainment hypothesis based on the concept of turbulent eddies breaking in the viscous sublayer and acting directly on the particles at the granular surface. Although the details of such interactions, as conceptualized by Sutherland, are not totally correct in the light of present knowledge of turbulent structures, his hypothesis delineates the basic mechanics of such phenomena.

Drake *et al.* (1988) filmed the bedload transport in a field experiment. The flow conditions in the 6.5 m wide and 0.35 m deep stream were $Re_h = 2 \cdot 10^5$ and $\Theta = 2 \Theta_c$, the mean grain diameter was $d = 4$ mm. High rates of sediment entrainment were observed at sweeps of downward-moving high-forward speed impinged on the bed. These events momentarily raised the bed shear up to $3 \Theta_c$. Sweeps occupied 9% of the bed area at any given time and accounted for about 70% of the total transport. Consequently, these events were seen to be of most importance in bedload transport at low excess bed shear stresses.

Accurate measurements of the interactions between turbulent bursting and sediment motion were first made possible with a synchronized laser-Doppler velocimetry (LDV) and high-speed cinematography by Nelson *et al.* (1995). They found that sweeps collectively move the majority of the sediment, outward interactions individually move as much sediment as sweeps. However, both ejections and inward interactions move much less sediment than the former two.

The impact of coherent turbulent structures on the entrainment and the transport of particles on both smooth and rough beds were shown by García *et al.* (1996). The results point out the influence of bursts, which are directly correlated with the transport of fluid from the viscous sublayer to the outer flow. Sechet & Le Guennec (1999) studied

2 Governing Processes

the velocity field and the particle concentration in open-channel flow. They identified the dominating influence of the ejection and sweep processes and confirm the results of García *et al.*: The turbulent structures with high energy are decisive for the entrainment and the resuspension of particles. The analysis shows that these structures play an important role for the Reynolds stresses in the roughness layer. Sechet & Le Guennec (1999) showed by experiments that the entrainment of bed particles is directly correlated to the ejections. The beginning of transport can be explained by the bursting phenomenon.

Hofland & Booij (2004) measured the flow field during the actual entrainment of a single stone using 2D PIV technique. In order to determine the flow structures that are responsible for this entrainment the flow field was conditionally averaged over many entrainment events. The resulting flow fields show that two structures are responsible for the entrainment. The first structure, a small-scale vertical fluctuation σ_v , initiate the motion of the stone. These fluctuations are embedded in a second structure, a large-scale sweep that moves the stone further over its pivot point. This observation is supported by the fact that the intensities of these patterns are negatively correlated: if one of them is more intense, the other does not have to be as intense. Fig. 2.16 depicts a characteristic flow field just before the movement of a stone. The single large vortex in the middle is expected to be responsible for lifting the stone, as it causes a low-pressure area under its core. A shear layer with a typical HVP (Adrian *et al.*, 2000*b*) is visible (highlighted by a dashed line).

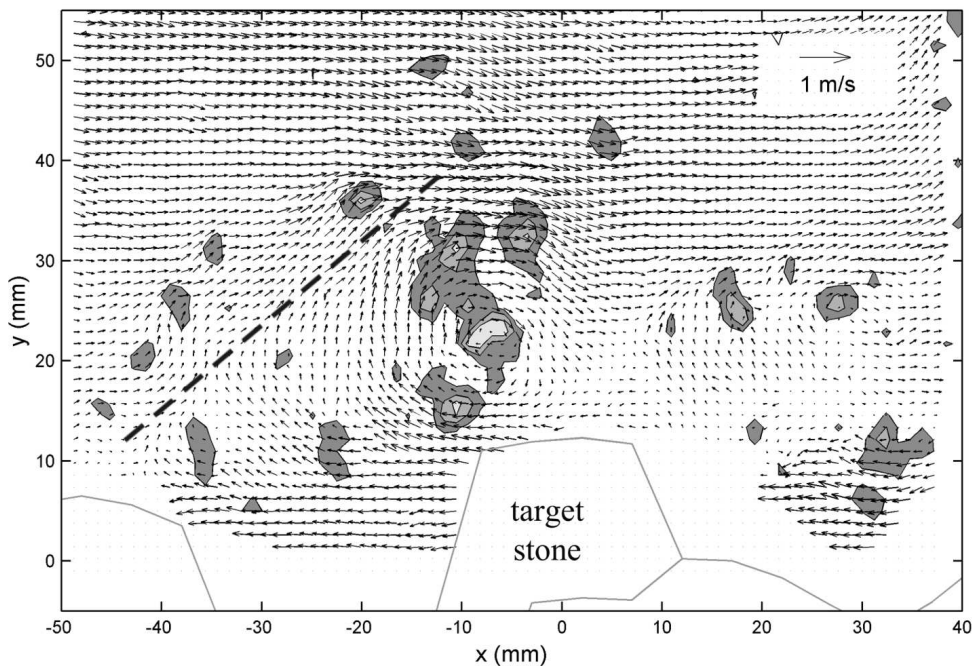


Figure 2.16: Detail of typical instantaneous flow field just before movement of the target stone. 2D PIV from Hofland & Booij (2004). Vectors are $u' - 0.65\langle\bar{u}\rangle$. Shading indicates vortex-cores, identified by the λ_{ci}^2 criterion (Zhou *et al.*, 1999).

High speed 2D PIV measurements were conducted by Cameron *et al.* (2006). They found that sweep flow events dominate the entrainment of spherical roughness elements in a tight packing. No correlation between flow ejection and entrainment was identified.

Wu & Jiang (2007) numerically investigated the interaction of turbulent bursting and sediment entrainment. They implemented a probability distribution of near-bed two-dimensional instantaneous velocities into a simple mechanistic model. Results showed that entrainment of fine sediment mixtures is dominated by the lifting mode, whereas the entrainment of coarse sediments is dominated by rolling. Sweeps revealed to be consistently the most significant contributor to entrainment under various types of sediment mixtures.

2.8 Concluding Remarks

The interaction between free flow and a porous bed is complicated. A key factor for process understanding is founded in the knowledge of coherent structures. The state of knowledge concerning coherent motions at smooth boundaries is considered to be satisfying. Hairpin vortices or deformed versions thereof have their genesis in the viscous sublayer. Adrian *et al.* (2000*b*) proposed an extended model for the outer flow, where these vortices cluster and promote the formation of coherent flow patterns. This model has gained considerable popularity in recent years. In opposite to this, there is a definite deficit in the description of coherent flow patterns for rough boundary conditions. Observations for rough bed flows indicate strong similarities to smooth boundary flow (*e.g.* Roy *et al.*, 2004; Stösser *et al.*, 2005), but the scaling in the near-bed region is different. To identify these structures and to refine the model understanding, there is a need for qualitative flow data that are highly resolved in time and space.

Most of the approaches to determine the initial point of sediment motion use threshold concepts as proposed by Shields (1936), but they do not incorporate the actual physical processes on the gravel bed. Spatio-temporal 3D flow effects as well as grain protrusion and orientation usually are not accounted for. Flow studies in the last decade revealed that both sweeps and ejections are correlated with an initial particle movement. Indications are on hand that entrainment generally takes place during flow events with increased longitudinal velocity. However, the relationship between flow patterns and bed texture requires further clarification.

Recent developments in measuring techniques are full of promise to help in improving the basic knowledge of the interaction between turbulent open-channel flow and the flow in porous granular beds. Hoffland & Booij (2004) and Cameron *et al.* (2006) studied the incipient motion of respectively individual bed elements by a 2D PIV setup. Additionally, Hoffland *et al.* (2005) used single piezo-resistive pressure sensors to gain supplemental information. However, these and previous flow studies focussed on the velocity field in its streamwise vertical extension, disregarding the lateral extension as well as bed permeability effects and pressure fields. Up to now, a comprehensive measurement campaign has not been used to develop a synoptic understanding of the individual hydrodynamic processes and their interaction. To overcome this lack of knowledge is the main objective of the present study.

3 Experimental Studies

Abstract. *This chapter describes the arrangement of physical experiments to observe the flow above and within streambeds in a laboratory water flume. It includes illustrations of the techniques, the methods, and their performance. Three different types of bed material were laid and investigated underlying turbulent open-channel flow so that natural streambed conditions were simulated in full-scale. Measurements were carried out by an array of up to 16 pressure sensors within the bed and slightly above it, a 2D particle image velocimetry system measuring in streamwise vertical or horizontal planes, and a 1D acoustic Doppler current profiler. As main measurements, these subsystems were operated simultaneously to obtain synoptic data sets of the hydrodynamics above and within porous beds.*

3.1 Laboratory Facilities

The experiments were carried out in a rectangular laboratory flume at the Institute for Hydromechanics (IfH), University of Karlsruhe, with an effective length of $L = 17.0$ m and a width of $B = 0.9$ m. The water depth ranged from $h = 0.13$ - 0.22 m. The inlet was located at $x^1 = -10.5$ m in relative to the measurement area to guarantee a fully developed boundary layer. The outlet at $x = +6.5$ m was controlled by a vertical thin-plate weir. Hence, influences of both inlet and outlet were small. The bottom of the non-tilting flume had a slight declination of $S_b = 0.5\%$. Three different bed-variations were inserted: spheres, uniform gravel, and gravel from the river Rhine. The slope of the flume bottom was roughly adopted to these beds. However, due to a slight inevitable erosion that started at the outlet, the slope increased downstream of the measurement area, roughly over the last 3 m of the flume. The water depth h was measured at three points at $x = [-9.33, 0.00, +4.42]$ m by ultrasonic probes. They were mounted on external cylindrical water tanks that were in hydraulic interconnection with the porous bed via flexible tubes (25 mm in diameter). In this, fluctuations and small-scale oscillations of the actual water level were low-pass filtered.

Fig. 3.1 illustrates the measurement setup. It consisted of an array of up to 16 miniaturized piezometric pressure sensors (MPPS) located within and slightly above the gravel layer, and a 2D Particle Image Velocimetry (PIV) system. The latter technique was used for measuring velocities both in a centerline plane perpendicular to the bed (xy -plane:

¹Exactly as in §2.2, a right-handed coordinate system is implied, where x is orientated positive in global, streamwise flow direction, y in upwards vertical and z in transverse direction. $x = 0$ holds at the middle of the measurement area. $y = 0$ defines a notional wall level, where an extrapolated log fit of $\langle \bar{u} \rangle(y)$ would reach zero. $z = 0$ is located in the centerline of the flume. The velocity components u, v and w correspond to x, y and z .

3 Experimental Studies

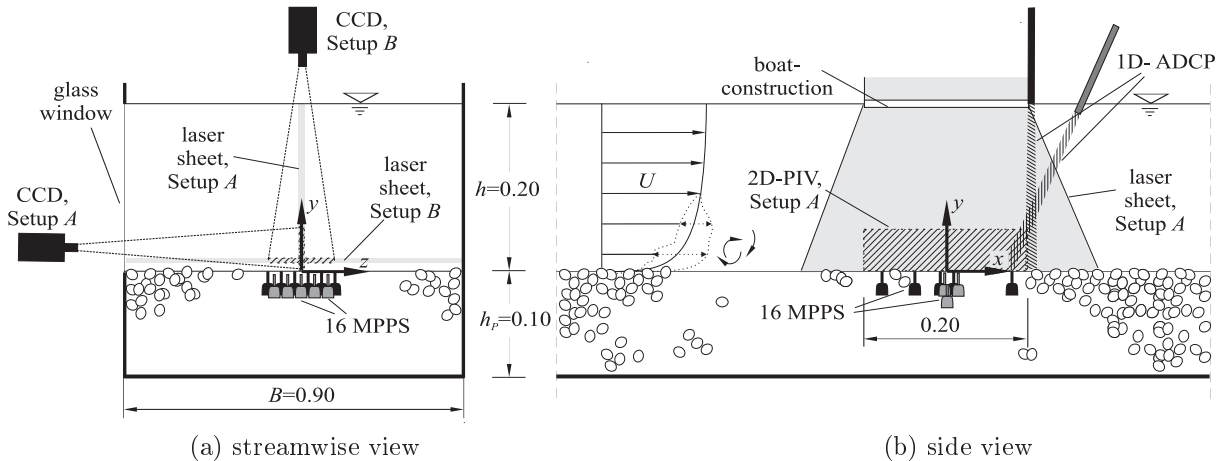


Figure 3.1: Sketch of experimental setup, dimensions in (m), not to scale. a) view in streamwise direction, with both 2D PIV arrangements of setup A and B. b) side view, where the positions of the 1D ADCP probe can also be seen.

setup A) and in horizontal planes 5-23 mm directly above the upper grain crest (xz -plane: setup B). Optical access was given on the larboard-side² of the flume by a 4.0 m long glass window. Additional insight into the velocity regime was gained by an acoustic Doppler³current profiler (ADCP) in order to double-check the PIV results. Typically, the data acquisition was carried out simultaneously for 16 MPPS, the 2D PIV system, and one single ADCP probe for 205 s. Within the next three chapters, the measurement subsystems are described in detail.

3.2 Particle Image Velocimetry (PIV)

Measurement Principle. At present, PIV is the most common and best known method for quantitative, non-intrusive visualization of flow fields. The rapid development in computer, laser, optics, electronics, and video techniques since the 1990s was necessary to be able to use PIV in an efficient manner (compare Adrian, 1991 with Adrian *et al.*, 2000a).

For evaluating flow fields, digital image recordings of a 2D plane of the flow have to be taken, where the flow field is seeded with appropriate tracer particles. The choice of proper tracer particles is a difficult part of the PIV setup. The tracer particles have to be neutrally buoyant in the fluid. Another important parameter is the size of the particles. Very small particles are invisible to the camera, or they evoke peak-locking effects, *i.e.* the vector field contains strong peaks at the position of the integer pixel displacement. Raffel *et al.* suggested using particles with a diameter bigger than 1.5 pix on the camera chip. If the particles appear smaller, a slight defocusing of the camera optics increases

²larboard = left hand side in streamwise direction

³Christian Andreas Doppler: * 29/11/1803 in Salzburg (A); † 17/03/1853 in Venice (I)

their pixel size in the recordings. If the particles are too large, they do not follow the real flow, due to inertial forces. Flow structures can be adequately resolved if their length scale is at least 5 times bigger than the particle diameter (Raffel *et al.*, 1998, Weitbrecht, 2004). The tracer particles must be able to follow the flow structures and must be able to scatter the light. As the seeding particles are very small, a powerful illumination of the measuring area is needed. Usually, a laser light sheet is used to illuminate a required plane in the flow.

The basic means of obtaining velocity vectors is based on the well-known kinematic equation, *i.e.* velocity equals distance divided by time. The procedure is as follows: A so-called area-of-interest (AOI) is cut out of the digital image and divided into small subareas, called interrogation cells. A local displacement vector is determined for each interrogation cell between two sequentially recorded images by means of a cross correlation in the following form:

$$C(\Delta x, \Delta y) = \sum_{x=0, y=0}^{x<n, y<n} I_1(x, y) I_2(x + \Delta x, y + \Delta y) . \quad (3.1)$$

Hereby, I_1 and I_2 are the image intensity of the first and second interrogation cell. The 2D array C gives the correlation strength for all integer displacements $(\Delta x, \Delta y)$ between the two interrogation cells, while n is the size of the interrogation cell (Raffel *et al.*, 1998). Fig. 3.2 shows an example of a correlation distribution obtained using eq. 3.1 in which the highest peak represents the most probable displacement.

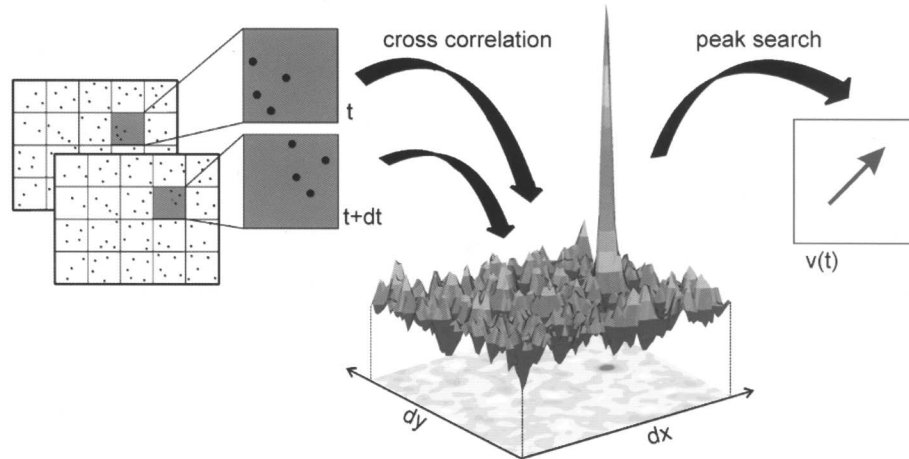


Figure 3.2: Principle of the PIV technique (source: *LaVision GmbH*).

Finally, the velocity vector can be deduced using

$$[u, v] = \frac{[\Delta x, \Delta y](C_{\max})}{\Delta t} , \quad (3.2)$$

where $[\Delta x, \Delta y](C_{\max})$ is equal to the most probable displacement and Δt is the time between two frames.

3 Experimental Studies

If the velocity vector for each interrogation cell is calculated, the result is a time series of vector fields. The temporal and spatial resolution depends on the optical quality of the camera system, the seeding particles, the illumination and the computer power.

Equipment. A commercial 2D PIV *LaVision*-system was used. This PIV package includes camera, laser-illumination, frame grabber, controlling and evaluation software. Digital images could be recorded by a (1280×1024) pix² 12-bit PCO camera with a CCD-sensor (*Flowmaster 3S*). To get a satisfying spatio-temporal resolution, a double frame mode had to be used. In this mode, two images are captured within a very short time. The first image is not read out directly (as in a simple single-frame mode), but shifted to the storage position on the camera chip and then the second frame is taken. The shortest time allowed between two frames in double frame mode is 0.4 ms. For the experiments an interval time of 2-8 ms was used to acquire one double frame according to the flow velocities. However, during the transfer of this double frame to the RAID system a relatively long read out time of 250 ms is necessary for a full double frame of $2 \times (1280 \times 1024)$ pix². Consequently, vectors are only able to compute between one image-pair of one double frame, but not between different double frames.

Special adoptions to the laboratory problem were made. Measurements were based upon seeding the flow with neutrally buoyant tracer particles (polyamide powder *Vestosint*[®], type 1101, $d \simeq 80-200 \mu\text{m}$, $\rho = 1.06 \text{ kg/m}^3$). The flow field was illuminated by a dual-cavity Q-switched Nd:Yag laser with a pulse energy of up to 25 mJ per pulse. The emitted light was green at a wavelength of 532 nm. The laser sheet was enlarged by a tophead lens and had a thickness of 1-2 mm. For *Setup A*, the laser sheet was guided into the water through a glass bottom of a streamlined hull construction of 15 mm breadth and 300 mm length. In this, no free surface was present where the sheet entered the water and, in turn, the sheet remained undistorted. Typically, the hull was immersed by <5 mm and caused small surface waves in the wake, but did not affect the flow in the near-bed region. In this, a plane perpendicular to the bed was illuminated in the centerline of the flume. No measurements were performed where the sheet was laterally translated from the centerline. For measuring a horizontal plane in *Setup B*, a similar construction for the camera was inserted. The streamlined boat-shaped construction was 100 mm in breadth and 300 mm as overall-length. Supplementary for *Setup B*, a wide angle lens (Nikon F-mount, 14 mm, distortion <1%) was used to increase the observed flow area. This lens provided high resolution combined with high luminosity, which is important for the measurement accuracy.

At *Setup A*, the size of the camera frames was vertically reduced to (1280×384) pix² to increase the read out duration of the camera chip. Thus, constant double frame rates of $f = 8.5 \text{ Hz}$ were reached, leading to 1740 double frames within 205 s. Hence, the optimal record length of 60-90 s to measure turbulence in fluvial boundary layers was preserved (Buffin-Bélanger & Roy, 2005). The camera was adjusted to a streamwise vertical xy -plane of $(202.0 \times 60.5) \text{ mm}^2$ directly above the bed, incurring a loss for the observation of the outer flow. Fig. 3.3 gives an example of a single PIV recording of this size. At *Setup B*, the size of the camera frames was laterally shortened to (1280×800) pix² for the experiments with the uniform gravel and the Rhine-gravel. For the experiments

3.3 Acoustic Doppler Current Profiler (ADCP)

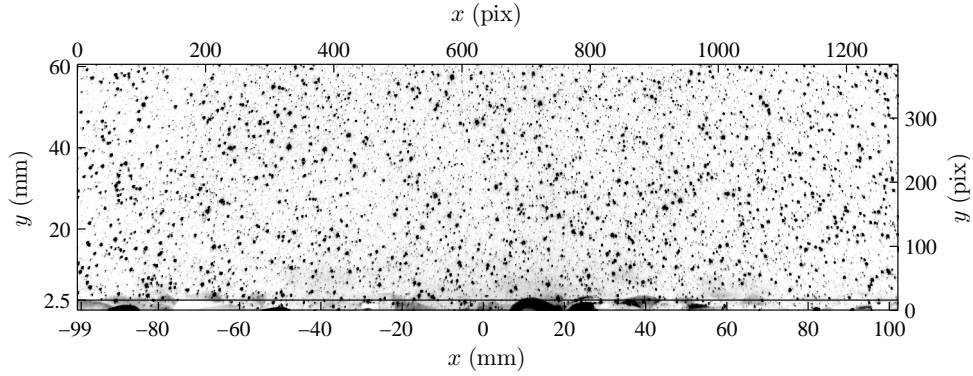


Figure 3.3: Single PIV frame (negative print), where the seeding and also the gravel bed becomes visible. Raw picture from *Setup A* (xy -plane), according to the hatched area in fig. 3.1(b). The roughness crest is located at $y = 2.5$ mm and $y = 16$ pix, respectively.

with spheres, the full frame size was read out. Consequently, double frame rates of $f = 4.9(4.0)$ Hz for the experiments with the gravel (spheres) were reached, leading to 1003 (819) double frames within 205 s. Typically, an xz -plane of (160×100) mm² ((144×115) mm²) could be observed.

The image processing was done by a multipass cross-correlation method with discrete window offset, where the intermediate vector fields were smoothed by a 3×3 Gaussian filter. A final window size of (16×16) pix² with 50% overlap was chosen. Thus, the vector spacing was half the spatial resolution in each case. The latter resulted in 2.52 mm for *Setup A*; for *Setup B* finally 1.98-2.06 mm (gravel) and 1.56-1.90 mm (spheres) were maintained, depending on the distance between the camera lens and the horizontal PIV-slice. The resulting vectors were checked by a median filter, an absolute allowed vector range and the distinctiveness of the highest correlation peak. Typically 75-95% of all vectors within one double frame were validated, depending on the density and homogeneity of the seeding.

3.3 Acoustic Doppler Current Profiler (ADCP)

Measurement Principle. The basic concept in pulsed Doppler ultrasound is similar to the biosonar as used by bats or whales. An emitter periodically sends out a short ultrasonic burst and a receiver continuously collects the echo issues from targets that may be present in the path of the ultrasonic beam. By sampling the incoming echoes at the same time relative to the emission of the bursts, the shift of positions of scatterers are measured. Velocities are derived from the shifts in positions between the pulses.

The distance between the emitter and the target (*e.g.* a seeding particle) can be computed from the knowledge of the time delay t between an emitted burst and the scattered echo from the particle:

$$\xi = \frac{c t}{2}, \quad (3.3)$$

3 Experimental Studies

where c is the sound velocity of the ultrasonic wave in the liquid. If the scattering particle is moving with a non-zero velocity component along the beam axis, a Doppler shift of the echoed frequency takes place. The velocity can be calculated by

$$u_\xi = \frac{c f_D}{2 f_e}, \quad (3.4)$$

where f_D is the Doppler frequency and f_e is the emitting frequency. The limitation of this measuring principle is ruled as follows. The maximum detectable depth and the maximum measurable velocity are related by

$$\max(\xi) \max(u_\xi) = \frac{c^2}{8} \frac{1}{f_e}. \quad (3.5)$$

Since for a given measuring situation both c and f_e are constant, the product $\max(\xi) \max(u_\xi)$ is also constant. This means that – for a given transmitting frequency – a compromise between maximum measurable depth and maximum measurable velocity has to be found for each measurement situation.

The velocity component u_ξ measured by the ADCP is always the component in the direction of the ultrasonic beam, ξ . However, if a single flow direction is predominant, its time averaged velocity component can be deduced from $\overline{u_\xi}$. Let θ be the angle of the beam against the streamwise direction. Then, a spatial vectorial decomposition reads

$$\begin{aligned} u_\xi &= \cos \theta u + \sin \theta v \\ \overline{u_\xi} + u'_\xi &= \cos \theta (\overline{u} + u') + \sin \theta (\overline{v} + v'). \end{aligned} \quad (3.6)$$

If $\overline{v} \ll \overline{u}$ holds, the time average of eq. 3.6 simplifies to:

$$\overline{u} = 1 / \cos \theta \overline{u_\xi}. \quad (3.7)$$

As in PIV, the velocimetry in ADCP is a non-intrusive technique. However, PIV provides results of whole velocity fields, whereas in ADCP only instantaneous velocity profiles are given. Moreover, the acoustic beam spreads from the transducer. Thus, in ADCP the spatial resolution decreases with distance. The main advantage of ADCP in comparison to PIV is that it is easier to handle. Safety precautions and time consuming postprocessing are not necessary.

Equipment. The ADCP instrumentation that was used in the experiments was a *DOP 1000* (Willemetz, 1997). The architecture of the velocimeter includes transducer, oscillator, amplifier, AD converter, controlling as well as evaluation hardware and software. A dimensional sketch of the transducer and the ultrasonic field is given in fig. 3.4.

The same transducer was used to both transmit ($f_e = 4$ MHz) and receive the ultrasonic signals. Just after the emission of the ultrasonic burst, the transducer switched from the emitting mode to the receiving mode. The incoming echoes were amplified, demodulated and then filtered to isolate the Doppler information. The Doppler signal was then sampled and converted into digital form by an AD converter. Finally, the Doppler frequency f_d

3.3 Acoustic Doppler Current Profiler (ADCP)

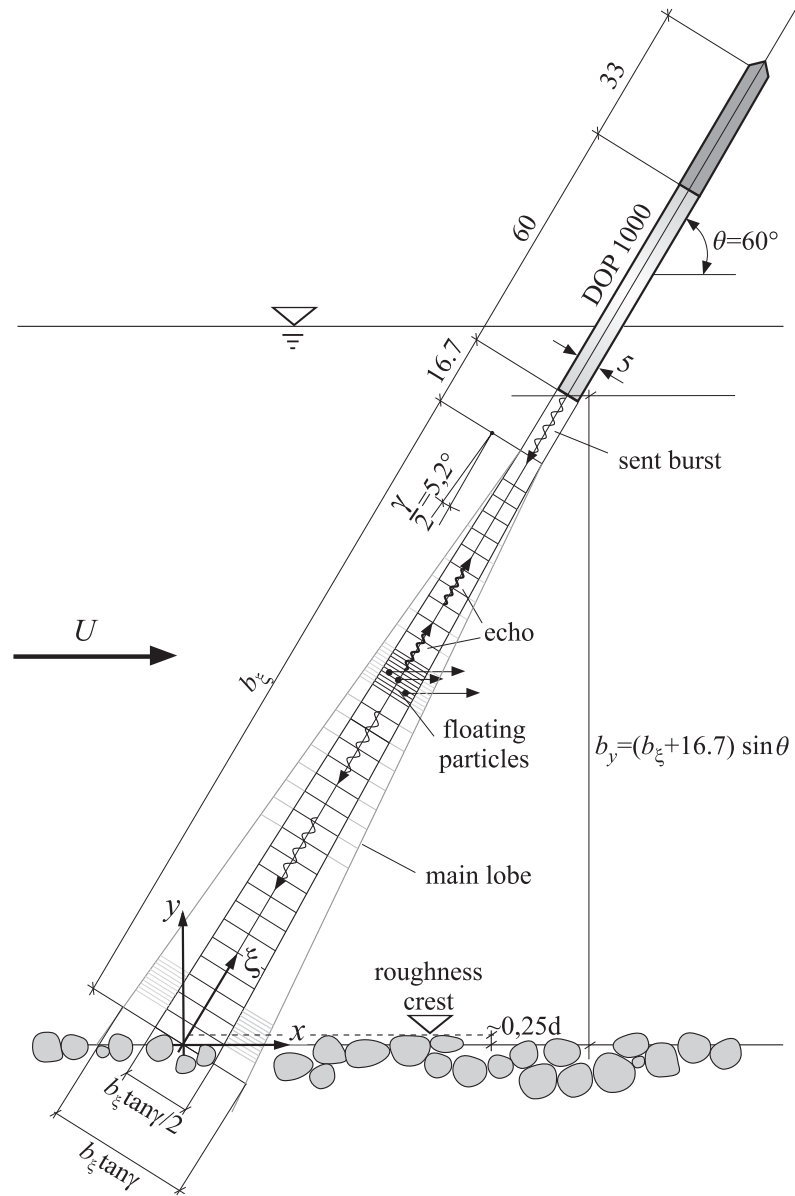


Figure 3.4: Geometry of the ADCP-probe and its acoustic field, adjusted to measure $\bar{u}(y)$. For recordings of instantaneous profiles of $v'(y)$, the transducer had to be orientated vertically ($\theta = 90^\circ$). Dimensions in (mm), not to scale.

3 Experimental Studies

was estimated by an auto-correlation algorithm. The results were then used to calculate the velocities $u_\xi(\xi)$ by applying eq. 3.3 and eq. 3.4. The resulting velocity information could be displayed on a monochromatic screen and recorded on a floppy disc.

The ADCP was used to reduce the spatial shortcomings of the PIV-system that focused solely on a near-bed domain in the centerline of the flume. Mainly, the ADCP was applied to record the instantaneous vertical velocity fluctuations $v'(y)$ over the entire water depth h , synchronously to the PIV measurements. The synchronization was realized by an external trigger start (TTL-pulse) from the PIV-system. Fortunately, for both ADCP and PIV the same seeding could be used. During the measurements, the ADCP transducer had to be slightly immersed into the water to be in permanent contact to the fluid. To minimize disturbances to the other measurement subsystems, the probe was installed in the stern of the streamlined hull construction of the PIV setup.

Supplementary to these centerline measurements synchronous to the PIV-system, profiles of $v'(y)$ and $\bar{u}(y)$ along the entire lateral extension were gained solely by the ADCP. By this, an insight into the whole velocity regime of the outer flow layer was possible, including an examination of secondary currents as well. For recording $\bar{u}(y)$ an angle of $\theta = 60^\circ$ was chosen (fig. 3.4). Consequently, eq. 3.7 reduces to the simple relation $\bar{u} = 2.0 \bar{u}_\xi$. Note again that this ratio is strictly valid only if secondary currents are negligible. Otherwise, the profiles of \bar{u} get biased, in case of $v' > 0$ towards larger values, in case of $v' < 0$ towards smaller values.

The main lobe of the ultrasonic far-field spreads from a diameter of 5 mm at an angle of $\gamma/2 = 5.2^\circ$. However, the acoustic energy is concentrated more at the axis: 85.5% of the radial integrated far field intensity is already contained its half diameter, 98% are reached in the full diameter of the main lobe. For distances typical for the measurements, *e.g.* $b_y = 190$ mm and $b_\xi = 203$ mm respectively, the half-diameter in the near-bed region reaches 18.5 mm. Consequently, the spreading of the beam acts like a large eddy filter to the small-scale fluctuations.

Due to the limitations described in eq. 3.5, the parameters had to be adjusted carefully to the existing conditions of flow velocity and water depth. Typically, profiles of $v'(y)$ were recorded at 39.2 Hz and $\bar{u}(y)$ at 10.8-38.4 Hz, respectively. The spatial resolution in the beam direction was mostly chosen to be 1.5 mm.

3.4 Miniaturized Piezo-resistive Pressure Sensors

Measurement Principle. The physical quantity pressure is defined as force per loaded unit area. When pressure is applied to a piezo⁴-electric material, it causes a mechanical deformation and a displacement of charges. A piezoelectric sensor is a device that uses the piezoelectric effect to measure the force per loaded area unit, by converting them to an electrical signal. The single disadvantage of piezoelectric sensors is that they cannot be used for true static measurements. A static force will result in a fixed amount of charges on the piezoelectric material. Working with conventional electronics, not perfect

⁴'Piezo' is derived from the Greek 'piézēin', which means to squeeze or press.

3.4 Miniaturized Piezo-resistive Pressure Sensors

insulating materials, and reduction in internal sensor resistance will result in a constant loss of electrons, yielding an inaccurate signal.

The principle of the miniaturized piezometric pressure sensors (MPPS) is based on the piezo-resistive effect. In contrast to the piezoelectric effect, the piezo-resistive effect only causes a change in resistance, it does not produce electrical charges. The core of the MPPS is a micromechanical silicon wafer with implanted piezo-resistors on its bending panel. Fig. 3.5 gives a sketch of the principle layout. A pressure load and the resulting mechanical bending stress causes a change of these piezo-resistors, suitably combined in a bridge circuit by anodic bonding. The output of the powered bridge is a voltage signal in the range of mV, proportional to pressure. The silicon device is connected with a glass base to ensure the restraint at the edges. To apply the reference pressure, the glass base has a hole. For the MPPS the differential pressure is measured with reference to atmospheric pressure p_{atm} . Temperature errors are compensated electronically.

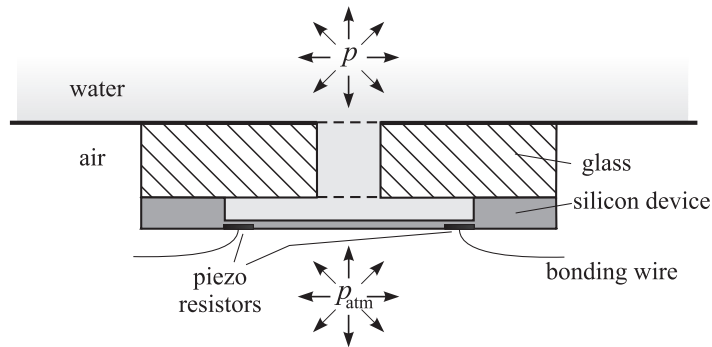


Figure 3.5: Schematic cross section of a piezo-resistive sensor to measure the differential pressure.

Equipment. The components for the MPPS were obtained from *Aktiv Sensor GmbH*, Berlin. The sensor elements *ATD 0.040-G00-BG-K1408* and *AU blank PGA-V0-D18A* were assembled at the *Institute for Hydromechanics* to adapt them to their application within the experimental flume. Fig. 3.6(a) gives a dimensional sketch of one pressure pick-up. Depending on their configuration, the sensors measure both the surrounding pressure and the velocity head. Thus, the sensed pressure reflects the effective force per pinhole area in direction of the pressure tube. When the pickup is facing upwards, it indicates the intensity of lift forces, F_L ; when the pickup is facing in streamwise direction, it indicates the intensity of drag forces F_D .

To miniaturize the pressure transducer the amplifying blankets had to be arranged in an external box. Unfortunately, the length of the flexible cables to the external amplifying board could not be shorter than 2.5 m, due to the boundaries of the experimental setup. Thus, the possibility of a slight antenna effect had to be accepted. Flexible PVC tubes were used to provide atmospheric pressure in the pick-up, also with a length of 2.5 m. The pick-ups of the MPPS were encapsulated with slowly hardening epoxy resin and sealed up with clear varnish to make them water resistant. In the end, the mean diameter of one sensor head was 15 mm. The ready-built sensors were point-calibrated by *Aktiv Sensor GmbH* to 1-9 V according to 0-4 kPa with a tolerance in accuracy of

3 Experimental Studies

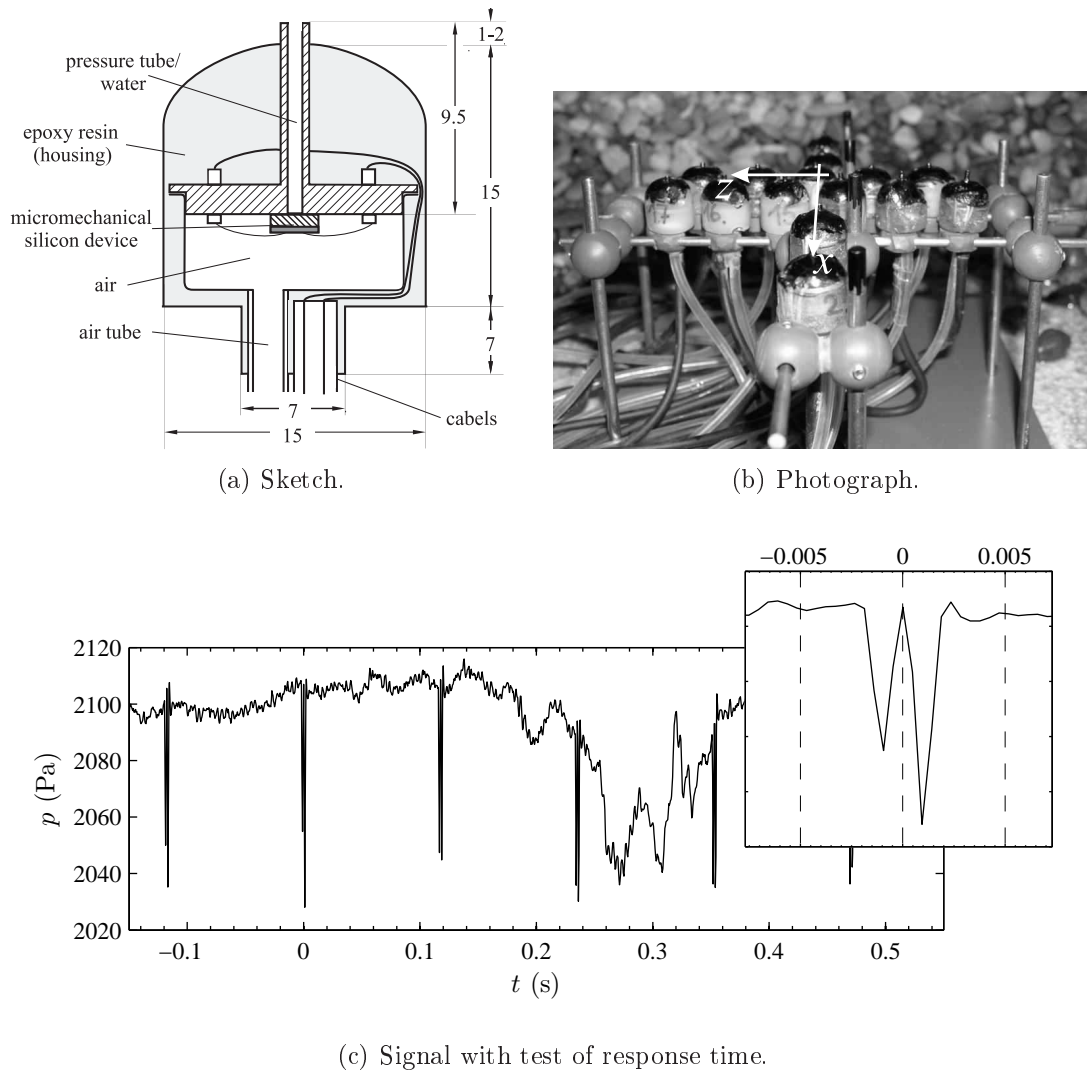


Figure 3.6: (a) Sketch of a pressure pickup (mm). (b) Array of MPPSs mounted on a grid, not covered by gravel yet. This arrangement was used in synchronous measurements of MPPS, PIV and ADCP. (c) Measurement to test the response time of the MPPS, where the sensor reacts on the double pulse of the PIV laser sheet of $\Delta t = 2$ ms.

less than 1.0% full scale. The response time guaranteed by the manufacturer was <10 ms, limited due to signal conditioning by the amplifying blankets. To avoid aliasing effects due to high frequency noise >2 kHz, the recording was made at $f \simeq 2125.7$ Hz, additionally supported by a 4th order Butterworth low-pass filter with a cut-off frequency of 500 Hz (*Data Translation SAK 52-150-501-10*). A 16-bit AD-Card (*Data Translation 321*) allowed a theoretical resolution corresponding to a $\text{LSB} = 20/8 \cdot 4000/2^{16} = 0.15$ Pa. Within the flume, the sensors were locally fixed on a grid to keep them in an accurately defined position. Fig. 3.6(b) gives an example of an array of MPPS, arranged to indicate the horizontal extensions of lift forces.

Synchronous measurements were started by a TTL (transistor–transistor logic) trigger pulse from the PIV-system. The TTL signals of the PIV frame grabber were additionally recorded by the 16-bit AD-Card, to enable a fine-tuning of the synchronization afterwards. Furthermore, tests under flume conditions showed that the MPPS were even able to react within 2 ms. In one measurement arrangement four sensors were aligned within the laser sheet. The laser double pulses were clearly identifiable in the signal, as shown in fig. 3.6(c). This unforeseen effect was used to validate the synchronization of the PIV and the MPPS. Besides the measurements conducted synchronous to the other subsystems, additional measurements were performed where solely the MPPS came into use. In these experiments, the sensors were vertically distributed on top and within the porous bed to measure both time series of drag and lift.

3.5 Bed Material

Flow measurements were performed over three different types of porous beds: spheres, uniform gravel, and gravel from the river Rhine. Tab. 3.1 summarizes the properties of the bed parameters; special features concerning experimental methods and characteristics are treated in detail hereafter. The grain sizes d_i were gained by sieve analysis. The permeability coefficient k_f was gained following Hazen’s (1892) equation

$$k_f = 100 d_{10}^2, \quad (3.8)$$

where d_{10} , is denoted as the ‘effective’ size in (mm) and k_f is in (m/s).

Index	bed	$[d_{15}, d, d_{85}]$ (mm)	ϕ (-)	k_f (m/s)	ρ_s (10^3kg/m^3)	packing
#uni	uniform gravel	[7.7, 10.2, 13.2]	0.39 ± 0.02	0.7	2.46	loose
#rhi	Rhine, armored	[13.8, 26.1, 38.8]	0.33 ± 0.02	1.5	2.51	loose
#sph	spheres	[25.4]	0.26	-	1.36	densest

Table 3.1: Parameter of the bed materials uniform gravel, gravel from the river Rhine (armoring layer), and spheres. The weighted mean of the whole grain size distribution is represented by d (eq. 2.35). For #uni $d \approx d_{50}$ and for #rhi $d \approx d_{70}$ holds. ϕ is the roughness geometry parameter (eq. 2.3).

3 Experimental Studies

Uniform Gravel. The basic configuration for the flume bed was arranged using gravel with a uniform grain size. This single grain size material ranged between the complex characteristics of gravel found in natural streams and the simple geometries of spheres, as often used in abstracted model approximations and numeric simulations. In this setup, with an almost homogeneous design of the bed, the experimental studies gave a general approach to the flow regime on a rough porous bed. The results are attended as reference for the two other bed materials. Fig. 3.7(a) shows a photograph of the material as it was inserted in the flume. This material is the same as used by Detert *et al.* (2007), but with a slightly different measurement setup. Therefore, comparisons and supplementations between the experimental results are possible.

The grain size quantiles $d_{15} = 7.7$ mm and $d_{85} = 13.2$ mm were gained from sieve analysis, $d = 10.2$ mm represents the weighted mean of the whole grain size distribution (see eq. 2.35). The roughness geometry parameter ϕ was determined by an external experimental setup. Fig. 3.7(b) shows the cylindrical tank, where the void volume of the pores was determined by volumetric dosing. Adherent air bubbles in the watered gravel were removed under low pressure conditions.

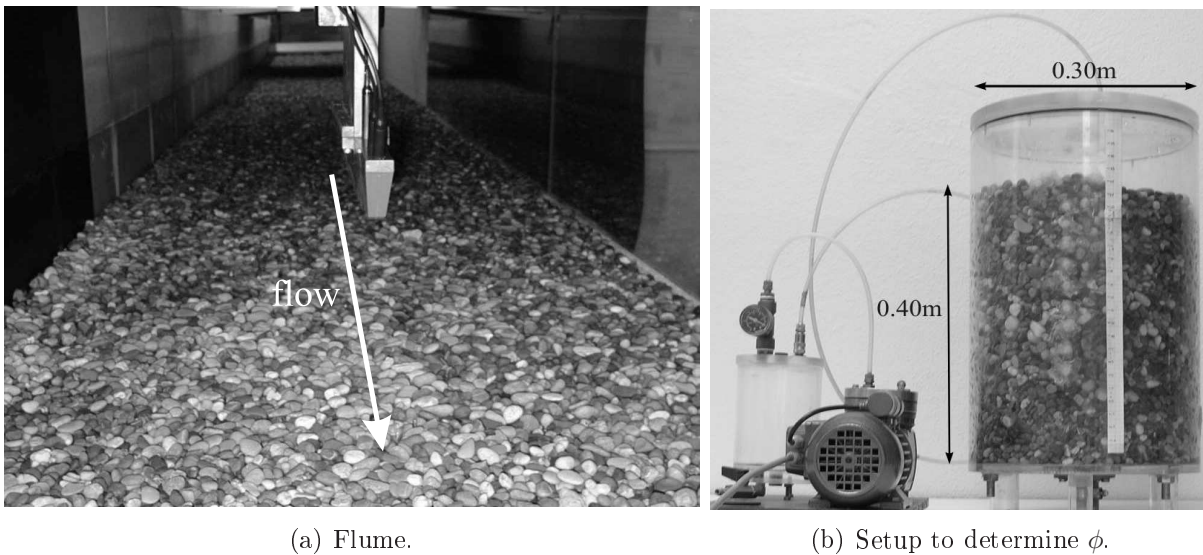


Figure 3.7: Gravel with uniform grain size. a) Installation for flume experiments, where also the hull construction can be seen. b) Experimental setup to determine the roughness geometry parameter.

Rhine Gravel. Additional measurements were performed with gravel originating from the Rhine river. In this, the porous bed texture and consequently the rough bed flow was as natural as it was possible within a laboratory experimental setup. Fig. 3.8(a) shows a photograph of the gravel bank ~ 10 km downstream of the Iffezheim-barrage, where the material was removed at low water conditions (02.08.2006). An armoring layer with a thickness of $1-2 d$ was distinctive. A sieve analysis gave $d = 26.1$ mm and $d_{85}/d_{15} = 2.81$.

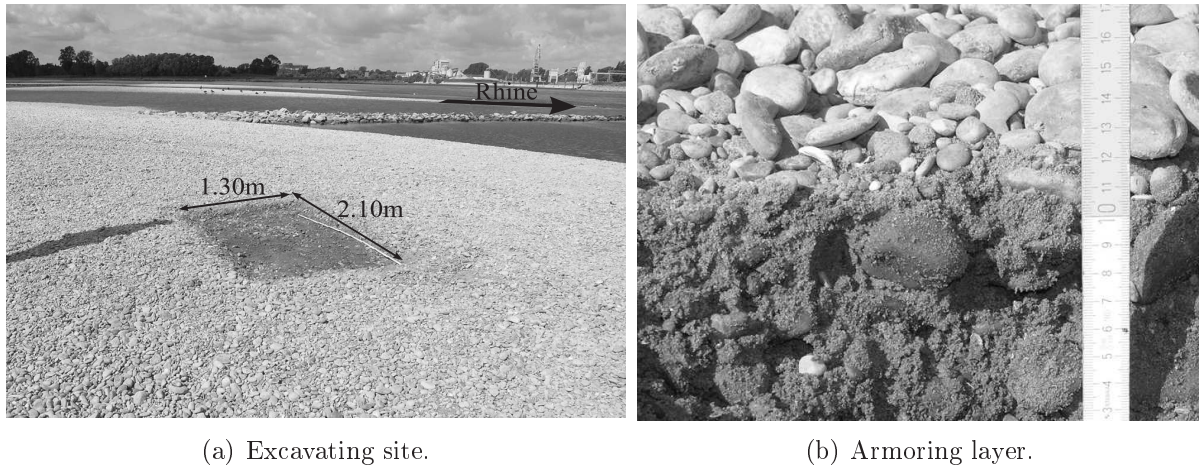


Figure 3.8: In-situ photographs from a gravel bank at the river Rhine on 02.08.2006 (low water). a) Place of excavation for the non-uniform material. b) Armoring layer and substructure.

The underlying material as shown in fig. 3.8(b) revealed to be bimodal, with centers at $d_{10} = 0.4$ mm for 15% of weight and $d_{60} = 14.7$ mm for 85% of the weight.

To simulate the Rhine bed in the experiments, the uniform gravel was replaced by the non-uniform material on a length of $x = -4.0$ to 0.5 m in streamwise reference to the measuring area on the whole breadth of the flume. The reproduction was made as it was found in situ: The substructure was built by the bimodal material with a thickness of 60-80 mm, an armoring layer with a thickness of $1-2 d$ was replicated on top of it. However, it was not possible to copy the dense package of the armoring layer in the flume, as otherwise the cables of the MPPS would have been damaged. Thus, ϕ was < 0.33 for the real armoring layer in the river Rhine.

Spheres. The third bed structure installation was of three layers of spheres in densest packing. This type of bed provided an abstracted bed geometry, as it is often used in numerical and analytical models. These experiments had two intentions. On the one hand, the results could be used as a reference case for numerical simulations or simple theoretical approaches. On the other hand, the results help in classifying the transferability of flow characteristics over a spherical bed to natural porous rough bed flow. The spheres used in the experiments were originally manufactured as balls for deodorant roll-ons. For the experiments, they were filled with fine sand to avoid buoyancy effects. The fill-hole was closed with epoxy resin. For the experiments, the uniform gravel bed was only partly replaced by spheres. Three layers of spheres were inserted at $x = -460$ to 290 mm and $z = -150$ to 150 mm. The uppermost layer was lengthened upstream to $x = -1160$ mm to provide fully developed sphere-flow conditions (fig. 3.9(a)). The roughness geometry parameter $\phi = 0.26$ for spheres in pyramidal packaging – as shown in fig. 3.9(b) – was taken from the analytical-numerical derivation of Bowen & Radin (2003).

3 Experimental Studies

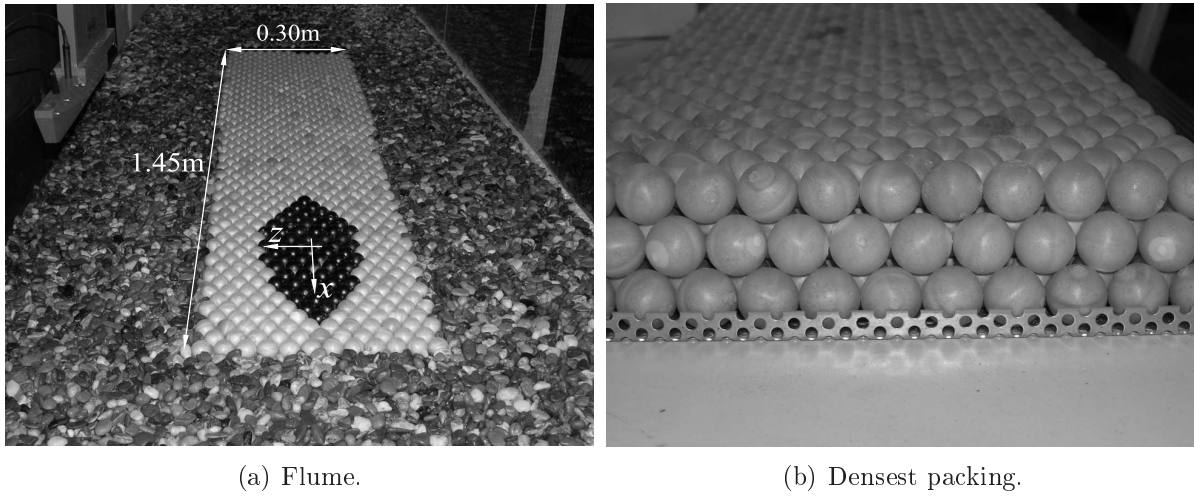


Figure 3.9: a) Flume bed prepared for the spheres experiments. The spheres in the vicinity of the laser sheet were painted black to minimize reflections of the laser sheet. b) Three layers of spheres in densest (pyramidal) package.

3.6 Experimental Program

Flow Conditions. Tab. 3.2 gives the flow conditions that were provided during the measurements. Q is the flow rate, the bulk velocity is determined by $U = Q/(Bh)$. The bulk Reynolds-number is defined by $Re_h = Uh/\nu$, with the kinematic viscosity of water $\nu = 10^{-6} \text{ m}^2/\text{s}$ at 20°C . The runs #uni3,6,9 included a velocity spectrum from stable bed conditions up to very slight sediment transport. The flow condition provided for the Rhine-bed were adopted from #uni9, where Re_h was the same. The experiments with the bed roughened by spheres were conducted at lower Re_h numbers to keep them in the

Index	Q (l/s)	h (m)	U (m/s)	Re_h (-)
#uni3	56.6	0.200	0.314	$62.8 \cdot 10^3$
#uni6	120.0	0.200	0.667	$133.4 \cdot 10^3$
#uni9	180.0	0.211	0.948	$200.0 \cdot 10^3$
#rhi9	180.0	0.215	0.930	$200.0 \cdot 10^3$
#sph1	18.6	0.129	0.160	$20.6 \cdot 10^3$
#sph3	56.6	0.199	0.316	$62.9 \cdot 10^3$

Table 3.2: Experimental flow conditions. The integers [1,3,6,9] at the end of the indices refer approximately to the ratios of Q_i , U_i , and $Re_{h,i}$. At #uni9 the provided flow led to very slight sediment transport, where single grains were moving from time to time.

range that can be reached by contemporary numerical simulations.⁵

Measurement Performance. As main measurements, the three subsystems PIV, MPPS and ADCP were operated simultaneously to get synoptic data sets of the hydrodynamics above and within the porous beds. For these measurements, the PIV was installed to observe the near-bed centerlined xy -plane or in different near-bed horizontal xz -planes. The MPPSs were arranged in a horizontal array, as shown in fig. 3.6(b), facing upwards to indicate the lift force intensity. This was the optimal way to obtain pressure information in a horizontal layer without the pick-ups affecting the flow. By mounting the MPPS array at different reference heights to the bed, different horizontal layers were examined. The ADCP was applied to record the instantaneous velocity fluctuations $v'(y)$. As the transducer was mounted at the stern of the streamlined glass hull, these recordings of velocity fluctuations accord to velocity fluctuations slightly downstream of the PIV frames.

Additional, single measurements were performed where only the MPPS or the ADCP came into use. The MPPSs were arranged to indicate both, lift and drag forces, in different vertical positions above and within the porous beds. The ADCP was used to measure the lateral distribution of $\bar{u}(y)$ and $v'(y)$.

Tab. 3.3 summarizes the parameters of the synchronous and the additional measurements.

Index	synchronous measurements		additional single measurements
	PIV	MPPS	
#uni3,6,9	<i>Setup A</i> (centerline)	$F_L(y = 0.0 \text{ mm})$	MPPS; ADCP;
	<i>Setup A</i> (centerline)	$F_L(y = 10.0 \text{ mm})$	$F_L(y = 18.0 \text{ and } 7.5 \text{ mm});$
	<i>Setup B</i> ($y = 7.5 \text{ mm}$)	$F_L(y = -1.5 \text{ mm})$	$F_D(y = 5.0 \text{ and } 7.5 \text{ mm})$
	<i>Setup B</i> ($y = 17.5 \text{ mm}$)	$F_L(y = -1.5 \text{ mm})$	
#rhi9	<i>Setup A</i> (centerline)	$F_L(y = 2.0 \text{ mm})$	MPPS; ADCP;
	<i>Setup B</i> ($y = 11.5 \text{ mm}$)	$F_L(y = 3.0 \text{ mm})$	$F_L(y = 25.0 \text{ mm})$
	<i>Setup B</i> ($y = 21.5 \text{ mm}$)	$F_L(y = 3.0 \text{ mm})$	
#sph1,3	<i>Setup A</i> (centerline)	$F_L(y = 5.0 \text{ mm})$	MPPS; ADCP;
	<i>Setup B</i> ($y = 13.5 \text{ mm}$)	$F_L(y = 5.0 \text{ mm})$	<i>Setup B</i> ($y = 9.5 \text{ mm}; \#sph1$)
	<i>Setup B</i> ($y = 27.5 \text{ mm}$)	$F_L(y = 5.0 \text{ mm})$	

Table 3.3: Performance of the synchronous and the additional measurements.

⁵For instance, the need for computational power in flow simulations by DNS increases proportional to $\text{Re}^{11/4}$ (Hinterberger, 2004).

4 Experimental Results

***Abstract.** Experimental flume measurements of flow velocity and pressure fluctuations above and within three types of porous streambeds are analyzed. The flow conditions examined include a broad diversity of hydrodynamic loads and roughness parameters as can be found in natural, non-moving gravel beds. In a streamwise vertical plane large-scale wedge-like flow structures are observed, where in the sense of a sweep event zones of faster fluid overrun zones with slower fluid. The resulting shear layer inclines at an angle of 10-20° to the bed, densely populated with clockwise rotating eddies. On average, this mechanism occurs with sufficient frequency and shape to leave an imprint on the statistics of the flow. Typically, this flow pattern structure assembles near the bed, say in the logarithmic layer. However, the biggest structures can spread over the whole water depth. In a horizontal near-bed view, macroturbulent structures form a patched chessboard with regions of lower and higher velocity zones that are elongated in streamwise direction. Their near-bed lateral extension is typically 3-4 times the equivalent sand roughness and increases linearly with bed distance. The length of these elongated structures can reach up to the order of several water depths. These structural findings are consistent with models originally developed for smooth wall flows and they support the observations made in rough bed flume experiments, large eddy simulations and natural rivers as well. However, for the first time they are studied by image processing techniques in both streamwise vertical and horizontal near-bed views. The point measurements of pressure fluctuations show that the intensity of turbulent pressure fluctuations decays exponentially in the porous bed. Fields of bed-pressure fluctuations are reconstructed by applying Taylor's frozen turbulence hypothesis on data gained by an array of pressure sensors. By conditional sampling of essential pressure drop events to the synchronously recorded velocity fields, a significant bed destabilizing flow-pressure pattern is identified: If high speed fluid in the wake of large-scale wedge-like flow structures reaches the vicinity of the bed, the Bernoulli effect leads to a marked low-pressure field. The resulting force is able to cause an initial lift of single grains. In this, both the grain's exposed area and its angle of repose are increased such that entrainment by the fast fluid zone becomes possible.*

4.1 Bulk Parameters

In this section, a summary of the bulk parameters that characterize the experimental flow conditions are given. Some have already been presented in §3.5 and §3.6, some are firstly revealed in detail later on.

4 Experimental Results

Shear Stresses. In turbulent open-channel flow, the momentum transfer within the fluid domain is directly linked to the drag at the bed-wall perimeter. The distribution of shear stresses essentially dominates the flow properties. For analyzing and assessing the velocity characteristics, first the structure and the distribution of the shear stress has to be clarified. The parameters characterizing the shear τ_o and the shear velocity u_* are given in table 4.1.

index	icon	$\langle \tau_o \rangle_{\text{us}}$ (N/m ²)	$\langle \tau_o \rangle_{\text{ds}}$ (N/m ²)	$\langle u_* \rangle_{\text{us}}$ (m/s)	$\langle u_* \rangle_{\text{ds}}$ (m/s)	u_{*uv} (m/s)	$u_{*\log} \equiv u_*$ (m/s)	τ_o (N/m ²)
#uni3	▲	0.69	0.40	0.026	0.020	0.027	0.030	0.90
#uni6	◆	3.45	3.70	0.059	0.061	0.059	0.063	3.97
#uni9	■	8.40	20.5	0.092	0.143	0.087	0.095	9.03
#rhi9	★	12.5		0.112		0.081	0.086	7.40
#sph1	•	0.27	0.16	0.016	0.013	0.013	0.015	0.23
#sph3	●	-	0.45	-	0.021	0.028	0.030	0.90

Table 4.1: Shear parameters. $\langle \tau_o \rangle$ is calculated by eq. 2.13, and $\langle u_* \rangle$ was derived from them by applying eq. 2.15. The indices $\langle \cdot \rangle_{\text{us}}$ and $\langle \cdot \rangle_{\text{ds}}$ denote the spatial average of the upstream area ($x = -9.33$ to 0.0 m) and the downstream area ($x = 0.0$ to 4.42 m), respectively. u_{*uv} was estimated by extrapolating $-\langle \overline{u'v'} \rangle$ to $y = 0$ (eq. 2.7). $u_* \equiv u_{*\log}$ is gained from log-law fit (eq. 2.16).

The spatial averaged $\langle \tau_o \rangle$ and $\langle u_* \rangle$ are derived from the mean water surface inclination by applying eqs 2.13 and 2.15. The momentum non-uniformity parameter is determined to be $\beta = 1.03$ (eq. 2.14), from both PIV and ADCP data. The bed slope is constant at $S_b = 0.5\%$. The estimations to the spatial averaged $\langle \tau_o \rangle$ and $\langle u_* \rangle$ give a handle to qualitative statements. For #uni6, $\langle \tau_o \rangle_{\text{us}} \simeq \langle \tau_o \rangle_{\text{ds}}$ holds. Thus the provided flow for #uni6 is considered to be uniform. However, as the bed slope is the same for all experiments, the other flow conditions are consequently non-uniform: #uni3 provides slightly decelerated flow, #uni9 provides accelerated flow. At #rhi9, the ultrasonic probe for $h(x = 0)$ showed unrealistic values. Thus, the calculation for $\langle \tau_o \rangle$ and $\langle u_* \rangle$ was conducted as a longitudinal average from upstream to downstream. As the flow conditions are similar to #uni9, the flow must be also accelerated. At #sph3, the ultrasonic probe at $h(x = -9.33$ m) was defective. However, as the flow conditions are very similar to #uni3, the flow is expected to be slightly decelerated as well. The shear stress estimations for #sph1 are too small to give a definite statement whether the flow is uniform or not.

Following the empirical rule of $u_* = (0.05-0.10) U$ for natural rivers, the calculated $\langle u_* \rangle$ generally provide trustworthy estimations to the lower and upper limits. Consequently, this holds for $\langle \tau_o \rangle$ as well. However, these limits are to inexact for reliable determinations. For a more precise, quantitative description of the shear in the measurement area, two further methods were chosen: (1) u_{*uv} was estimated from the PIV measurements by extrapolating the centerline Reynolds-stresses $-\rho \overline{u'v'}$ to $y = 0$ (eqs 2.7 and 2.15); (2) $u_{*\log}$ was gained by least squares fits of the mean centerline velocity $\overline{u}(y)$ to the log-law

(eq. 2.16, $\kappa = 0.41$, $C = 8.4-8.6$). $u_{*\log}$ was determined from independent PIV and ADCP measurements with tolerances of $\pm 3\%$. For further considerations in this study, $u_{*\log}$ is taken as the 'controlling' shear velocity u_* . Consequently

$$\rho u_{*\log}^2 \equiv \rho u_*^2 \equiv \tau_o \quad (4.1)$$

is applied for estimating the shear in the measurement area. The justification is discussed in the following: As has been worked out in §2.2, the determination of τ_o by extrapolation of the primary Reynolds-stresses to the wall is strictly-spoken only valid for 2D flows, as additional terms due to secondary currents cannot be neglected (see eq. 2.10). A second uncertainty of this method is the dependency on the definition of the vertical origin ($y = 0$), as for a rough porous bed different definitions are reasonable. On the other hand, the determination $u_{*\log}$ depends on the applicability of the chosen ranges for κ , C , and y/h . Typically, $y/h < 0.2$ holds, but this limit is empirical as well. Thus, the second method is also subject to inexactitudes. The difference between u_{*uv} and $u_{*\log}$ differs only by $\mathcal{O}(\text{mm/s})$, which seems to be not that much. However, a closer inspection reveals that $u_{*uv}/u_{*\log}$ is about $90 \pm 3\%$ and consequently, the derivation of $\tau_o (\propto u_*^2)$ would differ by 13-17%. The fact that the shear parameter gained from the Reynolds-stresses throughout are smaller than the parameter gained from the log-fits supports the assumption of secondary currents' influence. Therefore, $u_{*\log}$ is assumed to give a better approach to the integrated, overall global shear; whereas u_{*uv} 'only' gives a measure of the shear resulting from motions in a streamwise vertical plane. It should be noted that most of $u_{*\log}$ is ruled by u_{*uv} .

Geometric Length Scales. Table 4.2 presents the relevant geometric parameters. The water depth was preassigned to $h = 200$ mm. However, testing under flume conditions showed that this depth never could be reached for #uni9 and #rhi9 in the measurement area. Here, the convex water surface slope due to non-uniform flow conditions led to a minimum of 211 mm and 215 mm, respectively. For #sph1, a lower water depth was chosen to obtain flow conditions with lower Reynolds-number. The depth was decreased to $h = 129$ mm, *i.e.* the minimum possible depth compatible with the geometrical boundaries of the measurement setup.

The centerline location of the dip strength parameter $\delta_h = y(\bar{u}_{\max})$, was determined from $\bar{u}(y)$ gained by ADCP. Unfortunately, an accurate locating of $y(\bar{u}_{\max})$ was not possible in steps less than of 5 mm. Beside the results for #sph1, the presence of the dip phenomenon becomes clear, as $\delta_h/h < 1.0$ holds. For the uniform flow conditions of #run6, the dip phenomenon is least distinctive ($\delta_h/h < 0.88$), whereas the centerline \bar{u}_{\max} for the experiments with the accelerated flow was found at approximately $h/4$ below the surface.

The equivalent sand roughness k_s was gained by fitting the centerline $\bar{u}(y)$ to the log law (eq. 2.16), within the same procedure as for $u_{*\log}$. The value of $k_s/d = 2.6$ for #uni9 is in the typical range of $k_s/d = 1-4$ as can be found for natural beds (e.g. Dittrich, 1998, pp. 31-33). The ratio $k_s/d = 0.6$ for the armoring layer (#rhi9) appears to be slightly too small, however. The reason for this is unclear. One possible explanation is that the use of d (eq. 2.35) as denominator is misleading here. For instance, $k_s/d_{15} = 1.1$ reaches

4 Experimental Results

index	h (mm)	δ_h (mm)	δ_h/h (-)	d (mm)	k_s (mm)	k_s/d (-)	y_t-y (mm)	$y(\delta_R)$ (mm)	θ_m (mm)	η (mm)
#uni3	200	165	0.83					22	20	0.29
#uni6	200	175	0.88	10.2	26.5 ± 3	2.6	2.6 ± 2	12	21	0.17
#uni9	211	155	0.73					12	16	0.12
#rhi9	215	155	0.72	26.1	15.5 ± 3	0.6	6.6 ± 3	13	14	0.14
#sph1	129	125	0.97	25.4	20.5 ± 1.5	0.8	5.0 ± 0.5	13.7	13	0.44
#sph3	199	170	0.86					14.4	18	0.29

Table 4.2: Geometric parameters. h = water depth measured by ultrasonic probes, $\delta_h = y(\bar{u}_{\max})$, d = characteristic grain size (eq. 2.35), k_s = equivalent sand roughness, $y_t - y$ = zero plane displacement, $y(\delta_R)$ = upper boundary of the roughness layer, θ_m = momentum thickness, η = Kolmogorov length scale.

the lower range of k_s/d for natural stream beds. Another reason might be that the almost spherical shape of the Rhine gravel leads to similar characteristics as found for spheres: For the spheres experiments $k_s/d = 0.8$ holds, similar to the range of $k_s/d = 0.68-0.82$ given by Grass *et al.* (1991) and $k_s/d = 0.67$ Defina (1996).

The zero-plane displacement is defined by the vertical distance between the height of roughness tops and the zero crossing of the extrapolated logarithmic velocity profile, $y_t - y$. The values found for the uniform gravel and the Rhine gravel generally confirm the simplified approach of $y_t - y = 0.25d$ made by van Rijn (1984) (compare §2.3.1), although it could not be determined more precisely than $\pm(2-3)$ mm. For the spheres experiments, $0.20d$ holds. This value is similar to results from Grass *et al.* (1991) who found $(0.20-0.22)d$ by physical experiments, as well as the result of $0.22 d$ from Stösser *et al.* (2005) found by LES. The upper boundary of the roughness layer $y(\delta_R)$ is estimated by the location of $y(\overline{u'v'}_{\max})$, as found by the PIV results.

Table 4.2 is completed by the momentum thickness θ_m , another parameter often used to classify (near) wall effects. It is defined as

$$\theta_m = \int_0^\infty \frac{\bar{u}(y)}{\bar{u}_{\max}} \left(1 - \frac{\bar{u}(y)}{\bar{u}_{\max}} \right) dy . \quad (4.2)$$

Typically, this length scale is used in wind tunnel experiments. A closer inspection shows that both, $y(\delta_R)$ and θ_m , are of the same order. Approximately, they reach 10-15% of the water depth, with the tendency of higher percentages at lower Reynolds numbers. However, a larger deviation is recognizable at #rhi9, where $y(\delta_R) = 12.0$ mm and $\theta_m = 21$ mm. The reason remains unclear.

The smallest length scale is the Kolmogorov microscale η . Following Nezu & Nakagawa (1993, p.30), this microscale is approximated by

$$\eta \approx h / \text{Re}_{*h}^{3/4} . \quad (4.3)$$

The resulting scales of $\eta = (0.12-0.44)$ mm were not resolved within the velocity measurements, where the spatial resolution typically resulted in $(1.6-2.5)$ mm (§3.2).

Flow Properties. General flow properties are listed in tab. 4.3. The flow rate Q , the bulk velocity U and the bulk Reynolds-number Re_h give a recall to tab. 3.2. The Reynolds-numbers Re_{*h} , $Re_{*\delta}$ and the grain Reynolds-number Re_{*d} provide additional parameters that characterize rough bed turbulence.

Two versions of the bulk Froude number, $Fr_h = U^2/(gh)$ and $\sqrt{Fr_h}$, are frequently used in literature (and unfortunately, both are sometimes mixed up). To prevent confusion, in table 4.3 the latter notation is used. The bulk Froude number is seen below 1.0 throughout. Thus, the flow conditions provided are entirely subcritical. The densimetric Froude-number equals the Shields-parameter Θ . The runs #uni*i* included a velocity spectrum from stable bed conditions up to very slight sediment transport. For #uni9, the value of $\Theta = 0.062$ (highlighted in bold print) indicates the onset of sediment motion, as it reaches the range of $\Theta_c = 0.030$ - 0.086 (Buffington & Montgomery, 1997).

index	icon	Q (l/s)	U (m/s)	u_* (m/s)	Re_h ($\cdot 10^3$)	Re_{*h} ($\cdot 10^3$)	$Re_{*\delta}$ ($\cdot 10^3$)	Re_{*d} (-)	$\sqrt{Fr_h}$ (-)	$Fr_{*\Delta} \equiv \Theta$ (-)
#uni3	▲	56.6	0.314	0.030	62.8	6.00	4.95	306	0.22	0.006
#uni6	◆	120.0	0.667	0.063	133.4	12.60	11.03	643	0.46	0.027
#uni9	■	180.0	0.948	0.095	200.0	20.05	14.73	969	0.68	0.062
#rhi9	★	180.0	0.930	0.086	200.0	18.49	13.33	2245	0.64	0.019
#sph1	•	18.6	0.160	0.015	20.6	1.94	1.88	377	0.14	0.003
#sph3	●	56.6	0.316	0.030	62.9	5.97	5.10	753	0.23	0.010

Table 4.3: Flow properties. Q = flow rate, $U = Q/(Bh)$ = bulk velocity, u_* = shear velocity, Reynolds-numbers: $Re_h = Uh/\nu$, $Re_{*h} = u_*h/\nu$, $Re_{*\delta} = u_*\delta_h/\nu$, $Re_{*d} = u_*d/\nu$, Froude-numbers: $Fr_h = U^2/(gh)$, $Fr_{*\Delta} = u_*^2/(\Delta gd)$, with $\Delta = \rho_s/\rho - 1$.

4.2 Measured Velocities

4.2.1 Time averaged flow

Cross Sectional View. Song (1994) has shown that an aspect ratio of $B/h = 4$ is limiting for the 2D/3D-transition in the near-bed center of rough bed open-channel flow. As the experiments presented here were conducted at an aspect ratio not smaller than $B/h = 4.2$ for a similar experimental setup, 3D effects should be expected to be of minor importance. However, this has to be subject to close inspection.

Iso-surfaces of time-averaged $\bar{u}(y, z)$ are given for the slightly decelerated flow of #uni3 in fig. 4.1(a), and for the uniform flow of #uni6 in fig. 4.1(b), respectively. The velocities are scaled by U . The cross sectional views were reconstructed from independent ADCP measurements at nine lateral positions. To record \bar{u} , a single ADCP probe was mounted at an angle of $\theta = 60^\circ$ to the flow direction (see fig. 3.4) and measured 188 s at 10.9 Hz.

4 Experimental Results

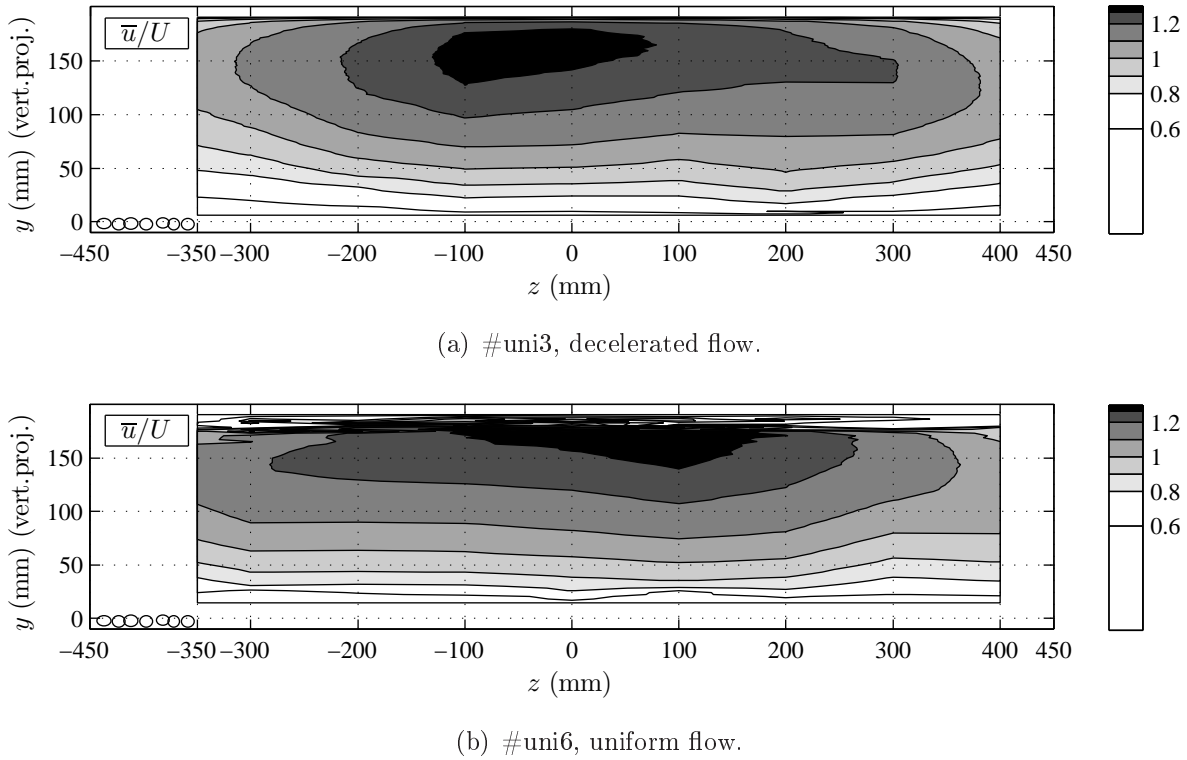


Figure 4.1: Velocity contour plots $\bar{u}(y, z)$, scaled with outer variable U . Cross sectional view in streamwise direction for (a) #uni3, and (b) #uni6. The nine positions of the ADCP probe are indicated by the dotted vertical grid. As an indication of secondary currents, the maximum centerline velocity \bar{u}_{\max} is located below the water surface.

After the recordings were done at one position, the probe was shifted to a neighboring position to start the next measurement.

The contours show a relatively regular lateral distribution of the velocities. For the time-averaged $\bar{u}(y, z)$, a clear tendency to slower velocities at the bed-wall perimeter and a dipped velocity maximum in the centerline becomes prominent. For #uni3 (fig. 4.1(a)), the maximum velocity \bar{u}_{\max} is detected at $\delta_h/h \simeq 0.83$. This gives an indication of the presence of secondary currents, where a weak near-wall fluid transport upwards to the water surface and there in direction to the flume centerline is superposed on the dominating streamwise main flow. As a consequence, the location of \bar{u}_{\max} is shifted from the water surface towards the bed. In comparison with #uni6 (fig. 4.1(b)), this phenomenon is not that marked, as \bar{u}_{\max} is only shifted to $\delta_h/h \simeq 0.88$. Consequently, secondary currents can be assumed to be weaker for #uni6.

The ratio of $\delta_h/h \simeq 0.88$ for the uniform flow of #uni6 confirms exactly the relation that is predicted by eq. 2.11. However, eq. 2.11 does not consider effects of non-uniform flow conditions, which might explain the more pronounced vertical shift of $y(\bar{u}_{\max})$ away from the water surface at the slightly decelerated flow conditions of #uni3 ($\delta_h/h \simeq 0.83$). For the experiments with accelerated flow (#uni9 and #rhi9), the shift of the \bar{u}_{\max} -location

is even more distinctive (not shown here). The observed ratios are $\delta_h/h \simeq 0.73$ and 0.72 , respectively. This gives a clear indication that the velocity dip phenomenon (and equivalent to this the presence of secondary currents) is influenced by both the ratio B/h and the longitudinal non-uniformity of the flow.

However, within an area of $-0.25 < z/B < 0.25$ and $y \lesssim h/2$ the observed isolines are almost horizontal at all experiments. Consequently, the lateral differences for the averaged streamwise velocity must be small in this area. Although the presence of secondary flow effects can not be denied, they are seen to be of minor importance for the main flow regime. As a first approximation the flow is considered to be a 2D-flow in the near-bed centerline region in the following.

Typically, the flow velocities of secondary currents are very small in comparison to the bulk flow velocity. For the actual measurements, their intensity can be rated by a closer examination of the time averaged vertical velocities $\bar{v}(y, z)$ (not plotted here). On average $|\bar{v}|/U \leq \pm 0.02$ and $\bar{v}_{\max}/U \simeq \pm 0.03$ holds for all cross sections and flow conditions monitored by the ADCP. These observations are consistent with results from Naot (1984) for similar boundaries ($B/h = 4$, rough bed, smooth walls). He computed by an algebraic stress model that on average $|\bar{v}|/U \simeq \pm 0.02$ and $\bar{v}_{\max}/U \simeq \pm 0.04$ holds. The largest values were observed in the corners and at the wall, respectively.

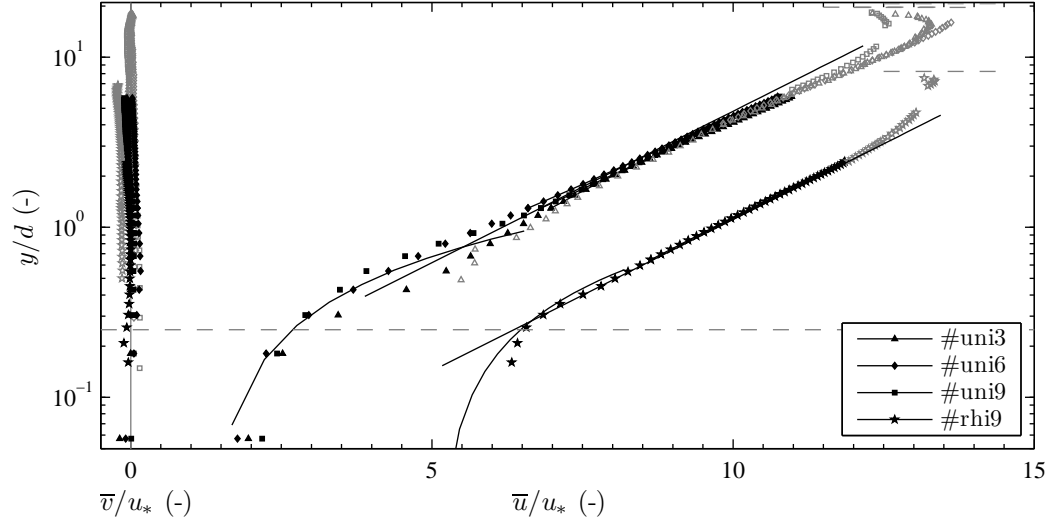
Vertical Velocity Profiles. Fig. 4.2 presents the vertical velocity profiles of the time averaged $\bar{u}(y)$ and $\bar{v}(y)$ for all experimental runs, measured by both PIV and ADCP in the centerline of the flume. Least square fits to the log-law (eq. 2.16) showed that all curves of $\bar{u}(y)$ collapsed onto a single curve. Regardless, in fig. 4.2 the velocities are plotted with the average grain size d , and not with k_s . In this, differences between the flow over the three different bed roughness types are shown.

Eq. 2.16 was derived by the 2D-assumption that a single, constant friction velocity u_* can be adopted to characterize the momentum transfer from the outer flow to the bed. In 3D open-channel flows with secondary currents, this simple approach is inadequate, as the total shear $\langle \overline{\tau_o} \rangle = \rho u_*^2$ is distributed nonlinearly at the bed-wall perimeter (§2.2). However, Nezu & Rodi (1985) showed by measurements in a hydraulically smooth and narrow flume ($B/h = 2$) that the log-law coincides well with experimental data except near the corners. Within the lateral extension $-0.4 < z/B < 0.4$, $\tau_b(z)$ only varies between $0.98 - 1.1 \langle \tau_b \rangle(z)$. Thus, an enlargement to 3D flows above rough beds is possible to gain a certain range of u_* from the log-law. The work of Song (1994) confirms this applicability to a rough bed flume study ($d = 0.012$ m, $B/h \geq 3.5$). As can be seen in fig. 4.2, the fitted log-law matches all curves of $\bar{u}(y)$ onto a single curve. Therefore, $u_{*\log}$ is used as the overall global shear velocity u_* . (Note that the resulting fit-parameters u_* and k_s are already discussed in §4.1, last section in 'Shear Stresses' as well as second section in 'Geometric Length Scales'.)

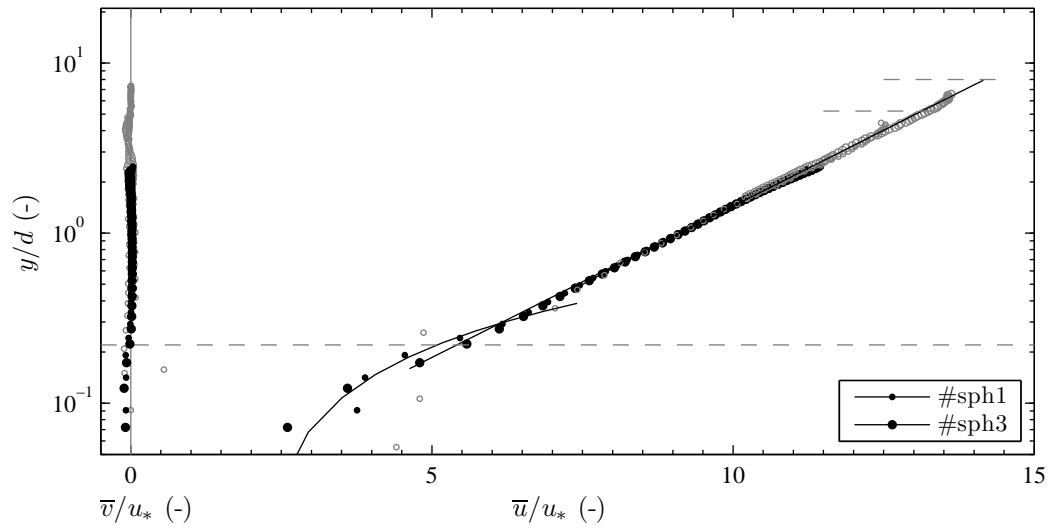
Fig. 4.2 also includes fits to the linear velocity distribution in the roughness layer, adapted to the flow in rough permeable beds. It reads

$$\frac{\langle \bar{u} \rangle(y)}{u_*} = C \frac{y}{\delta_R} + C_\phi, \quad (4.4)$$

4 Experimental Results



(a) Flow velocities over uniform gravel and Rhine gravel, respectively.



(b) Flow velocities over spheres.

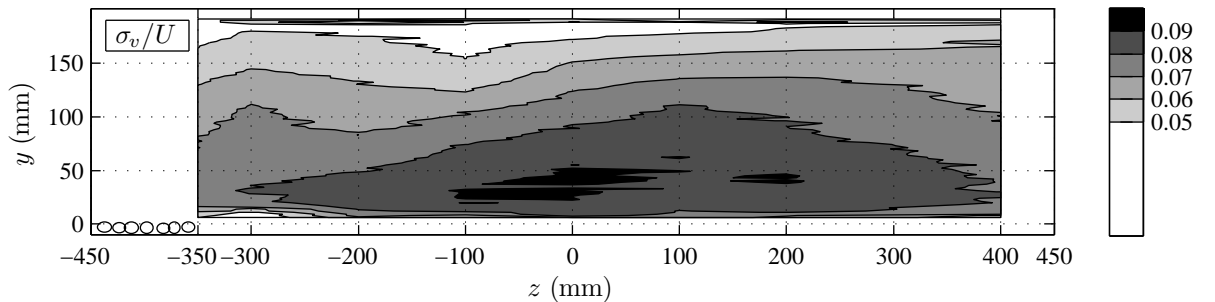
Figure 4.2: Vertical distribution of time averaged velocity components $\bar{v}(y)$ and $\bar{u}(y)$ in the centerline of the flume. Scaled with inner variable $u_* \equiv u_{*\log}$, plotted with grain size d . (A plot with k_s would match the curves.) Data gained by PIV (filled, black markers) and ADCP (unfilled, light markers). Lines show best fits for eqs 2.16 and 4.4. Dashed lines indicate respectively the water surfaces and the upper grain crest for each measurement.

where C_ϕ is an additional parameter applying for a constant seepage flow in the porous bed. As the thickness of the roughness layer, δ_R , could not be determined precisely for the experiments, an approach was made by using the grain size d instead. In fig. 4.2, eq. 4.4 was fitted to $[C, C_\phi] = [5.5, 1.3]$ for #uni*i* and $[C, C_\phi] = [5.5, 5.1]$ for #rhi9. The slope ruled by C agrees with the proposed values for gravel beds (Nikora *et al.*, 2001). For the experiments of #sph, $[C, C_\phi] = [14, 2.0]$ was found.

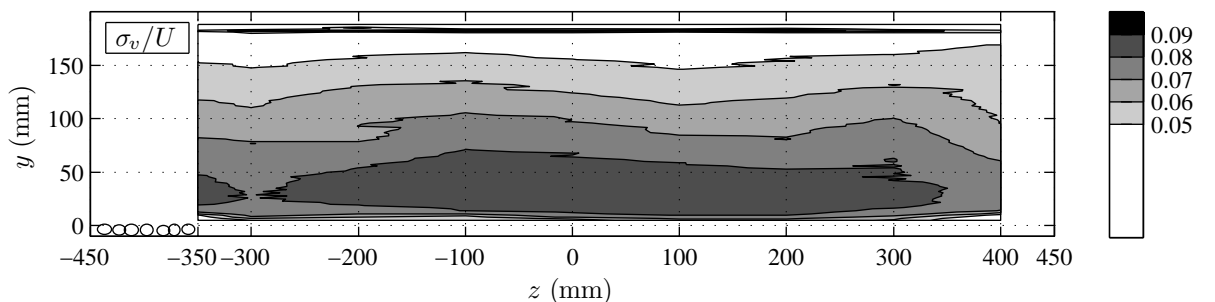
The profiles of $\bar{v}(y)$ given in fig. 4.2 indicate again the presence of secondary currents. However, in comparison with the streamwise velocity component they are very small $\bar{v}(y)$, roughly limited by $\bar{v}(y) < u_*/4$.

4.2.2 Turbulence intensities

Cross sectional view. Contours of vertical turbulence intensities $\sigma_v(y, z)$ are shown in fig. 4.3, for the same experimental conditions as given in fig. 4.1. To record σ_v , ADCP measurements were performed for 102 s at 25.0 Hz ($\theta = 90^\circ$). Principle findings for $\bar{u}(y, z)$ are confirmed: Secondary currents slightly influence the shape of the cross sectional view to the (vertical) turbulence intensities. However, within the near-bed centerline region ($-0.25 < z/B < 0.25$, $y \lesssim h/2$) the flow can be adequately viewed as a 2D-flow.



(a) #uni3, decelerated flow.



(b) #uni6, uniform flow.

Figure 4.3: Contour-plots of turbulence intensities $\sigma_v(y, z)/U$. Cross sectional view for (a) #uni3, and (b) #uni6.

4 Experimental Results

Spectral analysis. Before analyzing the PIV results with respect to turbulence properties, a closer look is taken at their spectral configuration. As has been shown in table 4.2, the Kolmogorov length scale η is not resolved within the PIV recordings. Consequently, turbulent fluctuations with scales smaller than the spatial resolution will cause noise in the calculation of the vector fields. Peak locking effects combined with sub-pixel displacements also lead to inaccurate velocity vectors, especially if they are combined with strong velocity gradients – as is typical in the near-bed region. This section addresses the question to what extent sources of errors influence the turbulence statistics of the PIV measurements.

As an example, spectra S_{uu} of the velocity signal at a vertical bed distance of $y/\delta_h \simeq^1 0.2$ are given in fig. 4.4. They are estimated by Welch’s method with a window length of $n = 2^6$ using rectangular and no overlapping windows. The spectra are based on PIV vector fields that were processed without overlapping. Thus, an ambiguity due to a difference between spatial resolutions and vector spacing is avoided. (Recall that generally all vector fields analyzed in this study are processed using an overlapping of 50% to increase the velocity information). All spectra given in fig. 4.4 follow the expected tendency within the inertial subrange, where a decrease by $k^{-5/3}$ can be observed. At larger scales, this slope shifts – at least in tendency – towards k^{-1} , indicating a stronger interaction between the mean flow and its fluctuating part (Nikora, 1999). However, this characteristic is not well-pronounced here. Wavelengths larger than $L = 161.2$ mm or smaller than twice the spatial resolution, $L = 2 \cdot 2.52$ mm, are not resolved, thus the production range and the viscous range are not displayed.

At smaller scales, irregularities become prominent in the curve progressions. The spectra for #uni3 and #uni6 (thin lines) trend towards a horizontal line indicating a high level of (white) noise. A belated inspection of the PIV settings revealed that the time step $\Delta t = 2$ ms between each two recordings of a double frame was chosen slightly too short for these flow conditions. Consequently, sub-pixel displacements (*i.e.* small-scale fluctuations) are not resolved adequately. Here, exceptionally a 3×3 Gaussian filter is applied to clean the signal, causing a loss of smaller scaled fluctuations (bold lines). The influence of small-scale noise can also be seen in the given examples of #sph1 and #rhi9, but the revealing small appendix is not very distinctive. Thus no filter is applied here.

The spectrum for #rhi9 shows another trend differing negatively from $k^{-5/3}$. A similar behavior is observed for all spectra of #rhi9 and #uni9 (not shown here). At these flow conditions at higher Reynolds-numbers a continuous seeding was hardly able to be provided. Thus, low validation rates of the calculated vector fields are the consequence. For the velocity field of #rhi9 only 65% of the computed vectors are confirmed. To compute the spectra, the missing vectors are filled by a neighbor smoothing technique. Thus, effectively an uneven spatial filter is applied, taking a loss of small-scale fluctuations. Consequently, S_{uu} from #rhi9 lies slightly below the expected decrease by $k^{-5/3}$ and crosses the spectra of #uni6.

¹Here, the symbol \simeq is used instead of $=$, as a precise resolution of $y_{\text{ref}}/\delta_h = 0.20$ could not be matched exactly due to the vector spacing of 1.3 mm.

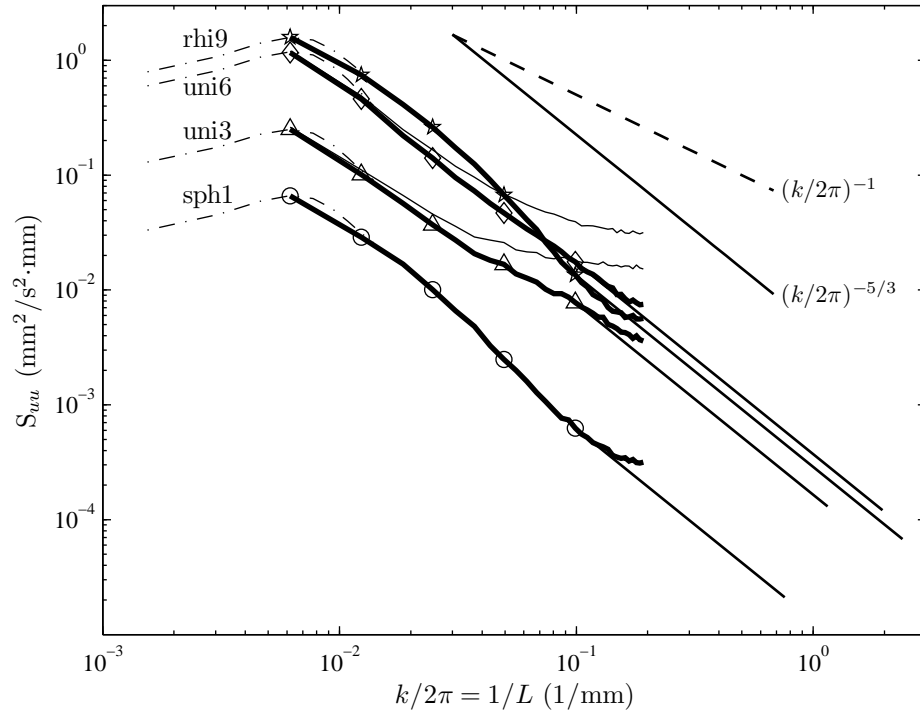


Figure 4.4: One-sided spectra $S_{uu}(y/\delta_h \simeq 0.2)$. The bold lines denote the spectra from PIV recordings calculated using Welch's method with a window length of $n = 2^6$ (rectangular and no overlapping). Symbols indicate wave lengths of $L = n \cdot 2.52$ mm with $n = 2^{[6,5,\dots,2]}$. The thin lines for #uni3 and #uni6 denote S_{uu} for PIV recordings with a high noise level, as the time step Δt between two double frames was chosen too short. Here, exceptionally a 3×3 Gaussian filter was applied (bold lines). The lines declining by $(k/2\pi)^{-5/3}$ give an extrapolation to 3η . The dashed lines denote spectra estimated using Welch's method with a maximum window length of $n = 2^6 + 16$. The apparent maxima of the spectra are due to the limited streamwise length of the PIV frame, the real maximum is expected to be larger.

4 Experimental Results

The spatial resolution of turbulent fluctuations is evaluated by spectral analysis in the following. Let $\sigma_{u,\text{tot}}^2$ be the total variance of the velocity signal u , consisting of σ_{PIV}^2 and the residual σ_r^2 . Then, the variances are related by

$$\sigma_{u,\text{tot}}^2 = \sigma_{\text{PIV}}^2 + \sigma_r^2 . \quad (4.5)$$

Recalling of eq. 2.21, the total variance can also be expressed by its one-sided spectrum as

$$\sigma_{u,\text{tot}}^2 = \int_0^\infty S_{uu} dk . \quad (4.6)$$

In other words, if S_{uu} is plotted against the wave number k , the area below the curve equals the variance $\sigma_{u,\text{tot}}^2$. As the velocities gained from the PIV-data represent the larger scales, an extrapolation of the $k^{-5/3}$ cascade can be used to estimate the residual σ_r^2 . This approach reads

$$\begin{aligned} \sigma_r^2 &= \int_{2\pi/L_N}^{2\pi/\eta_k} \frac{S_{uu}(k_N)}{k_N^{-5/3}} k^{-5/3} dk \\ &= -3/2 \frac{S_{uu}(k_N)}{k_N^{-5/3}} \frac{1}{(2\pi)^{2/3}} \left(\eta_k^{2/3} - L_N^{2/3} \right) , \end{aligned} \quad (4.7)$$

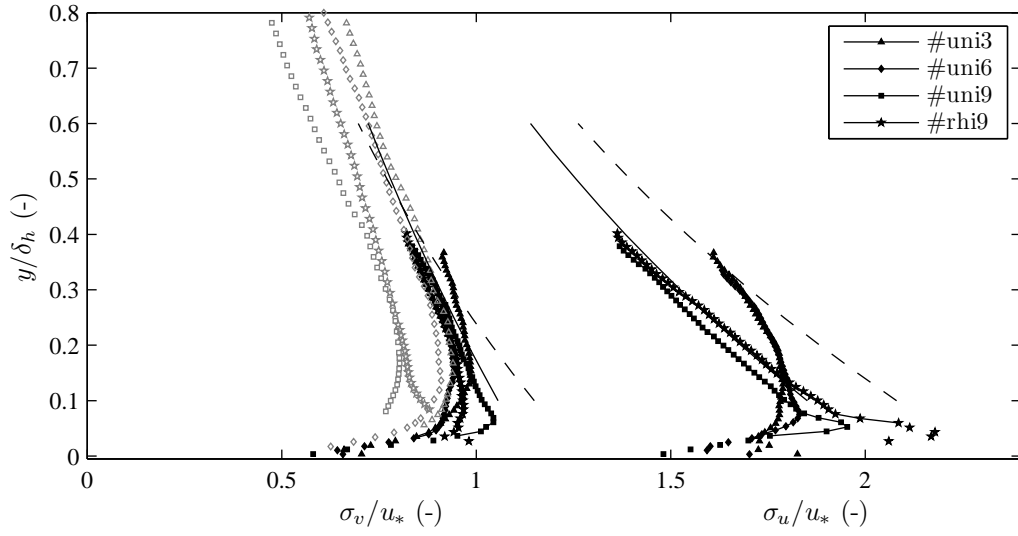
where L_N is twice the final window size applied in vector processing, $k_N = 2\pi/L_N$ is the corresponding wave number, and the smallest relevant scale is denoted by η_k ($> \eta$). If σ_r^2 is known, the quality of the PIV vector fields can be rated by the quotient of the resolved turbulence intensities, $\sigma_{\text{PIV}}/\sigma_{u,\text{tot}}$, *i. e.*

$$\frac{\sigma_{\text{PIV}}}{\sigma_{u,\text{tot}}} = \sqrt{\frac{\sigma_{\text{PIV}}^2}{\sigma_{\text{PIV}}^2 + \sigma_r^2}} . \quad (4.8)$$

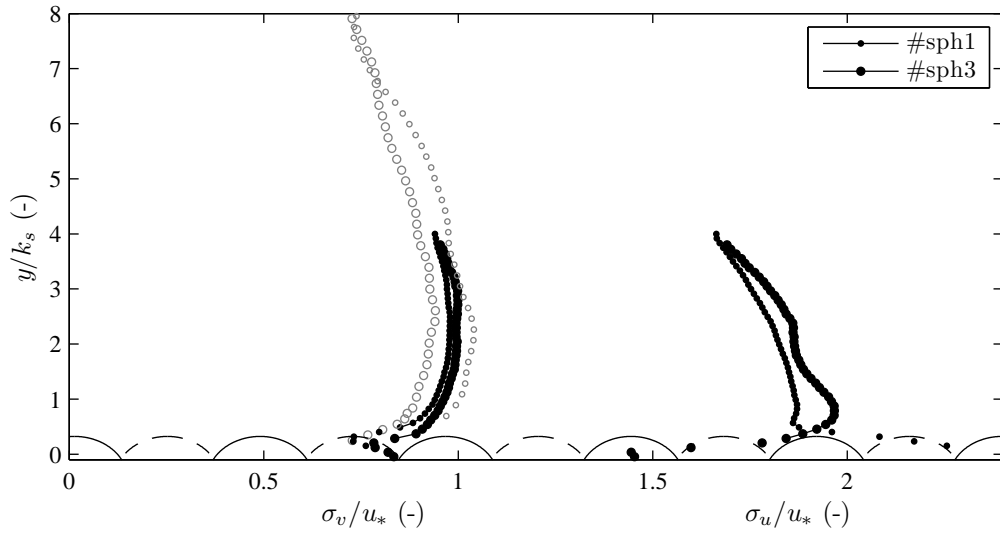
Eqs 4.7 and 4.8 are applied to the PIV data. The smallest relevant scale is approximated by $\eta_k = 3\eta$. The lines declining as $(k/2\pi)^{-5/3}$ give the extrapolation to 3η (see fig. 4.4), for which $S_{uu}(2L_N)$ was chosen as starting point instead of $S_{uu}(L_N)$ due to the noise effects at the smaller scales. The spectral analysis shows an excellent quality of $\sigma_{\text{PIV}}/\sigma_{u,\text{tot}} > 0.98$ for the low Reynolds-number experiments of #sph1, and $\sigma_{\text{PIV}}/\sigma_{u,\text{tot}} > 0.95$ holds for the other experiments with higher Reynolds-numbers. Further analysis reveals that these lower limits estimations are also valid for the vertical fluctuations σ_v . Thus, within the vector fields obtained by the PIV-system at least more than 95% of the turbulence intensity is resolved. However, in some cases a spatial filtering has to be applied to remove noise effects.

Turbulence intensity profiles. Fig. 4.5 shows the turbulence intensity profiles $\sigma_u(y)$ and $\sigma_v(y)$ measured in the centerline of the flume by the PIV system (setup A). Additionally, the profiles gained by the ADCP give an extended view of σ_v in the outer flow region.

The turbulence intensities of #uni1 and #rhi9 given in fig. 4.5(a) correspond reasonably well to eq. 2.23 applied with parameters from Kironoto & Graf (1994) for rough walls.



(a) Turbulence intensities for flow over uniform gravel and Rhine gravel, respectively.



(b) Turbulence intensities for flow over spheres.

Figure 4.5: Vertical distribution of turbulence intensities $\sigma_v(y)$ and $\sigma_u(y)$ at the centerline of the flume, scaled with inner variable u_* . Data gained by PIV (filled, black symbols) and ADCP (unfilled, light symbols). (a) Data for $\#uni_i$ and $\#rhi9$, plotted with outer variable δ_h . The velocity fields for $\#uni3$ and $\#uni6$ are filtered by a 3×3 Gaussian filter to compensate peak-locking noise. Dashed lines show eq. 2.23 with parameters from Nezu & Nakagawa (1993) for smooth walls. Lines show eq. 2.23 with parameters from Kironoto & Graf (1994) for rough walls. (b) Data for $\#sphi_i$, plotted with inner variable k_s .

4 Experimental Results

The slightly smaller values of σ_v measured by the ADCP for #uni9 and #rhi9 are due to the lowered spatial resolution of this measurement technique at higher velocities. Similar to the findings of Song (1994), σ_v reaches its maximum at $y/\delta_h \approx 0.2$. Below that, it decreases towards the bed – opposite to the increase as predicted by the exponential behavior of eq. 2.23. Physically this can be explained as follows: the eddies created by the bed roughness are hindered in their vertical development near the bed due to the boundary limitation.

The profiles of σ_u for #uni3 and #uni6 also have a more convex shape in the near-bed region. In the outer flow they tend towards the curve found by Nezu & Nakagawa (1993). A similar bellied shape is observed for the spheres experiments shown in fig. 4.5(b). Here, a better matching is realized by plotting the profiles with inner variables, k_s or d , instead of the outer variable δ_h . This scaling is probably caused by the low δ_h/k_s ratio (Wang *et al.*, 1993).

4.2.3 Stresses

Fig. 4.6 presents the vertical stress distributions calculated from the PIV-data, normalized on the basis of $u_{*log}^2 \equiv u_*^2$. In fig. 4.6(a), the stresses on the uniform gravel and Rhine gravel are plotted with δ_h . As the relation of u_{*uv}/u_* was found to be $90 \pm 3\%$ (§4.1, last section in 'Shear Stresses'), a stress distribution assumed to be valid in a linear-fit as

$$\frac{-\rho \langle \overline{u'v'} \rangle}{\tau_o} = \left(1 - \frac{y}{\delta_h}\right) \left(\frac{u_{*uv}}{u_*}\right)^2. \quad (4.9)$$

is also included in fig. 4.6(a). The measured Reynolds-stresses are in good agreement with eq. 4.9. Slight deviations at $y/\delta_h > 0.3$ for the accelerated flow conditions of #uni9 and #rhi9 cause a concave shaped distribution (Song, 1994). In the roughness layer ($y/\delta_h \lesssim 0.08$), the Reynolds-stresses decrease almost linearly towards zero and the form induced stresses become prominent. The maximum values are $\langle \tilde{u}\tilde{v} \rangle / u_*^2 < 0.2$, a similar limit to Nikora *et al.* (2007b) for gravel beds. In fig. 4.6(b), the fluid stresses on top of the spheres are plotted with inner variable k_s instead of the outer variable δ_h . Thus, a better matching is realized, analogous to the turbulence intensities measured for the spherical bed.

Fig. 4.7 shows the correlation coefficients, which are a measure of the efficiency of wall-normal motions to transport streamwise momentum. In a larger part of the outer flow typical values scattering around 40% are reached for #uni6, #uni9, and #rhi9, being in good agreement with results from *e.g.* Breugem (2005) and Adrian *et al.* (2000b). However, for runs with lower Reynolds-number and decelerated flow, the correlation coefficient tend to be smaller.

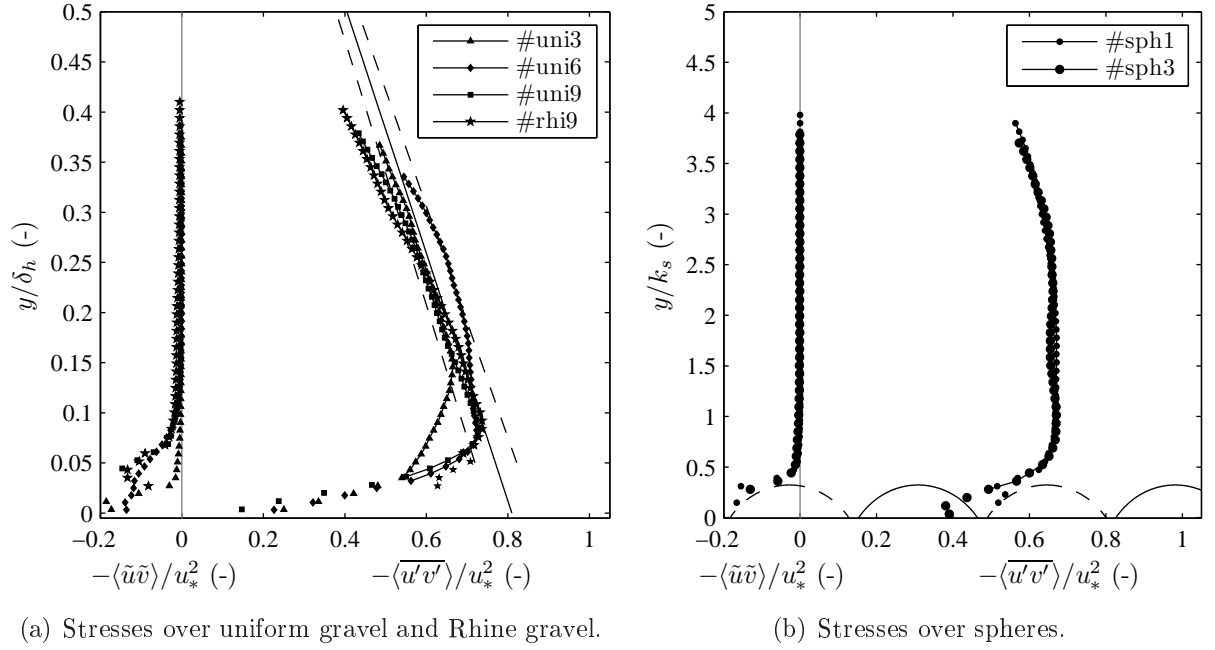


Figure 4.6: Vertical distributions of form-induced stresses and Reynolds stresses, scaled with inner variable u_*^2 . (a) #uni*i* and #rhi9 plotted with outer variable δ_h . The velocity fields for #uni3 and #uni6 are filtered by a 3×3 Gaussian filter to compensate peak-locking noise. The line refers to eq. 4.9 with $u_{*uv}/u_* = 90\%$, the dashed lines gives variations of $\pm 3\%$. (b) #sph*i* plotted with inner variable k_s .

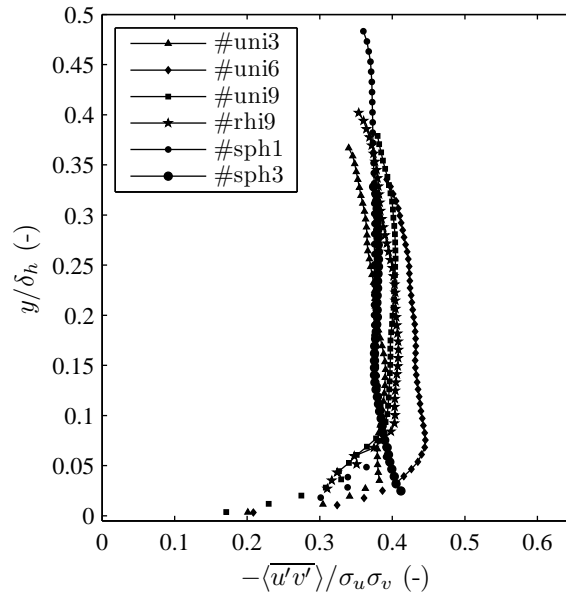


Figure 4.7: Correlation coefficient, plotted with outer variable δ_h .

4.2.4 Flow Structures

Streamwise Vertical View. In fig. 4.8 a sequence of four instantaneous velocity fields is given, measured in a streamwise vertical plane on top of the spherical bed (#sph1). The passage of two large-scale fluid packets can be observed, where a faster packet in the sense of a sweep (or Q_4) event ($u' > 0, v' < 0$) interacts with a slower fluid packet that behaves in the sense of an ejection (or Q_2) event ($u' < 0, v' > 0$). Together they form an angle of approximately 20° inclined to streamwise direction. Due to its propagation velocity, the faster fluid packet overrolls the slower one. Within the shear layer between both zones, small eddies are generated. The presence of vortex cores are indicated by values of the swirling strength λ_{ci}^2 . It is defined as the imaginary part of the complex eigenvalue of the velocity gradient tensor (*e.g.* Adrian *et al.*, 2000*a*). For 2D-flows, its calculation reads

$$\lambda_{ci}^2 = \max \left[0, -\frac{\partial u}{\partial y} \frac{\partial v}{\partial x} + \frac{1}{2} \frac{\partial u}{\partial x} \frac{\partial v}{\partial y} - \frac{1}{4} \left(\frac{\partial u}{\partial x} \right)^2 - \frac{1}{4} \left(\frac{\partial v}{\partial y} \right)^2 \right]. \quad (4.10)$$

The above mentioned findings agree well with the model proposed by Adrian *et al.* (2000*b*) for the organization of vortex structures in the logarithmic layer of smooth walls. In terms of Adrian *et al.*, the eddies in the shear layer are called hairpin vortex packages (HVP). Ramp-angles of 10 - 25° agree well with results from Tomkins (2001) for wind tunnel experiments, roughened with low-density hemispheres, and observations in natural gravel bed rivers as described by Roy *et al.* (2004) (see §2.5).

Fig. 4.9 shows pictures of wedge-like structures as they were seen in the flow fields on top of the three different types of bed. In general, the flow experiments over the spherical bed gave the most characteristic flow textures, where the HVP's could be identified unambiguously in most of the cases, and the demarcation line between the two fluid packets was more or less linear. For the gravel bed experiments #uni*i* and #rhi9, the characteristics of the wedge-like structures were less pronounced, but also recognizable. Obviously, the occurrence of ramp-like structures is independent of the type of bed roughness.

It is observable in all velocity fields made in this study that self-similar wedge-like structures are repeating roughly with a frequency of (0.2-2) Hz. Sometimes they are well pronounced. However, sometimes the observer needs some imagination to identify them. Additionally, further structural features like large-scale rollers or declining ramps are seen from time to time within an otherwise less textured turbulent flow regime. Thus, the question arises, whether ramp-like structures in the sense of Adrians HVPs are typical features for rough bed flows as well, or whether they are just insignificant coincidences due to turbulence effects. To test this, the velocity fields are analyzed statistically in the following.

Christensen & Adrian (2001) conducted two-point correlations between the swirling strength and the velocity field to give statistical evidence of HPVs in smooth wall turbulence. A similar procedure is now applied to the rough bed flow realization of this study. A cross correlation function $C_{\lambda u}(r_x, y)$ may be written as

$$C_{\lambda u}(r_x, y) = \frac{\langle \lambda_{ci}^2(x, y_{\text{ref}}) u'(x + r_x, y) \rangle}{\sigma_{\lambda}(y_{\text{ref}}) \sigma_u(y)}, \quad (4.11)$$

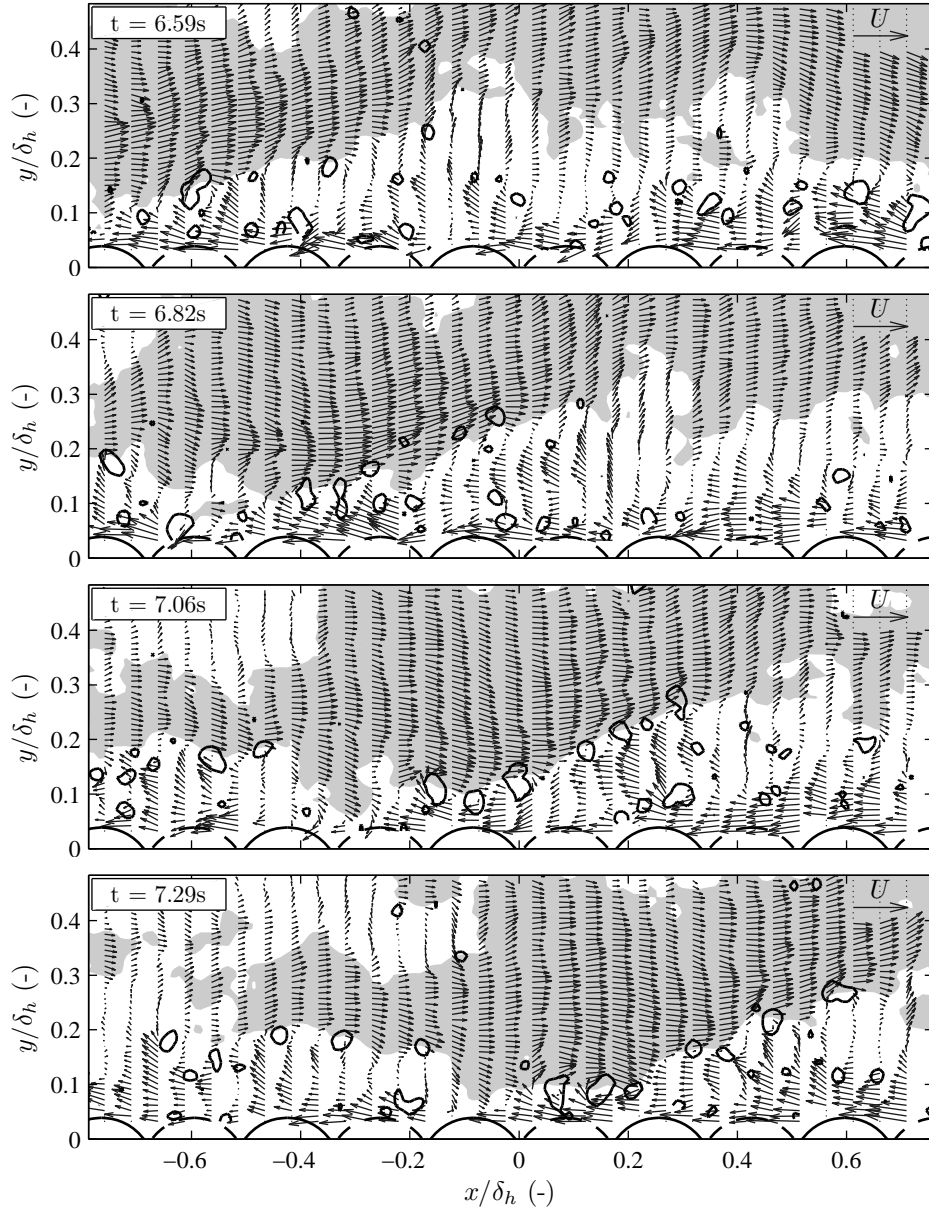
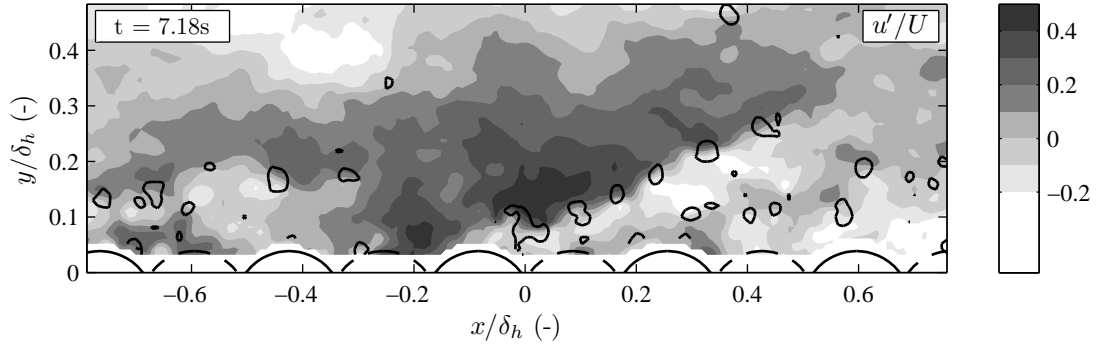
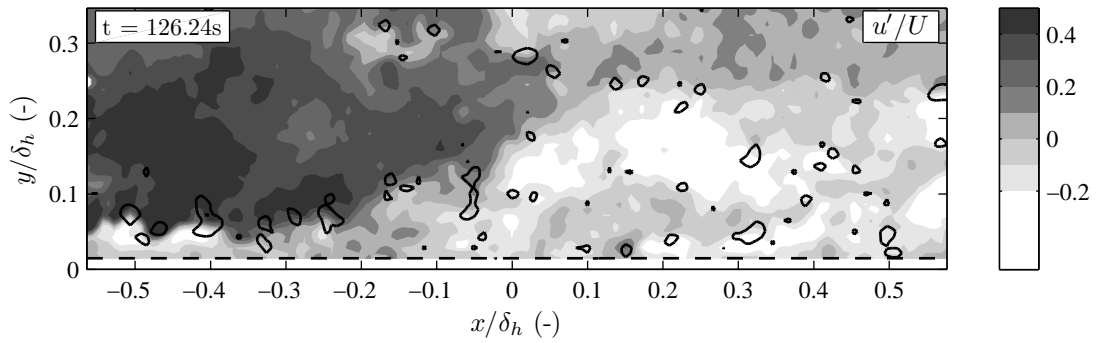


Figure 4.8: Sequence of instantaneous velocity fields for #sph1, where the passage of a large-scale wedge-like fluid structure can be observed. Only every second frame is plotted. The velocity field was filtered by a 2×2 filter. For visualization, the vectors are presented with a constant convection velocity $\vec{u}_c = [0.85U, 0]$ removed. In x , only every fifth vector is plotted. Contours of λ_{ci}^2 highlight the location of vortex cores. The shading indicates $\sqrt{(u^2 + v^2)} > U$. The shear layer between the faster and the slower moving fluid zones is densely populated with eddies.

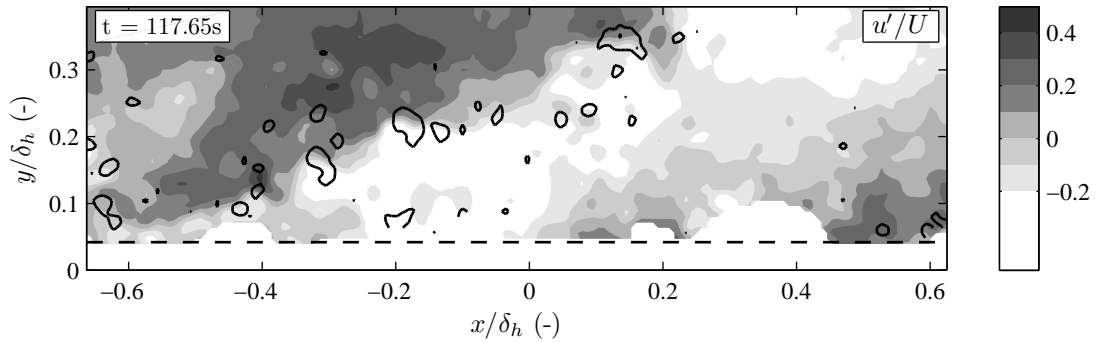
4 Experimental Results



(a) Flow over spheres.



(b) Flow over uniform gravel.



(c) Flow over Rhine gravel.

Figure 4.9: Typical pictures of wedge-like flow structures as observed for (a) #sph1, (b) #uni6, and (c) #rhi9. The velocity field was filtered by a 2×2 filter. Contours of λ_{ci}^2 are shown to highlight the location of vortex cores. The shading indicates u'/U in steps of 0.1.

where r_x denotes the horizontal correlation shift in x , and y_{ref} is the reference height at which the swirling strength is taken. Note that $\lambda_{ci}^2 \geq 0$ holds by definition, so $C_{\lambda u}(r_x, y)$ retains the sign of u' . Therefore, the correlation function embodies also structural information on the flow texture. The unbiased estimate of the cross-correlation function will be chosen for normalization, *i.e.* each cell of the resulting correlation matrix represents not the sum, but the mean of the individual products of u' and the conjugate complex of λ_{ci}^2 . Furthermore, to be consistent with Christensen & Adrian (2001), terms in eq. 4.11 have been non-dimensionalised dividing by the corresponding standard deviations. However, other parameters are reasonable as well.

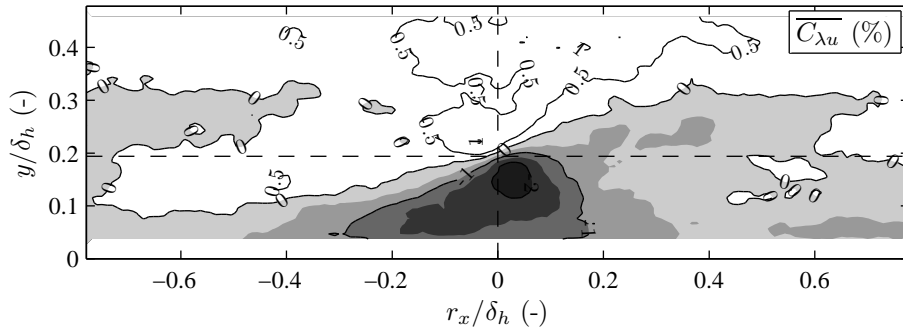
Fig. 4.10 illustrates the time averaged correlation $\overline{C_{\lambda u}}$ for the experimental conditions of #sph1, #uni6, and #rhi9. The correlation is based on sequences of each of 1740 velocity fields recorded within 205 s, thus statistical sampling errors are minimized. As reference height, $y_{\text{ref}}/\delta_h \simeq 0.2$ was chosen arbitrarily. As it could be expected, $\overline{C_{\lambda u}}$ is strongest at the reference line near $r_x = 0$. All three correlations give similar results: A large-scale interface, inclined at approximately 10-20° becomes obvious. In tendency, the correlation function is positive below and negative above this interface. That means, if swirling motion is detected at y_{ref} within a single vector field, it is most likely that swirling is also present in a line inclining at 10-20°. The corresponding flow is faster above and slower below this interface. In other words, the flow is dominated by aligned HVP that incline in a streamwise direction while a package with $u' > 0$ overruns another package with $u' < 0$. Thus, the result gives a statistical evidence that mean wedge-like flow structures exists above rough walls, where a series of clockwise rotating eddies are located along a line inclined in streamwise direction from the wall. On average, the instantaneous structures occur with sufficient frequency, strength, and order to leave an imprint on the statistics of the flow.

The three structures given in fig. 4.10 show definite similarity, indicating that this large-scale behavior is relatively insensitive to roughness type, water depth, and Reynolds number. However, the characteristics are less prominent for the gravel bed experiments of #uni6 and #rhi9 at $|r_x|/\delta_h > 0.3$. Statistically, the expected distinctiveness of $\overline{C_{\lambda u}}$ should have been vice versa, since the ratio of the bulk velocities of #sph1, #uni6 and #rhi9 –roughly given by 1 : 4 : 6– also represents the expected ratio of the numbers of observed wedges. So, the reason must be different. On the one hand, peak locking could have led to a smearing effect in the resolution of λ_{ci}^2 , on the other hand, it might be a simple fact that HVPs on randomly laid gravel beds are less definite than on an ordered spherical bed.

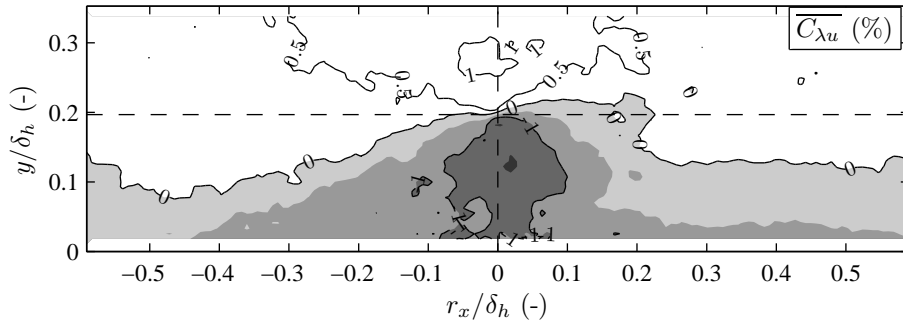
Sporadic ramp structures were observed that extended to the outer flow (and possibly up to the water surface). However, these events did not leave a marked imprint on $\overline{C_{\lambda u}}$, as large-scale zero-crossing interface disappears not far beyond $y_{\text{ref}}/\delta_h > 0.2$ in fig. 4.10.

Horizontal Near-Bed View. In fig. 4.11 a sequence of two instantaneous velocity fields is given, measured in a streamwise horizontal plane on top of the spherical bed (#sph1) at a vertical distance above the spheres' tops of $y_t = 4.5$ mm (identical to $y = 9.5$ mm). Elongated structures become visible, consisting of either high or low speed streaks alternating in the spanwise direction. Such streaky structures on top of a spherical bed are

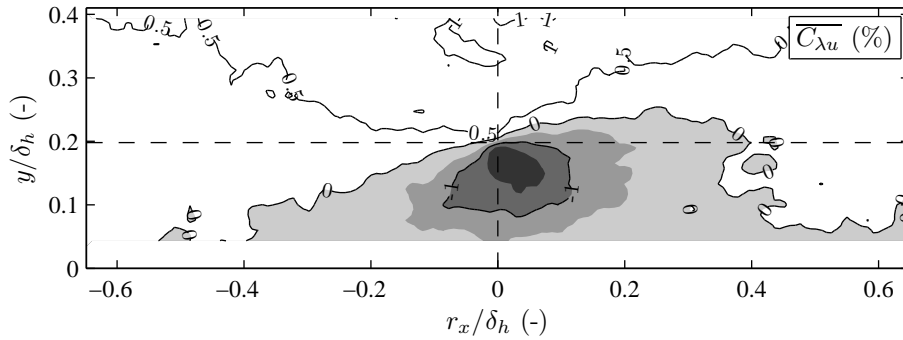
4 Experimental Results



(a) Structure over spheres.



(b) Structure over uniform gravel.



(c) Structure over Rhine gravel.

Figure 4.10: Time-averaged cross correlation $\overline{C_{\lambda u}}$ between each of 1740 velocity fields of $u'(x, y)$ and $\lambda_{ci}^2(y_{\text{ref}}/\delta_h \simeq 0.2)$ for (a) #sph1, (b) #uni6, and (c) #rhi9. Spacing contour is in steps of 0.5%. The frame sizes are plotted in the same size relation as originally seen by the camera. The result gives some evidence that mean wedge-like flow structures exist above rough walls, where a series of clockwise rotating eddies are located along a line inclined at approximately 10-20° from the wall (see zero line).

already well described in the dye visualizations of Defina (1996). He hypothesized that the shear layer between streaky structures consists of elongated vortices that counter-rotate around a streamwise axis. Unfortunately, eddies of such kind were not evidenced in his report nor can they be detected by a 2D horizontal view of the velocity regime as given in fig. 4.11. Indeed, small eddies can be seen sporadically within the shear band between the streaks, as indicated by λ_{ci}^2 . However, due to the given 2D horizontal view, the swirling strength criterion is limited to detect only vortices rotating horizontally, but not in a lateral-vertical plane.

Streaky structures are recognized at all velocity representations of near-bed horizontal views. Fig. 4.12 gives examples of pictures of stripe patterns as they were seen in the flow fields on top of the three different types of bed. Obviously, the occurrence of streaky structures is relatively insensitive to the variations of the roughness types, the water depth, and Reynolds number as well. However, in tendency the streaky behavior again has been seen to be more distinctive for the (well structured) spherical bed than the stripiness flow texture for the gravel beds of #uni1 and #rhi9 (not shown).

As was pointed out by several researchers in the past (e.g. Grass *et al.*, 1991), the streak spacing should scale with the roughness height k_s . To test this against the present data, the horizontal velocity fields are analyzed statistically in a similar manner as the vertical streamwise velocity fields before. However, due to the reasons mentioned above, a correlation to λ_{ci}^2 is suitable to a limited extent only. Therefore, a two-point correlation is realized by a 'quasi' two-point auto-correlation of u' . It reads

$$C_{u_z u}(r_x, z) = \frac{\langle u'(x, z_{\text{ref}}) u'(x + r_x, z) \rangle}{\sigma_u(z_{\text{ref}}) \sigma_u(z)}, \quad (4.12)$$

where $z_{\text{ref}} = 0$ is the reference for u' . Fig. 4.13 illustrates the results of the time averaged correlation $\overline{C_{u_z u}}$ for #sph1, #uni6, and #rhi9. All three correlations give similar results: $\overline{C_{u_z u}}$ is elongated, and it is strongest at the reference line z_{ref} near $r_x = 0$. Note that, since the algebraic sign of the two correlated streamwise fluctuations is the same, $C_{u_z u}$ is positive by definition. Thus, the correlation embodies the structural information on the streaks as well. The area $\overline{C_{u_z u}} > 0$ can be interpreted as the mean extensions of one streak. Consequently, the streamwise extension of the streaks must be much larger than the longitudinal limits plotted in fig. 4.13, as it is throughout positive at least within $|z|/k_s \lesssim 1.5$.

The lateral streak extension λ_z can be determined directly by taking the transversal distance of the zero crossing. However, in all three cases λ_z is smallest at $r_x = 0$ and grows with increasing $|r_x|$. This characteristic might be due to a meandering nature of the streaks. Thus, an estimation of λ_z should concentrate only on small r_x . Within $-1.5 < r_x/k_s < 1.5$ the transversal spacing is almost constant. Therefore, the streak spacing was determined as follows: First, $\overline{C_{u_z u}}(r_x=0)$ and the averaged values of $\overline{C_{u_z u}}(|r_x|/k_s=1.5)$ were calculated for all horizontal near-bed velocity realizations. Fig. 4.14 gives the results. In a second step λ_z was identified directly by taking the distance of the corresponding zero crossings. The resulting values are plotted in fig. 4.15, being in good agreement with the supplemented data from Defina (1996). A linear fit to the whole plotted data set gives

$$\lambda_z = 1.5y_t + 2.4k_s . \quad (4.13)$$

4 Experimental Results

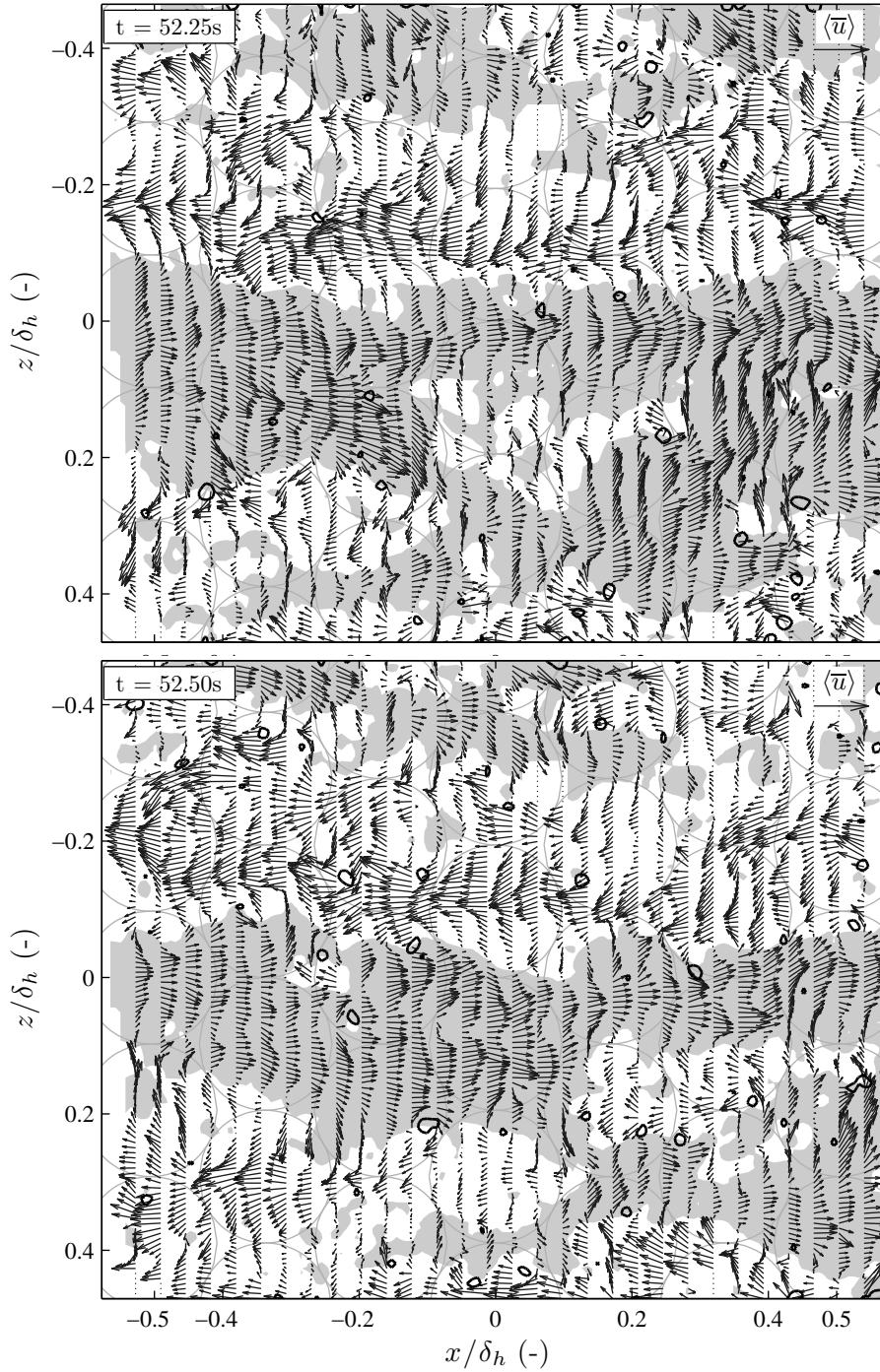


Figure 4.11: Sequence of two instantaneous velocity fields for #sph1, where the passage of elongated streaky structures can be observed. Top view on a horizontal layer at $y_t = 4.5$ mm above the spheres' crest (identical with $y = 9.5$ mm). The velocity fields are filtered twice by a 3×3 Gaussian filter. For visualization, the vectors are presented with the convection velocity $\vec{u}_c = [\langle \bar{u} \rangle, 0]$ removed. In x , only every fifth vector is plotted. Contours of swirling strength highlight the location of vortex cores rotating around a vertical axis. The shading indicates $\sqrt{(u^2 + v^2)} > \langle \bar{u} \rangle$.

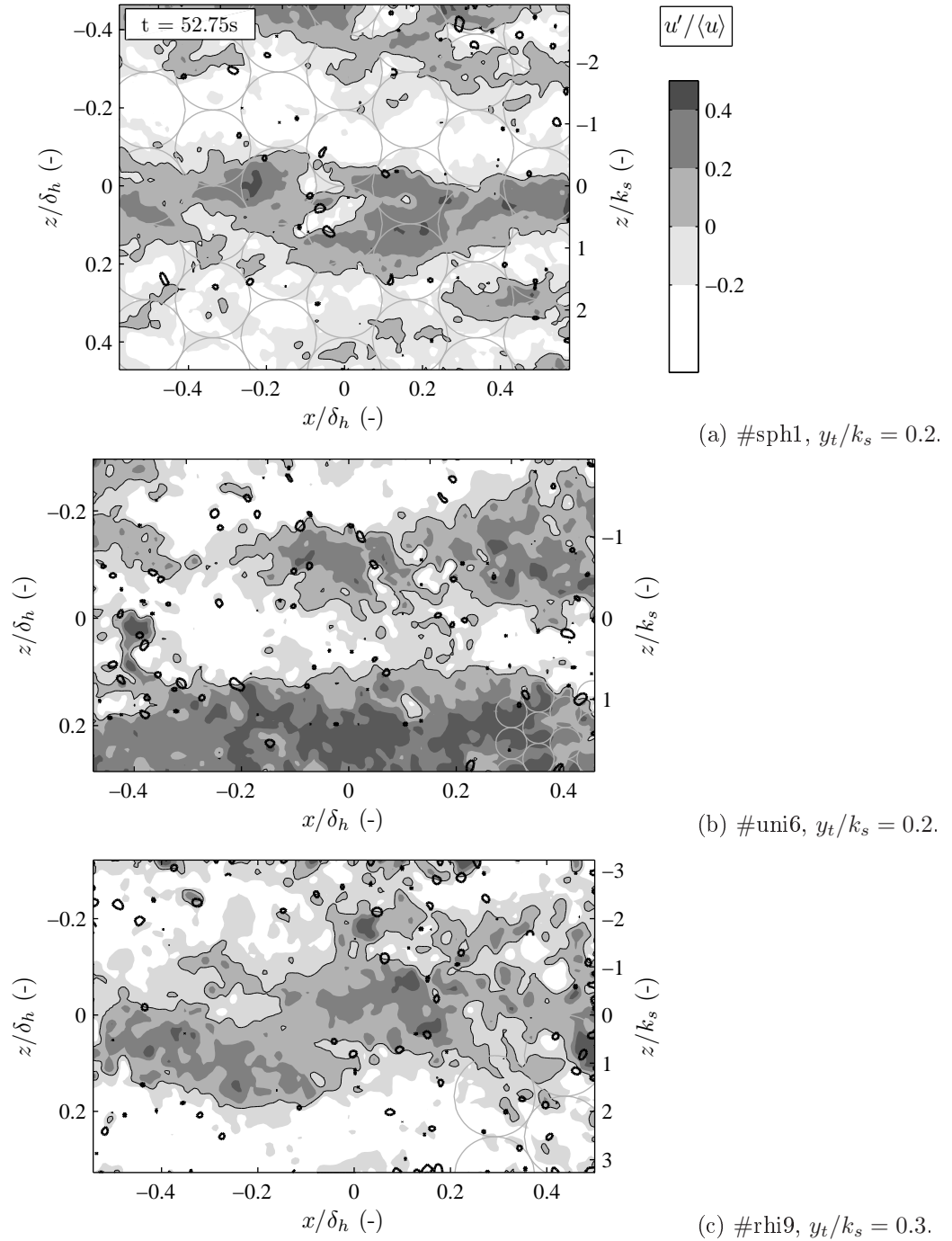
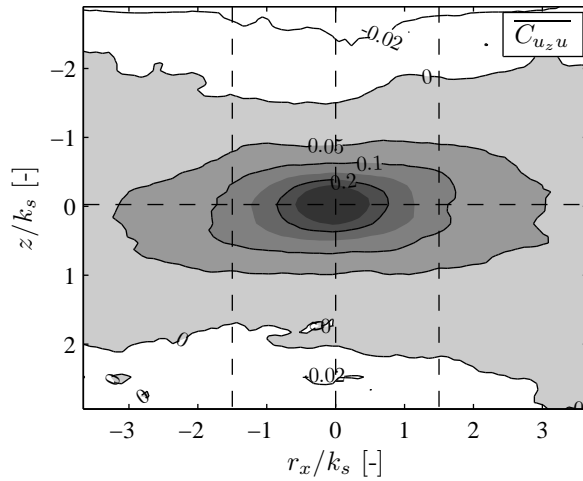
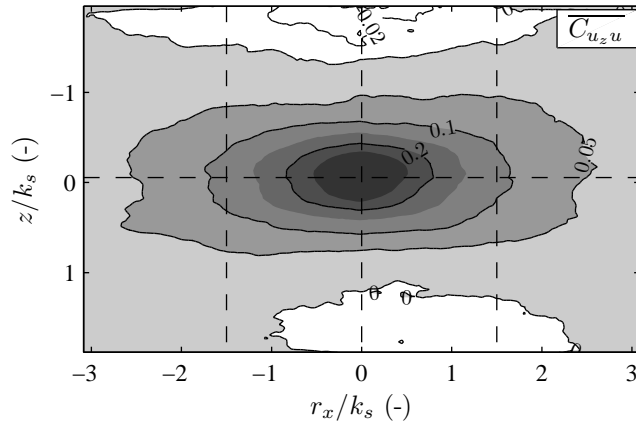


Figure 4.12: Top view of instantaneous velocity fields of $u'/\langle u \rangle$ near the bed. Typical pictures of streaky structures can be seen for three different types of bed: (a) spheres, $[y_t, y] = [4.5, 9.5]$ mm (sequel to fig. 4.12), (b) uniform gravel, $[y_t, y] = [5, 7.5]$ mm, and (c) Rhine gravel, $[y_t, y] = [5, 11.5]$ mm. The velocity fields are filtered by a 3×3 Gaussian filter. Bold contours of swirling strength highlight the location of vortex cores. $u'/\langle u \rangle = 0$ is pronounced by thin lines. The representative grain size d is indicated in the background. The frame sizes are plotted in the same size relation as originally seen by the camera.

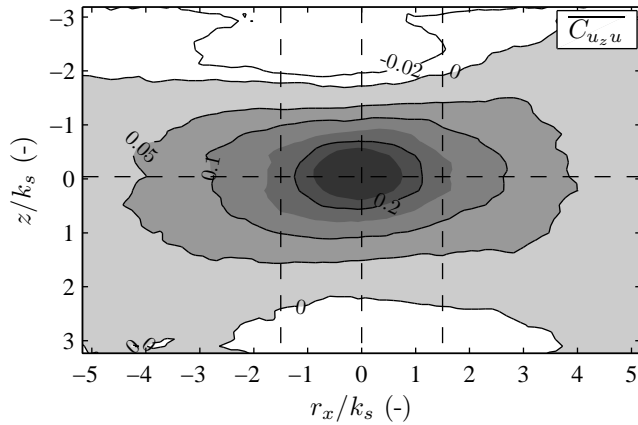
4 Experimental Results



(a) #sph1, $y_t/k_s = 0.2$.



(b) #uni6, $y_t/k_s = 0.3$.



(c) #rhi9, $y_t/k_s = 0.3$.

Figure 4.13: Time-averaged cross correlation $\overline{C_{u_z u}}$ between each of (a) 819 fields, and (b),(c) 1003 velocity fields of $u'(x, z)$ and $u'(z_{\text{ref}})$. The horizontal dashed lines give z_{ref} , the vertical dashed lines give $r_x/k_s = [\pm 1.5, 0]$ in reference to fig. 4.14. Contour spacing is in steps of 5%. The results show that flow structures in the near-bed region of rough beds own the inherent tendency to be elongated. Their breadth λ_z scales adequately with k_s . In reference to the instantaneous velocity fields of fig. 4.12, the given $\overline{C_{u_z u}}$ are based on exactly the same experimental runs.

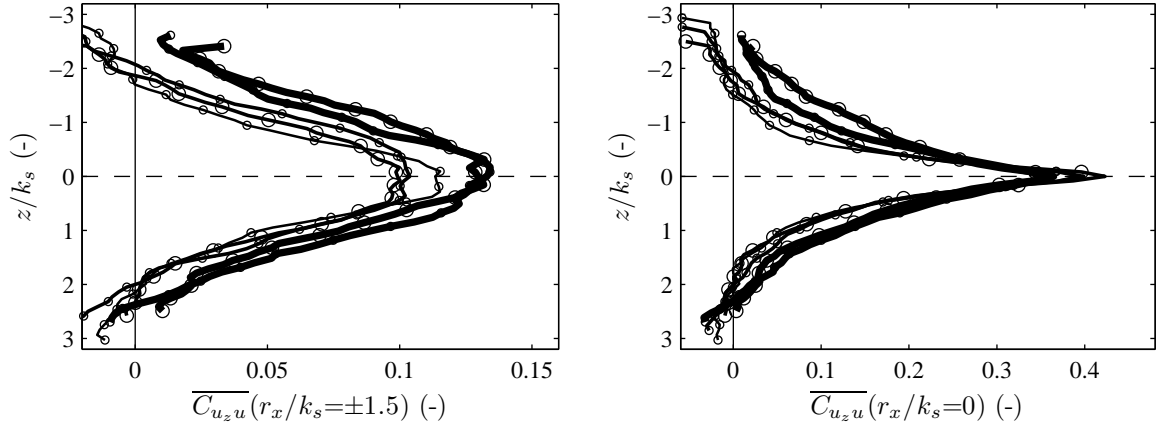
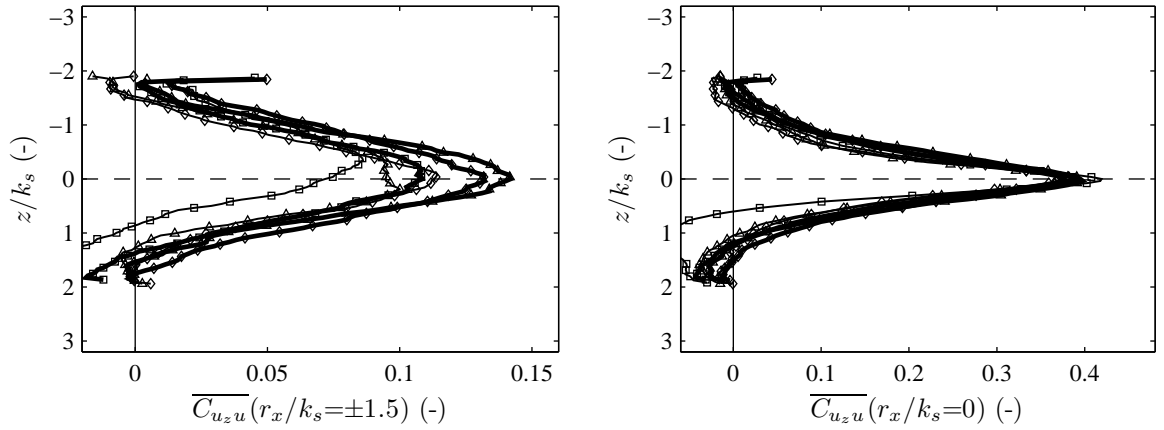
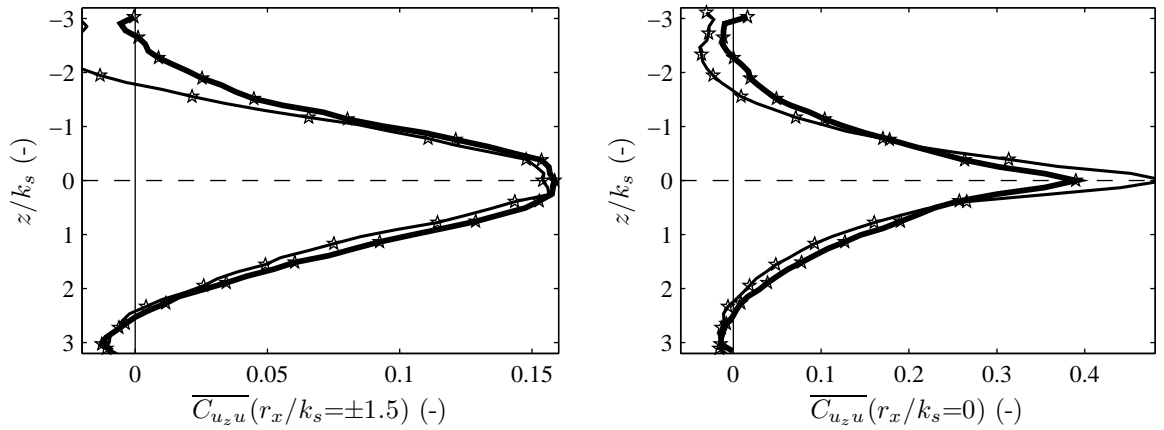
(a) #sphi for $y_t/k_s = [0.2, 0.4, 1.1]$ (b) #uni for $y_t/k_s = [0.2, 0.55]$ (c) #rhi9 for $y_t/k_s = [0.3, 0.95]$

Figure 4.14: Time-averaged cross correlation $\overline{C_{u_z u}}$ for (a) #sphi, (b) #uni, and (c) #rhi9 at $r_x/k_s = [\pm 1.5, 0]$ (see fig. 4.13). The thicker the lines, the larger the vertical distance to the roughness tops y_t . The zero-crossing distances of the lines is interpreted as a measure of the streak spacing λ_z , *i.e.* the distance between the centerlines of streaks with the same algebraic sign.

4 Experimental Results

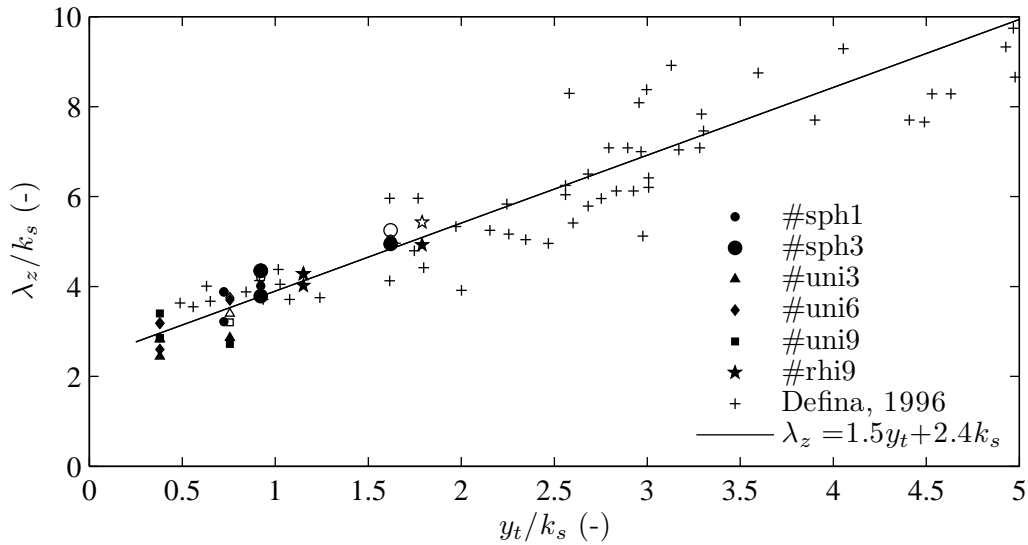


Figure 4.15: Streak spacing λ_z plotted with the distance to the roughness tops, y_t , and scaled with k_s . Filled symbols indicate the spacing at $r_x/k_s = 0$, unfilled symbols indicate the spacing at $r_x/k_s = \pm 1.5$. The figure is supplemented by data from Defina (1996) and a linear fit to the whole plotted data set (eq. 4.13).

4.3 Measurements of Pressure Fluctuations

In this section, results of the pressure measurements are presented. The following concentrates mainly on the uniform flow conditions of #uni6, as these measurements gave representative results for all experimental runs of #sph*i*, #uni*i*, and #rhi9. Two different arrangements of the miniaturized piezo-resistive pressure sensors (MPPS) are applied, where the signals are indicators of fluctuating drag and lift, as illustrated in fig. 4.16.

In the arrangements of fig. 4.16(a) a positive pressure deviation (over pressure), refers to a drag in the streamwise direction, $D' = p'$. In the arrangements of fig. 4.16(b) a

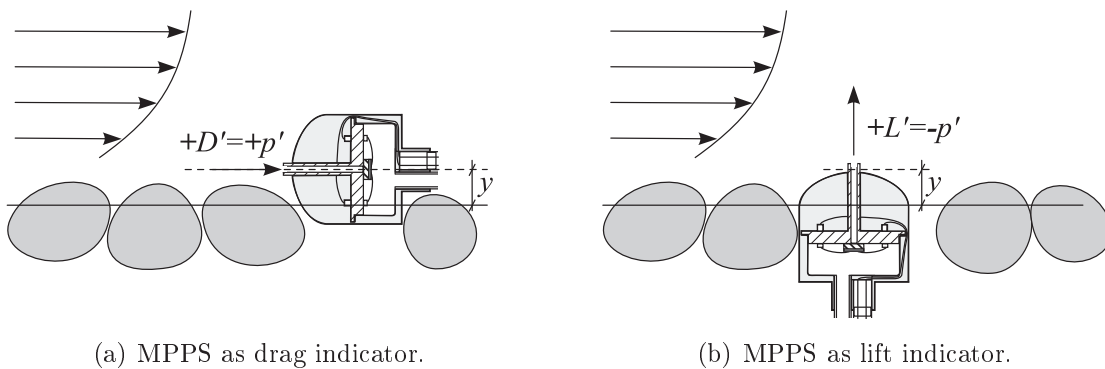


Figure 4.16: Arrangements of the MPPS.

negative pressure deviation (low pressure) refers to a lift in vertical direction, $L' = -p'$. For simplicity, the pressure fluctuations measured in the latter arrangement are denoted by L' and the former by D' in the following.

4.3.1 Time series

Fig. 4.17 shows synchronous time series of pressure fluctuations $p'(t)$ measured with the experimental conditions of #uni6 over $t = 3.0$ s. The pinholes of the four pressure pickups were vertically positioned at $y = [+10, +5, -7, -22]$ mm. The MPPS at $y = +5$ mm was facing upwards as shown in fig. 4.16(b), thus it indicates the fluctuating lift. The other sensors were arranged horizontally, with the pinhole facing upstream, as depicted in fig. 4.16(a). Thus, these sensors indicate the fluctuating drag. For the measurements given in fig. 4.17, the sensors indicating D' were vertically aligned in the centerline of the flume, whereas the L' -sensor was positioned at a lateral distance of 80 mm relative to the others.

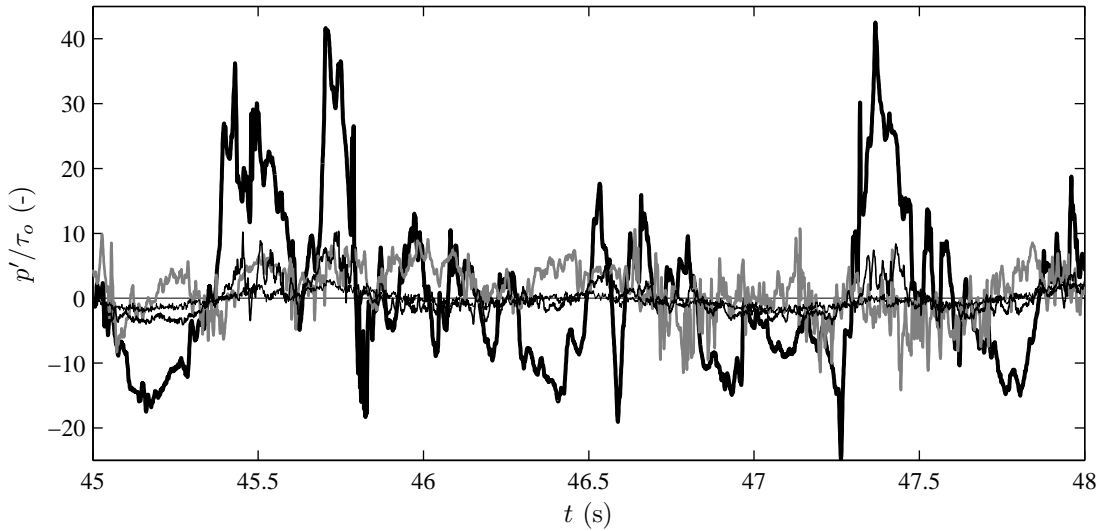


Figure 4.17: Simultaneous times series of pressure fluctuations $p'(t)$ for #uni6. Line widths from thick to thin correspond to $y = [+10, +5, -7, -22]$ (mm), indicating the fluctuating part of drag and lift as $[D', L', D', D']$. Here, the sensors indicating drag fluctuations are vertically aligned; the sensor indicating lift fluctuations is at $\Delta z = +80$ mm relative to the other sensors (light gray line).

By comparing the signals given in fig. 4.17, the damping of higher frequencies with increasing depth into gravel becomes obvious. As expected, the most buried sensor at $y = -22$ mm gives the smallest pressure fluctuations. However, the fluctuations recorded by the second sensor that was buried at $y = -7$ mm (*i.e.* one grain diameter below the roughness tops) can hardly be distinguished. More intense small-scale fluctuations can be seen only synchronous to positive peaks of the most exposed sensor,

4 Experimental Results

at $t = [45.5, 45.8, 46.6, 47.4]$ s. Due to its lateral distance from the other sensors, the signal of the L' -sensor slightly above the roughness crest shows no correlation with the other sensors. However, the recorded fluctuations are clearly more turbulent in comparison to the sensors within the gravel bed. The measured signal of the most exposed sensor gives the most extreme pressure fluctuations. Maximal positive pressure peaks reach up to $p'/\tau_o \simeq +40$, whereas the negative pressure peaks are less extreme around $p'/\tau_o \simeq -20$. This indicates that positive peaks of D' are more extreme than the negative peaks, *i.e.* the signal is skewed. A closer examination of this is given in the next section.

4.3.2 Histograms

Characteristic histograms of the measured pressure signals are presented in the following. They are compared with a probability density function (PDF) derived by Hofland & Battjes (2006). This PDF is capable of describing instantaneous drag forces on bed roughness elements. It is distantly related to the χ^2 -distribution, which was proposed by Papanicolaou *et al.* (2002) for the PDF of drag forces. However, the χ^2 -distribution includes a summation from 0 to infinity, whereas Hoflands formulation is easier to use in practice.

Hoflands formulation is derived by assuming a characteristic, normally distributed near-bed velocity u_b that is proportional to the drag force by $F_D = \alpha|u_b|u_b$. This single characteristic u_b is seen to be the only source for drag forces. The PDF is derived as

$$P(F_D) = \frac{1}{2\sqrt{2\pi\alpha|F_D|}} \exp\left[-\frac{1}{2}\left(\sqrt{|F_D|/\alpha} - \text{sign}(F_D)\delta_\sigma\right)^2\right], \quad (4.14)$$

where the non-centrality parameter,

$$\delta_\sigma = \bar{u}_b/\sigma_{u_b}, \quad (4.15)$$

gives the reciprocal of the relative near-bed turbulence intensity ruled by u_b . Fits to the mean and standard deviation are given by

$$\mu_{\text{fit}} = (\delta_\sigma^2 + 1) - \exp(-1.63 \delta_\sigma) \quad (4.16)$$

and

$$\sigma_{\text{fit}} = \sqrt{4\delta_\sigma^2 + 2 + \exp(-0.55 \delta_\sigma^2)}, \quad (4.17)$$

respectively. (Note, that eq. 4.16 and eq. 4.17 are inhomogeneous in dimensions, as δ_σ is dimensionless, but μ_{fit} and σ_{fit} result in units of the drag force $\alpha|u_b|u_b$). The PDF is negatively skewed, *i.e.* events of $F_D > 0$ are more extreme. This is due to the fact that the square of a normally distributed variable, here u_b , has a skewed distribution. Hofland & Battjes (2006) tested eq. 4.14 against their own measurements. As a proxy to the streamwise force F_D , they used the streamwise pressure differential D measured at a cubic model stone ($d = 30$ mm). The shape of the PDF was predicted almost perfectly for lower drag intensities, say $\pm 2\sigma_D$. However, slight differences for extreme drag values were observed, where the trend of D' was better described by an alternation of δ_σ . In

his Ph.D. report, Hofland also tested pressure measurements indicating lift fluctuations, L' , against an adopted version of eq. 4.14. However, the measured distributions of L' did not follow the theoretical curve. Instead, they revealed to be almost Gaussian shaped between $\pm 2\sigma_L$, and beyond that the deviation was positive.

Next, eq. 4.14 – and with this its included pressure generating mechanism – will be examined as to how far it can be used to describe the PDFs of the pressure measurements made within the present study. The following figs 4.18 - 4.20 present PDFs from measurements at the experimental conditions of #uni6, for both arrangements to record D' and L' . Three different bed exposures are analyzed, $y/d = 0.7$ in fig. 4.18, $y/d = 0$ in fig. 4.19, and $y/d < -2$ in fig. 4.20. The former two figures include plots of Hofland's PDF, adopted for both D' and L' .

A definite 'near-bed' δ_σ cannot be found for D' and L' , since \bar{u}_b and σ_{u_b} are subjected to a larger scatter (see figs 4.2(a) and 4.5(a)). Thus the plots of eq. 4.14 were obtained with $\delta_\sigma = [2.7, 5.4]$ to cover the reasonable range gained by the velocity measurements. The figures also include plots of the standard Gaussian² (or standard-normal) density distribution that reads, *e.g.* for D'

$$P(D'/\sigma_D) = \frac{1}{\sigma_D\sqrt{2\pi}} \exp \left[-\frac{1}{2} \left(\frac{D' - \bar{D}}{\sigma_D} \right)^2 \right], \quad (4.18)$$

with $[\sigma_D, \bar{D}] = [1, 0]$.

A closer look now to fig. 4.18 reveals that Hofland's PDF (eq. 4.14) provides a good approach to both histograms of D' and L' at $y/d = 0.7$. In tendency, $\delta_\sigma = 2.7$ gives an acceptable approximation to the measured shape. However, negative deviations can be seen around the mode value and the negative tails for $< -1.8(D', L')$. In the semi-logarithmic plot it can be seen that the positive tail of D' is described well by values of $\delta_\sigma = 2.7-5.4$, whereas the maxima of its negative tails are better approximated for $\delta_\sigma > 5.4$. For L' a similar tendency is revealed. The positive tail of L' is described well by values of $\delta_\sigma < 2.7$, whereas the maxima of its negative tail are approximated for $\delta_\sigma > 5.4$. (Note that Hofland's PDF equals the Gaussian distribution if it is applied with $\delta_\sigma = \infty$.) These findings lead to the following conclusions concerning the properties of pressure fluctuations measured slightly on top of the gravel bed: (1) as both PDFs of D' and L' can be approached by Hofland's PDF, here both the local drag and the local lift must be mainly influenced by the near-bed velocities. In the sense of Hofland (2005), the underlying process is called a quasi-steady mechanism, as it is (mainly) due to large-scale velocity fluctuations. However, his measurements did not show that this dependency also holds for L' , although he expected this for higher exposures (Hofland, 2005, p.105). Note that Hofland had a slightly different setup with crushed stones and a relative large cubical housing of 30 mm for his pressure sensors. (2) The positive tails of $> 3(D', L')$ are better described by higher relative near-bed turbulence intensities, $1/\delta_\sigma$, than the negative tails. In other words: At higher near-bed turbulence intensities, the drag and lift is more likely to be positive than negative.

²Johann Carl Friedrich Gauß: * 1777 in Braunschweig (D); † 1855 in Göttingen (D)

4 Experimental Results

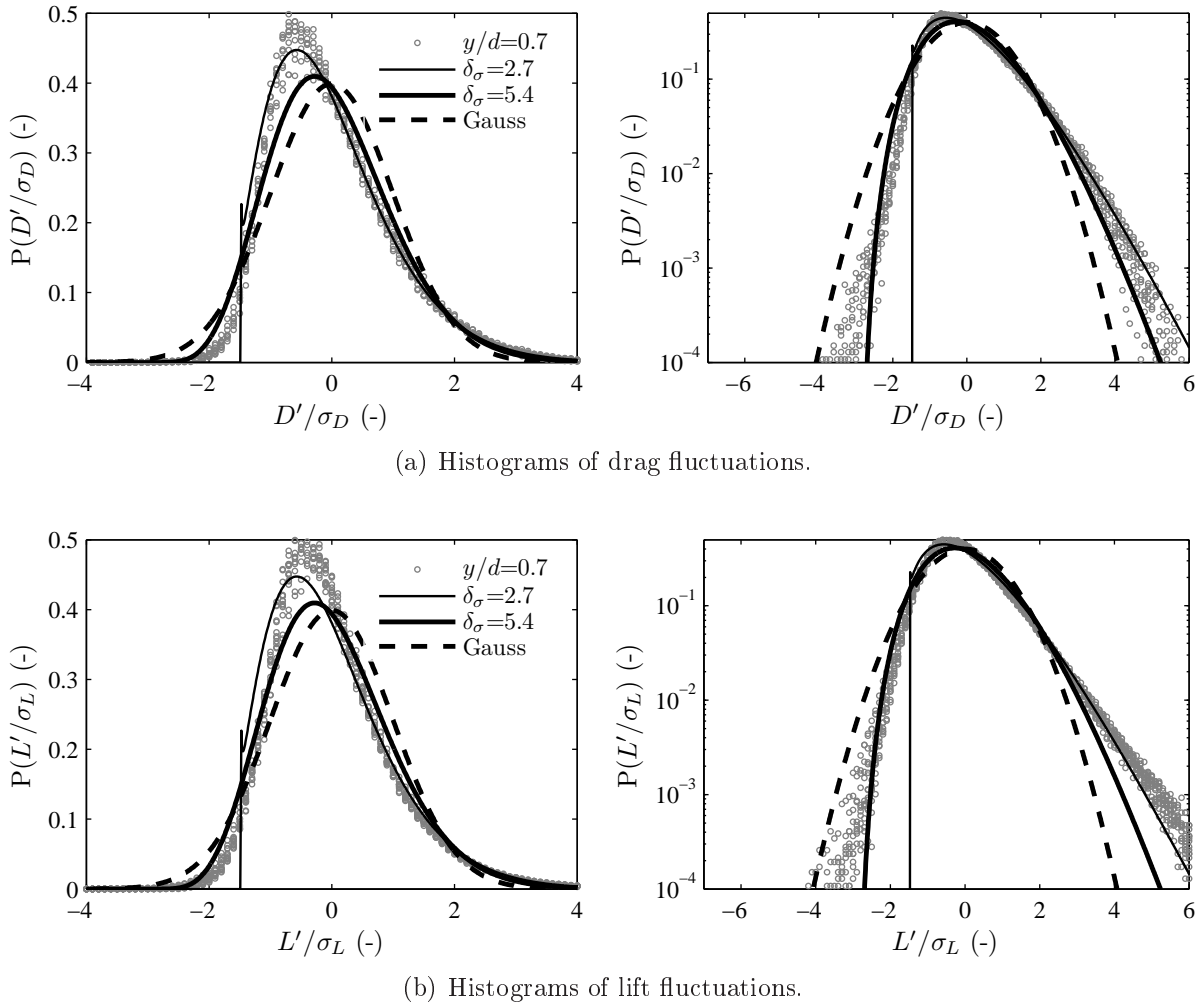
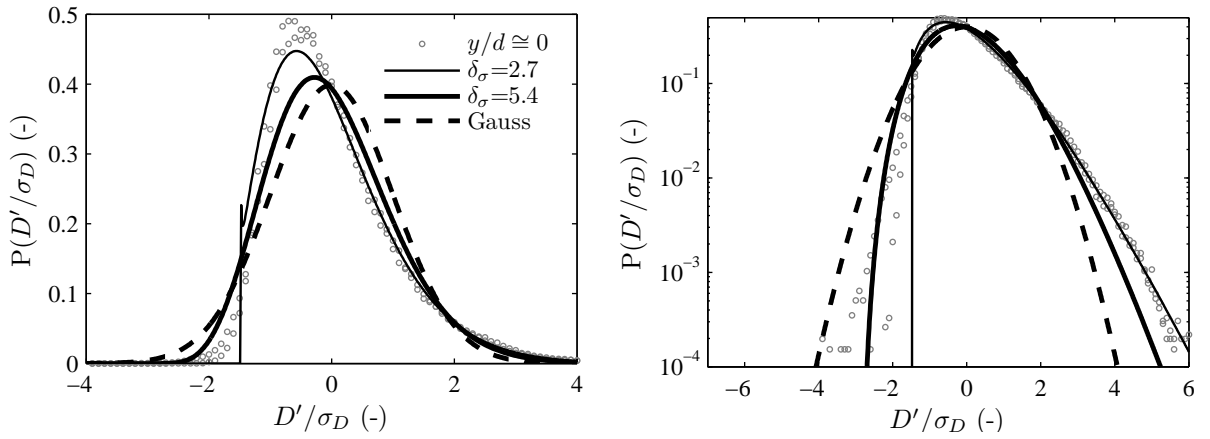
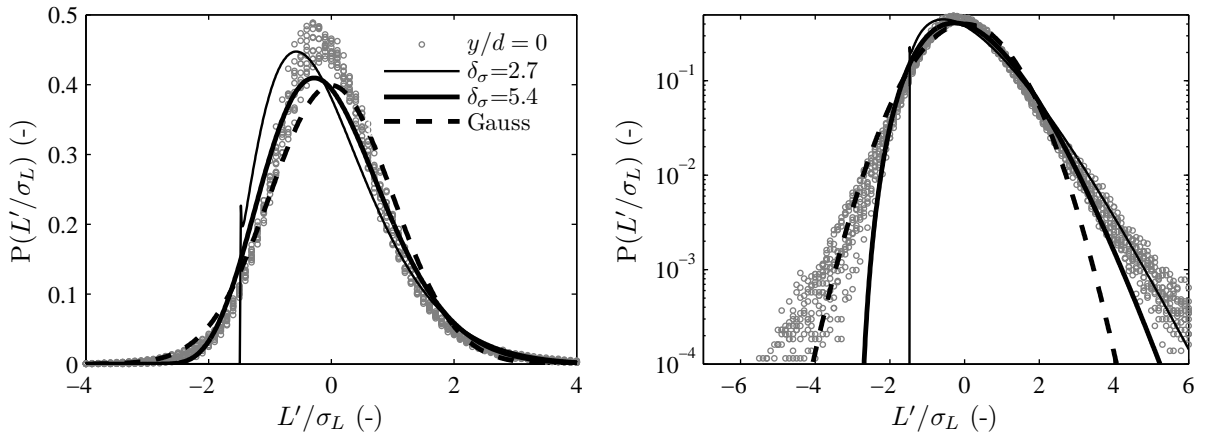


Figure 4.18: PDFs of measured instantaneous pressure fluctuations slightly above the gravel crest (#uni6). (a) D' (10 independent signals), (b) L' (14 independent signals), compared with eqs 4.14 and 4.18, and normalized by its respective standard deviation σ_i . The two on the left are plotted with linear scales in order to evaluate the shape of the distribution around the mean; the two on the right are plotted with semi-logarithmic scales to better represent the shape of the tails.



(a) Histograms of drag fluctuations.



(b) Histograms of lift fluctuations.

Figure 4.19: PDFs of measured instantaneous pressure fluctuations at the gravel tops (#uni6). (a) D' (2 independent signals). (b) L' (14 independent signals).

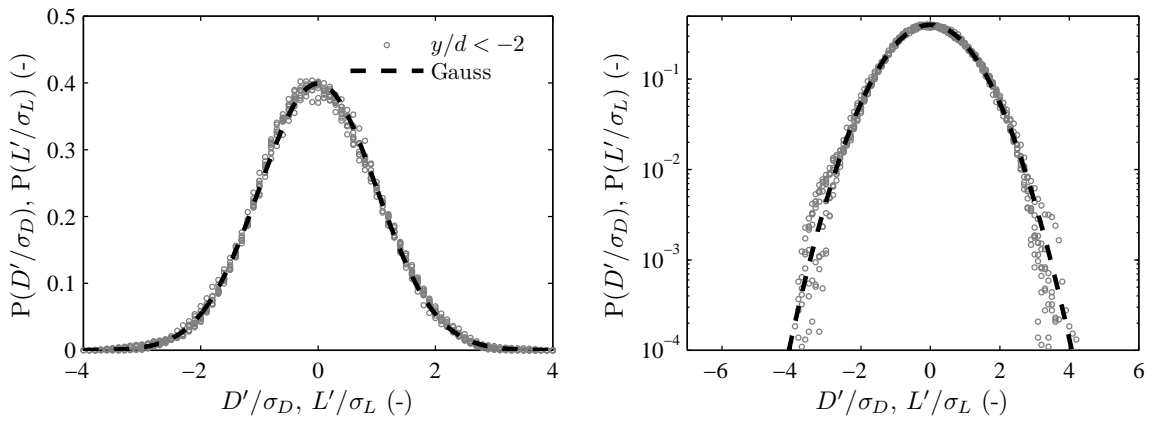


Figure 4.20: PDFs of measured instantaneous pressure fluctuations with the gravel bed (#uni6, 9 independent signals).

4 Experimental Results

Similar findings hold for the measured PDFs at the gravel tops, as shown in fig. 4.19. Again, $\delta_\sigma = 2.7$ gives – at least in tendency – an acceptable approximation to the measured shape, where the positive tails of D' and L' are predicted almost perfectly by this value. The negative tails obtain a better matching for lower turbulence intensities, where D' can be approximated by $\delta_\sigma = 5.4$ and L' by $\delta_\sigma = \infty$. Thus, the trend goes to lower near-bed turbulence intensities. Nevertheless, the quasi-steady mechanism is still dominant.

As shown in fig. 4.20, all PDFs of D' and L' lose their skewness deeper in the gravel at $y/d < 2$. The PDFs are well predicted by a simple Gaussian distribution, or in the sense of Hofland's PDF (eq. 4.14) $\delta_\sigma = \infty$ holds, i.e. $\bar{u}_b \gg \sigma_{u_b}$. Thus, turbulence due to near-bed velocity fluctuations plays no further role. In the sense of Hofland (2005, e.g. fig. 6.1) turbulent wall pressure (TWP) fluctuations now can be seen as the responsible mechanism. TWP are due to convecting pressure fields and not due to near-bed velocity fields. Consequently, a symmetrical (*i.e.* a non-skewed) PDF can be expected.

To sum up, the PDFs measured at $y/d = 0.7$, $y/d = 0$, and $y/d < -2$ revealed that the interfacial layer (say $0 < y/d < 2$) gives a sharp boundary, whereas above, drag and lift are more related to the near-bed velocity, and below they are more related to TWP. A closer examination of this transition layer will be the topic of the next section.

4.3.3 Turbulence intensities

Spectral analysis. Before describing the pressure measurements with respect to turbulence intensities, a closer look is taken at the spectral configuration of the signals. This addresses the question of the genesis, damping, and dissipation of pressure fluctuations, and the question as to what extent noise influences the turbulence statistics. The frequency-characteristics of the pressure signals are examined by means of spectra.

Fig. 4.21 shows typical representative power spectra of the measured signals at different vertical positions. They refer to the same pressure signals that were already presented as time-series in fig. 4.17. Additionally, fig. 4.21 includes a supplementary signal recorded at $y = -38$ mm deeper within the gravel layer. The one-sided spectra are estimated by Welch's averaged modified periodogram method of spectral estimation. Segment lengths of $n = 2^{17}$ (61.7 s) with 50% overlap were used, with Hamming windows of the same length. The results were smoothed by a moving average window of 50 elements, with the shape preserved.

With an overall view of fig. 4.21, the damping of the pressure fluctuations within the gravel layer becomes obvious, as the spectra of the signals of the more sheltered sensors throughout are below the more exposed ones. Furthermore, it can be seen to what extent the larger frequency scales contain also the larger part of the turbulent energy. Only the spectrum of the signal measured by the uppermost sensor follows clearly the expected Kolmogorov-scaling tendency within the inertial subrange. At frequencies of $f > 10$ Hz, its curve declination conforms to the classical $-7/3$ power-law for pressure. This scaling also roughly holds for the spectra at $y = [-22, -38]$ mm deeper in the gravel. However, since the turbulent fluctuations are damped within the porous layer, the resulting curves are shifted towards lower values of S_{pp} and f , respectively. As all spectra deeper in the bed were found nearly to resemble these two spectra (not shown here), it is concluded

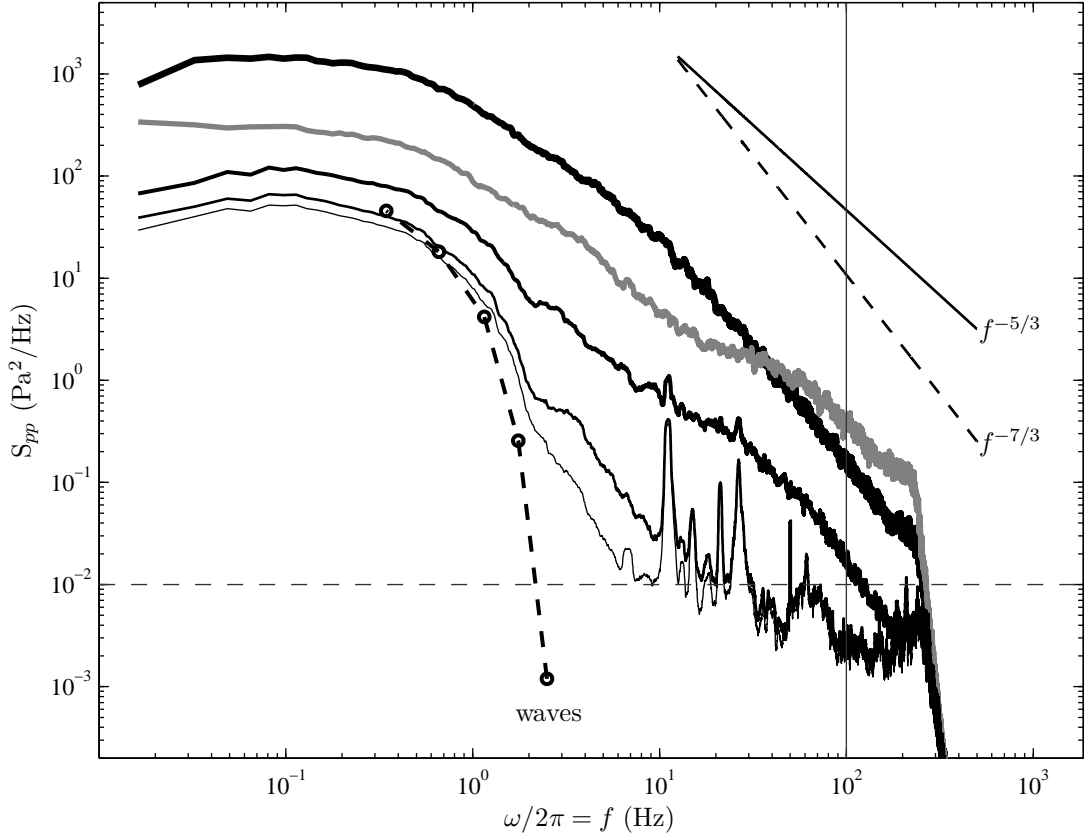


Figure 4.21: One-sided power spectra for pressure signals at different vertical positions (#uni6). The area under the curves equals the variances σ^2 . Line widths from thick to thin correspond to $y = [10, 5, -7, -22, -38]$ (mm), indicating the fluctuating part of drag and lift as $[D', L', D', D', D']$ (recall fig. 4.16). Here, the sensors indicating drag fluctuations are vertically aligned; the sensor indicating lift fluctuations is at $\Delta z = 80$ mm relative to the other sensors (light gray line, see also fig. 4.17). The dashed curve denotes the possible influence of long-waves in the outer flow (eqs 4.19 and 4.20). The vertical line highlights the response time of 10 ms guaranteed by the manufacturer. The dotted horizontal line refers approximately to the white noise level. The influence of the low pass filter with the cut-off frequency at 500 Hz becomes prominent for $f > 200$ Hz.

4 Experimental Results

that deeper than $(2-3)d$, no essential damping takes place. The variance σ_p , *i.e.* the area under the curves, stays almost constant.

In contrast to this Kolmogorov-conformity, the signals measured in the roughness layer at $y = [+5, -7]$ mm reveal a different spectral behavior for the turbulent energy cascade. Here, the curves show a decrease slower than $f^{-7/3}$. At $f > 30$ Hz, the curve of the MPPS at $y = +5$ mm even crosses the spectrum of the uppermost sensor. This leaves open the place for interpretation: as there is no distinctive peak, misleading measurement errors due to *e.g.* organ-pipe effects (sensor was facing upwards, see fig. 4.16(b)) are implausible. By this, a peak with the eigenfrequency of the pressure tube should be expected. Another reason seems more likely: an energy transfer from the horizontal to the vertical fluctuations. As the free stream flow in the streamwise direction is hindered due to single grains in the roughness layer, it transforms to a more 3D flow within the interstices. Therefore, kinetic energy from the streamwise flow might be shifted towards the vertical and transversal directions. Within the gravel layer, the classical $-7/3$ power cascade that indicates isotropic behavior is enhanced by a transformation of small-scale turbulent kinetic energy. However, beside this speculation it has to be noted that the validity of a $-7/3$ -law for pressure is not generally accepted. Although Lee & Sung (2002) and Hofland (2005, p. 106) found solely a $-7/3$ power-law for their TWP spectra, Gotoh & Rogallo (1999) proposed a second range at $f^{-5/3}$. Lately, Tsuji *et al.* (2007) found even characteristic isotropy at exponents of $\lesssim -5/3$, but they never observed a $-7/3$ power-law in their pressure spectra at all.

Next, the focus goes to the origin of the observed large-scale oscillations with $f < 1$ Hz that are not damped within the porous gravel layer. It is hypothesized that these pressure fluctuations are dominated by a long-wave oscillating water level. An approach to this is made in the following. By neglecting the surface tension, the first-order wave theory gives the resulting standard deviation of the bed-pressure due to surface waves

$$\sigma_p = \frac{\rho g a}{\sqrt{2} \cosh(kh)}, \quad (4.19)$$

where the wave number is given by $k = 2\pi/L$ and the denominator $\sqrt{2}$ is introduced so as to give σ_p/p_{\max} for a sine function. Within the transition from deep to shallow water between $0.05 < h/L < 0.5$, the corresponding wave frequency reads

$$f = \frac{1}{L} \sqrt{g/k \tanh(kh)}. \quad (4.20)$$

Fig. 4.21 includes a plot of equations 4.19 and 4.20, where wave lengths of $L = (0.25 - 4.0)$ m and a constant small amplitude of $a = 0.6$ mm is assumed. The plot matches the spectra at $f \approx 1$ Hz reasonably well. Consequently, the long wave oscillations of the outer flow are hypothesized to dominate σ_p within the gravel layer. However, it can not be answered definitely whether they are due to long-wave oscillations of the water level or if they are due to macro pressure fields resulting from coherent flow structures.

Two kinds of noise can be identified in the spectra. Although the recording was obtained by applying a low-pass filter (see §3.4), high frequencies still produces aliasing noise. The resulting peaks can be seen in a band of (10-30) Hz in the spectra of the sensors at

$y = [-22, -38]$ mm, where the signal was too small to absorb these interferences. The second noise is the white noise, which is unavoidable. In the spectra it can be identified at approximately $< 10^2$ Pa²/Hz. Consequently, a spectral separation of the fluctuating pressure signal can be made as follows

$$\sigma_{p,\text{tot}}^2 = \sigma_{p,t}^2 + \sigma_{p,w}^2 + \sigma_N^2, \quad (4.21)$$

where $\sigma_{p,\text{tot}}^2$ denotes the total variance, $\sigma_{p,t}^2$ is the part due to turbulence, $\sigma_{p,w}^2$ is the part due to (long) wave oscillations, and σ_N^2 is the part due to noise. Since σ_N^2 is independent of the flow conditions, the measured signals at low turbulence intensities are subjected to a low signal-to-noise ratio. Especially for measurements within the bed for #sphi and #uni3, the significance of $\sigma_{p,t}^2$ and $\sigma_{p,w}^2$ is low.

Turbulence intensity profiles. In fig. 4.22, vertical profiles of the standard deviation of the drag and lift, σ_D and σ_L , for all runs of #uni*i* are given. In fig. 4.22(a), a scaling was applied by τ_o . In this, the turbulence intensities obtained at the different flow conditions match appropriately in the roughness layer and in the outer flow. However, within the subsurface layer deeper than $2d$ a constant, non-zero value is reached for both σ_D and σ_L . Thus, the variances are independent of the orientation of the pressure pick-up. Here, a scaling is performed with respect to seepage flow, as can be seen in fig. 4.22(b). The normalization was done using a seepage flow variable $\rho g u_*/k_f$. In this, one constant (k_f) considers seepage flow, and another (u_*) accounts for the outer flow, u_* . This velocity is also proportional to the bulk velocity and consequently also to a convection velocity. This provides a further indication that the long wave oscillations in the subsurface layer are dominated by pressure fields that are convected in the outer flow.

Next, a separate examination is given of σ_D and σ_L for the three different kinds of bed. In figs 4.23(a)-(c), the variances have removed long wave oscillations in the seepage flow (assumed to be constant, see fig. 4.22) and white noise (see level at fig. 4.21) by applying eq. 4.21. Thus, solely the turbulent fluctuations are considered. At $y/d < -0.5$, marginal differences are recognized between σ_D and σ_L . Therefore, plots of σ_D also contain σ_L below this horizon, and vice versa.

For all three bed types, an exponential decay within the roughness layer becomes obvious. This substantiates the findings of Vollmer *et al.* (2002) and Breugem *et al.* (2006), where the pressure fluctuations also were found to decrease exponentially inside the bed. At the interface of the free-flow to the porous bed, Breugem *et al.* (2006) found values $\sigma_p/\tau_o = 1.6$ ($\text{Re}_{*\delta}=176$, $\phi = 0.60$) and $\sigma_p/\tau_o = 3.0$ ($\text{Re}_{*\delta}=500$, $\phi = 0.95$), indicating that $\sigma_p = f(\text{Re})$. A Reynolds-dependency was also proposed by Farabee & Casarella (1991) (see eq. 2.28), and a comparable tendency is found in the actual data. Whereas the reference values for #uni*i* scatter around $\sigma_D/\tau_o = 9$ and $\sigma_L/\tau_o = 3$, the respecting ratios are larger for #rhi9 and smaller for #sphi. However, for a detailed analysis of a Reynolds-dependency, the statistical spread is too large.

A curve fitting was conducted for the data of #uni*i*. The vertical decay of σ_L could be

4 Experimental Results

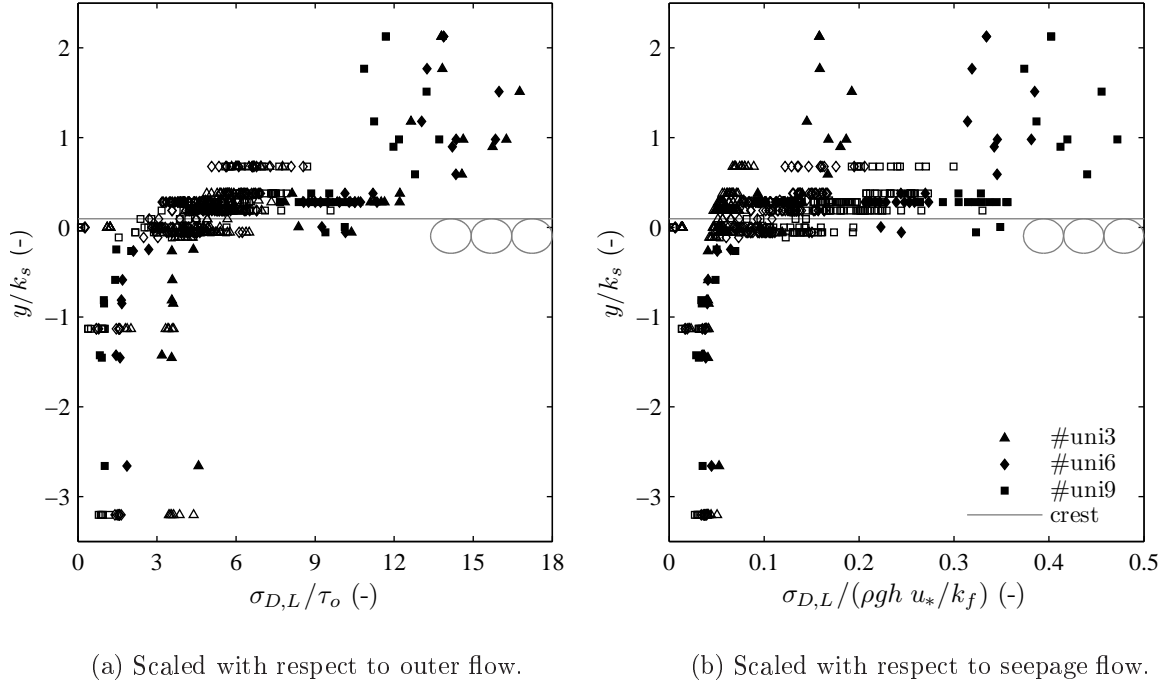


Figure 4.22: Vertical profiles of the standard deviation of the drag and lift, σ_D and σ_L , for runs #uni*i*, plotted with k_s (a) Scaled with open-channel flow variable τ_o . (b) Scaled with seepage flow variable $\rho g h u_* / k_f$. The position of the roughness crest ($y_t = 0$) is highlighted by the horizontal line. Filled symbols refer to σ_D , unfilled symbols refer to σ_L . The measured signals are filtered from white noise (see level at fig. 4.21).

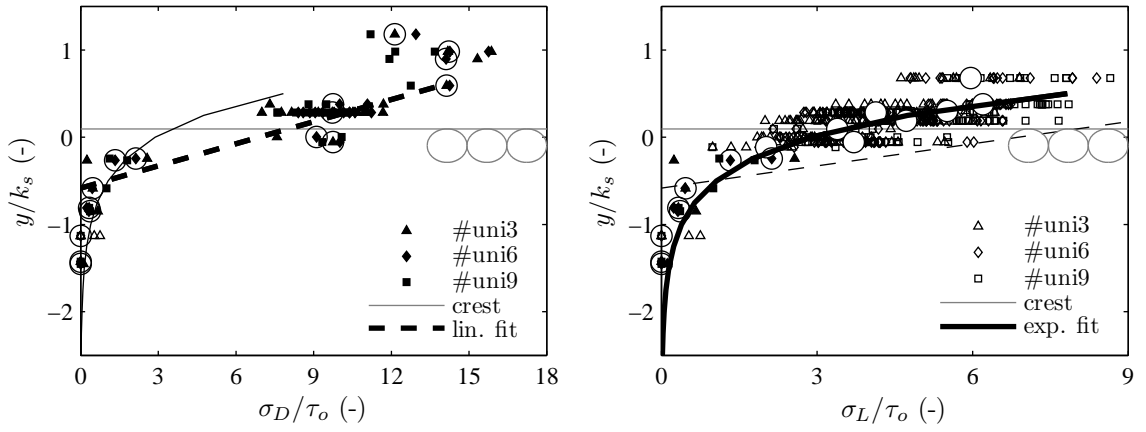
matched well by an exponential fit,

$$\sigma_L / \tau_o = 2.88 \exp\left(\frac{y}{k_s / 2.0}\right). \quad (4.22)$$

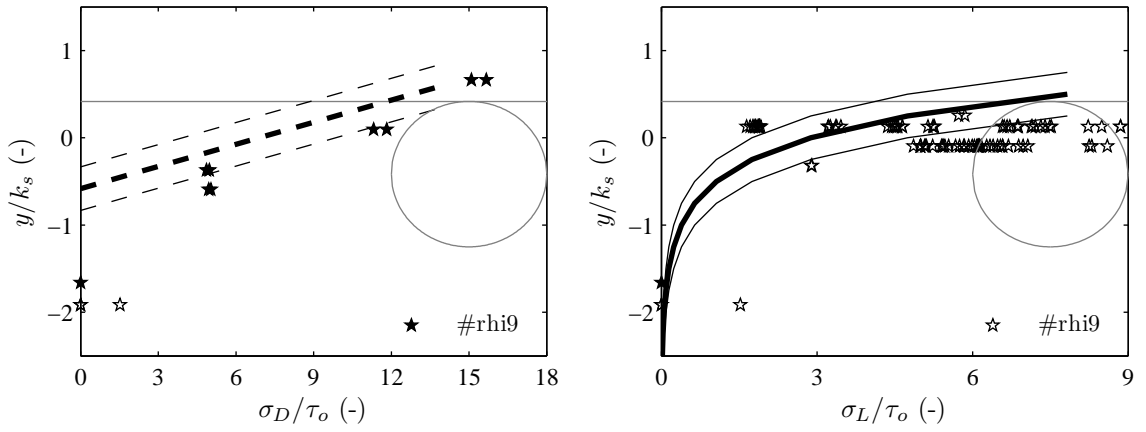
In contrast to this, the vertical decay of σ_D was harder to describe by a fit of such kind. Here, a simple linear description was applied:

$$\sigma_D / \tau_o = 6.89 + 11.84 y / k_s. \quad (4.23)$$

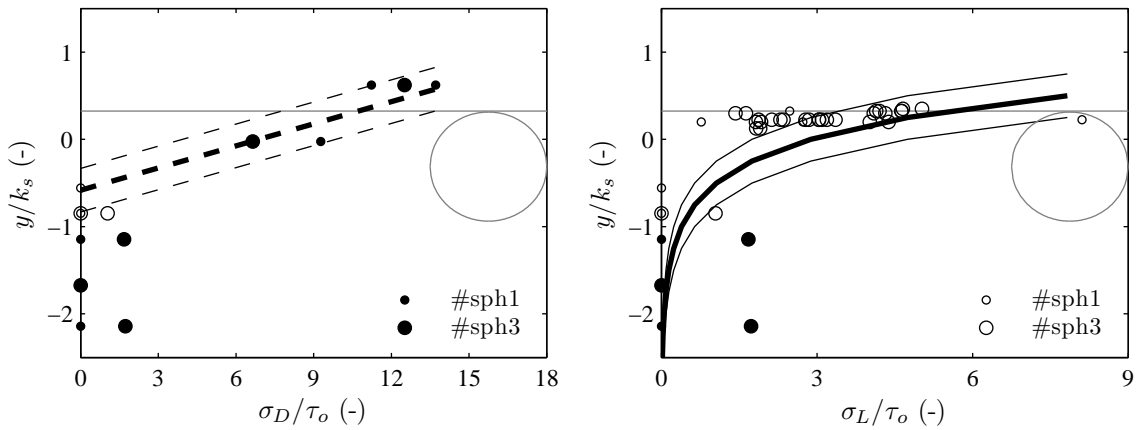
Both relations are plotted in figs 4.23(a)-(c). With respect to the shortcomings in defining, as well as in detecting, the origin in y , lines parallel to eqs 4.22 and 4.23 give a vertical range of $\pm 0.25 y / k_s$. In principle, the shapes of σ_D and σ_L are approximated adequately by eqs 4.22 and 4.23.



(a) Uniform gravel bed. Here, circles respect to horizontal averages.



(b) Rhine gravel bed.



(c) Spheres bed.

Figure 4.23: Vertical profiles of σ_D/τ_o (left column) and σ_L/τ_o (right column) for (a) #uni*i*, (b) #rhi9, and (c) #sph*i*. The given data points have removed both long wave oscillations in the seepage flow and white noise. The fits of eq. 4.23 and eq. 4.22 are given by dashed and continuous lines, respectively. Roughness crest and grain diameter d are shown in the background. Filled (unfilled) symbols refer to σ_D (σ_L). The thinner parallel lines give a vertical range of $\pm 0.25 y/k_s$.

4.4 Simultaneous Consideration of Velocity and Pressure Fluctuations (Event analysis)

4.4.1 Time Series

Before analyzing simultaneously recorded pressure and velocity measurements, a closer look is taken at the question on how to compare between them. Therefore, firstly a simplified steady but turbulent 1D open-channel flow is considered, independent of the actual 2D/3D flow conditions.

On a plane of constant elevation the Bernoulli equation gives

$$2 p/\rho + u^2 = C , \quad (4.24)$$

with C being a constant along a streamline. Now, this relation is transferred to the fluctuating part by a Reynolds-decomposition. Similar as in §2.6.2 the result reads

$$2/\rho p' + (2\bar{u}u' + (u'u' - \overline{u'u'})) = C . \quad (4.25)$$

Since $u \gg u'$ holds, the term $2(\bar{u}u')$ is expected to represent most of the fluctuating part. Thus, eq. 4.25 can be simplified to

$$1/\rho p' \approx -\bar{u}u' + \hat{C} , \quad (4.26)$$

where the constant can be approximated by $\hat{C} = 0$, if $u \gg u'$ is applicable. Eq. 4.26 reveals a similar structure to eq. 2.33 (van Radecke & Schulz-DuBois, 1988) if only the Bernoulli-effect is considered. (Note that this term was found to be responsible for most of the variance of the fluctuations.) Furthermore, eq. 4.26 reveals also a similar structure to the Poisson-eq. 2.27 for fluctuating pressure, if only the mean-shear source term is considered. Therefore, $\bar{u}u'$ may be denoted as 'quasi'-mean-shear source term. Recall that the pressure fluctuations are influenced by source terms in the entire fluid domain, where the impact of single sources decreases with distance. Thus, an approximation to real flow conditions is given, if an adequate spatial average of the quasi-mean-shear source term is considered.

The above mentioned considerations are now tested against synchronous time series with pressure fluctuations in comparison to the velocity fluctuations. Fig. 4.24, for example, gives a sequence of $\Delta t = 15$ s measured at the flow conditions of #uni6. Here, the head of the MPPS was vertically orientated as shown in fig. 4.16(b), thus it indicates a vertical lift by $L = -p$. To reveal the significant structure of the signal, the recording was digitally resampled from 2125 Hz to 40 Hz by an FIR-filter. The synchronous PIV measurements were performed in a vertical streamwise plane above the sensor head (setup A). To compute $\langle \bar{u}u' \rangle$, a spatial averaging was performed within an arbitrarily chosen window of 5×5 mm² over the top of the MPPS. Fig. 4.24 reveals a clear negative correlation between p'/τ_o and the quasi-mean-shear term $\langle \bar{u}u' \rangle$. Significant pressure drops occur simultaneously with events of high velocity, where in the given sequence extreme values can be observed at $t = 110.8, 121.2, \text{ and } 126.5$ s. (A second source term, $\langle \bar{w}v' \rangle$ as proposed

4.4 Simultaneous Consideration of Velocity and Pressure Fluctuations (Event analysis)

by van Radecke & Schulz-DuBois, was also tested against the pressure fluctuations. It showed to be of minor importance, therefore it is omitted in the plot of fig. 4.24.)

The extreme events are related to the occurrences of characteristic coherent structures that are presented later during this present section. Firstly, however, a closer inspection of the latter event is given in fig. 4.25, where a cutout of $\Delta t = 126-126.7$ s is shown. Up to 126.37 s, the pressure increases slowly, here within 0.25 s from $p'/\tau_o = -6$ to $+8$ if the 40 Hz in reference to the filtered signal. Then an essential pressure drop can be observed. This drop is accompanied by increased small-scale pressure fluctuations. In this example, p'/τ_o decreases within 0.12 s rapidly to minimum values around -40 , if the small-scale fluctuations are also taken into consideration. A simple estimate reveals that pressure drops of such a kind have the potential to entrain single grains from the bed: A force balance considering buoyancy and neglecting friction and inertia shows that – in the case of -139 Pa (what equals $-40 \tau_o$ in fig. 4.25) acting on at least 36% of the surface of a single (sphere shaped) gravel grain – it can be lifted. Consequently, extreme events of such kind must play an important rule in sediment entrainment.

To correlate this pressure signal with the simultaneously measured velocity fields, the frames 1072-1076 will be analyzed in the next section.

4.4.2 Splicing method

Hoffland (2005) applied a hybrid technique to enlarge the spatially limited view of velocity fields. By merging a sequence of PIV-recordings, large-scale flow structures were visualized. He called this technique splicing, after the technique used for joining pieces of rope by interweaving strands. A similar technique will be used in the following.

First, the distance Δx_{shift} has to be determined that a flow structure (if present) moves within the time step Δt_{PIV} of two subsequent velocity fields. Hoffland performed this by a two-dimensional correlation method applied to each of two sequential recordings. However, this technique failed for the present measurements – especially for the high Reynolds number experiments – for two reasons: (1) Hoffland recorded his measurements at 20 Hz, whereas in the present study only (4-8.5) Hz could be reached. Thus, only short overlapping lengths $\Delta x_{\text{overlap}}$ were realizable, leading to less reliable correlations in tendency. (2) Hoffland performed his measurements over the entire water depth h , whereas in the present study the flow below $0.3 h$ was observed by PIV. If only a single near-bed flow structure with a definite transport velocity is present, the present measurements with limited vertical extent are superior, as the former spliced flow field would be subjected to a smearing-effect over the entire water depth. However, if two or more near-bed flow structures with several definite transport velocities are present, the actual measurements are inferior, as each structure provokes its characteristic Δx_{shift} . To avoid these effects, the shift distance between two images is approached by

$$\Delta x_{\text{shift}} = \frac{0.5(\langle u_1 \rangle + \langle u_2 \rangle)}{\Delta t_{\text{PIV}}}, \quad (4.27)$$

4 Experimental Results

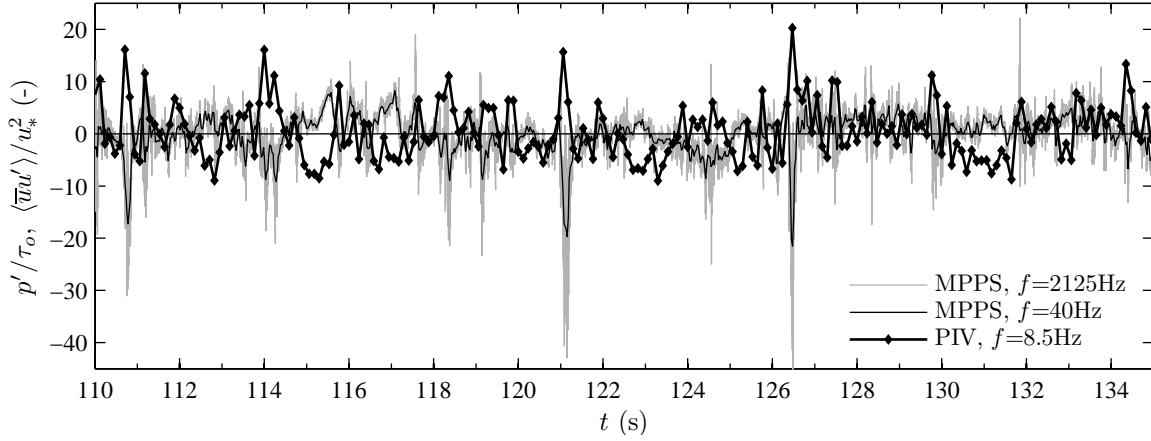


Figure 4.24: Typical synchronous time series of pressure fluctuations p'/τ_o at $y = 0$ in comparison with the velocity fluctuations $\langle \bar{u}u' \rangle / u_*^2$ spatially averaged over a vertical streamwise area of (5×5) mm² above the pressure sensor (#uni6). Lift is indicated by $L' = -p'$ (compare fig. 4.16(b))

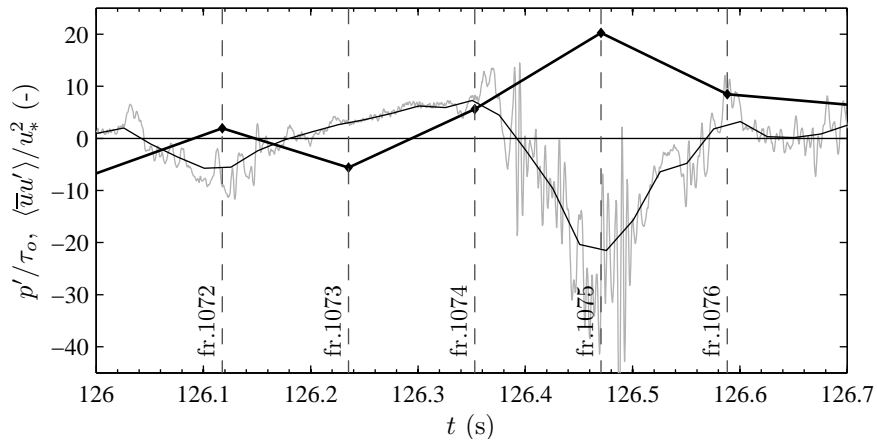


Figure 4.25: Time series of 0.7 s, where a noteworthy pressure drop is recognized (cut-out of fig. 4.24). The vertical dashed lines refer to the corresponding PIV-frames 1072-1076.

4.4 Simultaneous Consideration of Velocity and Pressure Fluctuations (Event analysis)

where $\langle u_1 \rangle$ and $\langle u_2 \rangle$ denote the spatial averaged velocity fields of the two subsequent PIV frames. A new flow field is created by averaging the velocity fields of the overlapping parts defined by $\Delta x_{\text{overlap}}$, *i.e.* the difference between the frame length in streamwise direction and Δx_{shift} . The process can be continued to enlarge the flow-field by splicing a third frame, a fourth frame and so on.

In fig. 4.26, an example of five separate recordings and the resulting spliced velocity field is pictured. The field in fig. 4.26 refers directly to the time series that was already presented in fig. 4.25. However, before the revealing flow structure is analyzed in detail, first it has to be classified to what extent this spliced flow field is representative for the real flow field.

The splicing method is similar to Taylor's³ hypothesis of 'frozen' turbulence (*e.g.* Nikora & Goring, 2000). The way it is performed is more precisely described as a 'reverse' application of Taylor's approach, since here properties of the time domain are deduced from the spatial domain, and not vice versa. In the sense of Taylor, eq. 4.30 had to be resolved to Δt_{PIV} . Two further differences are that: (1) The convection velocity $\Delta x_{\text{shift}}/\Delta t_{\text{PIV}}$ only has to be constant between two subsequent frames, but not for the entire time series. (2) A single convection velocity is applied for two overlapping regions of two successive PIV frames, while Taylor's hypothesis has been formulated for a particular distance from the bed. That means, the splicing method applied here disregards an own convection velocity for each layer between two PIV-frames, but takes the mean over the whole frame.

Although strong similarities of the overlapping flow regions become visible in fig. 4.26, the splicing method fails for smaller flow structures. Obviously, the assumption of a '100%-frozen' turbulence is questionable. Especially in the near-bed region, where large shear values are typical, the assumption of a spatial-averaged overall convection velocity is misleading for the spliced flow field. To evaluate the applicability of the splicing method, the 2D correlation coefficients r_{12} of each overlapping region were determined as follows

$$r_{12} = \frac{\sum_m \sum_n u'_{1,mn} u'_{2,mn}}{\sqrt{\left(\sum_m \sum_n (u'_{1,mn})^2 \right) \left(\sum_m \sum_n (u'_{2,mn})^2 \right)}} . \quad (4.28)$$

For the current example, $r_{12} = [0.65, 0.74, 0.73, 0.79]$ is reached. Although the values of r are far away from the ideal value of unity ($= 1.0$), the computed values indicate that the application of the splicing method is feasible.

Now, a closer look is taken at the flow structure that is revealed in fig. 4.26. Starting at $t = 126.12$ s (frame 1072), a slower fluid packet with an angle of approximately 20° inclined to streamwise direction is prominent for the flow near the bed. Keeping its wedge-like structure, the packet moves forward, followed by a larger second fluid area of higher velocity ($t = 126.24$ - 126.47 s, frames 1073-1075). Due to its faster propagation velocity,

³Geoffrey Ingram Taylor: * 1886 in St John's Wood (UK); † 1975 in Cambridge (UK)

4 Experimental Results

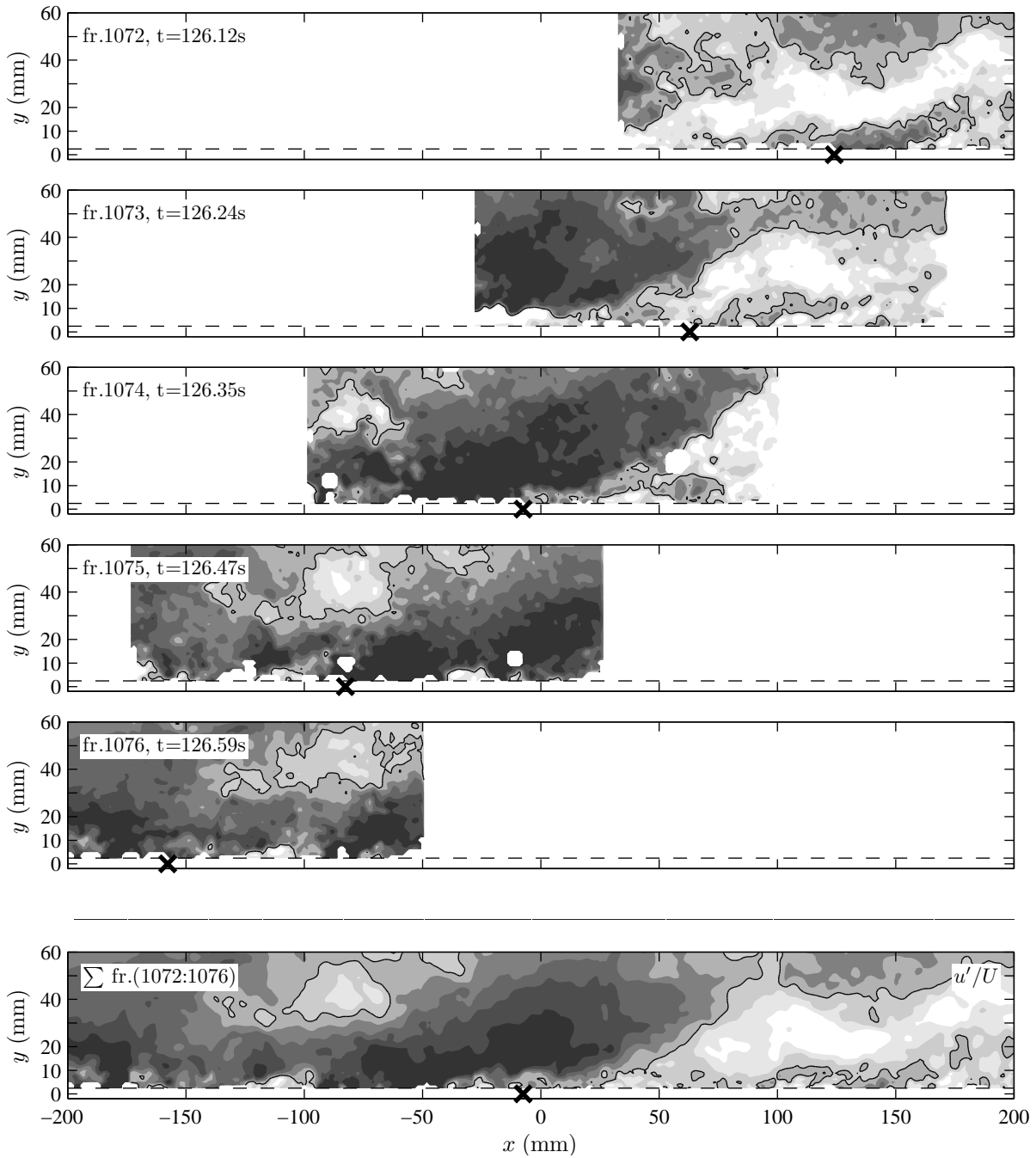


Figure 4.26: Five original images of $u'(x, y)$ together with the spliced image obtained from them (bottom). The single frames were smoothed by a 3×3 Gaussian filter, the spliced image was finally smoothed by a 3×3 moving average filter. The shading indicates u'/U in steps of 0.1 (colorbar: see fig. 4.9), the isoline denotes $u'/U = 0$. The cross refers to the position of the pressure sensor, whose measured signal is given in fig. 4.24.

4.4 Simultaneous Consideration of Velocity and Pressure Fluctuations (Event analysis)

the second fluid packet overruns the first one. Within the shear layer between both zones, small eddies are generated. This is not shown here, but in fig. 4.9(b), where frame 1073 has been presented already. At $t = 126.47$ s (frame 1075), the structure with lower velocity has completely passed the actual frame. A closer look back to fig. 4.25 shows that p' drops significantly when the tail of the slower wedge-like fluid structure has passed the location of the pressure sensor and the faster fluid zone becomes dominant. Thus, the pressure drop measured at this flow event is strongly correlated with an acceleration of the near-bed streamwise velocity. This in turn indicates that the measured pressure drop at this event is mainly due to the Bernoulli effect resulting from the interaction between the two fluid packets. The attendant small-scale pressure fluctuations are expected to result from eddy shedding or eddies generated at the shear interface of the two fluid zones.

Next, the splicing method will be applied to some velocity fields recorded at the same time when noteworthy pressure drops can be seen.

4.4.3 Synoptic View

In §4.4 a cut-out of a time-series measured by a single MPPS was presented. In this, information on the fluctuating pressure in the time domain of a single point was given. If Taylor's frozen turbulence hypothesis is assumed to be applicable to the pressure signal as well, spatial information can be deduced from time series of point measurements. This will be done here.

Within the experimental runs, the pressure was recorded simultaneously by an array of up to 16 MPPSs. Thus, if Taylor's approach is applied, footprints of ensemble pressure fields can be reconstructed from these point measurements. During the synchronous measurements of the PIV-system and the MPPSs, the pressure sensors typically were arranged in an array as pictured in fig. 4.27 (see also fig. 3.6(b)). The time signals of the 11 MPPSs located at $-8 < x < 8$ (mm) can be used to reconstruct horizontal pressure fields by applying Taylor's hypothesis of frozen turbulence. To this end, the time domain of their signals has to be transformed to a longitudinal dimension

$$x_\lambda = -U_c t, \quad (4.29)$$

where U_c denotes the mean transport velocity of the pressure fields. Then, the x_λ -direction reflects the dimensions 'sensed' by a stationary observer (Eulerian view). However, in assuming a constant U_c , longitudinal dimensions of faster moving pressure fields are underestimated, and longitudinal dimensions of slower fields are overestimated, respectively. Tests were made to determine the 'optimal' U_c . In a first approach, U_c was gained from signal-correlation of the upstream to the downstream MPPSs (see again fig. 4.27). However, this led to problems especially for experiments at lower Reynolds numbers (*i.e.* #shpi and #uni3). Here, $U_c \propto \sqrt{gh} > U^4$ was found for the transport velocity of pressure fields, indicating that (surface) waves passing by have a strong influence on the bed-pressure. For the other runs at higher Reynolds numbers, typically values of $U_c = (0.6-0.8)U$ were found. This indicates that the dominating pressure fields propagate with near-bed velocities. Therefore, U_c is estimated by the actual $\langle u \rangle$ of the (spliced)

⁴Recall, that $U = Q/(Bh)$ is the bulk velocity (tab. 3.2, tab. 4.3)

4 Experimental Results

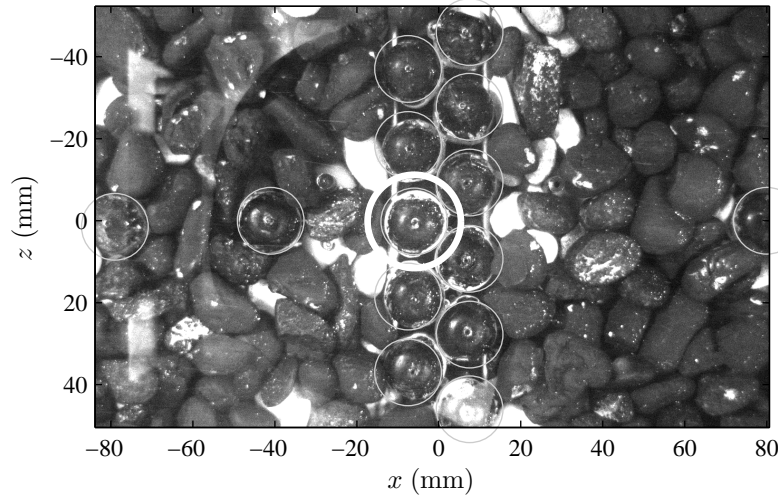


Figure 4.27: Top view on the MPPSs mounted in the gravel layer, here in the arrangement as used for synchronous PIV measurements of setup *B*. The white circle highlights the target sensor head at $[x, y, z] = [-6.0, -1.5, 0.2]$ (mm). The size of the frame is exactly the same as in fig. 4.12.

flow field as determined by the PIV measurements. This also implicates the benefit that the actual flow situation is described more precisely.

Now, a closer look is taken to typical results. The next figs 4.28 and 4.29 present two pressure fields reconstructed from experimental data at #uni6, where simultaneous PIV-measurements were performed in a streamwise-vertical plane (setup *A*). The synoptic view of the flow is given by this: the upper plot describes the vector field, the next two plots give $v'\bar{u}$ and $u'\bar{u}$ (van Radecke & Schulz-DuBois, 1988), and the bottom plot pictures the bed-pressure field.

The flow event pictured in fig. 4.28 again gives recall to the same situation that was already described in figs 4.25 and 4.26. To reconstruct the bed-pressure field, $U_c = 0.91 U$ was adopted from the mean streamwise velocity of the spliced velocity field. Note that the array of 11 MPPSs had to be arranged in two lateral alignments of each 5 and 6 MPPSs due to the dimensions of the sensor heads. To compensate this shortcoming while reproducing the pressure fields, the spatial-domain of the 6 downstream-MPPSs were shifted upstream to the streamwise position of the 5 upstream-MPPSs. This performance is marked in the plots by the small crosses and the 6 arrows. Each signal was FIR filtered to 200 Hz, smoothed by a motion filter to achieve approximate equally spaced xz -axes. Finally, a 3×3 Gaussian filter was applied. The resulting pressure field reveals two dominating zones: an elongated and slightly bent high-pressure field at $x_\lambda = (-20 \text{ to } +100)$ mm, and a low-pressure field at $x_\lambda = (-150 \text{ to } -40)$ mm. It should be remembered that the sensed flow direction is from left to right, whereas the time increases from right to left. If only the maximum values of the latter are considered, the structure of the low-pressure field can be characterized as elongated as well.

Next, the focus is on the corresponding velocity field. As has been detected by the analysis of the point measurements (§4.4.1), there is a strong negative correlation between

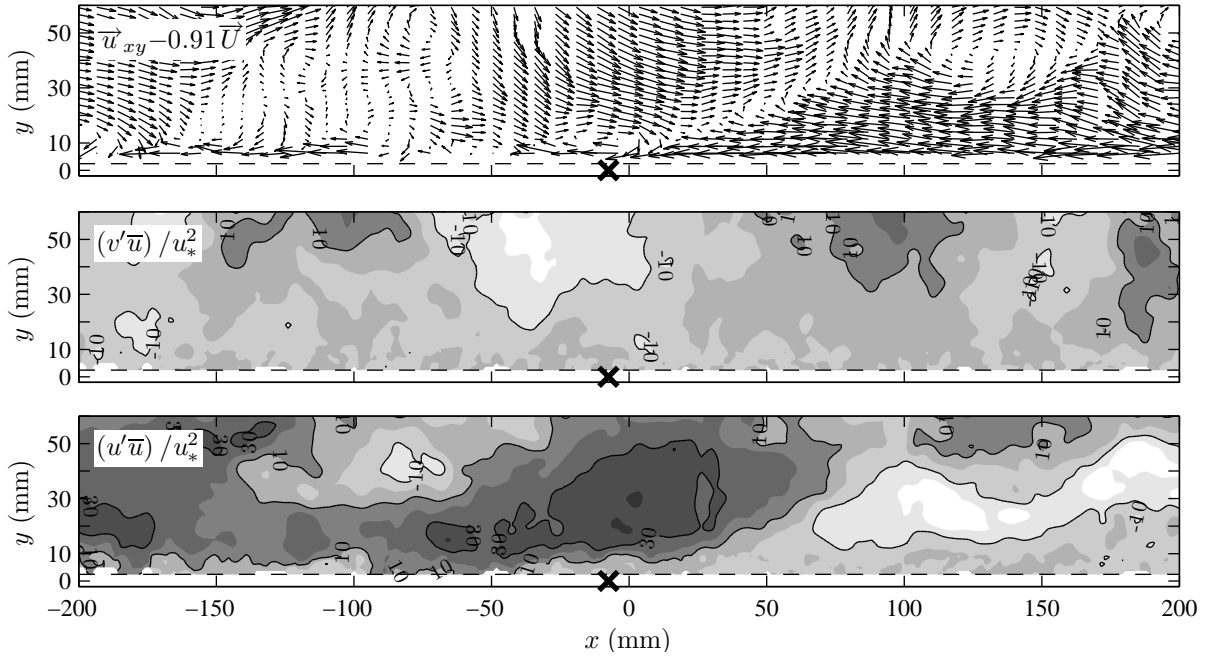
4.4 Simultaneous Consideration of Velocity and Pressure Fluctuations (Event analysis)

the 'quasi'-mean-shear source term $\bar{u}u'$ and the pressure fluctuations p' . The high-pressure field is located directly under the decelerated velocity zone, and the low-pressure field lies under the accelerated velocity zone. The transition between the two pressure fields is well defined if the inclined interfacial shear layer is extended to the bed. Consequently, the Bernoulli-effect is considered to be the main cause of the extreme pressure drop and the structural appearance of the (reconstructed) pressure field. In opposite to $\bar{u}u'$, the term $v'\bar{u}$ reveals no distinctive features in the near-bed region. Thus, $v'\bar{u}$ must be of minor importance to the genesis of the large-scale pressure field. This is remarkable, as the low-pressure field here is similar to a field with a strong lift, and – at first thought – one would expect a strong upwards component of the velocity. The spliced vector field reveals clearly the two velocity zones and the typical inclining shear layer between both. At the upper end of this interface, a striking clockwise rotating eddy becomes obvious. Its diameter can be estimated to be $(1/4-1/3) h$. (Note that its distorted oval appearance is most likely due to the splicing method.) Concerning its scale, the eddy can be also interpreted as a large-scale roller in the sense of Shvidchenko & Pender (2001). The macro-turbulent structure behaves like a motor, as it promotes the fluid to accelerate on top and to decelerate below its core. As this large-scale eddy is strongly connected to the entire flow structure, the question arises, if this roller is the direct cause of it or vice versa. (Similar to the philosophical chicken-or-egg question.) Since the minimal pressure can be found at a distance of not less than four eddy-radii upstream of the vortex core, it seems to be more likely that the eddy is caused by the shear layer. Thus, in the sense of Adrian *et al.* (2000*b*) it can be interpreted as the oversized head of a hairpin-like vortex.

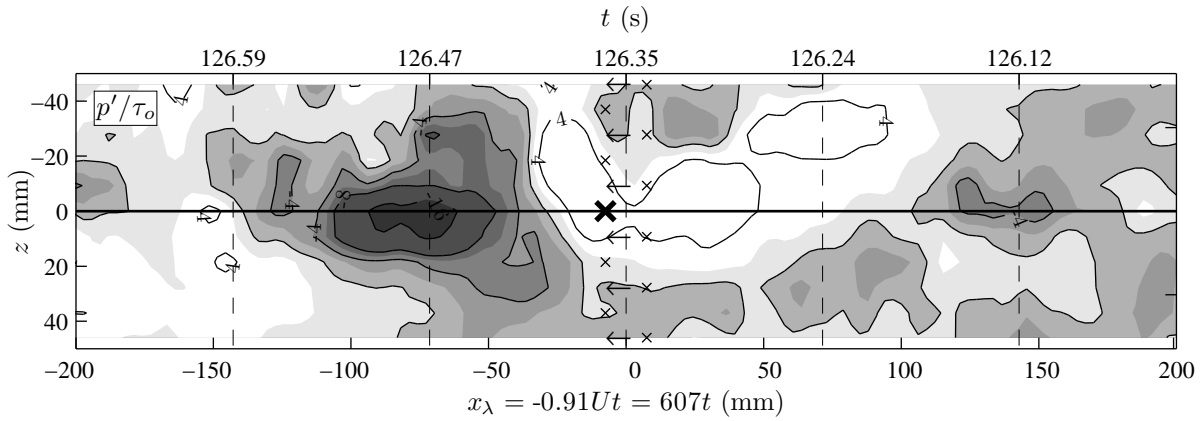
In fig. 4.29 a similar event is given, recorded in the same experimental run. The propagation velocity of $0.76 U$ is slower in relation to $0.91 U$ as before. In opposition to the extreme pressure drop shown in fig. 4.28, the event illustrated now gives an example of a more typical moderate pressure drop. In principle, the same findings hold as have been deduced before. The pressure fields are in tendency elongated. The pressure drop is strongly connected to a streamwise acceleration of the near-bed fluid, whereas the vertical velocity component appears to be of minor importance to the large-scale structures. The vector plot reveals the typical wedge-like structure. However, at the upper end of the interfacial shear layer no remarkable eddy can be seen this time. Consequently it can be deduced that the flow-pattern itself is not necessarily dependent on the presence of a noteworthy eddy at the upper end of the inclining shear layer. However, an indication is given that a large-scale eddy forces the velocity differences and in turn the bed-pressure differences.

Next, the horizontal appearance of these coherent flow structures will be analyzed in a similar manner. To this end, the PIV measurements performed in setup *B* will be used. Two synoptic views of spliced velocity fields and their corresponding reconstructed bed-pressure fluctuations are shown in figs 4.30 and 4.31. The experimental conditions are again those of #uni6, thus the results are directly comparable with figs 4.28, and 4.29 obtained by setup *A*. The measurements of setup *A* were not performed simultaneously with setup *B*. In each figure, the upper plot gives the vector fields, the next plot pictures the 'quasi'-mean-shear source term, and the bottom plot represents the bed-pressure field.

4 Experimental Results



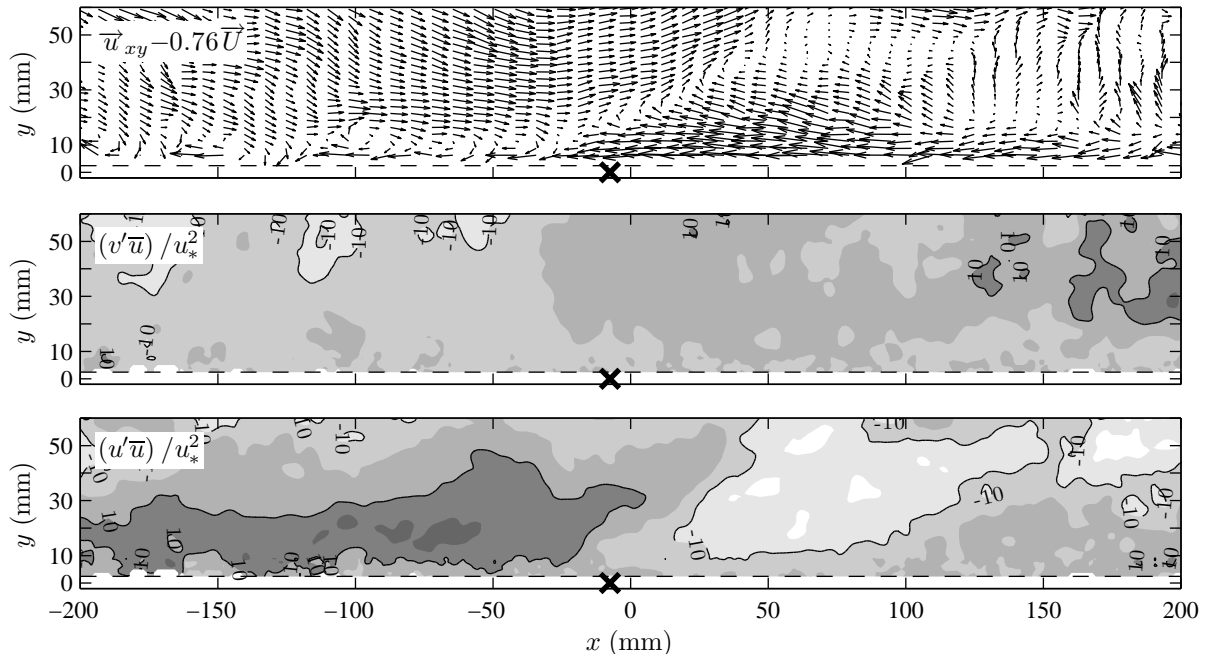
(a) Spliced velocity field in a streamwise vertical plane.



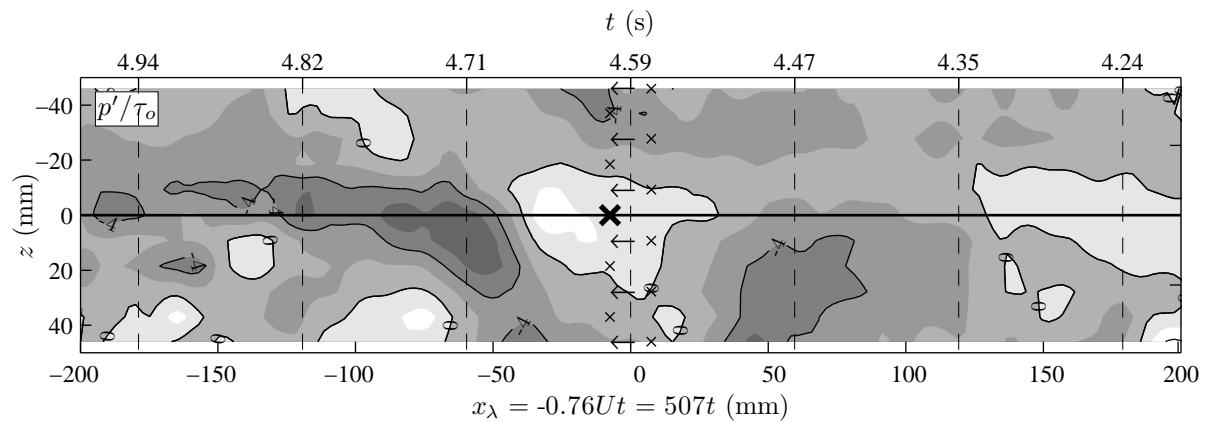
(b) Bed pressure fluctuations at $y = 0$. The horizontal line marks the PIV-axis.

Figure 4.28: Synoptic view of spliced velocity field and the corresponding reconstructed bed-pressure fluctuations (#uni6). The visualization gives a spatial view of the extreme pressure drop event as shown in fig. 4.25.

4.4 Simultaneous Consideration of Velocity and Pressure Fluctuations (Event analysis)



(a) Spliced velocity field in a streamwise vertical plane.

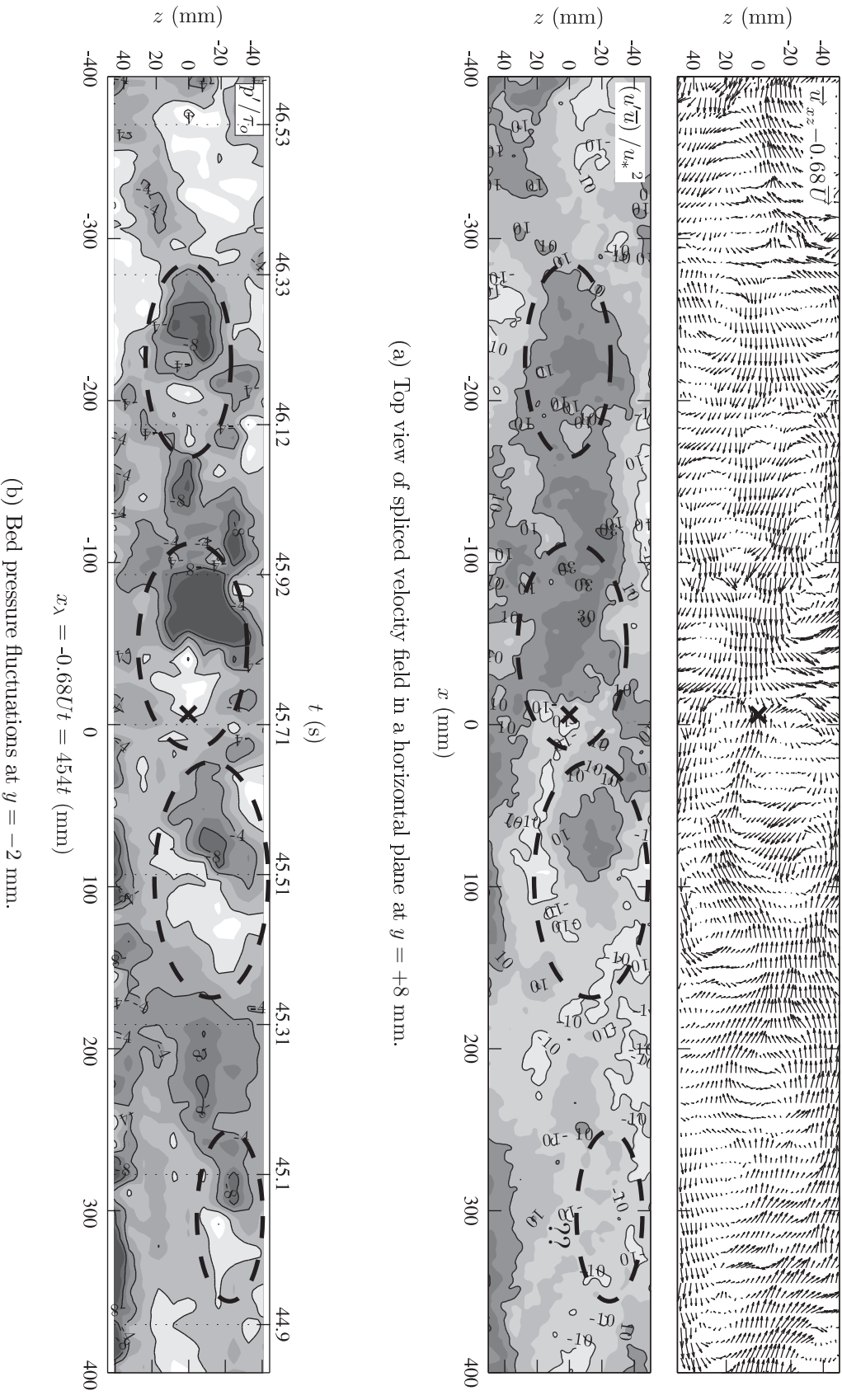


(b) Bed pressure fluctuations at $y = 0$. The horizontal line marks the PIV-axis.

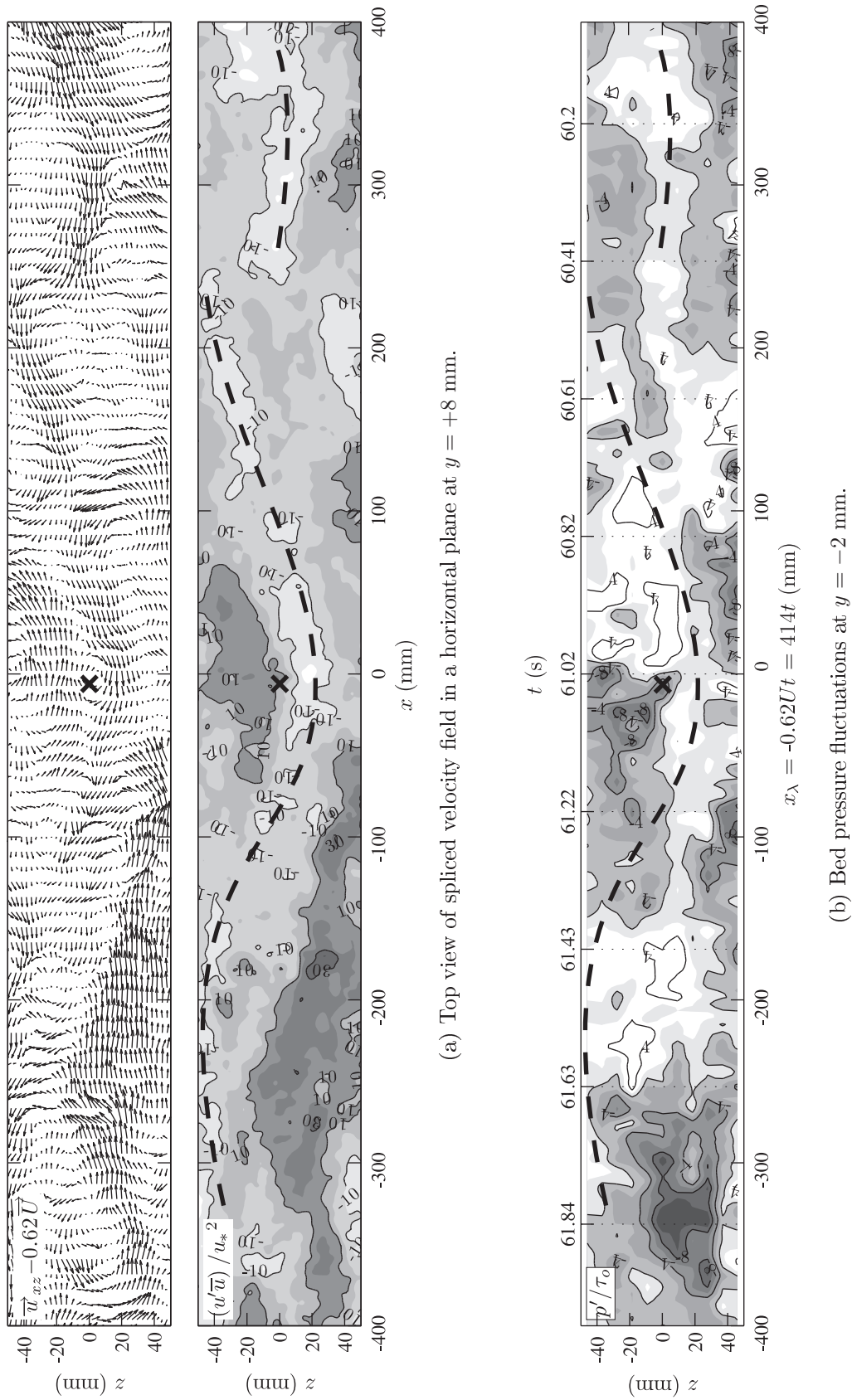
Figure 4.29: Synoptic view of spliced velocity field and the corresponding reconstructed bed-pressure fluctuations (#uni6). In opposition to fig. 4.28, this event gives an example of a more typical moderate pressure drop event.

4 Experimental Results

Figure 4.30: Synoptic view of a spliced velocity field and the corresponding reconstructed bed-pressure fluctuations (#um6). Four dashed ellipsoids highlight pressure drop events and the assumed area of the corresponding velocity-fields.



4.4 Simultaneous Consideration of Velocity and Pressure Fluctuations (Event analysis)



(a) Top view of spliced velocity field in a horizontal plane at $y = +8$ mm.

(b) Bed pressure fluctuations at $y = -2$ mm.

Figure 4.31: Synoptic view of a spliced velocity field and the corresponding reconstructed bed-pressure fluctuations (#uni6). The dashed lines retrace a meandering low velocity streak and the corresponding p' -field.

4 Experimental Results

To increase the image size laterally, the PIV recordings at setup *B* were performed with a lower frame rate (4.9 Hz) than at setup *A* (8.5 Hz). Thus, the overlapping lengths of the spliced $[u, w]$ -field are shorter and with this, the representativeness of the reconstructed field to the real flow field is lowered. However, a small benefit is drawn from the slower convection velocity throughout, as the measurements of setup *B* were only performed in the near-bed region. As a result, each spliced value of $[u, w]$ is based on the average of roughly two overlapping velocity fields, since the structures move about half of the observed area between the recording of two double frames. For comparison, setup *A* enabled roughly three overlapping vector fields while splicing the $[u, v]$ -fields. For the correlation coefficients typically a range of $r_{12} = 0.65 - 0.75$ is reached (eq. 4.28). The velocity fields are finally filtered twice by a 3×3 moving average filter to enable interpretation. To be consistent with fig. 4.28 and fig. 4.29, $x = x_\lambda = 0$ originates from the coordinate system of the PIV-frame in the center of the spliced flow field. The pressure field is reconstructed from 11 signals of $p'(t)$ in the same manner as before.

The pressure field given in fig. 4.30 presents a 1.76 s-cutout of a time series. In reference to the spliced synchronous velocity field, its actual transport velocity was estimated to be $U_c = 0.68 U$. Consequently, the given view extends over $4 h$ in the streamwise direction. The pressure field in the given example is populated with four 'footprints' of typical pressure drop patterns, highlighted by dashed ellipsoids. These textures consist of a downstream area with $p' > 0$ and an upstream area with $p' < 0$. Here, their longitudinal scale is in $\mathcal{O}(h/2)$ and their lateral extension is in $\mathcal{O}(2 k_s)$, similar to the pressure drop pattern shown in fig. 4.30 and fig. 4.31. The corresponding large-scale velocity field describes the flow at $\Delta y = 10 \text{ mm} \approx d$ above the reconstructed bed-pressure field. Only few similarities can be seen between the structures of velocity and pressure, which is most likely due to this vertical distance. Generally, a faster fluid zone becomes obvious at $-300 < x < 0 \text{ mm}$, and a slower fluid zone at $100 < x < 400 \text{ mm}$. However, a closer look at the areas according to the pressure drop pattern reveals similar observations which support the previous findings: Zones with $p' > 0$ correlate with $u' < 0$ and zones with $p' < 0$ correspond to $u' > 0$. The transition from a slow to a fast fluid zone is strongly connected to a significant pressure drop. Only for the smallest zone of the four pressure drop events, located at $x_\lambda = 300 \text{ mm}$, does this finding not hold. Most likely the causal flow structure is too weak to leave a distinct imprint on the velocity field $\Delta y \approx d$ above the pressure field.

Fig. 4.31 shows an example, where the structures of the pressure and the flow field are more similar. Here, an elongated meandering low speed streak becomes obvious. The streaky structure appears to be even longer than $3 h$. Its lateral extension is in the order of $2 - 3 k_s$, which conforms with the findings of eq. 4.13. To highlight this feature, it is retraced by a dashed line and also plotted in the corresponding p' -field. The pressure field shows a similar structural appearance: the trace of the low speed streak is clearly visible. At $x_\lambda \approx 61.1 \text{ s}$ and 61.8 s two low pressure zones can be seen that are located downstream of a high pressure area. However, the related velocity fields on top of the ($p' > 0$)-field hardly indicate a slower velocity than on top of the ($p' < 0$)-field. Presumably, low speed fluid is pent up in a small layer between the bed and the layer observed by the PIV-

system, comparable to the situation as in fig. 4.28. Thus, these pressure drop events are not necessarily in contradiction to the previous findings.

4.4.4 Conditional Sampling

Within the last sections, several individual flow events have been presented that are more or less correlated to a pressure drop at the bed. The observed sudden decreases in the bed-pressure appear to be strongly connected to a fluid acceleration in the direct vicinity of the bed, akin to a Bernoulli-lift with a missing obstacle. However, it is not clear yet, whether these individual events represent a typical flow-bed interaction or whether they are just coincidences due to the chaotic nature of turbulence. Furthermore, in case a characteristic mechanism does indeed exist, the question arises, whether typical dimensions can be revealed. This will be investigated next.

Fig. 4.32 shows an ensemble of pressure drops, conditionally sampled to the maximum peak and to the minimum peak, respectively. A conditional sampling method was used as follows: First, the pressure signal of the 'target' pressure sensor was FIR-filtered to 200 Hz. Then, a dp/dt criterion was used to detect extremely decreasing events in the pressure signal. This criterion was arbitrarily chosen to $> \tau_o/4$ within 0.1 s for the present flow situation of #uni6. In this, 25 events were collected within a time series of 205 s. Also other values for dp/dt were tested, leading to the detection of different numbers of events with a more or less distinctive mean of the ensemble. A closer look now at the results given in fig. 4.32 shows that the ensemble average of the minimum peak is more pronounced than the maximum peak. Here, $p' > 0$ lasts on average < 0.12 s, whereas the duration of $p' < 0$ is about twice this amount. A similar ratio is given by $p'_{\min}/p'_{\max} \approx 2$. This skewness was expected and it confirms the dependency on the near-bed velocity as discussed already in §4.3.2.

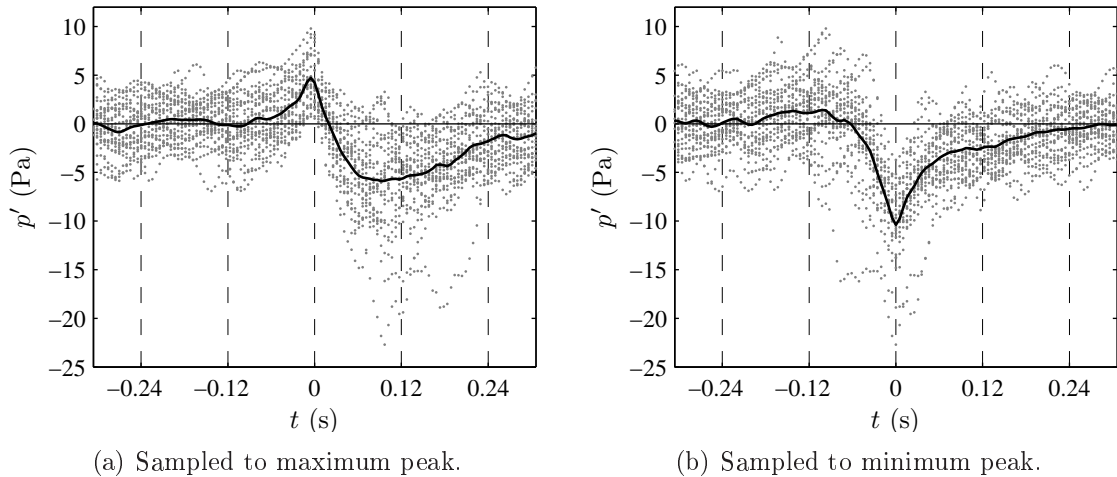


Figure 4.32: Ensemble averaged time history of 25 essential pressure drops (lift) at #uni6. Measured at $y = 0$ synchronous to 1740 PIV recordings ($8.5 \text{ Hz} = 1/0.12 \text{ s}^{-1}$). Conditionally sampled to (a) maximum peak, (b) minimum peak.

4 Experimental Results

Now, the collected time events will be used to get an average view of the related flow structure. To this end, the time-steps found by the maximum-peak-sampling will be applied, keeping in mind that the averaged minimum peak consequently will be subjected to smearing. In fig. 4.32, the vertical grid distance of < 0.12 s is in units of the synchronously recorded PIV frame rates (setup *A*). However, it does not directly represent the actual time steps of the PIV frames. Thus, the PIV recordings have to be 'resampled' to the conditionally sampled pressure drop events. This was done by a Taylor approach as follows: first, the nearest (time-step) neighboring PIV frames were collected. Then they were shifted by

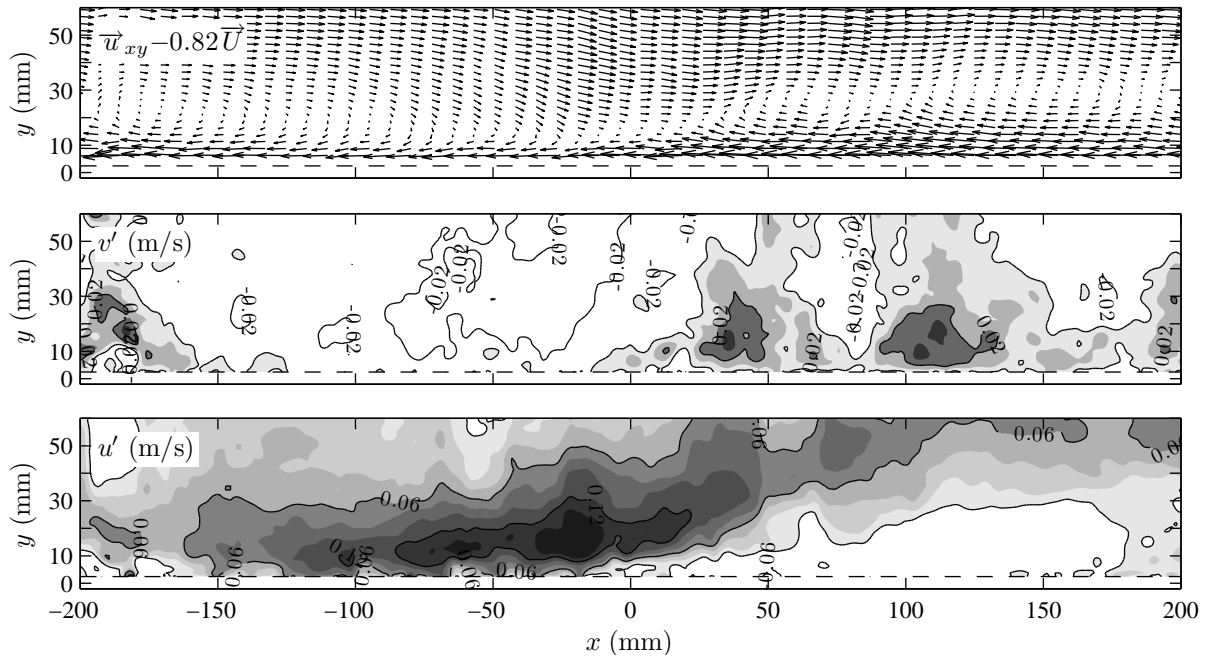
$$\Delta x_{\text{cd}} = \frac{\langle u \rangle}{t_{p\text{-drop}} - t_{\text{PIV}}} , \quad (4.30)$$

where Δx_{cd} denotes the 'spatial-resample'-correction of the velocity field, $\langle u \rangle$ gives the streamwise velocity spatially averaged over the actual PIV frame as an estimate of the propagation velocity of the present flow structure, $t_{p\text{-drop}}$ is the event time of p'_{max} and t_{PIV} is real time of the nearest neighbor PIV-frame. After this, the flow field was spliced and finally filtered twice by a 3×3 moving average filter to facilitate interpretation.

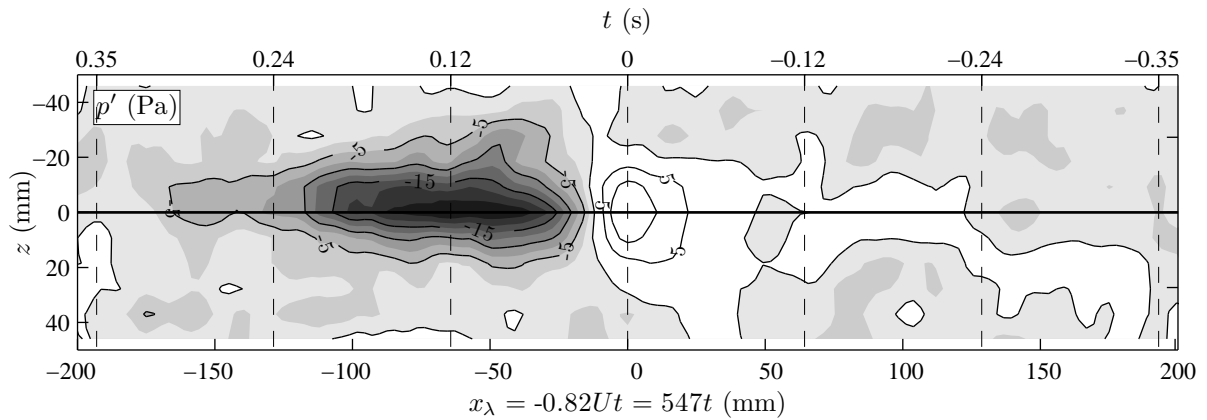
Fig. 4.33 illustrates the resulting averaged flow field in xy and the corresponding reconstructed bed-pressure fluctuations (#uni6). In general, this output conforms with the structural findings from above quite well: A fast large-scale fluid packet overruns a slower one, in which a typical shear zone inclines from the bed at approximately 20° in the streamwise direction. As the faster fluid is in the direct vicinity of the bed, its streamwise component, here illustrated by u' , causes an essential lift at the bed – akin to a Bernoulli-lift. The vertical flow component, here pictured by v' , seems to be of minor importance to this mechanism. In fact, it seems to cause the opposite effect to the bed-pressure than the streamwise component: Above the low-pressure zone, it indicates a downward flow, and at the high-pressure zone vice versa. The streamwise extension of the faster fluid packet is $\mathcal{O}(h)$ and is seen to reach up to half of the water depth. The induced low and high-pressure fields show longitudinal dimensions of each $\mathcal{O}(h/2)$, whereas their lateral extension gives in tendency $\mathcal{O}(2-3k_s)$, as found for the lateral streak spacing in eq. 4.13.

A more detailed view of the lateral extensions is given in fig. 4.34. Here, the conditional sampling technique was applied to the measurements conducted at setup *B*. 25 events were detected in 205 s for the same criterion as above. As the number of events is very similar to the one found before (24 events), the pressure measurements are seen to give robust statistics. Not surprisingly, the reconstructed, conditionally averaged bed-pressure field at fig. 4.34 resembles the corresponding description in fig. 4.33 in a satisfying manner. However, the averaged flow fields are subjected to a large scatter. Two causes might be responsible for this: (1) The measurements were performed with a lower frame rate, thus the 'nearest-neighbor' shift Δx_{cd} is bigger and – in turn – the similarity to the exact flow field at the pressure drop event decreases. (2) The streaks tend to meander laterally (fig. 4.31). Consequently, a large-scale horizontal view gets biased more easily than a streamwise vertical view. Nevertheless, the resulting field of the streamwise velocity components fits – in general – quite well with the related streamwise-vertical view given before. The longitudinal extensions scale by $\mathcal{O}(h)$, and the lateral dimensions are roughly similar to the one of the pressure field. The transverse velocity information reveals that

4.4 Simultaneous Consideration of Velocity and Pressure Fluctuations (Event analysis)



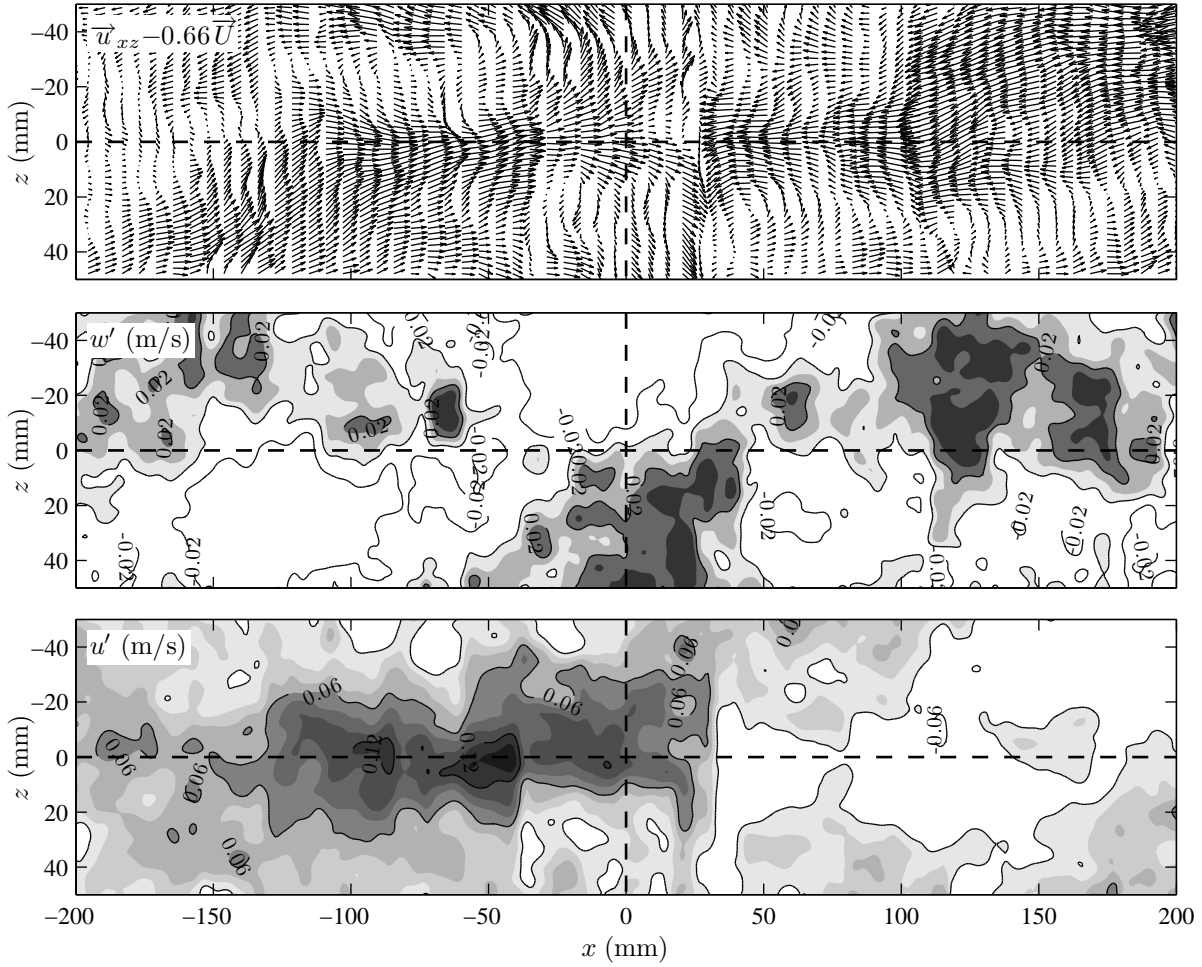
(a) Spliced velocity field in a streamwise vertical plane (flume centerline).



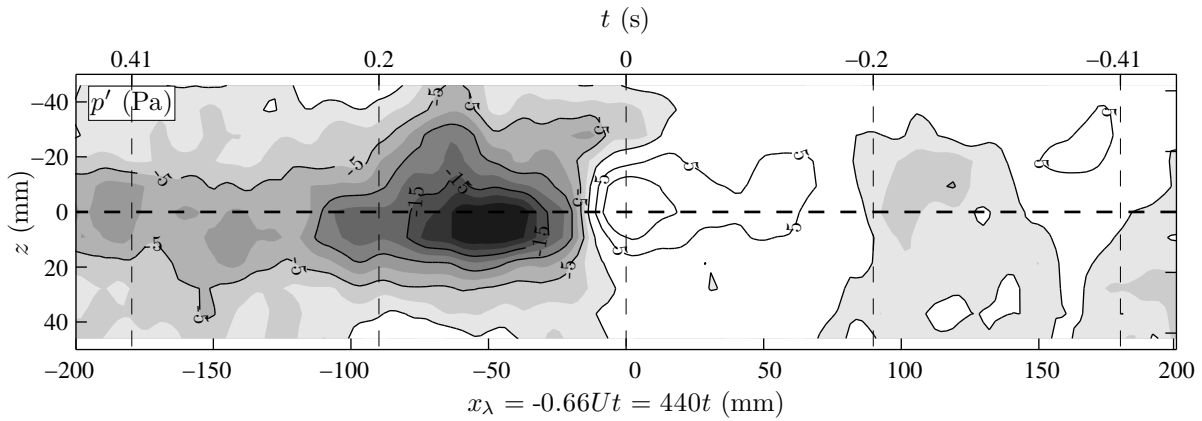
(b) Bed pressure fluctuations at $y = 0$ mm.

Figure 4.33: Ensemble average of (a) the near-bed velocity field (side view) and (b) corresponding reconstructed bed-pressure fluctuations (#uni6). From 25 spliced PIV frames conditionally sampled from the maximum peak of 25 most essential pressure drops (criteria: $0.79 \text{ Pa}/0.1 \text{ s}$). The velocity field was finally filtered twice by a 3×3 moving average filter to facilitate interpretation. Due to sampling of the maximum pressure peak, the distinctiveness of the low-pressure field is weakened.

4 Experimental Results



(a) Top view of spliced velocity field in a horizontal plane at $y = 8$ mm.



(b) Bed pressure fluctuations at $y = -2$ mm.

Figure 4.34: Ensemble average of (a) near-bed velocity field (top view) and (b) corresponding reconstructed bed-pressure fluctuations (#uni6). From 24 spliced PIV frames conditionally sampled from the maximum peak of 24 most essential pressure drops (criteria: $0.79 \text{ Pa}/0.1 \text{ s}$). The velocity field was finally filtered twice by a 3×3 moving average filter. Due to sampling of the maximum pressure peak, the distinctiveness of the low-pressure field is weakened.

the upstream part of the faster fluid zone is spreading away from the centerline, whereas the downstream part of the flow is slightly concentrating towards the centerline. With respect to the dominating vertical flow direction shown in fig. 4.33, the interpretation is this: At the downstream part, fast fluid from the outer flow is pumped downwards. At the upstream part this mechanism is hindered, as it is blocked by the slower fluid zone. Consequently, it spreads away to the sides and goes up again, forming the typical inclining shear layer.

4.5 Concluding Discussion

Summary of Findings. Experimental flume measurements of flow velocity and pressure fluctuations above and within three types of porous streambeds were analyzed. The key findings of these results can be summarized as follows:

- In a streamwise vertical plane large-scale wedge-like flow structures are observable, where – in the sense of a sweep event (or Q_4 event, *i.e.* $u' > 0, v' < 0$) – a zone of faster fluid over-rolls a zone with slower fluid. The resulting shear layer inclines at an angle of 10-20° to the bed, densely populated with clockwise rotating eddies. On average, this phenomenon occurs with sufficient frequency and shape to leave an imprint on the statistics of the flow. Typically, this flow pattern forms near the bed, approximately scaling with the logarithmic layer. However, the biggest structures have the capability to spread over the whole water depth.
- In a horizontal near-bed view, macroturbulent structures form a patched chessboard with regions of lower and higher velocity zones that are elongated in the streamwise direction. The lateral extension of these streaky structures is typically 2-3 times the equivalent sand roughness k_s and increases linearly with distance from the bed. The length of these elongated structures reaches up to the order of several water depths. In the shear zones between the streaky structures, horizontally rotating eddies are observable, but their occurrence is not very distinctive.
- The bed-pressure fluctuations p' and the 'quasi'-mean-shear source term $u'\bar{u}$ are correlated negatively. Typically, high-pressure fields are located directly under decelerated velocity zones, and low-pressure fields lie under accelerated velocity zones. Consequently, the lift akin to a Bernoulli-lift is considered to be the main cause of extreme pressure drops and the structural appearance of the bed-pressure field. Unlike $u'\bar{u}$, the term $v'\bar{u}$ reveals no distinctive features in the near-bed region. Thus, $v'\bar{u}$ must be of minor importance to the genesis of large-scale pressure fields.
- Vertical profiles of the pressure fluctuations at different flow conditions match appropriately with the actual shear stress τ_o and equivalent sand-roughness k_s . Flow turbulence of the open-channel flow strongly influences the standard deviation of pressure, σ_p , above and in the roughness layer, where the lift fluctuations decay exponentially with increasing depth of cover. However, within the subsurface layer σ_p

4 Experimental Results

reaches a non-zero constant, mainly dominated by pressure fields that are convected in the outer flow.

Wedge-like fluid structures were also detected by Adrian *et al.* (2000*b*) and co-workers in wind tunnel experiments; and by Roy *et al.* (2004) in natural gravel-bed rivers, where the streamwise extension scaled by $\mathcal{O}(h)$. This resembles also the structures normally occurring in open-channel flow (Buffin-Bélanger *et al.*, 2000; Hofland, 2005, p. 133). The observed lateral extension of $\mathcal{O}(2-3k_s)$, however, is slightly smaller than the findings of *e.g.* Defina (1996) or Stösser *et al.* (2005). Similar findings concerning the essential Bernoulli-akin-lift on the bed were made by Thomas & Bull (1983), who found a strong correlation between the (smooth-)wall pressure and the ramp-like velocity pattern moving overhead. Within the present study, the vertical velocity component was seen to be of minor importance to this mechanism. In fact, indications were found that it causes the opposite effect to the bed-pressure than does the streamwise component: Above the high-pressure zone, it indicates an upward flow, and above the low-pressure zone, vice versa. Support for this observation is given by Hofland (2005, p. 130), who found a negative vertical velocity typically connected to a dominating flow structure with increased streamwise velocity.

Consequently, it can be concluded that these structural findings concerning the flow-bed interaction are representative for general channel flow processes.

Conceptual Model. As conditionally averaged flow and pressure fields show persistent features, the above bullet points can be synthesized into a characteristic flow mechanism leading to a marked bed-pressure drop equivalent to a lift force. Its possible genesis is suggested in the following.

Due to undulations in the turbulent shear flow, faster fluid from the outer flow arrives in the near-bed zone in the sense of a sweep event. In interaction with near-bed slower fluid a typical ramp-like pattern is generated, where the slower fluid is over-rolled by the faster one. The shear zone inclines from the bed in streamwise direction. This is connected to the generation of vortices or spanwise rollers that rotate clockwise due to the shear effect. These eddy structures may stabilize or even reinforce the velocity gradient since they tend to decelerate the slower fluid. Moreover, these rollers do not extend inevitably spanwise, but also may rotate around axes tilted spanwise-vertical or almost vertical. This, in turn, may stabilize or even reinforce the formation of low speed and high speed zones that are elongated in streamwise direction. Due to demerging effects of the tilted spanwise-vertical roller structures with increasing bed vicinity, the mean lateral extension of the streaks decreases linearly. The bed-pressure is intensely influenced, since faster fluid from the outer flow reaches the immediate vicinity of the bed – in the sense of a sweep event. Then, the streamwise velocity component of the faster fluid causes an essential Bernoulli-akin-lift on the bed. Pressure fluctuations are damped exponentially in the upper layers of the bed.

The structural flow mechanism described here conforms almost with Adrian's model for smooth-wall flows (Adrian *et al.*, 2000*b*, Tomkins & Adrian, 2003). It provides support for the model's applicability to rough-bed flows and gives an extension further to the

behavior of the bed-pressure. However, the difference is that in Adrian’s model, hairpin-like vortices or derivations thereof originate at the bed and then grow and merge with bed distance, leading to the appearance of low and high speed regions that dominate the outer flow. Thus, Adrian’s model is viewing the mechanism of the genesis of coherent structures from the bed to the outer flow. However, the above suggested genesis is originated and dominated by sweeps from the outer flow that influence the near-bed region, ergo its process understanding is vice versa.

Sediment Entrainment. Next, the above findings were applied to the entrainment mechanism of single particles in rough bed flows. In contrast to similar experimental studies of Hofland (2005) and Cameron (2006), in the present study the entrainment of single particles was not considered explicitly. However, the new findings concerning typical pressure-fields connected with a large-scale flow structure give a useful means to confirm and to supplement their entrainment models.

The experiments of Cameron indicate that particle entrainment at rough bed flow is typically associated with periods of high streamwise velocity and downwards-directed vertical velocity (*i.e.* sweep flow events). Initially, this is in excellent agreement with the findings of Hofland. However, during the initial movement Hofland often found a small-scale ejection event ($u' < 0, v' > 0$) nestling between the large-scale sweep structures – in contrast to his own observations of a typical, normal near-bed sweep that caused no particle movement. Usually, the embedded small-scale event is connected to the presence of a spanwise clockwise rotating vortex. In this, the target stone gets an initial lift and the exposed area is increased, such that the stone is moved more easily by the streamwise drag. Within the experiments of Cameron, this embedded structure was never recognized during particle entrainment. The apparent difference might be attributed to the different particle shapes (crushed rock for Hofland and spheres for Cameron) that led to different near-bed turbulence properties. Another reason might be that in the latter’s experiments the spheres were exposed throughout. Thus, an initial lift to the particle was less important than in Hofland’s experiments.

The reconstructed bed-pressure fields provided in the present study indicate that the bed is generally subjected to an up-lift when a normal near-bed sweep is dominating the flow. Thus, an additional second lift related to a vertical upward velocity is not necessarily required to raise a particle such that it can be moved away. This might have been the case in Cameron’s experiments. However, the present measurements showed that essential pressure drops typically are accompanied by intense small-scale fluctuations (compare the 40 Hz and the 2125 Hz data in fig. 4.24 and fig. 4.25). The fluctuations might be due to eddy shedding or due to vortices in the inclined shear layer. These fluctuations might have been more prominent in Hofland’s experiments.

Consequently, the present study corroborates the results from both Hofland and Cameron. The consensus is that: coherent flow structures in the sense of sweep events are the driving impacts on a (gravel) bed. They induce a sharp change between a downward lift to an upward lift at the bed. Exceptional intense events with high magnitude – eventually combined with small-scale spanwise rotating eddies – are seen to be the cause of particle entrainment.

Potential of Numerical Simulations. Numerical calculations provide much more spatial information than physical measurements, especially in the interstices of the grain texture. Thus, in general numerical simulations have a high capability of refining the process of understanding the onset of sediment motion.

Several numerical studies describing coherent flow structures above rough (permeable) beds have been published recently (*e.g.* Stösser *et al.*, 2005; Flores & Jiménez, 2006; Singh *et al.*, 2007). However, a typical mechanism of flow-bed interaction that leads or might lead to the entrainment of individual particles was not revealed clearly. The progress suffers from several shortcomings: (1) Long term statistics are hard to achieve, as adequate numerical simulations like LES or DNS typically last only a few seconds – limited by the computational power. However, any coherent features are difficult to identify without the possibility of resorting to conditional averaging methods. (2) Numerical simulations are generally performed at lower Reynolds-numbers that barely resemble natural flow conditions at streambeds. (3) The adequate discretization of complex boundaries like spheres or pebbles is difficult. If the spatial resolution is too coarse the reduction leads to an inaccurate flow field and to non-physical contact forces between the particles. However, a finer resolution also increases the needed computational power. (4) An ambitious challenge is the simulation of the particle motion by avoiding additional modeling. To the knowledge of the author, up to now only one study focussed on that topic: Uhlmann & Fröhlich (2007) resolved not only the flow field but also the particles directly and thus yielded the instantaneous forces on the particles. Despite some shortcomings especially in the last-mentioned points (1) and (2), their studies show the high potential of numerical studies for gaining insight into the details of the local flow field as well as the particle forces and the particle motion.

Consequently, numerical simulation is capable for gaining detailed insight into the local, instantaneous flow field and the forces on single particles; whereas physical experiments are capable of gaining a broader view to coherent structures, general entrainment mechanisms and transport by long term statistics.

5 Application: Washout of Fine Sediments

***Abstract.** This chapter shows how turbulence can act to clean fine sediment from the pores of a stable gravel layer. The findings in §4.3.3 concerning the exponential distribution of the bed-pressure fluctuations are used to estimate the depth within a porous gravel bed from which fine sediment of a given size can be removed. The coarsest grain size of the fine sediment that might be washed out is of $\mathcal{O}(10^{-1})$ in relation to both the gravel grain size and the equivalent sand roughness. A higher equivalent sand roughness results in a larger absolute cleaning depth, whereas the averaged gravel grain size is seen to be less important. The results are successfully tested for plausibility against the grain size distributions of an armored gravel bed and its underlying bimodal layer as found in situ in the river Rhine. However, qualitative and quantitative experimental data for an in-depth validation are missing. The basic ideas and developments for the following approach are due to Prof. Gary Parker, University of Illinois.*

5.1 Problem Description

Flash floods are a means that are used frequently to clean stream beds whose original flow rate is reduced artificially *e.g.* due to dams for hydropower plants or navigation bypasses. To generate a flash flood, the flow rate is increased for a short time. A better ecological diversification is stimulated by the main effect: a wash out of finer material without a severe erosion of the bed. In this, the pore volume in the hyporrheic interstice is increased. Afterwards the discharge is adjusted back again to the low level flow rate. Typically, these man-made floods are dimensioned by empirical observations. However, (semi-)analytical design rules are rare.

If a gravel layer is subjected to a flow that is below the threshold of moving the gravel, turbulence acts to 'clean' fine sediment from the pores of this stable gravel layer. In §4.3.3 the exponential decay of pressure fluctuations within a porous bed was described. The formulation of eq. 4.22 offers a means of estimating the depth within the gravel from which fine sediment of a given size can be removed by turbulence.

5.2 Cleaning Fine Sediment from Gravel

Fig. 5.1 illustrates an idealized bed of gravel that underlies turbulent open-channel flow. Let the gravel size distribution be approximately uniform, with a relation of the grain size percentiles of $d_{85}/d_{15} < 3$. Then, the averaged characteristic size of the gravel $d \approx d_{50}$ and

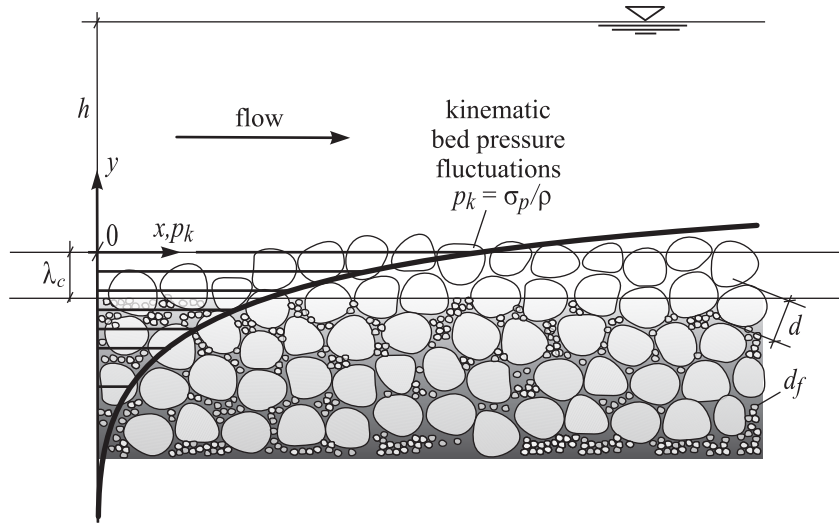


Figure 5.1: Bed pressure fluctuations p_k in a porous gravel bed underlying turbulent open-channel flow. The gravel is of approximately uniform size, the pores are filled with fine sediment. The cleaning depth due the influence of turbulence is denoted by λ_c .

the equivalent sand roughness k_s are related typically by $d = 0.5 - 3 k_s$. The flow over the bed is approximated as steady and uniform, so that boundary shear stress τ_o and shear velocity u_* are given by eqs 2.9 and 2.15 (§2.2). If the flow is in the hydraulically rough range, the vertical profile of the mean velocity then satisfies a universal relation given in eq. 2.16. The upward co-ordinate y has its origin slightly below the top of the gravel layer, *e.g.* as 'felt' by an extrapolation of the log-law (eq. 2.16). However, if the bed is porous, the flow velocity does not vanish at $y = 0$, but instead decays exponentially towards a seepage flow as $y \rightarrow -\infty$.

The vertical profile of the measured bed-pressure fluctuations σ_p was described reasonably well by an exponential fit as given in eq. 4.22. Fig. 5.1 illustrates this exponential decay of the pressure fluctuations, which are hereinafter denoted in their kinematic form as

$$p_k = \sigma_p / \rho . \quad (5.1)$$

A rearrangement of eqs 4.22 and 5.1 gives

$$p_k = A_p u_*^2 \exp \left(\frac{y}{k_s/2.0} \right) , \quad (5.2)$$

with $A_p = 2.88$. The denominator $k_s/2.0$ can be interpreted as an exponential-folding depth of penetration of the fluctuations. In the following, eq. 5.2 is used to estimate λ_c , the depth of cleaning a stream bed with characteristic size d from fine material (sand or silt) of a given size d_f . The wash-out is promoted by pressure fluctuations associated with flow that is below the threshold of motion of the gravel framework. It is assumed here that if the fine sediment can be suspended within the gravel layer, and if there is no replacement of this fine sediment from upstream, the fine sediment is gradually depleted

and washed downstream.

Let the pores of the gravel bed contain fine sediment with size d_f . Their corresponding fall velocity is v_f and $d_f \ll d$. The following approximate constraint after Bagnold (1966) is often used to characterize the threshold of significant suspension at the bed:

$$u_* = v_f . \quad (5.3)$$

Here, u_* serves as a surrogate for the intensity of the near-bed turbulence $-\overline{u'_i u'_j}$ ($i, j = 1, 2, 3$). Another equally appropriate surrogate is $p_k(0)$, where according to eq. 5.2

$$p_k(0) = A_p u_*^2 . \quad (5.4)$$

Casting eq. 5.3 in terms of $p_k(0)$ yields the following threshold condition for significant suspension at the bed:

$$p_k(0) = A_p v_f^2 . \quad (5.5)$$

The relation given by eq. 5.5 is now extended for conditions below the bed in accordance with eq. 5.2. Note that v_f refers to a certain d_f , whereas u_* is constant for one flow condition. In order to suspend sediment at a depth y below the bed surface, $p_k(y)$ must be at least as large as

$$\begin{aligned} p_k(y) &= A_p u_*^2 \exp\left(\frac{y}{k_s/2.0}\right) \\ &= A_p v_f^2 . \end{aligned} \quad (5.6)$$

The depth $y = \lambda_c$ at which the above relation is satisfied for a given fine sediment with fall velocity v_f represents the potential thickness of the layer that can be cleaned of fine sediment by turbulence. Thus from eq. 5.6,

$$\frac{\lambda_c}{k_s} = -1.0 \ln\left(\frac{u_*}{v_f}\right) . \quad (5.7)$$

To reduce eq. 5.7, both the gravel and fine sediment are assumed to have the same material density ρ_s . With the fluid density denoted by ρ , the submerged specific gravity Δ reads

$$\Delta = \rho_s/\rho - 1 \quad (5.8)$$

The dimensionless shear stress Θ characterizing the potential for gravel mobility was defined in eq. 2.36. By using eqs 2.15 and 5.8, Θ can be rewritten to

$$\Theta = \frac{u_*^2}{\Delta g d} . \quad (5.9)$$

5 Application: Washout of Fine Sediments

Thus, a fractional extension of eq. 5.3 by $\sqrt{\Delta g d_f d} / \sqrt{\Delta g d_f d}$ yields

$$\begin{aligned} \frac{u_*}{v_f} &= \frac{u_*}{\sqrt{\Delta g d}} \frac{\sqrt{\Delta g d_f}}{v_f} \sqrt{\frac{d}{d_f}} \\ &= \sqrt{\frac{\Theta}{\text{Fr}_{f\Delta}}} \sqrt{\frac{d}{d_f}}, \end{aligned} \quad (5.10)$$

where

$$\text{Fr}_{f\Delta} = \left(\frac{v_f}{\sqrt{\Delta g d}} \right)^2 \quad (5.11)$$

denotes the Froude-number for the fall velocity of fine sediment. Dietrich (1982) specified the following relation for fall velocity of natural sediment that

$$\text{Fr}_{f\Delta} = \left(\exp\left(-b_1 + b_2 \ln(\text{Re}_{f\Delta}) - b_3 \ln^2(\text{Re}_{f\Delta}) - b_4 \ln^3(\text{Re}_{f\Delta}) + b_5 \ln^4(\text{Re}_{f\Delta})\right) \right)^2, \quad (5.12)$$

where ν denotes the kinematic viscosity of water, and $\text{Re}_{f\Delta}$ denotes a particle Reynolds number for the fine sediment, defined as

$$\text{Re}_{f\Delta} = \frac{\sqrt{\Delta g d_f} d_f}{\nu}. \quad (5.13)$$

The coefficients b_i are given by

$$b = [2.891, 0.953, 5.68 \cdot 10^{-2}, 2.89 \cdot 10^{-3}, 2.45 \cdot 10^{-4}]. \quad (5.14)$$

Furthermore, flow conditions are assumed to be somewhat below the threshold of motion of gravel. Parker *et al.* (2003) offer the following adjusted version of the Shields criterion for the onset of motion of gravel (recall §2.7.3), in which Θ_c denotes the threshold of motion for the gravel and $\text{Re}_{d\Delta}$ denotes a particle Reynolds number for gravel size d , defined as

$$\text{Re}_{d\Delta} = \frac{\sqrt{\Delta g d} d}{\nu}. \quad (5.15)$$

With this, the estimation reads

$$\Theta_c = 0.5 \left(0.22 \text{Re}_{d\Delta}^{-0.6} + 0.06 \cdot 10^{(-7.7 \text{Re}_{d\Delta}^{-0.6})} \right). \quad (5.16)$$

The actual flow is assumed to satisfy the condition

$$\Theta = k_c \Theta_c, \quad (5.17)$$

where $k_c < 1$ in order for the flow to be below the threshold of motion for the gravel.

In reducing eq. 5.7 with eqs 5.10 and 5.17, the cleaning depth λ_c now can be written as

$$\frac{\lambda_c}{k_s} = -0.5 \ln \left(\frac{k_c \Theta_c (\text{Re}_{d\Delta}) d}{\text{Fr}_{f\Delta} (\text{Re}_{f\Delta}) d_f} \right). \quad (5.18)$$

The parentheses in $\Theta_c(\text{Re}_{d\Delta})$ and $\text{Fr}_{f\Delta}(\text{Re}_{f\Delta})$ refer to the relevant functional relations eqs 5.16 and 5.12, respectively.

5.3 Implementation and Discussion

Eq. 5.18 was tested by its plausibility. Fig. 5.2 illustrates the results. The calculations are based on the geometrical parameters for two bed materials that were used in the experiments (tables 3.1 and 4.2): the uniform gravel (#uni, fig. 5.2(a)) and the gravel excavated in the river Rhine (#rhi, fig. 5.2(b)). The relevant parameters for eq. 5.18 concerning the omitted third bed material (spheres, #sph) are similar to the armor layer material from the Rhine. The calculation was made with sizes of $d_f > 0.05$ mm according to the transition from coarse silt to fine sand, where cohesive clustering/agglomeration effects are assumed to be insignificant in a first approximation.

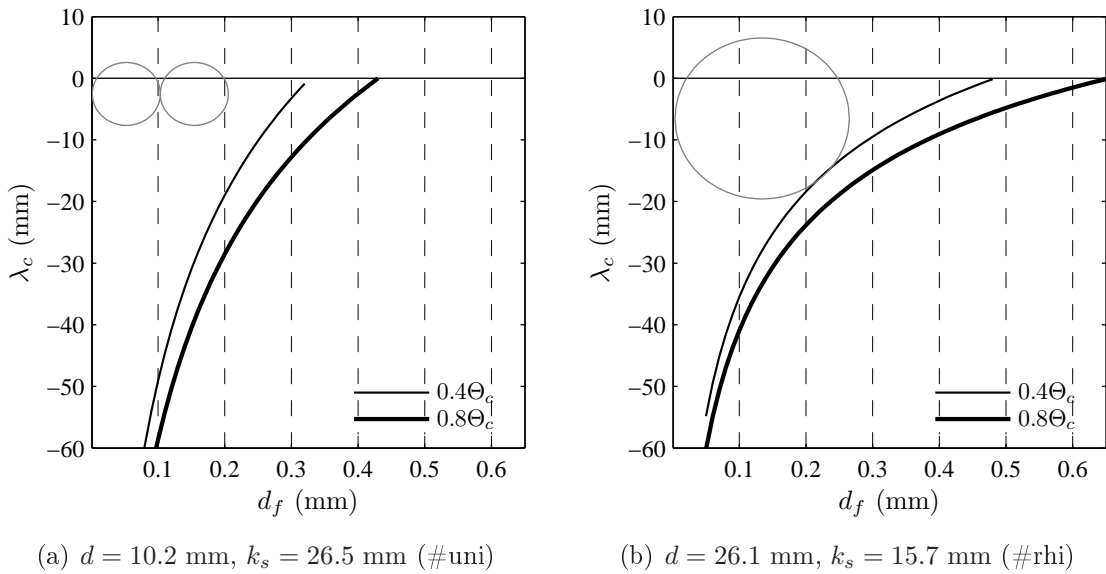


Figure 5.2: Cleaning depth λ_c for two different types of gravel bed, estimated from eq. 5.18. The circles sketch the reference grain size d in dimensions of the vertical axis. (a) Uniform gravel. (b) Rhine Gravel, armored layer.

Tests were made by adopting a hydrodynamic load of 0.4 and 0.8 Θ_c . For the latter, the coarsest size that can be suspended by the flow is computed to be 0.45 mm for #uni and 0.65 mm for #rhi, respectively. The resulting geometrical ratios d_f/d and d_f/k_s are both in a range of 2-4%. However, a quantitative analysis for results at $y/d > -0.5$ is misleading, because the applicability of eq. 5.18 is elusive. The reason is given as follows: The exponential-folding depth of $k_s/2$ (denominator in eq. 5.2) was taken from eq. 4.22 as a result of a least square fit to the measured lift fluctuations σ_L for $y/d < 1$ (#uni). The experimental data showed in turn that the drag fluctuation σ_D equals σ_L only for d_f at $y/d < -0.5$. However, above this value σ_D is larger than σ_L , *e.g.* $2\sigma_L \approx \sigma_D$ holds at $y = 0$. Therefore eq. 5.18 underestimates the influence of the fluctuating pressure. Consequently, the coarsest size that is able to be washed out by the flow can be expected to be bigger than the calculated size. A closer look at the calculated cleaning depths in fig. 5.2 helps to evaluate this underestimation: For half the hydrodynamic load, 0.4 Θ_c , the coarsest sizes of d_f are only slightly smaller, here by approximately 25%. Thus, the intensity of the

5 Application: Washout of Fine Sediments

hydrodynamic load seems to be of minor importance. In a first approximation, a change of the hydrodynamic load can be assumed to be linear-proportional to the intensity of pressure fluctuations. Consequently, rules of thumb for the coarsest size that can be suspended might be given by

$$d_f/k_s < \mathcal{O}(10^{-1}) \quad (5.19a)$$

$$d_f/d < \mathcal{O}(10^{-1}) . \quad (5.19b)$$

A rough confirmation of the above relations can be inferred from the grain size distributions of the armor layer and the grain size distribution of the underlying bed material as found in situ for #rhi (see §3.5). The armor layer has a thickness of $(1-2)d$, and 98% of the weight of the grains is > 4 mm in diameter. Smaller fractions are washed out almost completely. Thus, a ratio of $d_f/d < 4/26.1 = 15\%$ holds, which corroborates eq. 5.19b. The distribution for the underlying bed material is bimodal, with centers for the finer material between $0.2 \text{ mm} < d_f < 0.5 \text{ mm}$ for $\sim 13\%$ of the weight and for coarser material between $4 \text{ mm} < d < 40 \text{ mm}$ for $\sim 80\%$ of the weight. This confirms two further aspects: the assumption of $d_f \ll d$ is applicable and the sizes of the finer material that are washed out within the first $(1-2)d$ are in the range of submillimeters (see fig. 5.2).

Generally, the profiles in fig. 5.2(a) for #uni are steeper than the profiles in fig. 5.2(b) for #rhi, which results in a larger absolute cleaning depth λ_c for the former. Whereas grain sizes of *e.g.* $d_f = 0.1$ mm are calculated to be washed out up to $\lambda_c > -60$ mm for the material of #uni, the same size of d_f for the material #rhi is estimated to be depleted from not deeper than $\lambda_c > -40$ mm. Considering the geometrical parameters used in eq. 5.18, an adequate scaling can be found by λ_c/k_s , as the ratio is in tendency similar for both materials ($\lambda_c/k_s = 2.3$ for #uni and 2.5 for #rhi). In opposite to this, the ratio λ_c/d differs by a factor of ($\lambda_c/d = 5.9$ for #uni and 1.5 for #rhi). Here, d is unsuitable for scaling. To sum up, a higher k_s results in a larger absolute cleaning depth λ_c , whereas the averaged gravel grain size d is less important.

However, eq. 5.18 is suffering from a general inadequacy. Pore blocking effects due to smaller gravel grains or sorted finer material were disregarded. Therefore, the vertical extension of the cleaning depth λ_c for a stream bed with natural grain size distribution will be overestimated by eq. 5.18. Unfortunately, quantitative experimental data to validate and/or improve eq. 5.18 do not exist.

6 Summary and Recommendations

6.1 Summary

This thesis aims to improve the fundamental understanding of the flow-sediment interaction at non-moving streambeds. The focus is aimed at the hydrodynamical processes that occur above and within rough porous beds underlying turbulent open-channel flow. Laboratory measurements and their detailed analysis are the core of this work. The hydrodynamics of open-channel flow, interstitial pore flow, and especially their interaction were investigated in a physical flume experiment. Measurements were carried out by an array of up to 16 miniaturized piezo-resistive pressure sensors within the bed and slightly above it, a 2D particle image velocimetry system measuring in streamwise vertical or horizontal planes, and a 1D acoustic Doppler current profiler. Three different types of bed material were laid and investigated underlying turbulent open-channel flow so that natural streambed conditions were simulated in full-scale. The examined flow conditions include a broad diversity of hydrodynamic loads and roughness parameters as can be found in natural, non-moving gravel beds.

In a streamwise vertical plane, large-scale wedge-like flow structures were observed where – in the sense of a sweep event – a zone of faster fluid over-rolled a zone with slower fluid. The resulting shear layer inclined at an angle of 10-20° to the bed, densely populated with clockwise rotating eddies. On average, this mechanism occurred with sufficient frequency and shape to leave an imprint on the statistics of the flow. Typically, this flow pattern formed near the bed, approximately scaling with the logarithmic layer. However, the biggest structures had the capability to spread over the whole water depth. In a horizontal near-bed view, macroturbulent structures formed a patched chessboard with regions of lower and higher velocity zones that were elongated in the streamwise direction. Their lateral extension was typically 2-3 times the equivalent sand roughness and increased linearly with distance from the bed. The length of these elongated structures reached up to the order of several water depths. These structural findings concerning coherent flow structures are consistent with models originally developed for smooth wall flows and they support the observations made in rough bed flume experiments, numerical simulations, and natural rivers as well. However, for the first time they have been studied in-depth by image processing techniques in both streamwise vertical and horizontal near-bed views, conducted in water flume experiments over porous gravel beds. Speculations are made about a structural flow mechanism similar to Adrian's model for smooth-wall flows (Adrian *et al.*, 2000b, Tomkins & Adrian, 2003). Differences are that: the suggested genesis originates from, and is dominated by, sweeps from the outer flow that influence the near-bed region, whereas it is vice versa in Adrian's sense.

Fields of bed-pressure fluctuations were reconstructed by applying Taylor's frozen tur-

6 Summary and Recommendations

bulence hypothesis on data obtained by an array of pressure sensors. By conditional sampling of marked pressure drop events to the synchronously recorded velocity fields, a significant bed destabilizing flow-pressure pattern was identified: If high speed fluid in the wake of a large-scale wedge-like flow structure reaches the vicinity of the bed, a phenomenon akin to a Bernoulli-effect leads to a distinctive low-pressure field. A force balance considering buoyancy and neglecting friction and inertia showed that the resulting force is able to give an initial lift to a single grain. In this fashion, the exposed area of the grain as well as its angle of repose is increased such that entrainment by the fast fluid zone becomes possible. Furthermore, this flow-pressure pattern can be seen as the fundamental promoter for the exchange of mass and momentum from the free stream to the hyporrheic interstice and vice versa – a pivotal factor for the ecological equilibrium of the whole aquatic system.

Point measurements of pressure fluctuations showed that the intensity of turbulent pressure fluctuations decays exponentially in the porous bed. An empirical data fit formulation was used to estimate the depth within a porous gravel bed from which fine sediment of a given size could be removed. The coarsest grain size of the fine sediment that might be washed out was of $\mathcal{O}(10^{-1})$ in relation to both the gravel grain size and the equivalent sand roughness. A higher equivalent sand roughness resulted in a larger absolute cleaning depth, whereas the averaged gravel grain size revealed to be less important. The results were successfully tested for plausibility against the grain size distributions of an armored gravel bed and its underlying bimodal layer as found in situ in the river Rhine. Thus, a tool is given to estimate the morphological and in turn ecological efficiency of flash floods downstream of water power plants.

6.2 Recommendations for further studies

Sediment cleaner. Within this thesis, a formula was developed which estimates the wash-out efficiency of flash floods. However, experimental data for an in-depth validation were not available. These data can be gained by simple flume experiments, where the bed consists of a bimodal material of gravel and fine sand. If the fine sand is colored differently from the gravel, image processing techniques can be used to determine the cleaning depth after the bed has been exposed to open-channel flow up to the incipient motion of single gravel grains.

Pressure measurements. In recent years, much research has been done to gain insight into the velocity regime of rough bed flows. Pressure measurements were considered with less interest, although they had given a direct insight into the loads due to the flow. In this study, it has been shown that especially piezo-resistive pressure sensors give a powerful tool to observe the turbulent forces at the water-sediment interface. Further studies especially in the fields of rough bed flow and sediment transport should focus on using these sensor techniques. A miniaturization up to diameter less than 5 mm seems to be possible. Furthermore, these techniques can be used in field experiments, as it has been shown lately by Smart & Habersack (2007).

Velocity measurements. Within this study, a 2D PIV system was used to resolve the relevant flow scales and structures in a streamwise vertical plane and in several horizontal planes near a stable bed. However, the frame size had to be reduced to increase the frame rate for an appropriate resolution in time. Nowadays faster 2D or quasi 3D PIV high speed systems are available. Thus it is possible to observe simultaneously both the near-bed flow structures and the large-scale flow structures that extend over the whole flow depth. Furthermore, it would be interesting to obtain velocity information in a transversal-vertical plane to study the streaky nature of near-bed flow and its assumed meandering or rotating character. If recordings were made in a horizontal layer slightly above a moving bed, the sediment transport rate and the velocity could be studied from the same data set.

Numerical simulations. Besides physical experiments, in recent years numerical investigations have become a powerful tool to study rough bed flows. Especially the use of large eddy simulation (LES) is capable of providing pressure and velocity fields with a high resolution in space and time in flows at realistic Reynolds-numbers and feasible use of computer power. Thus, access is given to flow regions that are hardly observable in physical experiments, and a refined process-understanding is possible. However, both the strengths of advanced numerical simulation techniques and laboratory experimentation have to be combined to significantly improve the understanding of the physical processes involved in the erosion and near-bed transport of sediments. A conceptual framework for designing better tools to predict sediment erosion and transport in engineering applications should be as follows: The first goal must be to formulate a general transport model including the real physics – in opposite to the models built up on the classical approach of Shields. Recently, numerical studies were published that show the valuable potential of numerical simulations to gain a detailed view of coherent structures (*e.g.* Stösser *et al.*, 2007), particle forces (Singh *et al.*, 2007) and particle motion without modeling (Uhlmann & Fröhlich, 2007). In combination with the findings of Hofland (2005), Cameron (2006), and this thesis, these results are very promising on the way to develop a new physically-based formulation for predictive relationships. Once this new conceptual transport model is developed, it has to be implemented into a simplified 2D or 1D numerical approach, ideally with modeling the shape of single particles as 1D mass centroids or as two-phase flow (*e.g.* Marchioli *et al.*, 2006). In this, a physically-founded tool with minimal scatter between prediction and actual morphodynamic development will be given that will be used in practical engineering applications.

Notation

Roman symbols

A	area, or PIV setup A
a	empirical constant (various uses)
B	width of flume, or PIV setup B
b	empirical constant (various uses)
b_ξ	width of ultrasonic beam
C	empirical constant (various uses)
C_D	drag coefficient
C_L	lift coefficient
C_{xy}	cross correlation of x and y
c	sound velocity
D	drag indicator in units of pressure (fig. 4.16), or empirical constant (various uses)
Da	Darcy number ($K/(h + h_p)^2$)
D_{tv}	turbulent and viscous diffusion terms
d	characteristic grain diameter ($= \sum_{i=1}^n d_i \Delta p_i$)
d_f	effective pore diameter (\sqrt{K}), or diameter of fine sediment
d_i	grain size quantiles of $i\%$ sieve screening
d_n	nominal grain diameter ($= \sqrt[3]{(m/\rho_s)}$)
e	$= 2.71828\dots$
F_D	drag force
F_G	gravitational force
F_L	lift force
F_o	total fluid force
F_b	friction force at the bed
F_c	contact force between two grains
F_s	friction force at the side walls
f	frequency
f_D	Doppler frequency

6 Summary and Recommendations

f_e	emitting frequency
Fr_h	bulk Froude number ($= U^2/(gh)$)
$Fr_{*\Delta}$	densimetric Froude number ($= u_*^2/(\Delta gd)$)
G	turbulent energy generation ($= -\overline{u'v'}\partial\langle\bar{u}\rangle/\partial y$) or gravity force
G'	buoyancy corrected weight
g	gravitational acceleration
h	water depth
I_1, I_2	image intensity of the first and second interrogation cell
i, j	integer numbers or dummy variable
ι, j	integer numbers used in Einstein notations ($= [1, 2, 3]$)
K	porous medium permeability ($= \nu k_f/g$)
k	wave number
k_E	turbulent kinetic energy
k_f	permeability coefficient
k_N	diameter of a filter kernel
k_s	equivalent sand roughness after Nikuradse
L	lift indicator in units of pressure (fig. 4.16), or length (of flume or wave)
m	mass (of a pebble etc.)
n	integer number
P	probability, or wetted perimeter (<i>e.g.</i> in rectangular channels $= b + 2h$)
p	pressure
p_k	pressure fluctuations in kinematic units ($= \sigma_p/\rho$)
S_b	bed slope
S_{int}	roughness-fluid surface interface
S_{xx}	auto spectra of x
Q	flow rate
R^2	coefficient of determination (statistic tool)
R_h	hydraulic radius ($= A/P$)
Re_h	bulk Reynolds number ($= Uh/\nu$)
Re_{*d}	grain Reynolds number ($= u_*d/\nu$)
$Re_{d\Delta}$	densimetric particle Reynolds number ($= \sqrt{(\Delta gd)d}/\nu$)
$Re_{*\delta}$	boundary layers Reynolds number ($= u_*\delta/\nu$)
t	time
U	bulk velocity ($= Q/(Bh)$)
u	streamwise velocity
u_b	near-bed velocity
U_c	bulk convection velocity

u_f	effective velocity within the pores ($\langle \bar{u}_f \rangle = \langle \bar{u} \rangle / \phi$)
u_*	shear velocity ($= \sqrt{\tau_o / \rho}$)
u_{*b}	shear velocity at the bed ($= \sqrt{\tau_b / \rho}$)
u_{*w}	shear velocity at the wall ($= \sqrt{\tau_w / \rho}$)
V_o	total volume
V_f	volume of fluid
v	upward velocity
v_f	fall velocity of fine sediment
w	transverse velocity
x	coordinate in streamwise flow direction
Y	$= y / y(\sigma_{u, \max})$
y	vertical coordinate, zero crossing gained by extrapolating the log-law
y_R	vertical coordinate for the roughness layer
y_t	vertical coordinate, zero crossing at the roughness tops
z	transverse coordinate

Greek symbols

α	empirical constant (various uses)
β	momentum non-uniformity parameter ($= (U^2 h)^{-1} \int (\bar{u}^2 + \overline{u'^2}) dh$)
γ	specific weight, or spreading angle of the acoustic far-field of an ultrasonic beam
Δ	specific submerged density of stone ($= \rho_s / \rho - 1$)
δ	boundary layer thickness, or channel half width
δ_R	roughness layer thickness
δ_{HB}	non-centrality parameter ($= u_b / \sigma_{u_b}$)
η	Kolmogorov length scale
ϵ	exposure, or total turbulent dissipation
ϕ	roughness geometry function ($= V_f / V_o$, with $1 \geq \phi \geq 0$)
φ	pivoting angle
κ	von Kármán constant
λ_c	cleaning depth of gravel in y
λ_{ci}^2	swirling strength
λ_x	mean extension of coherent structures in x
ν	kinematic viscosity
Π	protrusion of particle above mean level, or Coles' wake strenght parameter ($\approx 0.15-0.30$ for open-channel flow)
π	$= 3.14159\dots$
ρ	density of water

6 Summary and Recommendations

ρ_s	density of stone
σ_D	standard deviation of the drag indicating signal D (fig. 4.16)
σ_L	standard deviation of the lift indicating signal L (fig. 4.16)
σ_x	standard deviation of x ,
Θ	Shields parameter ($\equiv \text{Fr}_{*\Delta}$)
Θ_c	critical Shields parameter ($= f(\text{Re}_{*d})$)
θ	angle of the ultrasonic beam axis against the streamwise flow direction
θ_m	momentum thickness
τ	shear stress
τ_o	boundary shear stress
τ_b	bed shear stress
τ_c	critical shear stress
ω	angular frequency, or empirical wake function
ξ	coordinate of ultrasonic beam

Mathematics

$\exp(x)$	$= e^x$
$f(x)$	function of x
$\ln(x)$	natural logarithm of x
$\log(x)$	common logarithm of x
$\mathcal{O}(x)$	in the order of x
$ x $	absolute value of x
\vec{x}	x as vector
\bar{x}	temporal average of x
$\langle x \rangle$	spatial average of x
x'	temporal fluctuating part of x
\tilde{x}	spatial fluctuating part of x
x_{\max}	maximum of x
x_{\min}	minimum of x
Δx	difference between two values of x
∇	nabla-operator ($= (\partial/\partial x, \partial/\partial y, \partial/\partial z)$ in 3D)

Abbreviations

AD	analog-digital
ADCP	acoustic Doppler current profiler
AOI	area of interest
AS	Aktiv Sensor GmbH, Berlin, Germany
CCD	charge-coupled device
DNS	direct numerical simulation

6.2 Recommendations for further studies

FIR	finite impulse response (digital filter)
GHJ	Prof. Gerhard H. Jirka, Ph.D.
HVP	hairpin-vortex package
IBM	Immersed Boundary Method
IfH	Institute for Hydromechanics, University of Karlsruhe
LES	large eddy simulation
LSB	least significant bit
MPPS	miniaturized piezoresistive pressure sensor
PCO	PCO AG, manufacturer of specialized cameras, Kelheim, Germany
PDF	probability density functions
PIV	particle image velocimetry
PSP	pressure sensitive paint
PTV	particle tracking velocimetry
RAID	redundant array of independent disks
RANS	Reynolds-averaged Navier-Stokes equations
TTL	transistor-transistor logic
TTL	turbulence wall pressure
2D	two-dimensional
3D	three-dimensional

Bibliography

- ABERLE, J. & NIKORA, V. I. 2006 Statistical properties of armored gravel bed surfaces. *Water Resources Research* **42**, 1–11.
- ADRIAN, R. J. 1991 Particle-imaging techniques for experimental fluid mechanics. *Annual Review of Fluid Mechanics* **23**, 261–304.
- ADRIAN, R. J. 2007 Hairpin vortex organization in wall turbulence. *Physics of Fluids* **19**, 1–16.
- ADRIAN, R. J., CHRISTENSEN, K. T. & LIU, Z. C. 2000*a* Analysis and interpretation of instantaneous turbulent velocity fields. *Experiments in Fluids* **29**, 275–290.
- ADRIAN, R. J., MEINHART, C. D. & TOMKINS, C. D. 2000*b* Vortex organization in the outer region of the turbulent boundary layer. *Journal of Fluid Mechanics* **422**, 1–54.
- ANDREWS, E. D. & SMITH, J. D. 1992 A theoretical model for calculating marginal bedload transport. In *Gravel-Bed Rivers 3* (ed. R. D. Hey, C. R. Thorne & P. Billi), pp. 267–281. Wiley and Sons, New York.
- ARCALAR, M. S. & SMITH, J. D. 1987 A study of hairpin vortices in a laminar boundary layer. Part 1. Hairpin vortices generated by a hemisphere protuberance. *Journal of Fluid Mechanics* **175**, 1–41.
- BAGNOLD, R. A. 1941 *The physics of blown sand and desert dunes*. Methuen, London.
- BAGNOLD, R. A. 1966 An approach to the sediment transport problem from general physics. *US Geol. Survey Prof. Paper, Washington, D.C.* **422-I** (964), 235–297.
- BEZZOLA, G. R. 2002 Fließwiderstand und Sohlenstabilität natürlicher Gerinne. Ph.D., VAW ETH Zürich.
- BLAKE, W. K. 1970 Turbulent boundary-layer wall-pressure fluctuations on smooth and rough walls. *Journal of Fluid Mechanics* **44** (4), 637–660.
- BOWEN, L. & RADIN, C. 2003 Packing of equal spheres in hyperbolic space. *Discrete & Computational Geometry* **29**, 23–39.
- BREUGEM, W.P., BOERSMA, B. J. & UITTENBOGAARD, R. E. 2006 The influence of wall permeability on turbulent channel flow. *Journal of Fluid Mechanics* **562**, 35–72.

Bibliography

- BREUGEM, W. P. 2005 The influence of wall permeability on laminar and turbulent flows. Ph.D., TU Delft.
- BUFFIN-BÉLANGER, J. M. & ROY, A. 2005 1 min in the life of a river: selecting the optimal record length for the measurement of turbulence in fluvial boundary layers. *Geomorphologie* **68**, 77–94.
- BUFFIN-BÉLANGER, T., ROY, A. & KIRKBRIDE, A. D. 2000 On large-scale flow structures in a gravel-bed river. *Geomorphology* **32**, 417–435.
- BUFFINGTON, J. M. 1999 The legend of A. F. Shields. *Journal of Hydraulic Engineering* **125** (4), 376–387.
- BUFFINGTON, J. M. & MONTGOMERY, D. R. 1997 A systematic analysis of eight decades of incipient motion studies, with special reference to gravel-bedded rivers. *Water Resources Research* **33** (8), 1993–2029.
- CAMERON, S. M. 2006 Near-boundary flow structure and particle entrainment. Ph.D., University of Auckland.
- CAMERON, S. M., COLEMAN, S. E., MELVILLE, B. W. & NIKORA, V. I. 2006 Marbles in oil, just like a river? In *River Flow 2006* (ed. R. Ferreira, E. Alves, J. Leal & A. Cardoso). Tay. & Fra. Group.
- CARLING, P.A. KELSEY, A. & GLAISTER, M.S. 1992 Effect of bed roughness, particle shape and orientation on initial motion criteria. In *Gravel-Bed Rivers 3* (ed. R. D. Hey, C. R. Thorne & P. Billi), p. 23–40. Wiley and Sons, New York.
- CAROLLO, F. G., FERRO, V. & TERMINI, D. 2005 Analyzing turbulence intensity in gravel bed channels. *Journal of Hydraulic Engineering* **131** (12), 1050–1061.
- CHAN, H. C., LEU, J. M., LAI, C. J. & JIA, Y. 2007 Turbulent flow over a channel with fluid-saturated porous bed. *Journal of Hydraulic Engineering* **133** (6), 610–617.
- CHANG, P. A., PIOMELLI, U. & BLAKE, W. K. 1999 Relationship between wall-pressures and velocity-field sources. *Physics of Fluids A* **11** (11), 3434–3448.
- CHENG, C. M. 1953 On the spectrum of energy in turbulent shear flow. *Journal of Res. Nat. Bui. Standards* **50** (1), 51–62.
- CHENG, E. D. H. & CLYDE, C. G. 1972 Instantaneous hydrodynamic lift and drag forces on large roughness elements in turbulent open-channel flow. In *Sedimentation* (ed. H. W. Shen). Symposium to Honor Prof. H.A. Einstein.
- CHENG, N.-S. & CHUA, L. H. C. 2005 Comparisons of sidewall correction of bed shear stress in opne-channel flows. *Journal of Hydraulic Engineering* **131** (7), 605–609.
- CHEPIL, W.S. 1959 Equilibrium of soil grains at the threshold of movement by wind. *Soil Science Society of America* **23**, 422–428.

- CHIN, C. O. 1985 Stream bed armoring. *School of Engineering, Report, University of Auckland, New Zealand* **No. 272**.
- CHOW, V. T. 1959 *Open-Channel Hydraulics*. McGraw-Hill Book Company, New York.
- CHRISTENSEN, K. T. & ADRIAN, R. J. 2001 Statistical evidence of hairpin vortex packets in wall turbulence. *Journal of Fluid Mechanics* **431**, 433 – 443.
- COLEMAN, S. E., NIKORA, V. I., MCLEAN, S. R. & SCHLICKE, E. 2007 Spatial averaged turbulent flow over square ribs. *Journal of Engineering Mechanics* **133** (2), 194–204.
- COLES, D. 1956 The law of the wake in the turbulent boundary layer. *Journal of Fluid Mechanics* **1** (1), 191–226.
- DEFINA, A. 1996 Transverse spacing of low-speed streaks in a channel flow over a rough bed. In *Coherent Flow Structures in Open Channels* (ed. P.J. Ashworth, S.L. Bennett, J.L. Best & S.J. Mc Lelland). John Wiley & Sons Ltd. England.
- DETERT, M., KLAR, M., WENKA, T. & JIRKA, G.H. 2007 Pressure- and velocity-measurements above and within a porous gravel bed at the threshold of stability. In *Gravel Bed Rivers 6: From Process Understanding to the Restoration of Mountain Rivers* (ed. M. Rinaldi, H. Habersack & H. Piegay). A.A. Balkema, Rotterdam.
- DEY, S. L. & LAMBERT, M. F. 2005 Reynolds stress and bed shear in non-uniform unsteady open-channel flow. *Journal of Hydraulic Engineering* **131** (7), 610–613.
- DIETRICH, E. W. 1982 Settling velocity of natural particles. *Water Resources Research* **6** (18), 1615–1626.
- DITTRICH, A. 1998 Wechselwirkung Morphologie/ Strömung naturnaher Fließgewässer. Habilitation, Universität Karlsruhe (TH).
- DITTRICH, A. & KOLL, K. 2001 Stability of gravel bed rivers based on sieve analysis data. *International Journal of Sediment Research* **16** (2), 194–200.
- DRAKE, T., SHREVE, R., DIETRICH, W., WHITING, P. & LEOPOLD, L. 1988 Bed load transport of fine gravel observed by motion-picture photography. *Journal of Fluid Mechanics* **192**, 193–217.
- VAN DRIEST, E. R. 1956 On turbulent flow near a wall. *J. Aeron. Sci.* **23**, 1007–1011.
- ECKELMANN, H. 1988 A review of knowledge on pressure fluctuations. In *Near Wall Turbulence 1988 Zoran Zaric Memorial Conference* (ed. S. J. Kline & N. H. Afgan), *Proceedings of the International Centre of Heat and Mass Transfer*, vol. 28. Hemisphere Publishing Corporation.
- EINSTEIN, H. A. & EL-SAMNI, E. A. 1949 Hydrodynamic forces on a rough wall. *Reviews of Modern Physics* **21** (3), 520–524.

Bibliography

- EMMERLING, R. 1973 Die momentane Struktur des Wanddruckes einer turbulenten Grenzschichtströmung. In *Mitteilungen aus dem Max-Planck-Institut für Strömungsforschung und der Aerodynamischen Versuchsanstalt* (ed. E.-A. Müller & H. Schlichting). Deutsche Forschungs- und Versuchsanstalt für Luft- und Raumfahrt e.V.
- FARABEE, T. G. & CASARELLA, M. J. 1991 Spectral features of wall pressure fluctuations beneath turbulent boundary layers. *Physics of Fluids A* **3** (10), 2410–2420.
- FENTON, J. D. 2005 On the energy and momentum principles in hydraulics. *Proc. 31st Congress, Int. Assoc. Hydraulic Engng and Res., Seoul, Korea* pp. 625–636, published on CD.
- FENTON, J. D. & ABBOT, J. E. 1977 Initial movement of grains in a stream bed: the effect of relative protrusion. *Proceedings of the Royal Society of London, Series A* **352**, 523–537.
- FLORES, O. & JIMÉNEZ, J. 2006 Effect of wall-boundary disturbances on turbulent channel flows. *Journal of Fluid Mechanics* **566**, 357–376.
- FRANKEN, A., ARIENS, E. & KLATTER, H. 1995 Manual for the design of bed protections behind two-dimensional outflow constructions. *Bowwdienst Rijkswaterstaat BODR-95002*, technical report, in Dutch.
- GARCÍA, M. H., NINO, Y. & LÓPEZ, F. 1996 Laboratory observations of particle entrainment into suspension by turbulent bursting. In *Coherent Flow Structures in Open Channels* (ed. P. J. Ashworth, S. L. Bennett, J. L. Best & S. J. Mc Lelland). John Wiley & Sons Ltd.
- GESSLER, J. 1971 Beginning and ceasing of sediment motion. In *River Mechanics* (ed. H. W. Shen), , vol. 3-7, pp. 1–7. H. W. Shen, Fort Collins, Colorado.
- GILBERT, G. 1914 Transport of debris by running water. In *Prof. Paper 86*. U.S. Geological Survey, Washington.
- GOTOH, T. & ROGALLO, R. S. 1999 Intermittency and scaling of pressure at small. *Journal of Fluid Mechanics* **396**, 257–285.
- GRASS, A.J. & MANSOUR-TEHRANI, M. 1996 Generalized scaling of coherent bursting structures in the near-wall region of turbulent flow over smooth and rough boundaries. In *Coherent Flow Structures in Open Channels* (ed. P. J. Ashworth, S. J. Bennett, J. L. Best & S. J. Mc Lelland). John Wiley & Sons Ltd.
- GRASS, A. J. 1970 Initial instability of fine bed sands. *Journal of the Hydraulics Division, Proceedings of ASCE* **96** (HY3), 619–632.
- GRASS, A. J. 1971 Structural features of turbulent flow over smooth and rough boundaries. *Journal of Fluid Mechanics* **50**, 233–255.

- GRASS, A. J., STUART, R. J. & MANSOUR-TEHRANI, M. 1991 Vortical structures and coherent motion in turbulent flow over smooth and rough boundaries. *Philosophical Transactions of the Royal Society A: Mathematical, Physical & Engineering Sciences* **336**, 36–65.
- GUO, J. & JULIEN, P.-Y. 2005 Shear stress in smooth rectangular open-channel flows. *Journal of Hydraulic Engineering* **131** (1), 30–37.
- GUO, J. & JULIEN, P.-Y. 2008 Application of the modified log-wake law in open-channels. *Journal of Applied Fluid Mechanics* **1** (2), 17–23.
- GYR, A. & MÜLLER, A. 1996 The role of coherent structures in developing bedforms during sediment transport. In *Coherent Flow Structures in Open Channels* (ed. P. J. Ashworth, S. J. Bennet, Ja. L. Best & S. J. Mc Lelland). John Wiley & Sons Ltd.
- HAZEN, A. 1892 Physical properties of sands and gravels with reference to use in filtration. *Report to Mass. State Board of Health* **539**.
- HEAD, M. R. & BANDYOPADHYAY, P. 1981 New aspects of boundary layer structure. *Journal of Fluid Mechanics* **107**, 297–338.
- HINTERBERGER, C. 2004 Dreidimensionale und tiefengemittelte Large-Eddy-Simulation von Flachwasserströmungen. Ph.D., University of Karlsruhe, Institute for Hydromechanics.
- HJULSTRÖM 1935 The morphological activity of rivers as illustrated by river Fyris. *Bulletin of the Geological Institution of the University of Uppsala* **15**, 221–527.
- HOFFMANS, G. J. C. M. & AKKERMAN, G. 1998 Influence of turbulence on stone stability. In *7th International Conference on River Sedimentation*.
- HOFLAND, B. 2005 Rock & Roll. Ph.D., TU Delft, downloadable at: www.library.tudelft.nl → TUDelft publications → Hofland.
- HOFLAND, B. & BATTJES, J.A. 2006 Probability density function of instantaneous drag forces and shear stresses on a bed. *Journal of Hydraulic Engineering* **132** (11), 1169–1175.
- HOFLAND, B. & BOOIJ, R. 2004 Measuring the flow structures that initiate stone movement. In *River Flow 2004* (ed. M. Greco, A. Carravetta & R. Della Morte). A. A. Balkema, Rotterdam.
- HOFLAND, B., BOOIJ, R. & BATTJES, J.A. 2005 Measurement of fluctuating pressures on coarse bed material. *Journal of Hydraulic Engineering* **131** (9), 770–781.
- HURTHUR, D., LEMMIN, U. & TERRAY, E. A. 2007 Turbulent transport in the outer region of rough-wall open-channel flows. *Journal of Fluid Mechanics* **574**, 465–493.

Bibliography

- ISBASH, S. 1932 *Construction of dams by dumping stones into flowing water*. Tech. rept. Leningrad. Engineering division, Eastport Maine., translated by A. Dovjikov for the War Department of the US Engineer office.
- JACKSON, G. 1976 Sedimentological and fluid-dynamic implications of the turbulent bursting phenomenon in geophysical flows. *Journal of Fluid Mechanics* **77**, 531–560.
- JONGELING, T. H. G., BLOM, A., JAGERS, H. R. A., STOLKER, C. & VERHEIJ, H. J. 2003 *Design method granular protections*. Tech. rept. Q2933 / Q3018. WL|Delft Hydraulics, in Dutch.
- KALINSKE, A. A. 1947 Movement of sediments as bed load in rivers. *Trans. Am. Geophys. Union* **28** (4), 615–621.
- KIM, J. 1989 On the structure of pressure fluctuations in simulated turbulent channel flow. *Journal of Fluid Mechanics* **205**, 421–451.
- KIRCHNER, J. W., DIETRICH, W. E., ISEYA, F. & IKEDA, H. 1990 The variability of critical shear stress, friction angle, and grain protrusion in water-worked sediments. *Sedimentology* **37**, 647–672.
- KIRONOTO, B. & GRAF, H. W. 1994 Turbulence characteristics in rough uniform open-channel flow. *Proc. Inst. Civ. Engrs. Wat., Marit. & Energy* **106**, 333–344.
- KLINE, S. J., REYNOLDS, W. C., SCHRAUB, F. A. & RUNSTADLER, P. W. 1967 The Structure of Turbulent Boundary Layers. *Journal of Fluid Mechanics* **30**, 741–773.
- KNIGHT, D. W., DEMETRIOU, J. D. & HAMED, M. E. 1984 Boundary shear in smooth rectangular channels. *Journal of Hydraulic Engineering* **110**, 504–422.
- KRÖGSTAD, P.-A. & ANTONIA, R. A. 1999 Surface roughness effects in turbulent boundary layers. *Experiments in Fluids* **27**, 450–460.
- KRÖGSTAD, P.-A., ANTONIA, R. A. & BROWNE, L. W. B. 1992 Comparison between rough- and smooth-wall turbulent boundary layers. *Journal of Fluid Mechanics* **245**, 599–617.
- LEE, I. & SUNG, H. J. 2002 Multiple-arrayed pressure measurement for investigation of the unsteady flow structure of a reattaching shear layer. *Journal of Fluid Mechanics* **463**, 377–402.
- LING, C. H. 1995 Criteria for incipient motion of spherical sediment particles. *Journal of Hydraulic Engineering* **121** (6), 472–478.
- MARCHIOLI, C., ARMENIO, V., SALVETTI, M. V. & SOLDATIA, A. 2006 Mechanisms for deposition and resuspension of heavy particles in turbulent flow over wavy interfaces. *Physics of Fluids* **18** (2), 1–16.

- MAXEY, M. R. & RILEY, J. J. 1983 Equation of motion for a small rigid sphere in a non-uniform flow. *Physics of Fluids* **26** (4), 883–889.
- MCEWAN, I. & HEALD, J. 2001 Discrete particle modeling of entrainment from flat uniformly sized sediment beds. *Journal of Hydraulic Engineering* **127** (7), 588–597.
- MCEWAN, I., SØRENSEN, M., HEALD, J., TAIT, S., CUNNINGHAM, G., GORING, D. & WILLETS, B. 2004 Probabilistic modelling of bed-load composition. *Journal of Hydraulic Engineering* **130** (2), 129–139.
- MEYER-PETER, E. & MÜLLER, R. 1949 Eine Formel zur Berechnung des Geschiebetransports. *Schweizer Bauzeitung* **67** (3), 29–32.
- MILLER, M. C., MCCAVE, I. N. & KOMAR, P. D. 1977 Threshold of sediment motion under unidirectional currents. *Sedimentology* **24** (7), 507–527.
- MONIN, A. S. & YAGLOM, A. M. 1971 *Statistical fluid mechanics*. MIT-press, originally published in 1965 by Nauka Press, Moscow, under the title "Statisticheskaya gidromekhanika - Mekhanika Turbulentnosti".
- NAOT, D. 1984 Response of channel flow to roughness heterogeneity. *Journal of Hydraulic Engineering* **110** (11), 1568–1587.
- NELSON, J. M., SHREVE, R. L., MACLEAN, S. R. & DRAKE, T. G. 1995 Role of near-bed turbulence structure in bed load transport and bed form mechanics. *Water Resources Research* **31** (8), 2071–2086.
- NEZU, I. & NAKAGAWA, H. 1993 *Turbulence in open-channel flows*. Monograph Series . A.A. Balkema, Rotterdam.
- NEZU, I. & RODI, W. 1985 Experimental study on secondary currents in open-channel flow. In *Proceedings of 21st IAHR Congress*, , vol. 2, pp. 115–119. IAHR, Melbourne.
- NEZU, I. & RODI, W. 1986 Open-channel flow measurements with a laser doppler anemometer. *Journal of Hydraulic Engineering* **112** (5), 335–355.
- NIKORA, V.I., MCEWAN, I., MCLEAN, S., COLEMAN, S., WALTERS, R. & POKRAJAC, D. 2007a Double-averaging concept for rough-bed open-channel and overland flows: Theoretical background. *Journal Hydraulic Engineering* **133** (8), 873–883.
- NIKORA, V.I., MCLEAN, S., COLEMAN, S., POKRAJAC, D., MCEWAN, I., CAMPBELL, L., ABERLE, J., CLUNIE, D. & KOLL, K. 2007b Double-averaging concept for rough-bed open-channel and overland flows: Applications. *Journal Hydraulic Engineering* **133** (8), 884–895.
- NIKORA, V. I. 1999 Origin of the -1 spectral law in wall-bounded turbulence. *Physical Review Letters* **83** (4), 734–736.

Bibliography

- NIKORA, V. I. & GORING, D. G. 2000 Eddy convection velocity and Taylor's hypothesis of frozen turbulence in a rough-bed open-channel flow. *Journal of Hydraulics and Hydraulic Engineering* **18** (2), 75–91.
- NIKORA, V. I., GORING, D. G. & BIGGS, B. J. F. 1998 On gravel-bed roughness characterization. *Water Resources Research* **34** (3), 517–527.
- NIKORA, V. I., GORING, D. G., MACEWAN, I. & GRIFFITHS, G. 2001 Spatially averaged open-channel flow over rough bed. *Journal of Hydraulic Engineering* **127** (2), 123–133.
- NIKORA, V. I., KOLL, K., MCEWAN, I., MCLEAN, S. & DITTRICH, A. 2004 Velocity distribution in the roughness layer of rough-bed flows. *Journal Hydraulic Engineering* **130** (10), 1036–1024.
- PAIEMENT-PARADIS, G., BUFFIN-BELANGÉ, T. & ROY, A. 2003 Scalings for large turbulent flow structures in gravel-bed rivers. *Geophysical Research Letters* **30** (14), 1–4.
- PAPANICOLAOU, A. N., DIPLAS, P., EVAGGELOPOULOS, N. & FOTOPOULOS, S. 2002 Stochastic incipient motion criterion for spheres under various bed packing conditions. *Journal of Hydraulic Engineering* **128** (4), 369–380.
- PARKER, G. & KLINGEMAN, P. C. 1982 On why gravel bed streams are paved. *Water Resources Research* **18** (5), 1409–1423.
- PARKER, G., SOLARI, L. & SEMINARA, G. 2003 Bedload at low shields stress on arbitrarily sloping beds: alternative entrainment formulation. *Water Resources Research* **39** (7), 1183.
- PILARCZYK, K. W. 2001 Unification of stability formulae for revetements. In *Proceedings of 29th IAHR congress*. IAHR.
- POGGY, D., PORPORATO, A. & RIDOLFI, L. 2003 Analysis of the small-scale structure of turbulence on smooth and rough walls. *Physics of Fluids* **15** (1), 35–46.
- POKRAJAC, D., FINNIGAN, J.J., MANES, C., MCEWAN, I. & NIKORA, V. 2006 On the definition of shear velocity in rough bed open-channel flows. In *River Flow 2006* (ed. R. Ferreira, E. Alves, J. Leal & A. Cardoso). A.A. Balkema, Rotterdam.
- PRINOS, P. 2004 Turbulence models for flow in porous media: reality or myth? In *Proceedings of the 6th International Conference on Hydro-Science and -Engineering (31.05-3.06.2004)* (ed. M. S. Altinakar, S. S. Y. Wang, K. P. Holz & M. Kawahara). National Center of Computational Hydroscience and Engineering, ICHE.
- PRINOS, P., SOFIALIDIS, D. & KERAMARIS, E. 2003 Turbulent flow over and within a porous bed. *Journal of Hydraulic Engineering* **129** (9), 720–733.

- VAN RADECKE, H. & SCHULZ-DUBOIS, E.O. 1988 Linear response of fluctuating forces to turbulent velocity components. In *Applications of Laser Anemometry to Fluid Mechanics, Lisbon, Portugal*.
- RAFFEL, M., WILLERT, C. & KOMPENHANS, J. 1998 *Particle Image Velocimetry*. Springer, Berlin.
- RAUPACH, R. M. 1972 Conditional statistics of Reynolds stress in rough-wall and smooth-wall turbulent boundary layers. *Journal of Fluid Mechanics* **108**, 363–382.
- VAN RIJN, L. C. 1984 Sediment transport. Part I: Bed load transport. *Journal of Hydraulic Engineering* **110** (10), 1431–1456.
- VAN RIJN, L. C. 2007 Unified view of sediment transport by currents and waves. I: Initiation of motion, bed roughness, and bed-load transport. *Journal of Hydraulic Engineering* **133** (6), 649–667.
- ROBINSON, S. K. 1991 Coherent motions in the turbulent boundary layer. *Annual Review of Fluid Mechanics* **23**, 601–638.
- ROY, A. G., BUFFIN-BÉLANGER, T., LAMARRE, H. & KIRKBRIDE, A. D. 2004 Size, shape and dynamics of large-scale turbulent flow structures in a gravel bed river. *Journal of Fluid Mechanics* **500**, 1–27.
- SCHEWE, G. 1983 On the structure and resolution of wall-pressure fluctuations associated with turbulent boundary-layer flow. *Journal of Fluid Mechanics* **134**, 311–328.
- SCHMEECKLE, M. W. & NELSON, J. M. 2003 Direct numerical simulation of bed-load transport using a local, dynamic boundary condition. *Sedimentology* **50**, 279–301.
- SCHÖBERL, F. 1979 Zur Frage der Gefällsbildung beim Selbststabilisierungsprozess von erodierenden Flußstrecken. Ph.D., Institut für Konstruktiven Wasser- und Tunnelbau, Universität Innsbruck.
- SECHET, P. & LE GUENNEC, B. 1999 Bursting phenomenon and incipient motion of solid particles in bed-load transport. *Journal of Hydraulic Research* **37** (5), 683–696.
- SHIELDS, A. 1936 Anwendung der Ähnlichkeitsmechanik und der Turbulenzforschung auf die Geschiebebewegung. *Mitteilungen der Versuchsanstalt für Wasserbau und Schiffbau (Berlin)* **26**.
- SHIMIZU, Y., TSUJIMOTO, T. & NAKAGAWA, H. 1990 Experiment and macroscopic modelling of flow in highly permeable porous medium under free-surface flow. *Journal of Hydroscience and Hydraulic Engineering* **8** (1), 69–78.
- SHVIDCHENKO, A. B. & PENDER, G. 2001 Macro-turbulent structure of open-channel flow over gravel beds. *Water Resources Research* **37** (3), 709–719.

Bibliography

- SINGH, K. M., SANDHAM, N. D. & WILLIAMS, J. J. R. 2007 Numerical simulation of flow over a rough bed. *Journal of Hydraulic Engineering* **133** (4), 386–398.
- SMART, G. M. & HABERSACK, H. M. 2007 Pressure fluctuations and gravel entrainment in rivers. *Journal of Hydraulic Research* **45** (5), 661–673.
- SMITH, C. R. & METZLER, S. P. 1983 The characteristics of low-speed streaks in the near-wall region of a turbulent boundary layer. *Journal of Fluid Mechanics* **129**, 27–54.
- SONG, T. 1994 Velocity and turbulence distribution in non-uniform and unsteady open-channel flow. Ph.D., École Polytechnique Fédérale de Lausanne.
- STÖSSER, T., FRÖHLICH, J. & RODI, W. 2007 Turbulent open-channel flow over a permeable bed. In *Proceedings 32nd IAHR Congress, Venice*.
- STÖSSER, T., RODI, W. & FRÖHLICH, J. 2005 LES of open-channel flow over a layer of spheres. In *Proceedings of 31st IAHR Congress, Seoul*.
- SUTHERLAND, A. J. 1967 Proposed mechanism for sediment entrainment by turbulent flows. *Journal of Geophysical Research* **72** (24), 6183–6194.
- THOMAS, A. S. W. & BULL, M. K. 1983 On the role of wall-pressure fluctuations in deterministic motions in the turbulent boundary layer. *Journal of Fluid Mechanics* **128**, 283–322.
- TOMKINS, C. D. 2001 The structure of turbulence over smooth and rough walls. Ph.D., University of Illinois, Graduate College.
- TOMKINS, C. D. & ADRIAN, R. J. 2003 Spanwise structure and scale growth in turbulent boundary layers. *Journal of Fluid Mechanics* **490**, 37–74.
- TSUJI, Y., FRANSSON, J. H. M., ALFREDSSON, P. H. & V., JOHANSSON A. 2007 Pressure statistics and their scaling in high-Reynolds-number turbulent layers. *Journal of Fluid Mechanics* **585**, 1–40.
- UHLMANN, M. & FRÖHLICH, J. 2007 Transport of heavy spherical particles in horizontal channel flow. In *High performance computing in science and engineering 2007, HLRS, Springer (to appear)*.
- UITTENBOGAARD, R., HOFFMANS, G. & AKKERMAN, G. J. 1998 Turbulence schematization for stone stability assessment. *Tech. rept. Q2395.30. WL/Delft Hydraulics, Delft*.
- VOLLMER, S. & KLEINHANS, M. 2007 Predicting incipient motion, including the effect of turbulent pressure fluctuations in the bed. *Water Resources Research* (43), 1–16.
- VOLLMER, S., DE LOS SANTOS RAMOS, F., DAEBEL, H. & KÜHN, G. 2002 Micro scale exchange processes between surface and subsurface water. *Journal of Hydrology* **269**, 3–10.

- WANG, J., CHEN, C., DONG, Z. & XIA, Z. 1993 The effects of bed roughness on the distribution of turbulent intensities in open-channel flow. *Journal of Hydraulic Research* **31** (1), 89–98.
- WANG, Z.-Y. 1999 On density waves developed in gravity channel flows of granular materials. *International Journal of Sediment Research* **14** (2), 179–186.
- WEITBRECHT, V. 2004 Influence of dead-water zones on the dispersive mass transport in rivers. Ph.D., University of Karlsruhe, Institute for Hydromechanics.
- WIBERG, P. L. & SMITH, J. D. 1987 Calculations of the critical shear stress for motion of uniform and heterogeneous sediments. *Water Resources Reserach* **23**, 1471–1480.
- WILLEMETZ, J. C. 1997 *DOP1000. Signal Processing User's Manual*.
- WILLMARTH, W. W. 1975 Structure of turbulence in boundary layers. *Adv. Appl. Mech.* **15**, 159–254.
- WILLMARTH, W. W. & LU, S. S. 1972 Structures of Reynolds stress near the wall. *Journal of Fluid Mechanics* **55**, 56–92.
- WU, F.-C. & CHOU, Y.-J. 2003 Rolling and lifting probabilities for sediment entrainment. *Journal of Hydraulic Engineering* **129** (2), 110–119.
- WU, F.-C. & JIANG, M.-R 2007 Numerical investigation of the role of turbulent bursting in sediment entrainment. *Journal of Hydraulic Engineering* **133** (3), 329–334.
- XINGKUI, W. & FONTIJN, H. L. 1993 Experimental study of the hydrodynamic forces on a bed element in an open-channel with a backward-facing step. *Journal of Fluids and Structures* **7**, 299–318.
- YANG, S.-Q. 2005 Interactions of boundary shear stress, secondary currents, and velocity. *Fluid Dynamics Research* **36**, 121–136.
- YANG, S.-Q., TAN, S.-K & LIM, S.-Y 2004 Velocity distribution and dip-phenomenon in smooth uniform open-channel flows. *Journal of Hydraulic Engineering* **130** (12), 1179–1186.
- ZANKE, U. C. E. 2003 On the influence of turbulence on the initiation of sediment motion. *International Journal of Sediment Research* **18** (1), 17–31.
- ZHOU, J., ADRIAN, R. J. & BALACHANDAR, S. 1996 Autogeneration of near-wall vortical structures in channel flow. *Physics of Fluids* **8** (1), 288–290.
- ZHOU, J., ADRIAN, R. J., BALACHANDAR, S. & KENDALLY, T. M. 1999 Mechanisms for generating coherent packets of hairpin vortices in channel flow. *Journal of Fluid Mechanics* **387**, 353–396.

List of Figures

1.1	Schematic illustration of turbulence-related phenomena such as sediment transport, flow-biota interactions and pollutant spreading.	1
2.1	Flow influenced by the heterogeneity of a rough permeable bed and definition of the roughness geometry function ϕ	6
2.2	Definition of a right-handed coordinate system and the corresponding velocity components, as used hereinafter. The transverse axis is directed out of the plane.	7
2.3	Uniform, turbulent 2D open-channel flow. Vertical distribution of stresses and velocities.	8
2.4	3D open-channel flow. Idealized distribution of boundary shear and associated secondary currents in a rectangular, straight-lined flume ($B/h = 2$). Shear stress distribution estimated after Chow (1959), flow data taken from Nezu & Nakagawa (1993).	9
2.5	Measured vertical distributions of $-\overline{\rho u'v'}$ in a smooth rectangular channel ($B/h = 2$), where $\delta_h/h \simeq 0.65$ and $\tau_o \approx \langle \overline{\tau_o} \rangle_b$. Reference is given to a (hypothetical) 2D-case with frictionless sidewalls (eq. 2.8). Data from Nezu & Nakagawa (1993, p.108).	10
2.6	Flow layers for 2D open-channel flow with a rough permeable bed (after: Nikora <i>et al.</i> , 2001).	12
2.7	Idealized velocity auto-spectra $S_{uu}(k)$, in double-logarithmic scales. (1) Production range. (2) Inertial subrange. (3) Viscous range.	16
2.8	Velocity fluctuations σ_{u_f}/u_* within a porous gravel bed underlying open-channel flow. The turbulence intensity diminishes with gravel depth y/d . Data from Detert <i>et al.</i> , 2007, $Re_{*d} = u_*d/\nu = 260-640$, $y/h \simeq 20$, $\phi \simeq 0.4$	20
2.9	Visualization of a hairpin vortex packet, where in addition streaky structures can be seen. Taken from Zhou <i>et al.</i> (1999), DNS, $Re_{u_*} = \delta u_*/\nu = 180$. The streamwise length of the shown fluid domain is $1800 \nu/u_*$	21
2.10	Conceptual model of coherent turbulent structures, consisting of zones of equal momentum travelling with velocity U_c and nested packets of hairpin vortices between them (Adrian, 2007). For open-channel flows, some packets are assumed to bulge up to the water surface causing weak boils (according to a model from Nezu & Nakagawa, 1993, p. 232).	22

List of Figures

2.11	Intensities of pressure fluctuations. DNS results for σ_p/τ taken from Kim (1989) (smooth walls, $Re_{*\delta}=u_*\delta/\nu=179$) and Breugem <i>et al.</i> (2006) (rough permeable wall, $Re_{*\delta}=u_*\delta/\nu=176$, $\phi = 0.60$). Here, $y = 0$ refers to the smooth wall and the roughness tops, respectively.	25
2.12	Conceptual model of large-scale flow structure, including the associated wall pressure fluctuations (modified after Thomas & Bull, 1983).	27
2.13	Force balance for a single grain (after Hofland, 2005).	29
2.14	Redraft of Shields' diagram.	32
2.15	PDF-Sketches of $P(\tau_b)$, characterizing the flow attack and $P(\tau_c)$ characterizing the bed resistance against entrainment.	33
2.16	Detail of typical instantaneous flow field just before movement of the target stone. 2D PIV from Hofland & Booij (2004). Vectors are $u' - 0.65\langle\bar{u}\rangle$. Shading indicates vortex-cores, identified by the λ_{ci}^2 criterion (Zhou <i>et al.</i> , 1999).	36
3.1	Sketch of experimental setup, dimensions in (m), not to scale. a) view in streamwise direction, with both 2D PIV arrangements of setup A and B. b) side view, where the positions of the 1D ADCP probe can also be seen.	40
3.2	Principle of the PIV technique (source: <i>LaVision GmbH</i>).	41
3.3	Single PIV frame (negative print), where the seeding and also the gravel bed becomes visible. Raw picture from <i>Setup A</i> (xy-plane), according to the hatched area in fig. 3.1(b). The roughness crest is located at $y = 2.5$ mm and $y = 16$ pix, respectively.	43
3.4	Geometry of the ADCP-probe and its acoustic field, adjusted to measure $\bar{u}(y)$. For recordings of instantaneous profiles of $v'(y)$, the transducer had to be orientated vertically ($\theta = 90^\circ$). Dimensions in (mm), not to scale.	45
3.5	Schematic cross section of a piezo-resistive sensor to measure the differential pressure.	47
3.6	(a) Sketch of a pressure pickup (mm). (b) Array of MPPSs mounted on a grid, not covered by gravel yet. This arrangement was used in synchronous measurements of MPPS, PIV and ADCP. (c) Measurement to test the response time of the MPPS, where the sensor reacts on the double pulse of the PIV laser sheet of $\Delta t = 2$ ms.	48
3.7	Gravel with uniform grain size. a) Installation for flume experiments, where also the hull construction can be seen. b) Experimental setup to determine the roughness geometry parameter.	50
3.8	In-situ photographs from a gravel bank at the river Rhine on 02.08.2006 (low water). a) Place of excavation for the non-uniform material. b) Armoring layer and substructure.	51
3.9	a) Flume bed prepared for the spheres experiments. The spheres in the vicinity of the laser sheet were painted black to minimize reflections of the laser sheet. b) Three layers of spheres in densest (pyramidal) package.	52

- 4.1 Velocity contour plots $\bar{u}(y, z)$, scaled with outer variable U . Cross sectional view in streamwise direction for (a) #uni3, and (b) #uni6. The nine positions of the ADCP probe are indicated by the dotted vertical grid. As an indication of secondary currents, the maximum centerline velocity \bar{u}_{\max} is located below the water surface. 60
- 4.2 Vertical distribution of time averaged velocity components $\bar{v}(y)$ and $\bar{u}(y)$ in the centerline of the flume. Scaled with inner variable $u_* \equiv u_{*\log}$, plotted with grain size d . (A plot with k_s would match the curves.) Data gained by PIV (filled, black markers) and ADCP (unfilled, light markers). Lines show best fits for eqs 2.16 and 4.4. Dashed lines indicate respectively the water surfaces and the upper grain crest for each measurement. 62
- 4.3 Contour-plots of turbulence intensities $\sigma_v(y, z)/U$. Cross sectional view for (a) #uni3, and (b) #uni6. 63
- 4.4 One-sided spectra $S_{uu}(y/\delta_h \simeq 0.2)$. The bold lines denote the spectra from PIV recordings calculated using Welch's method with a window length of $n = 2^6$ (rectangular and no overlapping). Symbols indicate wave lengths of $L = n \cdot 2.52$ mm with $n = 2^{[6,5,\dots,2]}$. The thin lines for #uni3 and #uni6 denote S_{uu} for PIV recordings with a high noise level, as the time step Δt between two double frames was chosen too short. Here, exceptionally a 3×3 Gaussian filter was applied (bold lines). The lines declining by $(k/2\pi)^{-5/3}$ give an extrapolation to 3η . The dashed lines denote spectra estimated using Welch's method with a maximum window length of $n = 2^6 + 16$. The apparent maxima of the spectra are due to the limited streamwise length of the PIV frame, the real maximum is expected to be larger. 65
- 4.5 Vertical distribution of turbulence intensities $\sigma_v(y)$ and $\sigma_u(y)$ at the centerline of the flume, scaled with inner variable u_* . Data gained by PIV (filled, black symbols) and ADCP (unfilled, light symbols). (a) Data for #uni*i* and #rhi9, plotted with outer variable δ_h . The velocity fields for #uni3 and #uni6 are filtered by a 3×3 Gaussian filter to compensate peak-locking noise. Dashed lines show eq. 2.23 with parameters from Nezu & Nakagawa (1993) for smooth walls. Lines show eq. 2.23 with parameters from Kironoto & Graf (1994) for rough walls. (b) Data for #sphi, plotted with inner variable k_s 67
- 4.6 Vertical distributions of form-induced stresses and Reynolds stresses, scaled with inner variable u_*^2 . (a) #uni*i* and #rhi9 plotted with outer variable δ_h . The velocity fields for #uni3 and #uni6 are filtered by a 3×3 Gaussian filter to compensate peak-locking noise. The line refers to eq. 4.9 with $u_{*uv}/u_* = 90\%$, the dashed lines gives variations of $\pm 3\%$. (b) #sphi plotted with inner variable k_s 69
- 4.7 Correlation coefficient, plotted with outer variable δ_h 69

List of Figures

4.8	Sequence of instantaneous velocity fields for #sph1, where the passage of a large-scale wedge-like fluid structure can be observed. Only every second frame is plotted. The velocity field was filtered by a 2×2 filter. For visualization, the vectors are presented with a constant convection velocity $\vec{u}_c = [0.85U, 0]$ removed. In x , only every fifth vector is plotted. Contours of λ_{ci}^2 highlight the location of vortex cores. The shading indicates $\sqrt{(u^2 + v^2)} > U$. The shear layer between the faster and the slower moving fluid zones is densely populated with eddies.	71
4.9	Typical pictures of wedge-like flow structures as observed for (a) #sph1, (b) #uni6, and (c) #rhi9. The velocity field was filtered by a 2×2 filter. Contours of λ_{ci}^2 are shown to highlight the location of vortex cores. The shading indicates u'/U in steps of 0.1.	72
4.10	Time-averaged cross correlation $\overline{C_{\lambda u}}$ between each of 1740 velocity fields of $u'(x, y)$ and $\lambda_{ci}^2(y_{ref}/\delta_h \simeq 0.2)$ for (a) #sph1, (b) #uni6, and (c) #rhi9. Spacing contour is in steps of 0.5%. The frame sizes are plotted in the same size relation as originally seen by the camera. The result gives some evidence that mean wedge-like flow structures exist above rough walls, where a series of clockwise rotating eddies are located along a line inclined at approximately 10 - 20° from the wall (see zero line).	74
4.11	Sequence of two instantaneous velocity fields for #sph1, where the passage of elongated streaky structures can be observed. Top view on a horizontal layer at $y_t = 4.5$ mm above the spheres' crest (identical with $y = 9.5$ mm). The velocity fields are filtered twice by a 3×3 Gaussian filter. For visualization, the vectors are presented with the convection velocity $\vec{u}_c = [\langle \bar{u} \rangle, 0]$ removed. In x , only every fifth vector is plotted. Contours of swirling strength highlight the location of vortex cores rotating around a vertical axis. The shading indicates $\sqrt{(u^2 + v^2)} > \langle \bar{u} \rangle$	76
4.12	Top view of instantaneous velocity fields of $u'/\langle u \rangle$ near the bed. Typical pictures of streaky structures can be seen for three different types of bed: (a) spheres, $[y_t, y] = [4.5, 9.5]$ mm (sequel to fig. 4.12), (b) uniform gravel, $[y_t, y] = [5, 7.5]$ mm, and (c) Rhine gravel, $[y_t, y] = [5, 11.5]$ mm. The velocity fields are filtered by a 3×3 Gaussian filter. Bold contours of swirling strength highlight the location of vortex cores. $u'/\langle u \rangle = 0$ is pronounced by thin lines. The representative grain size d is indicated in the background. The frame sizes are plotted in the same size relation as originally seen by the camera.	77
4.13	Time-averaged cross correlation $\overline{C_{u_z u}}$ between each of (a) 819 fields, and (b),(c) 1003 velocity fields of $u'(x, z)$ and $u'(z_{ref})$. The horizontal dashed lines give z_{ref} , the vertical dashed lines give $r_x/k_s = [\pm 1.5, 0]$ in reference to fig. 4.14. Contour spacing is in steps of 5%. The results show that flow structures in the near-bed region of rough beds own the inherent tendency to be elongated. Their breadth λ_z scales adequately with k_s . In reference to the instantaneous velocity fields of fig. 4.12, the given $\overline{C_{u_z u}}$ are based on exactly the same experimental runs.	78

4.14 Time-averaged cross correlation $\overline{C_{u_z u}}$ for (a) #sphi, (b) #uni, and (c) #rhi9 at $r_x/k_s = [\pm 1.5, 0]$ (see fig. 4.13). The thicker the lines, the larger the vertical distance to the roughness tops y_t . The zero-crossing distances of the lines is interpreted as a measure of the streak spacing λ_z , *i.e.* the distance between the centerlines of streaks with the same algebraic sign. 79

4.15 Streak spacing λ_z plotted with the distance to the roughness tops, y_t , and scaled with k_s . Filled symbols indicate the spacing at $r_x/k_s = 0$, unfilled symbols indicate the spacing at $r_x/k_s = \pm 1.5$. The figure is supplemented by data from Defina (1996) and a linear fit to the whole plotted data set (eq. 4.13). 80

4.16 Arrangements of the MPPS. 80

4.17 Simultaneous times series of pressure fluctuations $p'(t)$ for #uni6. Line widths from thick to thin correspond to $y = [+10, +5, -7, -22]$ (mm), indicating the fluctuating part of drag and lift as $[D', L', D', D']$. Here, the sensors indicating drag fluctuations are vertically aligned; the sensor indicating lift fluctuations is at $\Delta z = +80$ mm relative to the other sensors (light gray line). 81

4.18 PDFs of measured instantaneous pressure fluctuations slightly above the gravel crest (#uni6). (a) D' (10 independent signals), (b) L' (14 independent signals), compared with eqs 4.14 and 4.18, and normalized by its respective standard deviation σ_i . The two on the left are plotted with linear scales in order to evaluate the shape of the distribution around the mean; the two on the right are plotted with semi-logarithmic scales to better represent the shape of the tails. 84

4.19 PDFs of measured instantaneous pressure fluctuations at the gravel tops (#uni6). (a) D' (2 independent signals). (b) L' (14 independent signals). 85

4.20 PDFs of measured instantaneous pressure fluctuations with the gravel bed (#uni6, 9 independent signals). 85

4.21 One-sided power spectra for pressure signals at different vertical positions (#uni6). The area under the curves equals the variances σ^2 . Line widths from thick to thin correspond to $y = [10, 5, -7, -22, -38]$ (mm), indicating the fluctuating part of drag and lift as $[D', L', D', D', D']$ (recall fig. 4.16). Here, the sensors indicating drag fluctuations are vertically aligned; the sensor indicating lift fluctuations is at $\Delta z = 80$ mm relative to the other sensors (light gray line, see also fig. 4.17). The dashed curve denotes the possible influence of long-waves in the outer flow (eqs 4.19 and 4.20). The vertical line highlights the response time of 10 ms guaranteed by the manufacturer. The dotted horizontal line refers approximately to the white noise level. The influence of the low pass filter with the cut-off frequency at 500 Hz becomes prominent for $f > 200$ Hz. 87

List of Figures

4.22 Vertical profiles of the standard deviation of the drag and lift, σ_D and σ_L , for runs #uni*i*, plotted with k_s (a) Scaled with open-channel flow variable τ_o . (b) Scaled with seepage flow variable $\rho g u_*/k_f$. The position of the roughness crest ($y_t = 0$) is highlighted by the horizontal line. Filled symbols refer to σ_D , unfilled symbols refer to σ_L . The measured signals are filtered from white noise (see level at fig. 4.21). 90

4.23 Vertical profiles of σ_D/τ_o (left column) and σ_L/τ_o (right column) for (a) #uni*i*, (b) #rhi9, and (c) #sphi. The given data points have removed both long wave oscillations in the seepage flow and white noise. The fits of eq. 4.23 and eq. 4.22 are given by dashed and continuous lines, respectively. Roughness crest and grain diameter d are shown in the background. Filled (unfilled) symbols refer to σ_D (σ_L). The thinner parallel lines give a vertical range of $\pm 0.25 y/k_s$ 91

4.24 Typical synchronous time series of pressure fluctuations p'/τ_o at $y = 0$ in comparison with the velocity fluctuations $\langle \overline{uu'} \rangle / u_*^2$ spatially averaged over a vertical streamwise area of (5×5) mm² above the pressure sensor (#uni6). Lift is indicated by $L' = -p'$ (compare fig. 4.16(b)) 94

4.25 Time series of 0.7 s, where a noteworthy pressure drop is recognized (cut-out of fig. 4.24). The vertical dashed lines refer to the corresponding PIV-frames 1072-1076. 94

4.26 Five original images of $u'(x, y)$ together with the spliced image obtained from them (bottom). The single frames were smoothed by a 3×3 Gaussian filter, the spliced image was finally smoothed by a 3×3 moving average filter. The shading indicates u'/U in steps of 0.1 (colorbar: see fig. 4.9), the isoline denotes $u'/U = 0$. The cross refers to the position of the pressure sensor, whose measured signal is given in fig. 4.24. 96

4.27 Top view on the MPPSs mounted in the gravel layer, here in the arrangement as used for synchronous PIV measurements of setup *B*. The white circle highlights the target sensor head at $[x, y, z] = [-6.0, -1.5, 0.2]$ (mm). The size of the frame is exactly the same as in fig. 4.12. 98

4.28 Synoptic view of spliced velocity field and the corresponding reconstructed bed-pressure fluctuations (#uni6). The visualization gives a spatial view of the extreme pressure drop event as shown in fig. 4.25. 100

4.29 Synoptic view of spliced velocity field and the corresponding reconstructed bed-pressure fluctuations (#uni6). In opposition to fig. 4.28, this event gives an example of a more typical moderate pressure drop event. 101

4.30 Synoptic view of a spliced velocity field and the corresponding reconstructed bed-pressure fluctuations (#uni6). Four dashed ellipsoids highlight pressure drop events and the assumed area of the corresponding velocity-fields. 102

4.31 Synoptic view of a spliced velocity field and the corresponding reconstructed bed-pressure fluctuations (#uni6). The dashed lines retrace a meandering low velocity streak and the corresponding p' -field. 103

4.32 Ensemble averaged time history of 25 essential pressure drops (lift) at #uni6. Measured at $y = 0$ synchronous to 1740 PIV recordings ($8.5 \text{ Hz} = 1/0.12 \text{ s}^{-1}$). Conditionally sampled to (a) maximum peak, (b) minimum peak. 105

4.33 Ensemble average of (a) the near-bed velocity field (side view) and (b) corresponding reconstructed bed-pressure fluctuations (#uni6). From 25 spliced PIV frames conditionally sampled from the maximum peak of 25 most essential pressure drops (criteria: $0.79 \text{ Pa}/0.1 \text{ s}$). The velocity field was finally filtered twice by a 3×3 moving average filter to facilitate interpretation. Due to sampling of the maximum pressure peak, the distinctiveness of the low-pressure field is weakened. 107

4.34 Ensemble average of (a) near-bed velocity field (top view) and (b) corresponding reconstructed bed-pressure fluctuations (#uni6). From 24 spliced PIV frames conditionally sampled from the maximum peak of 24 most essential pressure drops (criteria: $0.79 \text{ Pa}/0.1 \text{ s}$). The velocity field was finally filtered twice by a 3×3 moving average filter. Due to sampling of the maximum pressure peak, the distinctiveness of the low-pressure field is weakened. 108

5.1 Bed pressure fluctuations p_k in a porous gravel bed underlying turbulent open-channel flow. The gravel is of approximately uniform size, the pores are filled with fine sediment. The cleaning depth due the influence of turbulence is denoted by λ_c 114

5.2 Cleaning depth λ_c for two different types of gravel bed, estimated from eq. 5.18. The circles sketch the reference grain size d in dimensions of the vertical axis. (a) Uniform gravel. (b) Rhine Gravel, armored layer. 117

List of Tables

3.1	Parameter of the bed materials uniform gravel, gravel from the river Rhine (armoring layer), and spheres. The weighted mean of the whole grain size distribution is represented by d (eq. 2.35). For #uni $d \approx d_{50}$ and for #uni $d \approx d_{70}$ holds. ϕ is the roughness geometry parameter (eq. 2.3).	49
3.2	Experimental flow conditions. The integers [1,3,6,9] at the end of the indices refer approximately to the ratios of Q_i , U_i , and $Re_{h,i}$. At #uni9 the provided flow led to very slight sediment transport, where single grains were moving from time to time.	52
3.3	Performance of the synchronous and the additional measurements.	53
4.1	Shear parameters. $\langle \tau_o \rangle$ is calculated by eq. 2.13, and $\langle u_* \rangle$ was derived from them by applying eq. 2.15. The indices $\langle \cdot \rangle_{us}$ and $\langle \cdot \rangle_{ds}$ denote the spatial average of the upstream area ($x = -9.33$ to 0.0 m) and the downstream area ($x = 0.0$ to 4.42 m), respectively. u_{*uv} was estimated by extrapolating $-\langle u'v' \rangle$ to $y = 0$ (eq. 2.7). $u_* \equiv u_{*log}$ is gained from log-law fit (eq. 2.16).	56
4.2	Geometric parameters. h = water depth measured by ultrasonic probes, $\delta_h = y(\bar{u}_{max})$, d = characteristic grain size (eq. 2.35), k_s = equivalent sand roughness, $y_t - y$ = zero plane displacement, $y(\delta_R)$ = upper boundary of the roughness layer, θ_m = momentum thickness, η = Kolmogorov length scale.	58
4.3	Flow properties. Q = flow rate, $U = Q/(Bh)$ = bulk velocity, u_* = shear velocity, Reynolds-numbers: $Re_h = Uh/\nu$, $Re_{*h} = u_*h/\nu$, $Re_{*\delta} = u_*\delta_h/\nu$, $Re_{*d} = u_*d/\nu$, Froude-numbers: $Fr_h = U^2/(gh)$, $Fr_{*\Delta} = u_*^2/(\Delta gd)$, with $\Delta = \rho_s/\rho - 1$	59

Acknowledgements

First of all, I would like to express my sincere gratitude and appreciation to my advisor, Professor Gerhard H. Jirka, for his guidance, encouragement and support during my research. I also wish to thank my co-advisors, Professor Vladimir Nikora, and Professor Andreas Dittrich, for their valuable advice, as well as Emeritus Professor Wolfgang Rodi, and Emeritus Professor Hans H. Bernhart, for taking part in the advisor committee. Professor Gary Parker, University of Illinois, is gratefully acknowledged for the development of the ideas and the skeletal structure of the 'sediment cleaner' chapter. I am indebted to Bas Hofland's amazing Ph.D. thesis, which was particularly helpful to me. Once I recognized that it is impossible for me to reach his Champions-League standard, I slept well again.

I wish to thank all my colleagues at the Institute for Hydromechanics for their support during my work. In particular, I am very grateful to Volker Weitbrecht for his constructive discussion, to John Fenton for proof-reading my Germanical English, and to Anne Niepelt for her outstanding assistance, patience and cooperation, in particular during the elongated days of the gravel bed experiments. Many thanks to Gregor 'Gearloose' Kühn for his ingenious ideas, and to Roman von Rhein for being the goddess of L^AT_EX. I would also like to express my gratitude to the 'Werkstatt', incarnated by Jürgen Ulrich and Michael Ziegler. Thanks to Aktiv Sensor GmbH, Peter Giraud, Eva Stahl, and the Technical Service Center of the Institute of Production Science for their contribution in the development process of the miniaturized piezoresistive pressure sensors. Thanks to Weener Plastic Packaging Group for 4000 deodorant balls for free, and to the poor Eva Kaltenbach, for filling them with fine sand to weaken their buoyancy. Furthermore, thanks to Elena Radowski for the amazing PIV puppet theatre and for cleaning Augias literature stables. I am obliged to Eletta Negretti to be pleased with the flowers, and Cornelia Lang, Tobias Bleninger as well as Antje Haug simply for belonging to the IfH.

Support by the 'Baden-Württemberg Research Program Securing a Sustainable Living Environment' (BWPLUS, project BWR 25003) with funds of the State Baden-Württemberg is gratefully acknowledged. I appreciate the financial support from the Federal Waterways Engineering and Research Institute (BAW) for a previous project and the material support throughout the entire research that led to this doctoral thesis. I am deeply grateful to the State Baden-Württemberg for financing my teaching assistance position during most of the time at the IfH. Last but not least, I am very grateful to my parents, who have constantly and unconditionally supported me by much more than reanimated bicycles and East-Westphalian raspberry-foamcake for more than 33 years.

I like to give big thanks to the cleaning lady, representative for lots of co-workers contributed in their way to this thesis. Finally, thanks to every interested, stiff-necked reader who managed to study my thesis report even up to this sentence.

Curriculum Vitae

Personal data:

name: Martin Detert
date of birth: 27/09/74
place of birth: Lübbecke (Westphalia)
e-mail: detert@ifh.uka.de
Martin.Detert@web.de

school:

08/81 - 07/85 Primary School Gehlenbeck
07/85 - 06/94 Wittekind-Gymnasium Lübbecke

military service:

10/94 - 09/95 Pionierbrückenbataillon 130, Minden

higher education:

10/95 - 11/00 Civil engineering, University of Hanover,
Topic: hydraulic engineering
01/12/00 Graduation certificate: Dipl.-Ing.

professional experience:

01/01 - 03/02 Engineering office Dr.-Ing. V. Patzold
(dredging, mining, environmental engineering)
04/02 - 06/08 Institute for Hydromechanics, University of Karlsruhe
(teaching assistance and research)

Simultaneous 2D pressure and 2D velocity information at the rough water-sediment interface of streambeds were gained by a newly developed measurement setup. Structural findings concerning coherent flow structures are consistent with models originally developed for smooth walls. In the bed the pressure fluctuations decay exponentially within the first 1-2 equivalent sand roughnesses. For the first time a significant bed destabilizing flow-pressure pattern was identified: if high speed fluid in the wake of a large-scale sweep reaches the vicinity of the bed, it leads to a distinctive low-pressure field at the bed. This pattern is seen as the cause of sediment entrainment as well as the fundamental promoter for the exchange of mass and momentum.